IntechOpen

Magnesium Alloys

Properties in Solid and Liquid States

Edited by Frank Czerwinski

MAGNESIUM ALLOYS - PROPERTIES IN SOLID AND LIQUID STATES

Edited by **Frank Czerwinski**

Magnesium Alloys - Properties in Solid and Liquid States
http://dx.doi.org/10.5772/58293
Edited by Frank Czerwinski

Contributors

Henry Hu, Amany Mohamed Fekry, Masafumi Noda, Tomomi Ito, Hisashi Mori, Kunio Funami, Yoshio Gonda, Zuzanka Trojanova, Frank Czerwinski

Notice

First published in Croatia, 2014 by INTECH d.o.o.
eBook (PDF) Published by IN TECH d.o.o.
Place and year of publication of eBook (PDF): Rijeka, 2019.
IntechOpen is the global imprint of IN TECH d.o.o.
Printed in Croatia

Legal deposit, Croatia: National and University Library in Zagreb

Additional hard and PDF copies can be obtained from orders@intechopen.com

Magnesium Alloys - Properties in Solid and Liquid States
Edited by Frank Czerwinski

p. cm.

ISBN 978-953-51-1728-5

eBook (PDF) ISBN 978-953-51-6366-4

Meet the editor

Dr. Frank Czerwinski holds a Ph.D. degree in metallurgical engineering from McGill University, Montreal, Quebec, Canada and Ph.D. (Hons) and M.Sci. (Hons) degrees in materials science from the University of Mining and Metallurgy, Cracow, Poland. He has also completed post-doctoral studies at McMaster University, Hamilton, Ontario and at McGill University, Montreal, Quebec. During his professional career, Dr. Czerwinski was a University Professor of materials and metallurgical engineering and the faculty member. He was also Manager and Principal Scientist of numerous research projects sponsored by universities, research institutions and industry. After years of university teaching and research, he has joined, for over a decade, the global industrial sector. At present, he is with CanmetMATERIALS, Canada's principal federal research and development laboratory for materials. Dr. Czerwinski is the author of 2 monographs, 4 editorials, as well as the author and co-author of 16 patents and over 180 research papers in peer-review scientific journals and conference proceedings.

Contents

Preface XI

Section 1 Magnesium Alloys 1

Chapter 1 **Influence of Solute Atoms on Deformation Behaviour of Selected Magnesium Alloys 3**
Zuzanka Trojanová, Peter Palček, Pavel Lukáč and Zdeněk Drozd

Chapter 2 **Texture, Microstructure, and Mechanical Properties of Calcium-Containing Flame-Resistant Magnesium Alloy Sheets Produced by Twin-Roll Casting and Sequential Warm Rolling 49**
Masafumi Noda, Tomomi Ito, Yoshio Gonda, Hisashi Mori and Kunio Funami

Chapter 3 **Corrosion and Surface Treatment of Magnesium Alloys 67**
Henry Hu, Xueyuan Nie and Yueyu Ma

Chapter 4 **Corrosion Protection of Magnesium Alloys in Industrial Solutions 109**
Amany Mohamed Fekry

Chapter 5 **Corrosion of Materials in Liquid Magnesium Alloys and Its Prevention 131**
Frank Czerwinski

Preface

Magnesium alloys with their unique physical and chemical properties are important candidates for many modern engineering applications. Their density, being the lowest of all structural metals, makes them the primary choice in global attempts aimed at reducing the weight of transportation vehicles. Although it is not often emphasized, magnesium also creates challenges at certain stages of raw alloy melting, fabrication of net-shape components and their service. The first one is caused by very high affinity of magnesium to oxygen, which requires protective atmospheres increasing manufacturing cost and heavily contributing to greenhouse gas emissions. Another drawback is its relatively poor corrosion resistance in aqueous solutions and a susceptibility to galvanic corrosion, limiting many outdoor applications. A completely different challenge is caused by very high corrosivity of liquid magnesium towards materials it contacts, complicating processing of raw alloys and many manufacturing operations. Unfortunately, these drawbacks frequently overshadow the unique properties of magnesium including its high strength-to-weight ratio.

This book, created by contributions from experts in different fields of materials science, offers an overview of selected properties of magnesium and a variety of its alloys in solid and liquid states. Chapter 1 covers strengthening of alloys and fundamentals of plastic deformation, in particular an influence of solute atoms on deformation behavior of selected chemical combinations. The subject of mechanical properties is continued in chapter 2, emphasizing crystallographic texture, microstructure and mechanical properties of calcium-containing flame resistant magnesium alloy sheet, produced by twin roll casting and sequential warm rolling. This chapter provides a connection between bulk formability and surface reactivity of magnesium alloys. The essence of corrosion of magnesium in aqueous solutions is described in chapter 3, along with modern methods of surface engineering to build a barrier between the metallic surface and an active environment. As an extension of corrosion behavior, chapter 4 describes corrosion of magnesium alloys in industrial solutions, factors controlling corrosion reactions and modification of a solution chemistry to inhibit the reaction progress. While previous chapters consider corrosion of magnesium, the last chapter, 5, focusses on the opposite property of magnesium: its corrosivity in liquid state in regards to metallic and ceramic materials it contacts. As emphasized there, the corrosive attack of molten magnesium alloys imposes a challenge on the selection of materials applicable for hardware used for their processing. Each chapter contains a rich selection of references, useful for further reading.

A mixture of unique benefits and serious challenges of magnesium alloys in solid and liquid states, described in the book, makes it very useful for a broad audience of scientists and engineers from academia and industry. It is clear that in order to benefit from opportunities created by magnesium, its all characteristics should be fully understood. I hope that the book will contribute to progress in this understanding and attract an audience from all fields of metallurgy not only to generate the genuine research interest but also to create new application opportunities for magnesium and its alloys.

Frank Czerwinski
CanmetMATERIALS, Natural Resources Canada
Hamilton, Ontario
Canada

Section 1

Magnesium Alloys

Chapter 1

Influence of Solute Atoms on Deformation Behaviour of Selected Magnesium Alloys

Zuzanka Trojanová, Peter Palček, Pavel Lukáč and Zdeněk Drozd

Additional information is available at the end of the chapter

http://dx.doi.org/10.5772/58949

1. Introduction

Magnesium alloys due to their relative high specific strength and low density are used for a wide range of applications – for example in the automobile and transportation industries; they promise significant weight saving. Numerous studies have been performed in order to estimate their mechanical and physical properties. It is well known that many physical and mechanical properties of metals are influenced by alloying. The solute atoms cause an increase in the strengthening of materials. On the other hand, it is difficult to predict the effect of solute atoms on the strength and deformation behaviour of magnesium and its alloys because the experimental data concerning the critical resolved shear stress (CRSS) of single crystals of binary alloys are restricted.

In this chapter we deal with the effect of solute (foreign) atoms on the mechanical properties of magnesium. The foreign atoms are assumed to substitute for the matrix atoms and/or form precipitates. We restrict ourselves mainly to the yield stress and the true stress-true strain curves measured at a constant strain rate at room and higher temperatures. The deformation behaviour of polycrystals is influenced by the presence of crystal defects. Strength of a material is a result of strengthening mechanisms. One of the strengthening mechanisms is solution hardening defined as the increase of the initial flow stress as foreign atoms are dissolved in it [1, 2]. In this chapter original results of authors were used.

2. Fundamentals of plastic deformation

Plastic deformation of magnesium polycrystals occurs by glide of dislocations and/or twinning. Glide of dislocations with the Burgers vector of $1/3[11\bar{2}0]$ on (0001) basal plane is the

easiest slip mechanism; often called basal slip of <***a***> type dislocation. The CRSS is required to activate the glide of <***a***> type dislocations. In order to estimate the CRSS (the stress acting on the slip plane in the slip direction) for a binary magnesium alloy (Mg-X), experimental tests on single crystals are needed. The yield strength of polycrystals is connected with the CRSS of single crystals with help of the relationship $\sigma_y=M\tau_0$, where M is the Taylor orientation factor. The deformation behavior of magnesium and magnesium alloy polycrystals may be influenced by twinning and the activity of non-basal slip systems. Glide of <***a***> dislocations in prismatic planes and glide of<***c***+***a***> dislocations in the second-order pyramidal slip systems should be consider. However for explanation, it is important to consider not only the solute influence but also the effect of grain size. These factors may affect not only basal slip but also prismatic slip and twinning responsible for the mechanical properties. Crystallographic textures can also change the value of the yield strength as for instance for the case of rolled sheets deformed in the rolling direction [3, 4].

It is widely accepted that the stress necessary for the dislocation motion in the slip plane can be divided into two components:

$$\sigma_D = \sigma_i + \sigma^*, \tag{1}$$

where σ_i is the internal (athermal) contribution to the stress, resulting from long-range internal stresses impeding the plastic flow.

$$\sigma_i = \alpha_1 Gb \rho_t^{1/2}, \tag{2}$$

where G is the shear modulus, σ_1 is a constant describing interaction between dislocations, b is the Burgers vector of dislocations and ϱ_t is the total dislocation density. The effective stress σ^* acts on dislocations during their thermally activated motion when they overcome short range obstacles. The mean velocity of dislocations υ is connected with the plastic strain rate by the Orowan equation:

$$\dot{\varepsilon}=(1/M)\rho_m b v \tag{3}$$

where ϱ_m is the mobile dislocation density. The most common equation used in describing the average dislocation velocity as a function of the effective stress is an Arrhenius type. The plastic strain rate $\dot{\varepsilon}$ for a single thermally activated process can be expressed as:

$$\dot{\varepsilon}=\dot{\varepsilon}_0 \exp\left[-\Delta G\left(\sigma^*\right)/kT\right], \tag{4}$$

where $\dot{\varepsilon}_0$ is a pre-exponential factor containing the mobile dislocation density, the average area covered by the dislocations in every activation act, the dislocation Burgers vector, the vibration frequency of the dislocation line, and the geometric factor. T is the absolute temperature and k is the Boltzmann constant. $\Delta G(\sigma^*)$ is the change in the Gibbs free energy depending on the effective stress (thermal stress)$\sigma^*=\sigma_{ap}-\sigma_i$ and the simple form is

$$\Delta G(\sigma^*) = \Delta G_0 - V\sigma^* = \Delta G_0 - V(\sigma - \sigma_i). \quad (5)$$

Here ΔG_0 is the Gibbs free energy necessary for overcoming a short range obstacle without the stress (the barrier activation energy at zero stress) and V=bdL is the activation volume where d is the obstacle wide and L is the mean length of dislocation segments between obstacles. It should be mentioned that L may depend on the stress acting on dislocation segments. In a stress relaxation (SR) test, the specimen is deformed to a certain stress σ_0 and then the machine is stopped and the stress is allowed to relax. The stress decreases with the time t. The specimen can be again reloaded to a higher stress (load) and the SR test may be repeated. The time derivative $\dot{\sigma}=d\sigma/dt$ is the stress relaxation rate and $\sigma=\sigma(t)$ is the flow stress at time t during the SR. SR tests are very often analysed under the assumption that the SR rate is proportional to the strain rate $\dot{\varepsilon}$ and then $\sigma(t)$ can be expressed according to [5] as:

$$\Delta\sigma(t) = \sigma(0) - \sigma(t) = \alpha \ln(\beta t + 1), \quad (6)$$

where $\sigma(0) \equiv \sigma_0$ is the stress at the beginning of the stress relaxation at time t=0, β is a constant and $\alpha=kT/V$.

3. Mg-Li-Al (LAxy) alloys

3.1. Microstructure of Mg-Li alloys

Among Mg alloys, magnesium-lithium alloys, as the lightest metallic materials, are attractive for a large amount of applications. They are of great importance also for medicine purposes. Therefore, it is important to investigate mechanical properties at different temperatures and to estimate the deformation mechanisms responsible for the deformation behaviour of Mg-Li alloys at elevated temperatures. Pure Mg has hexagonal close packed structure. The density of Mg-Li alloy decreases with an increase of lithium content. The addition of Li increases ductility. The Mg–Li phase diagram shows that Li is soluble in hcp α-phase up to 4 wt%, while Mg alloyed with greater than 12 wt% Li has a bcc structure (β-phase) [6]. Ductility of the hcp α-phase are worse in comparison with the bcc alloys that are very good machinable and weldable. Disadvantages of Mg-Li alloys with bcc structure are a high chemical activity and poor corrosion resistivity. Some compromise would be an alloy with 8 wt% of Li (a mixture of phases $\alpha+\beta$) that might exhibit both improved mechanical properties as well as a good corrosion resistance. In light micrograph in Fig. 1, light α-phase and darker β-phase may be

visible. The alloys were produced by pressure infiltration under an argon pressure (up to 6 MPa) at temperatures of 615-635 K.

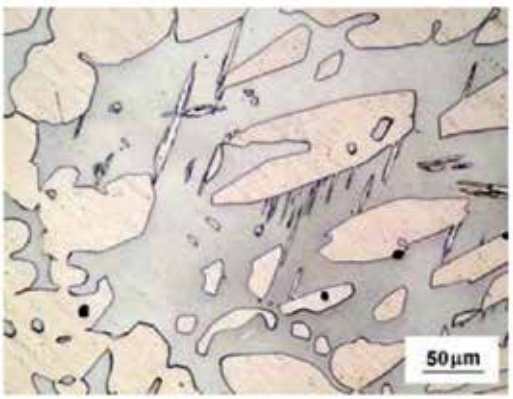

Figure 1. Light micrograph of the Mg8Li alloy.

3.2. Deformation of Mg-Li alloys

Compression tests were performed in an Instron type machine at a constant crosshead speed giving an initial strain rate of 2.4×10^{-4} s^{-1}. The argon atmosphere was used as a protecting atmosphere in the furnace at elevated temperatures. The compression yield stress (CYS), σ_{02}, was estimated as the flow stress at 0.2% offset strain. The ultimate compression strength (MCS), σ_{max}, corresponds to the maximum value of the flow stress. Samples were deformed to a predetermined strain of 0.3, and then deformation was interrupted.

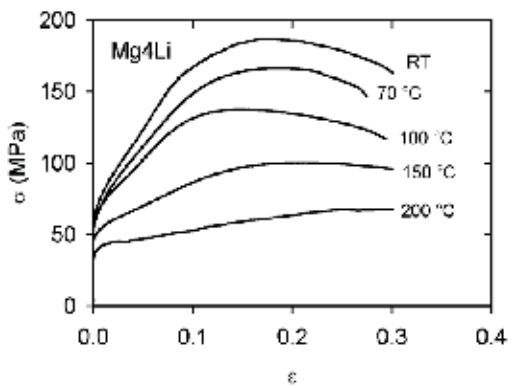

Figure 2. True stress-true strain curves estimated for Mg4Li alloy at various temperatures.

http://dx.doi.org/10.5772/58949

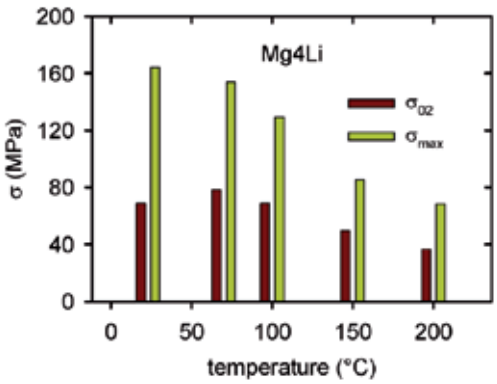

Figure 3. Temperature variation of the CYS and MCS estimated for Mg4Li alloy.

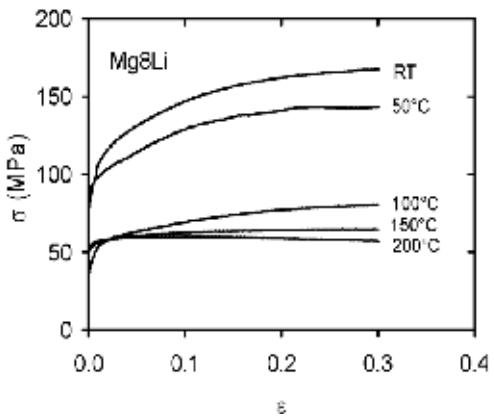

Figure 4. True stress-true strain curves estimated for Mg8Li alloy at various temperatures.

Figure 2 shows the true stress-true strain curves estimated at various temperatures. A significant hardening is obvious especially for lower temperatures. Figure 3 shows the temperature variation of the CYS, σ_{02}, as well as the MCS (σ_{max}) of Mg4Li alloy. It is apparent from Fig. 3 that the temperature variation of CYS exhibits a local maximum at a temperature of 70 °C. The MCS of Mg-4Li alloy decreases rapidly with increasing temperature. The differences between MCS and CYS exhibit a rapid decrease with increasing temperature. The true stress-true strain curves of Mg-8Li alloy measured in compression at various temperatures are shown in Fig. 4. A rapid decrease of the flow stresses at temperatures higher than 50 °C is obvious in Fig. 5. The temperature variation of the CYS exhibits a local maximum at 50 °C.

While the stress-strain curves estimated for Mg4Li exhibit a significant strain hardening, the curves observed for Mg12Li are very flat (Fig. 6); the difference between the CYS and MCS is relatively low and decreases with increasing temperature (Fig. 7).

The Mg-4Li alloy has *hcp* structure. The addition of Li to Mg increases the critical resolved shear stress (CRSS) for basal slip; the solid solution hardening is observed [7]. The CRSS of Mg4Li is almost independent on the temperature above room temperature while the CRSS for non-basal slip decreases with temperature below 200 °C as shown in [8]. The addition of Li causes a decrease of both ***a*** and ***c*** lattice parameters in Mg-Li solid solution [9].

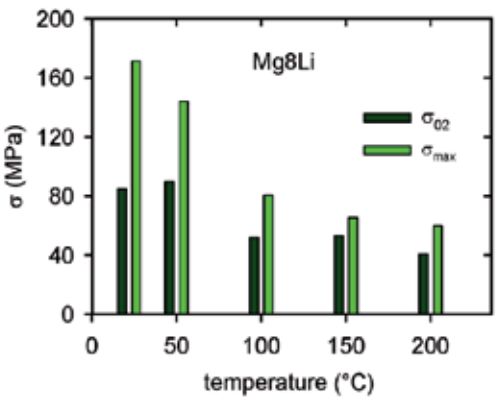

Figure 5. Temperature variation of the CYS and MCS estimated for Mg8Li alloy.

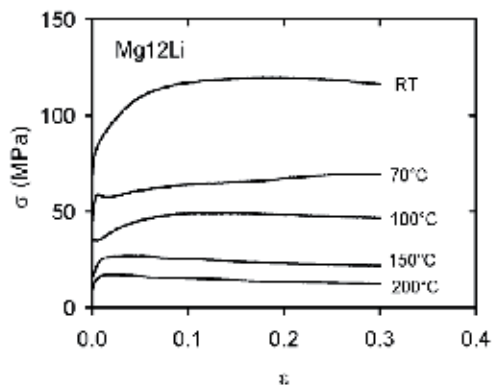

Figure 6. True stress-true strain curves of Mg12Li alloy at various temperatures.

http://dx.doi.org/10.5772/58949

It is well known that the dominant slip system in Mg and *hcp* Mg alloys at room temperature is the basal one. To fulfil von Mises criterion, a non-basal slip system should be active. The activity of non-basal slip systems plays an important role in dynamic recovery (softening). The pyramidal slip systems can be considered as non-basal slip systems. During deformation of magnesium alloy polycrystals, the motion not only **<a>** (basal) dislocations but also **<*c*+*a*>** (pyramidal) dislocations is assumed. Screw components of the <*c*+*a*> dislocations can move to the parallel slip planes by double cross slip and then annihilate, which causes a decrease in the strain hardening rate; softening is observed. With the addition of Li the c/a ratio decreases, which may result in a higher activity of non-basal slip [10]. Agnew et al. [11] revealed that the <*c*+*a*> dislocations in the pyramidal planes improve ductility of MgLi alloys. Pawelek et al. [12] studying acoustic emission from deformed Mg-Li alloys estimated a high level of acoustic emission in Mg4Li alloy as a result of non-basal slip in the prismatic and pyramidal slip systems.

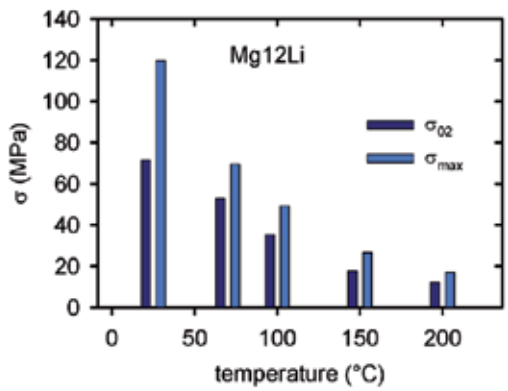

Figure 7. Temperature variation of the CYS and MCS estimated for Mg12Li alloy.

3.3. Microstructure of Mg-xLi-yAl alloys

To improve the mechanical properties, alloying with other elements can be used. The addition of Al atoms to Mg4Li causes the formation of precipitates. A combination of two different hardening mechanisms should be considered: solid solution hardening and precipitation hardening. The microstructure of as-cast Mg8LixAl alloys under consideration consists essentially of *hcp* magnesium-based α-phase and *bcc* lithium-based one (β-phase) and AlLi precipitates as well. Accordingly, interpenetrated (α+β) matrix structure with dominating α-phase is characteristic for LA83 and LA85 (see Fig. 8) alloys. Light micrograph of the Mg12Li3Al (LA123) alloy shows that the alloy does not contain only one phase (Fig. 9). Both phases (α and β) are present contrary to the alloy without Al because aluminium stabilises the *hcp*α-phase.

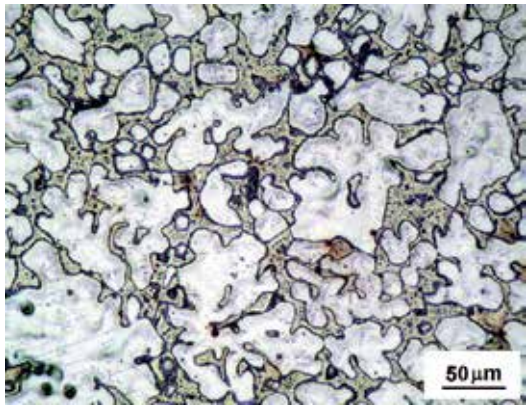

Figure 8. Light micrograph of the Mg8Li5Al alloy.

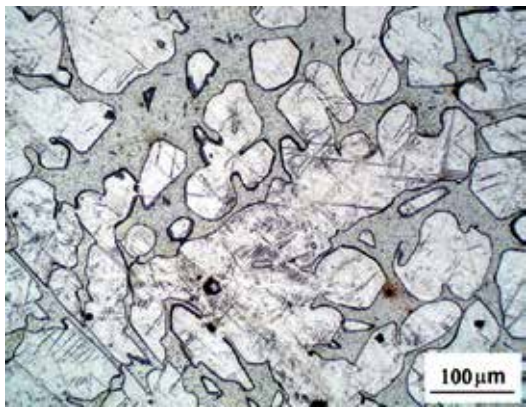

Figure 9. Light micrograph of the Mg12Li3Al.

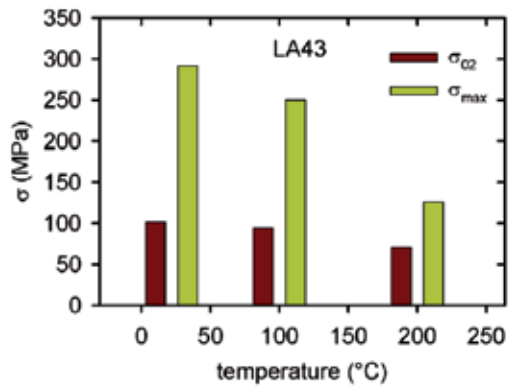

Figure 10. Temperature variation of the CYS and MCS estimated for Mg4Li3Al alloy.

http://dx.doi.org/10.5772/58949

3.4. Deformation of Mg-xLi-yAl alloys

The temperature dependence of the CYS and MCS estimated for LA43 (Mg-4Li-3Al) and LA45 (Mg-4Li-5Al) are introduced in Figs. 10 and 11. High differences between CYS and MCS, especially observed at lower temperatures, and moderate decrease of the characteristic stresses with temperature indicate significant hardening during plastic deformation. The presence of AlLi precipitates influences not only the yield stress but also the storage of dislocations during plastic deformation. In the LA43 (Mg4Li3Al) and LA45 (Mg4Li5Al) alloys, there are obstacles of non-dislocation types such as precipitates and the dislocation obstacles (forest dislocations). The observed high difference between the CYS and MCS indicates a significant hardening during the deformation process. A part of the moving dislocations stored at the obstacles contributes to hardening. On the other hand, processes such as cross slip and climb of dislocations contribute to softening– the difference between CYS and MCS decreases with increasing deformation temperature. The dislocation microstructure can change. For simplicity, the total dislocation density is considered as the characteristic parameter of the evolution of microstructure during deformation. According to the model of Lukáč and Balík [13], we take into account storage of dislocations at both impenetrable obstacles and forest dislocations, and annihilation of dislocations due to both cross slip and climb.

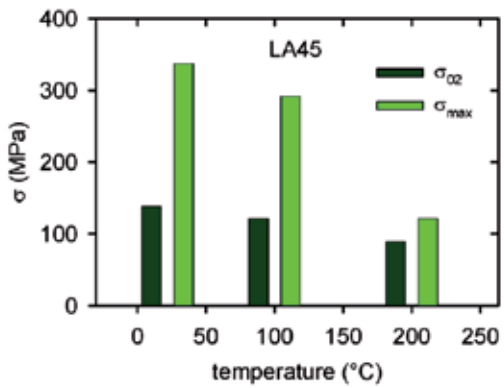

Figure 11. Temperature variation of the CYS and MCS estimated for Mg4Li5Al alloy.

The true stress-true strain curves of LA85 alloy estimated at various temperatures are shown in Fig. 12. The strain hardening is observed at temperatures up to 100 °C; the stress-strain curves obtained at higher temperatures are flat. The temperature variations of the CYS and MCS for LA83 and LA85 alloys are shown in Figs. 13 and 14. The strengthening effect of Al atoms in the case of LA85 alloy has been found to be really high even at 100 °C. A moderate decrease of both characteristic stresses with temperature classes this alloy as a material for industrial applications.

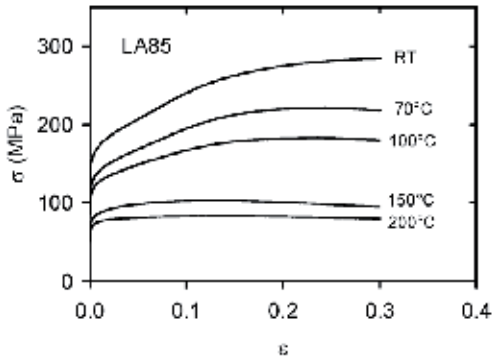

Figure 12. True stress-true strain curves of Mg8Li5Al alloy at various temperatures.

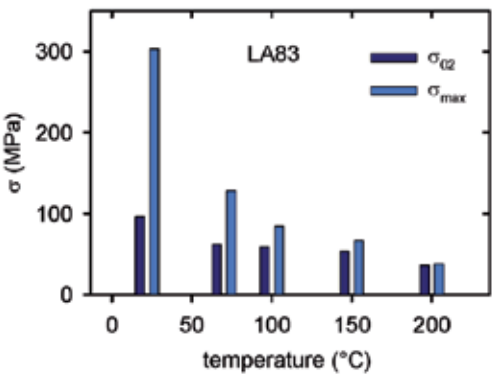

Figure 13. Temperature variation of the CYS and MCS estimated for Mg8Li3Al alloy.

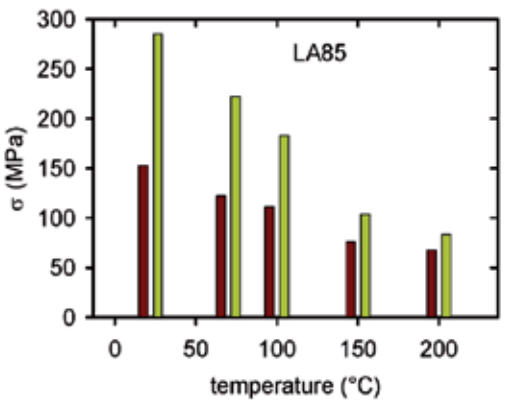

Figure 14. Temperature variation of the CYS and MCS for Mg8Li5Al alloy.

http://dx.doi.org/10.5772/58949

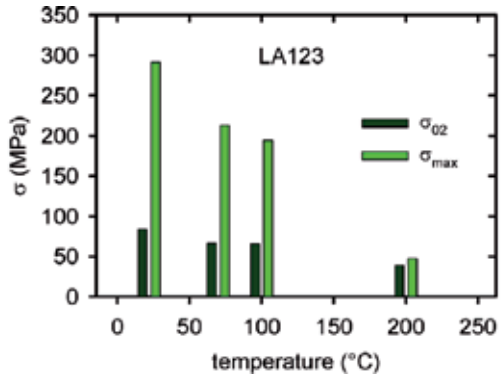

Figure 15. Temperature variation of the CYS and MCS estimated for Mg12Li3Al.

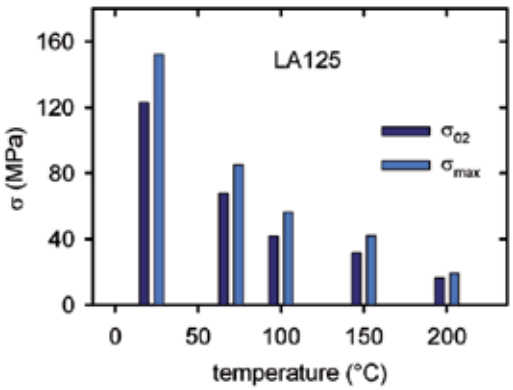

Figure 16. Temperature variation of the CYS and MCS estimated for Mg12Li5Al.

The temperature variations of both CYS and MCS are shown for LA123 and LA125 alloys in Figs. 15 and 16, respectively. The CYS is significantly higher for the alloy containing 5% of Al, while MCS exhibits higher values for the LA123 alloy. Thermal stability is higher in the case of LA125 alloy. The influence of Al on the mechanical characteristics of Mg-Li alloys at two temperatures is summarised in Table 1.

	LA40	LA43	LA45	LA80	LA83	LA85	LA120	LA123	LA125
					RT				
CYS (MPa)	68.9	103.7	138.4	84.8	96.2	152.7	71.4	83.9	122.8
MCS (MPa)	164.3	237.0	337.4	171.2	302.9	285.0	119.6	291.2	152.1
					100 °C				
CYS (MPa)	60.0	121.8	121.2	52.1	62.0	111.4	35.5	65.9	41.7
MCS (MPa)	129.0	292.0	292.0	80.5	84.3	183.0	49.4	194.5	84.8

Table 1. Influence of Al addition on CYS and MCS of Mg4Li, Mg8Li and Mg12Li alloys.

To conclude it is possible to say that the best mechanical properties of the superlight MgLi alloys were found for Mg8Li alloy with 5 wt% of Al. Combining of the stronger α phase with a more ductile β phase results in a material with the high specific strength.

4. Mg-Al-Sr (AJxy) alloys

4.1. Microstructure of the Mg-Al-Sr alloys

Special industrial applications require improvement of the high temperature properties. For these elevated temperature applications, alloys containing rare earth elements have been developed. New Mg-Al-Sr alloys are being developed with the aim to find cast alloys with good creep resistance and good strength and replace expensive rare earth alloying elements with some cheaper one. Pekguleryuz [14] reported that Mg-Al-Sr alloys show different microstructures based on the Sr/Al ratio. For Sr/Al ratio below about 0.3, only Al_4Sr intermetallic phase is present as the second phase in the structure. When the Sr/Al ratio is higher, a second intermetallic phase, a new, ternary Mg-Al-Sr compound, is observed. When the Sr/Al ratio is very low, there is insufficient amount of Sr to bind all Al atoms and the excess Al would form the $Mg_{17}Al_{12}$ phase. Figure 17 shows light micrograph of the squeeze cast AJ51 alloy. The primary Mg grains are surrounded by the interconnected network of the grain boundary phase. This phase is formed during solidification process and it has lamellar type morphology. The γ phase ($Mg_{17}Al_{12}$) is accompanied with Al_4Sr phase. Single items are better visible in Figs. 18 and 19, where SEM of AJ91 alloy is presented. Eutectic γ phase forms either continuous shapes or discontinuous precipitates. Light needles visible in both pictures are the Al_4Sr precipitates. Line scan of alloying elements present in particles shown in Fig. 19 is given in Fig. 20. Line scan analysis was performed along the light arrow showed in Fig. 19. Small content of Sr is present in the δ solid solution; higher in the position of a needle shaped particle.

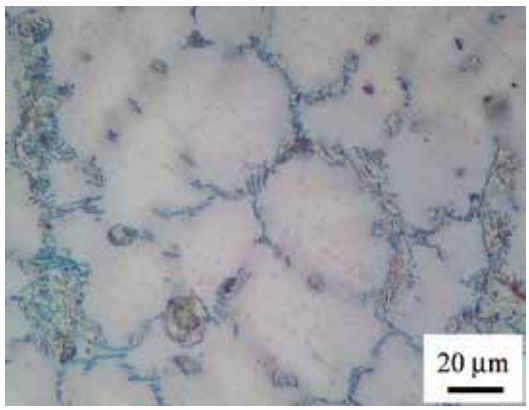

Figure 17. Light micrograph of the AJ51 alloy.

http://dx.doi.org/10.5772/58949

4.2. Deformation of the AJ alloys

The true stress-true strain curves of AJ51 alloy deformed in compression at various temperatures are shown in Fig. 21. Samples were deformed either to failure or the tests performed at temperatures higher than 100 °C were interrupted at a predetermined strain. Significant hardening at temperatures up to 150 °C is obvious. The curves obtained at temperatures higher are more or less flat – hardening and softening processes are in equilibrium.

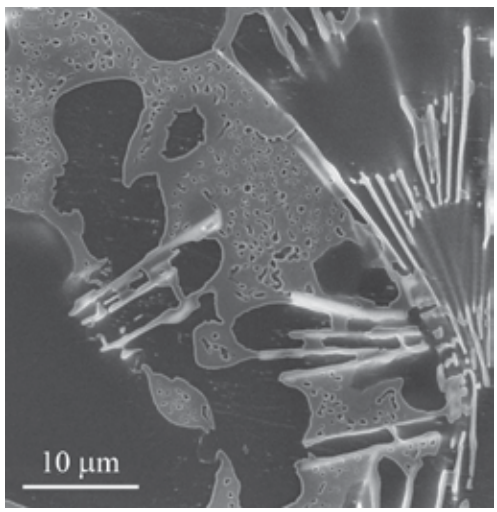

Figure 18. Scanning electron micrograph of as cast AJ91 alloy.

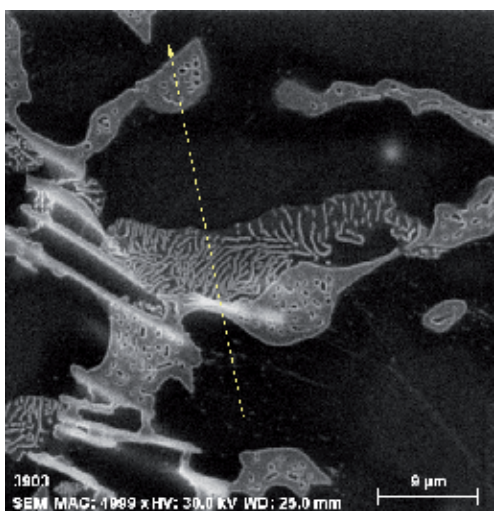

Figure 19. Scanning electron micrograph of as cast AJ91 alloy (different place).

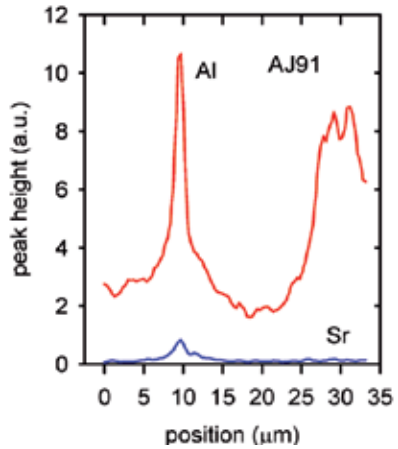

Figure 20. Line scan of alloying elements.

Figure 22 shows the temperature variation of the CYS as well as the MCS. Similar characteristics estimated in tension are shown in Fig. 23. While the values of the yield stress are practically the same for tension and compression, the values of the maximum stress are higher in compression tests. It is a consequence of higher ductility of the alloy in compression and significant hardening during plastic deformation at lower temperatures. The yield stress decreases with increasing temperature for samples deformed in compression. A small local maximum in the temperature dependence of the yield strength observed in the vicinity of 50 °C was observed in several Mg alloys and composites [15]. It is likely caused by a dynamic age hardening.

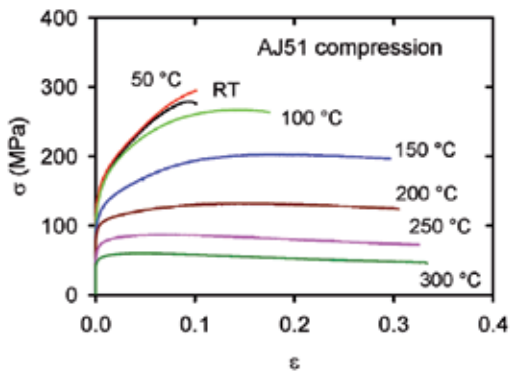

Figure 21. True stress-true strain curves estimated in compression for AJ51 alloy at various temperatures.

The true stress-true strain curves estimated for AJ91 alloy in compression are presented in Fig. 24. The values of the CYS and TYS (Figs. 25 and 26) are higher than the yield stress of the mostly used cast alloy AZ91. The temperature variations of MCS and MTS are shown in Figs. 25 and

26. Ductility of AJ91 alloy deformed in tension is low, at ambient temperature only several percent. Thermal stability is in comparison with AZ91 alloy also better; the CYS as well as TYS do not decrease with increasing test temperature up to 200 °C below 100 MPa. It is done by the thermal stability of Al_4Sr precipitates. Solid solution hardening plays in this case only minor role.

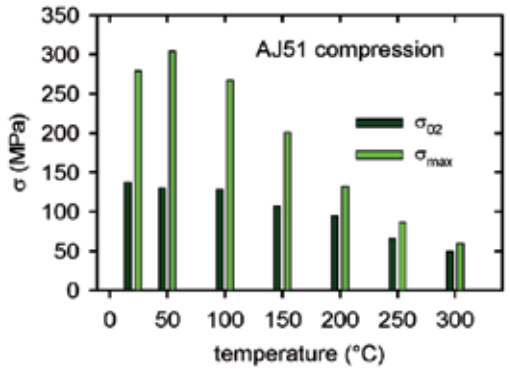

Figure 22. Temperature variation of CYS and MCS for AJ51 alloy.

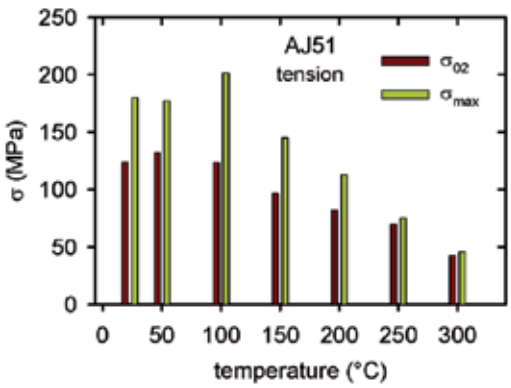

Figure 23. Temperature variation of TYS and MTS for AJ51 alloy.

4.3. Stress components in the AJ alloys

Stress necessary for dislocation motion is possible, according to eq. (1), divided into two components. The components of the applied stress (σ_i, σ^*) may be estimated using Li's method [16]. The SR curves are fitted to the power law function in the form:

$$\sigma - \sigma_i = \left[a(m-1) \right]^{\frac{1}{1-m}} \left(t + t_0 \right)^{\frac{1}{1-m}}, \tag{7}$$

where a, t_0 and m are fitting parameters. The influence of solute atoms on both stress components of AJ51 and AJ91 is obvious from Figs 27-29; it was estimate at three temperatures. At room temperature, an increase in the concentration of solute atoms influences only the internal stress. The observed increase of the internal stress is due to higher density of impenetrable precipitates which are obstacles for the dislocation motion. The effective stress σ* is practically the same for both alloys. From Fig. 27 it is obvious that the internal stress in both alloys is extremely high; it represents more than 90% of the applied stress. The difference between the internal stress of AJ51 and AJ91 alloys at 100 °C (Fig. 28) is relatively high and it indicates the reinforcing effect of the increased concentration of solute atoms. The effective stress is still for both alloys practically the same but the values of σ^* for both alloys are higher in comparison with the values obtained at room temperature. The internal stress estimated for AJ91 alloy at 200 °C (Fig. 29) is for strains up to approximately ε~ 0.08 higher as the effective stress. While the internal stress for AJ91 alloy decreases with strain, the effective stress continuously increases for both alloys. The decrease of the internal stress with strain estimated for both alloys is a consequence of the intensive activity of softening processes. This mechanism will be discussed in details later.

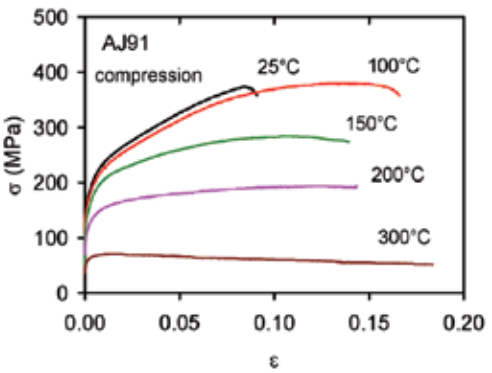

Figure 24. True stress-true strain curves of AJ91alloy deformed in compression at various temperatures.

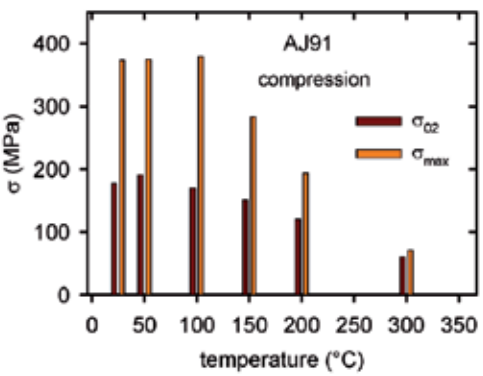

Figure 25. Temperature variation of CYS and MCS for AJ91 alloy.

http://dx.doi.org/10.5772/58949

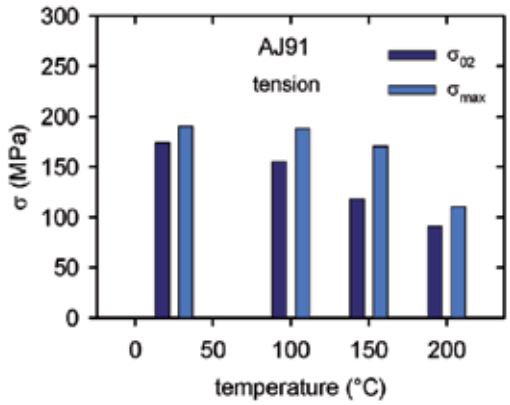

Figure 26. Temperature variation of TYS and MTS for AJ91 alloy.

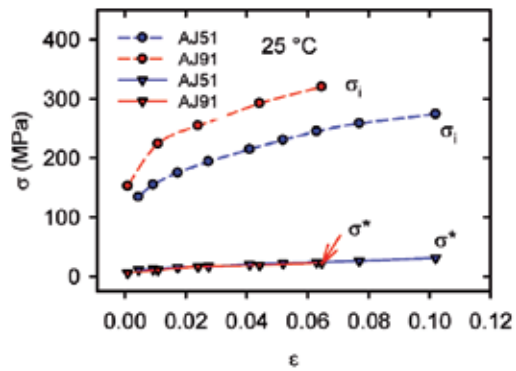

Figure 27. Strain dependence of the internal stress, σ_i, and effective stress, σ^*, for AJ51 and AJ91 alloys deformed at 25 °C

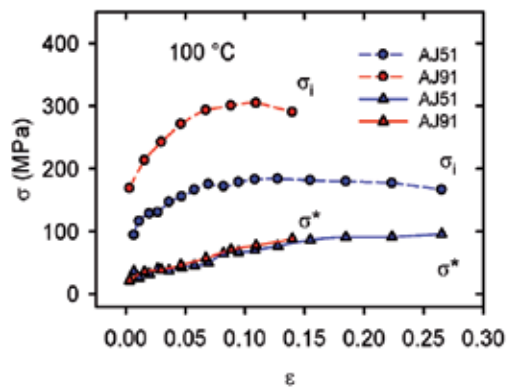

Figure 28. Strain dependence of the internal stress, σ_i, and effective stress, σ^*, for AJ51 and AJ91 alloys at 100 °C.

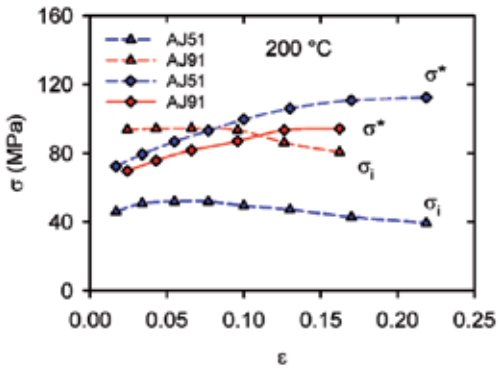

Figure 29. Strain dependence of the internal stress, σ_i, and effective stress, σ^*, for AJ51 and AJ91 alloys at 200 °C.

5. Mg-Al-Ca (AXxy) alloys

5.1. Microstructure of the AX alloys

When Ca is added to Mg-Al binary alloys, the type of precipitating compound depends on the Ca/Al mass ratio. When this ratio is higher than 0.8 the presence of both Mg_2Ca and Al_2Ca were detected. They may contribute to a considerable increase in hardness and the yield stress [17]. For the ratio below 0.8 only Al_2Ca Laves phase (C15-cubic) was observed to have been formed. Both types of precipitates were observed to form along the grain boundaries [18]. Gjestland et al. [19] showed that the creep resistance of AX alloy at 150 °C is similar to magnesium alloys containing rare earths with the added benefit of good corrosion resistance. Terada et al. [20] studied the creep mechanisms in the Mg-5Al-1.7Ca alloy. They found a change of deformation mechanism at the vicinity of 150 °C. Microstructure and mechanical properties of Mg-Al based alloy with Ca addition (AX series) were investigated by Du et al. [21]. They estimated that the small amount of Ca increased the thermal stability of $Mg_{17}Al_{12}$ intermetallic phase, so that the creep resistance at elevated temperatures was improved.

Microstructure of the squeeze cast AX41 alloy used in this study exhibits typical dendritic structure with γ Mg grains decorated by particles. SEM showed the details of the particles structure (Fig. 30); $Mg_{17}Al_{12}$ intermetallic phase surrounded with smaller particles of Al_2Ca. Microstructure of the squeeze cast AX91 alloy is displayed in Fig. 31. Two types of particles were identified, which is better evident in the back scattered electrons image (see Fig. 32). Dark particles in Fig. 32 are eutectics $Mg_{17}Al_{12}$; lighter skeleton-like particles containing Ca atoms.

http://dx.doi.org/10.5772/58949

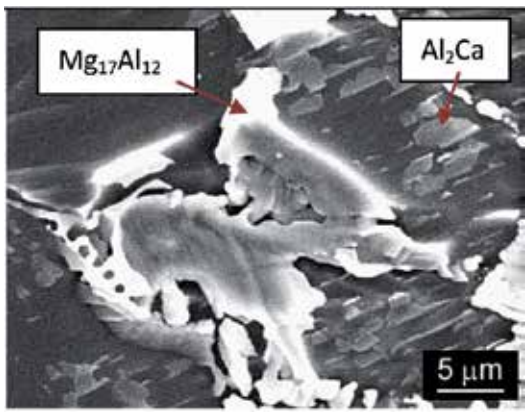

Figure 30. Scanning electron micrograph of as cast AX41 alloy showing the main phases present in the alloy.

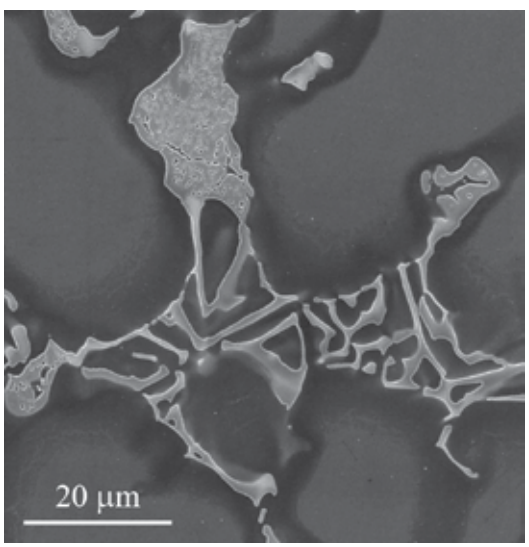

Figure 31. Scanning electron micrograph showing two main phases present in the AX91 alloy. The skeleton-like phase contains Ca.

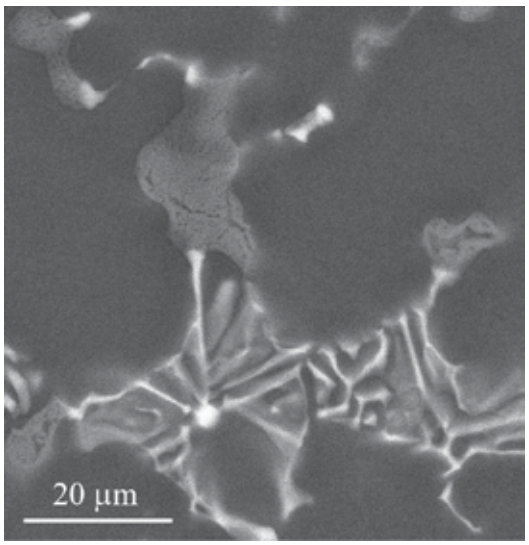

Figure 32. Back scattered electrons image of the same place as showed in Fig. 31.

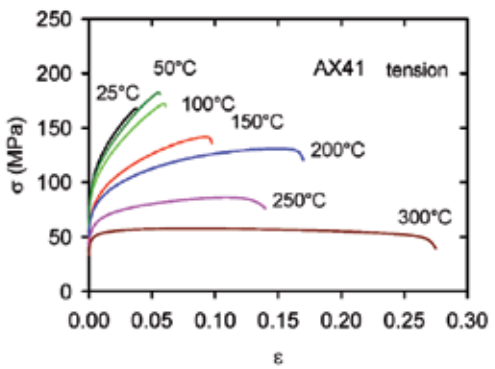

Figure 33. True stress-true strain curves of AX41 alloy deformed in tension at various temperatures.

http://dx.doi.org/10.5772/58949

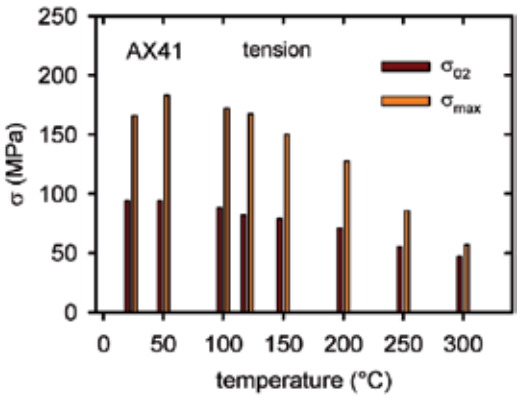

Figure 34. Temperature variation of TYS and MTS for AX41 alloy.

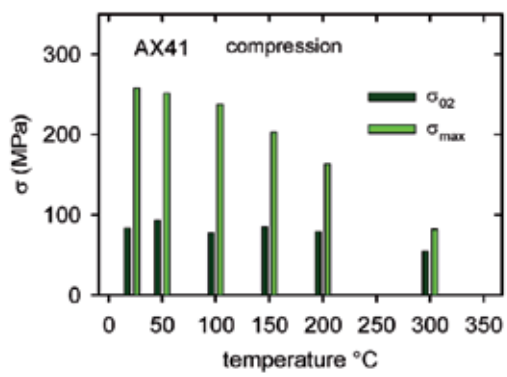

Figure 35. Temperature variation of CYS and MCS for AX41 alloy.

5.2. Deformation of the AX alloys

The true stress-true strain curves of AX41 alloy deformed in tension are presented in Fig. 33. Low ductility (about 5%) of the alloy was observed at lower temperatures below 100 °C; at higher temperatures ductility increases up to 27%. The temperature variations of the TYS and MTS are presented in Fig. 34.

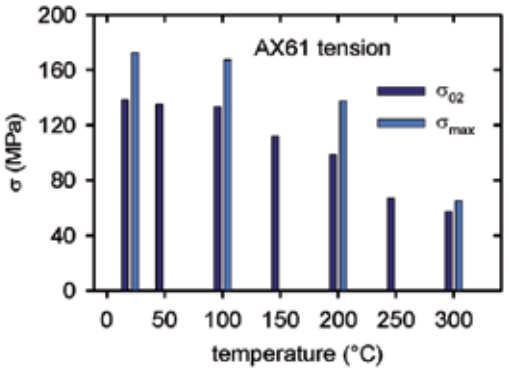

Figure 36. Temperature dependence of TYS and MTS for AX61 alloy.

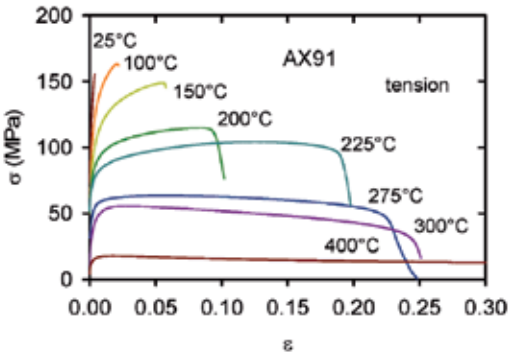

Figure 37. True stress-true strain curves of AX91 alloy deformed in tension at various temperatures.

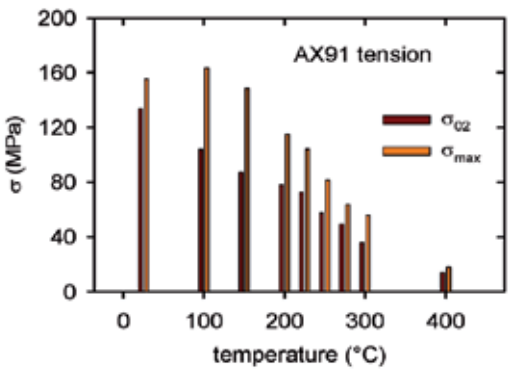

Figure 38. Temperature variation of TYS and MTS for AX91 alloy.

http://dx.doi.org/10.5772/58949

Analogously the values of the CYS and MCS at different temperatures are shown in Fig. 35. It can be seen that the TYS decreases with increasing temperature monotonously whereas the temperature variation of the CYS exhibits a local maximum at about 50 °C. The temperature variations of the TYS and MTS for squeeze cast AX61 alloy are presented in Fig. 36. The values of the TYS are relatively high and decrease only slightly with increasing temperature exhibiting at 200 °C still a value about 100 MPa. The true stress-true strain curves of AX91 alloy measured in tension at various temperatures are shown in Fig. 37. It is obvious from Fig. 37 that ductility of the alloy at temperatures up to 100 °C is limited; it increases up to 25 % at a temperature of 300 °C. The TYS at room temperature was estimated to be approximately equal to that measured for AX61 alloy. The observed rapid decrease of TYS of AX91 with temperature indicates a lower thermal stability of this alloy (Fig. 38). It is a different situation in comparison to the AJ91 alloy, for which the strength was found to be superior.

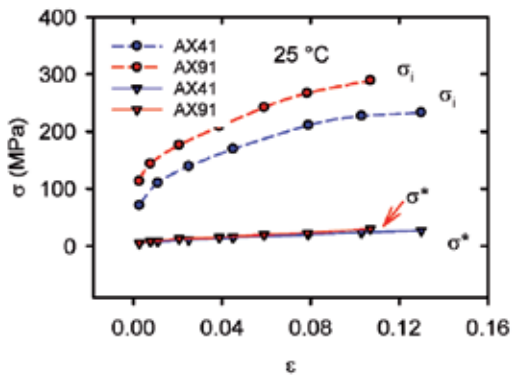

Figure 39. Strain dependence of the internal (σ_i) and effective (σ^*) stresses at 25 °C.

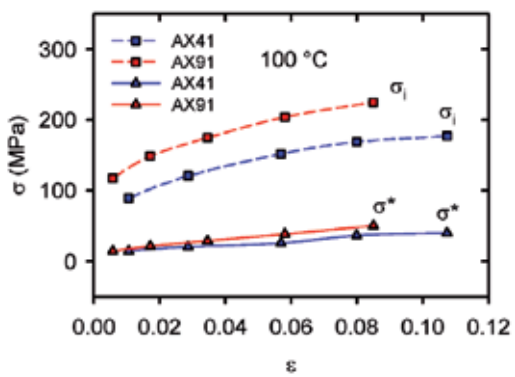

Figure 40. Strain dependence of the internal (σ_i) and effective (σ^*) stresses at 100 °C.

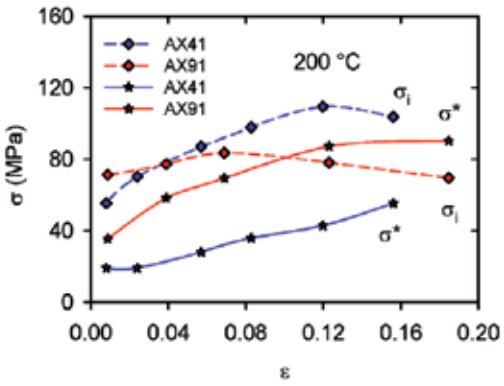

Figure 41. Strain dependence of the internal (σ_i) and effective (σ^*) stresses at 200 °C.

5.3. Stress components in the AX alloys

The applied stress components, σ_i, and, σ^*, for AX41 and AX91 alloys were estimated at three temperatures in compression (see Figs. 39-41). At lower temperatures, 25 and 100 °C, the solute atom concentration influences only the internal stress. The effective stress is for both alloys the same (at 25°C) or it is a bit higher (at 100 °C) for AJ91 alloy. In both cases the effective stress slightly increases with increasing strain. A different behaviour was found at 200 °C. While the internal stress estimated for AX41 alloy increases with increasing strain up to 12%, the internal stress in AX91 alloy slightly increases with strain up to 8% and then decreases. On the other hand, the effective stress increases in the whole strain range.

According to eq. (2) the internal stress, σ_i is proportional to $\varrho^{1/2}$ where ϱ is the density of dislocations. The internal stress, σ_i, generally, reflects the resistance of a metallic material against plastic deformation. Considering a constant microstructure, the deformation (flow) stresses are done by the evolution of the dislocation density with strain and temperature. The observed increase of the internal stress for all alloys AJ and AX series indicates an increase in the dislocation density. The moving dislocations can be stored at both non-dislocation and dislocation type obstacles. Non-dislocation obstacles may be grain boundaries, non-coherent precipitates and/or twins; the dislocation type obstacles are formed by reactions between dislocations. As mentioned in paragraph 2, in *hcp* magnesium alloys dislocations with the Burgers vector **<*a*>**=1/3[11$\bar{2}$0] may glide in basal, prismatic, and first−order pyramidal planes. Dislocations with the Burgers vector <*c*+*a*>=1/3[11$\bar{2}$3] can glide in the first− and second−order pyramidal planes. The basal <*a*> dislocations may react with the pyramidal <c+*a*>dislocations according to:

$$\tfrac{1}{3}\langle 2\bar{1}\bar{1}3\rangle + \tfrac{1}{3}\langle \bar{2}110\rangle \rightarrow \langle 0001\rangle. \qquad (8)$$

http://dx.doi.org/10.5772/58949

The resulting sessile**<*c*>** dislocations with the Burgers vector parallel to the c axis are not able to glide in the basal plane; therefore such dislocations are obstacles for moving dislocations.

Twins are another type of obstacles. Twinning plays an important role in plastic deformation of *hcp* magnesium alloys. Our experiments were performed in compression. It was shown [22-24] that $\{10\bar{1}0\}$ compressive twinning, $\{10\bar{1}1\}$-$\{10\bar{1}2\}$ double twining and $\{10\bar{1}3\}$-$\{10\bar{1}2\}$ double twinning could also accommodate compressive strains along the c-axis at lower temperatures. The nearly constant level or slightly decreasing tendency of the internal stress estimated at a temperature of 200 °C indicates a decrease in the dislocation density as a consequence of recovery process/-es. With rising temperature, the intensity of dynamic recovery is increasing – this can be related to dislocation climb and also to the activity of additional non-basal slip systems. It should be mentioned that <*c*> dislocations are not able to glide (conservative movement) in the basal plane, however they may climb at elevated temperatures and release the primary glide. Another dislocation reaction may yield a sessile **<*c*+*a*>** dislocation:

$$\frac{1}{3}\left\langle 2\bar{1}\bar{1}3\right\rangle + \frac{1}{3}\left\langle \bar{1}2\bar{1}0\right\rangle \rightarrow \frac{1}{3}\left\langle 11\bar{2}3\right\rangle. \tag{9}$$

A combination of two glissile**<*c*+*a*>** dislocations gives rise to a sessile dislocation of <*a*> type that lays along the intersection of the second order pyramidal planes according to the following reaction:

$$\frac{1}{3}\left\langle 2\bar{1}\bar{1}3\right\rangle + \frac{1}{3}\left\langle \bar{1}2\bar{1}\bar{3}\right\rangle \rightarrow \frac{1}{3}\left\langle 11\bar{2}0\right\rangle. \tag{10}$$

It can be seen that different dislocation reactions may produce both sessile and glissile dislocations. Production of sessile dislocations increases the density of the forest dislocations that are obstacles for moving dislocations. Therefore, an increase in the flow stress with straining (i.e. hardening) follows, which is observed in the experiment.

Dislocations may be stored in front of impenetrable, thermally stable, precipitates and therefore dislocation pile-ups can be formed. These pile-ups are very effective stress concentrators. Local stress produced by the dislocation pile-ups may support cross slip of screw dislocations and so contribute to softening of the alloy. A higher density of precipitates in AJ91 and AX91 alloys compared with AJ51 and AJ41 alloys is the main reason for higher values of the CYS/TYS observed at lower temperatures. On the other hand, the precipitates (significant stress concentrators) may make easier climb of dislocations at elevated temperatures. Higher mobility of dislocations in prismatic and pyramidal slip planes at elevated temperatures increases the probability of dislocation reactions between **<*c*+*a*>** dislocations leading to dynamic recovery in a *hcp* structure.

6. Influence of solute atoms on activation volume

While the internal stress is strongly influenced with the content of solute atoms, the effective stress was– up to 100 °C–not affected by solute atoms (in the case of AJxy and AXxy alloys). The observed increase of the effective stress at higher temperatures is not surprising; the thermally activated process at higher temperatures is complex. Solute atoms (or their small clusters) are considered as typical local obstacles for moving dislocations. In high-temperature regime, diffusion-controlled glide should be taken into account.

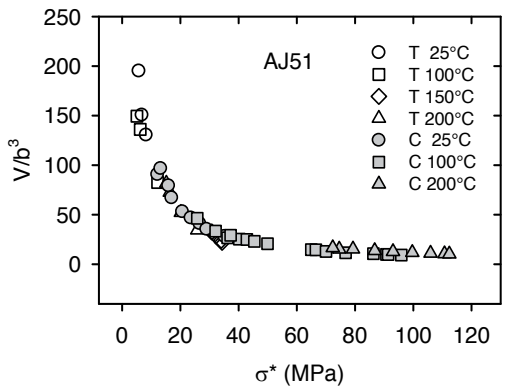

Figure 42. The plot of the activation volume in b^3 against the effective stress σ* for AJ51 alloy deformed in tension and compression at various temperatures.

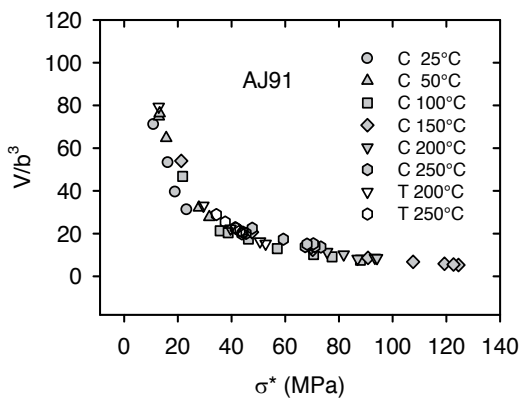

Figure 43. The plot of the activation volume in b^3 against the effective stress σ* for AJ91 alloy deformed in tension and compression at various temperatures.

http://dx.doi.org/10.5772/58949

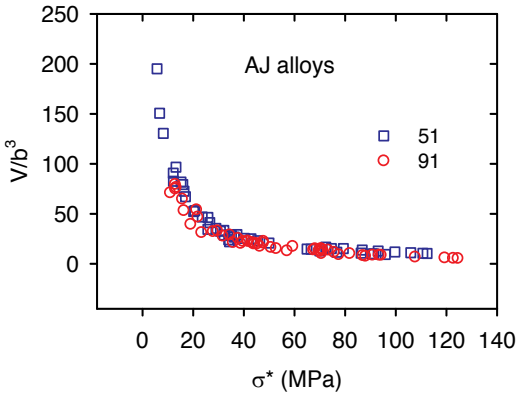

Figure 44. The plot of the activation volume in b^3 against the effective stress σ* for AJ51 and AJ91 alloys in tension and compression at all temperatures.

The values of the activation volume, V, were estimated in the stress relaxation experiments using equation (6). As usual, the values of the activation volume divided by b^3 for samples of AJ51 and AJ91 alloys deformed in tension as well as compression are plotted against the effective stress σ* for all testing temperatures in Figs 42-43 for tension (empty characters) and compression (full characters) deformation. The same analysis was performed for AX41 and AX91 alloys as it can be seen in Figs. 45-47. Plotting values of V against the effective stress for both AJ alloys into one diagram (Fig. 44) and those for both AX alloys in Fig. 47 shows that the activation volumes decrease with the effective stress and all the values lie on one line –"master curve". Kocks et al. [25] suggested an empirical equation between Gibbs free energy ΔG and the effective stress σ* in the following form:

$$\Delta G = \Delta G_0 \left[1 - \left(\frac{\sigma^*}{\sigma_0^*} \right)^p \right]^q , \tag{11}$$

where ΔG_0 and σ_0^* are Gibbs energy and the effective stress at 0 K. For the effective stress it follows:

$$\sigma^* = \sigma_0^* \left[1 - \left(\frac{kT}{\Delta G_0} \ln \frac{\dot{\varepsilon}_0}{\dot{\varepsilon}} \right)^{1/q} \right]^{1/p} , \tag{12}$$

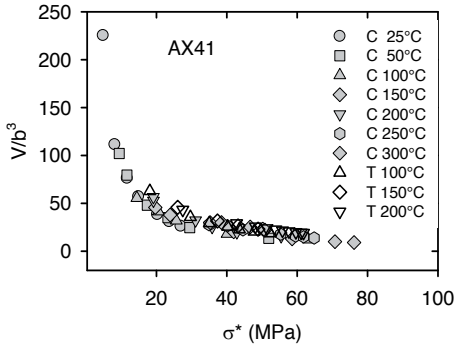

Figure 45. The plot of the activation volume in b^3 against the effective stress σ* estimated for AX41 alloy at various deformation temperatures in tension and compression.

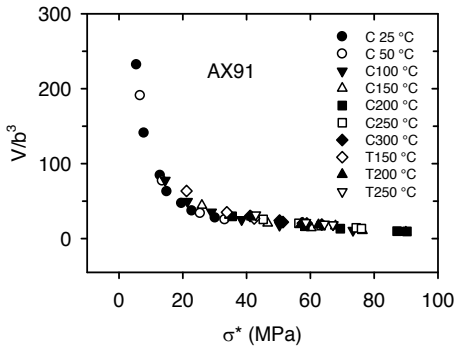

Figure 46. The plot of the activation volume in b^3 against the effective stress σ* estimated for AX91 alloy at various deformation temperatures in tension and compression.

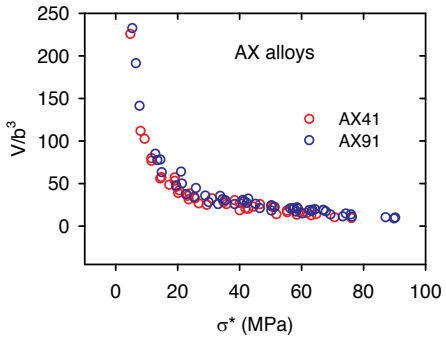

Figure 47. The plot of the activation volume in b^3 against the effective stress σ* estimated for AX41 and AX91 alloys at all temperatures in tension and compression.

where p and q are phenomenological parameters reflecting the shape of a resistance obstacle profile. The possible ranges of values p and q are limited by the conditions $0 < p \leq 1$ and $1 \leq$

http://dx.doi.org/10.5772/58949

$q \leq 2$. Ono [26], suggested that Equation (12) with p=1/2, q=3/2 describes a barrier shape profile that fits many predicted barrier shapes. Thermodynamics generally defines the activation volume as

$$V = -\left(\frac{d\Delta G}{d\sigma^*}\right)_T . \tag{13}$$

Equation (13) can be rewritten as

$$V = \frac{\Delta G_0 pq}{\sigma_0^*}\left[1-\left(\frac{\sigma^*}{\sigma_0^*}\right)^p\right]^{q-1}\left(\frac{\sigma^*}{\sigma_0^*}\right)^{p-1} . \tag{14}$$

The values of the activation volume should lie at the curve given by the equation (14). Results showing all values of the activation volumes being the same for alloys of AJ as well as AX series indicate that the thermal activation is not affected by various concentrations of solute atoms. It may be concluded that the thermally activated process(-es) is(are) determined with the dislocation motion and the solute atom role is less important. The values of the activation volume may help to identify thermally activated processes considering some of the common short−range barriers to dislocation motion [27]. The dislocation–dislocation interaction mechanism has an activation volume ranging from about 10^2–10^4 b^3, with the activation volume and enthalpy varying with strain. Couret and Caillard [28, 29] studied prismatic slip in magnesium in a wide temperature range using in situ experiments in TEM. They have reported that screw dislocations with the Burgers vector $1/3[11\bar{2}0]$ are able to glide on prismatic planes and their mobility is much lower than the mobility of edge dislocations. The deformation is controlled by thermally activated glide of those screw dislocation segments. A single controlling mechanism was identified as the Friedel−Escaig cross slip mechanism. This mechanism assumes dissociated dislocations on compact planes, like (0001), that joint together along a critical length L_r producing double kinks on non-compact planes. The activation volume is proportional to the critical length between two kinks. Amadieh et al. [30] found for the activation volume of the Friedel−Escaig mechanism a value of 70 b^3. Prismatic slip was also observed by Koike and Ohyama [31] in deformed AZ61 sheets. The activation of prismatic slip and subsequent annihilation of dislocation segments with opposite sign are probably the main reason for the observed internal stress decrease. The double cross slip may be a thermally activated process controlling the dislocation velocity. Beside this mechanism, the thermally activated glide of <***c+a***> dislocations should be taken into account. Mathis et al. [32] investigated the evolution of non−basal dislocations as a function of temperature in magnesium by X−ray diffraction. They found a majority of <***a***> dislocations in the as−cast state. During plastic deformation in tension the <***a***>−type dislocations remain dominant, however, the dislocation density increased by about a factor of three up to about 100 °C. At higher temperatures the fraction of <**c+*a***>−type dislocations increased at the cost of <***a***>−type dislocations and the

increase of the dislocation density is strongly reduced. The internal stress acting on dislocations is determined by the details of the internal structure at that moment and it is independent of the applied stress. The stress that changes when the applied stress is changed is only the effective stress. The internal stresses during plastic deformation of the alloys investigated here can be considered as the sum of stresses resulting from various dislocation arrangements and obstacles existing in the deformed material [33, 34]. At higher temperatures the solute atoms may diffuse to stacking fault and may influence double cross slip from basal to non-basal planes.

7. Dynamic strain ageing (DSA) in magnesium alloys

Plastic deformation of alloys exhibits many phenomena associated with solute strengthening. When solute atoms can move (they may diffuse) during plastic deformation the microstructure of the deformed alloy is unstable. This microstructure instability is due to solute atoms diffusion towards to moving dislocations– the dynamic strain ageing (DSA) effect. The segregation of solute atoms at dislocations results in many phenomena:

- positive or non-monotonous dependence of the flow stress on temperature,
- negative strain rate sensitivity in a certain temperature range,
- post relaxation effect,
- local maximum in the temperature dependence of the activation volume or stress sensitivity parameter,
- the Portevin-Le Châtelier effect.

Magnesium alloys exhibit dynamic strain ageing effects at relatively low temperatures. Portevin-Le Châtelier effect (PLC) was observed during plastic deformation of some Mg alloys [35-39]. The unstable microstructure of an alloy can influence the deformation behaviour of the alloy. It should be mentioned that room temperature is high enough to help invoking strain ageing processes in magnesium alloys.

7.1. Portevin-Le Châtelier effect

The Portevin-Le Châtelier (PLC) effect is a consequence of a complicated nature of the dislocation dynamics in metals, which depends on many structural parameters as the type of structure, grain size, texture, concentration and distribution of solute atoms. Plastic deformation occurs inhomogeneously on the microscopic scale due to thermally activated dislocation motion through a field of obstacles. Deformation inhomogeneities in time and space, observed experimentally, are caused by collective dislocation motion. These phenomena of unstable plastic deformation are associated with the sharp localised deformation bands. Three types of PLC bands have been found. The continuously propagating type A, intermittently propagating type B with regular stress drops and stochastically nucleating type C. Figure 48 shows a representative microstructure of the undeformed Mg+0.7wt.%Nd sample after T6 temper

http://dx.doi.org/10.5772/58949

(homogenisation at 525 °C for 5h, then quenching into water 65 °C warm with subsequent precipitation treating for 8 h at 204 °C).

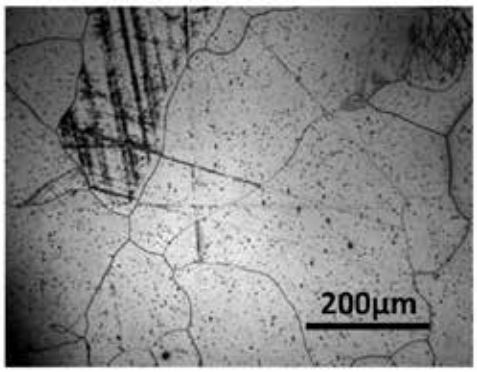

Figure 48. Microstructure of Mg-Nd alloy after T6 temper.

The true stress-true strain curves obtained at various temperatures are presented in Fig. 49 for tension and in Fig. 50 for compression tests. It can be seen a discontinuous character of curves obtained at elevated temperatures. Serrated yielding was observed at temperatures from 200 °C to 300 °C in tension and from 200 °C to 250 °C in compression. In compression tests the deformation at 300 °C was already smooth. While the shape of the serrations obtained in tension has character A, serrations found in compression have another shape, which is more of type B. PLC effect was also observed in an AZ91 (Mg-9Al-1Zn) alloy after thermal treatment T4 (homogenisation at 413 °C for 18 h, then quenching into water of ambient temperature). Tensile and compression tests were performed over a wide temperature range from 14 to 100 °C at an initial strain rate ranged in the 10^{-4} s^{-1}. The temperature dependence of the yield stress of Mg+0.7Nd exhibits a local maximum – a stress-hump (Fig. 51).

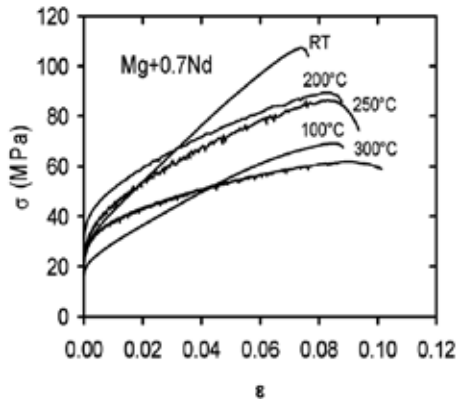

Figure 49. True stress-true strain curves of Mg+0.7Nd alloy deformed in tension.

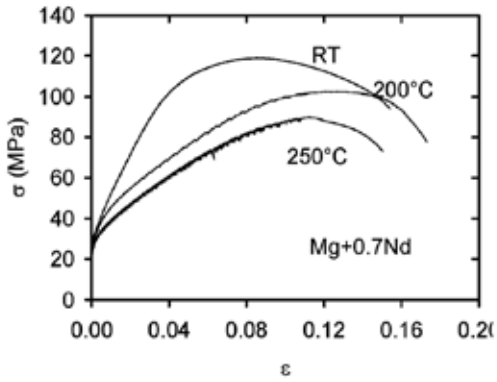

Figure 50. True stress–true strain curves of Mg+0.7 alloy deformed in compression at various temperatures.

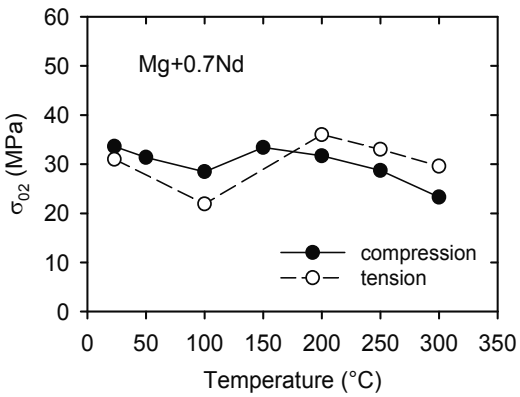

Figure 51. Temperature dependence of the yield stress of Mg+0.7Nd alloy deformed in tension and compression.

The stress-strain curve of AZ91 alloy obtained in tension at 21 °C is given in Fig. 52 together with the strain dependence of the strain hardening rate$\theta=d\sigma/d\varepsilon$. Serrations on stress-strain curves were observed at temperatures from room temperature up to 100 °C, the stress-strain curve obtained at temperature 150 °C exhibited no serrations; it was smooth. Similar experiments were performed in compression at an approximately same strain rate at temperatures from 15 to 100 °C. Character of serrations in compression is different in comparison with the tension tests as it is obvious from Fig.53. The stepwise character of curves indicates sudden elongation of the sample during the compression test.

http://dx.doi.org/10.5772/58949

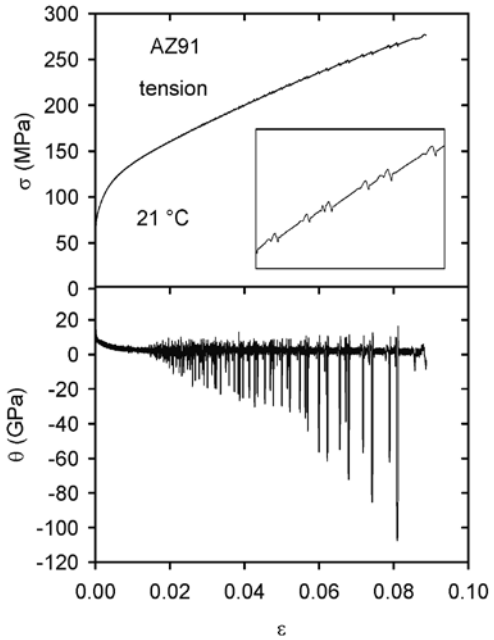

Figure 52. Stress-strain curve in tension obtained at 21 °C together with the strain dependence of the strain hardening rate.

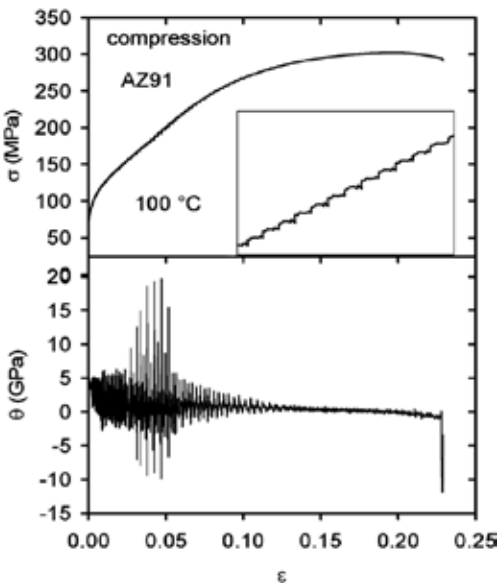

Figure 53. Stress strain curve and strain dependence of the strain hardening rate obtained in compression at 100 °C.

Lavrentev [40] have reported an important role of the dislocation forest in *hcp* structures with the main basal slip. Forest dislocations, which density was increased by prior movement of dislocation avalanche, are local obstacles for moving dislocations. Cores of dislocations waiting at forest dislocations during thermally activated motion in the slip plane may be occupied by solutes, which are movable due to pipe diffusion. These smaller dislocation groups of waiting dislocations are probably spread over a set of adjacent slip planes, rather than being strictly coplanar. They produce local stress concentrations, which may be a release pulse for break-away of dislocation pile ups. Precursor behaviour of the local strain associated with local stress relaxation prior to the strain avalanche may be characterised by the stress drop. This type of unstable flow is characteristic of the PLC flow, in which a drop in the load is possible if the strain rate during the formation of the slip bands exceeds the strain rate imposed by the tensile testing machine. A high level of the internal stress allow pass of these deformation bands through the whole sample. As each PLC band runs through the gauge length, the formation of new forest dislocations ensures that the process repeats itself. As the dislocation movement in the slip bands ceases or becomes too slow for the applied strain rate, for instance after a drop in the load or at the end of a PLC band, the applied stress must increase in order to resume deformation. Activation of new sources can only occurs by cutting through the forest dislocations created by secondary slip around slip bands no longer active. The forest dislocations increase the critical resolved shear stress for dislocation motion, but provide little strain hardening. If the activation of a source occurs under conditions of stable planar glide, dislocations can form a dynamic pile up able to move at increasing speed and decreasing levels of the applied stress because of the development of stress concentration ahead of the moving dislocations. This may spontaneously lead to an avalanche of dislocations that meets the general requirement for unstable tensile flow, since a drop in the load, as observed during the PLC effect, is possible only if the strain rate during the formation of the slip bands exceeds the strain rate imposed by the tensile testing machine. An additional factor is the following: as dislocations pile up in front of obstacles, the average dislocation velocity in the glide plane becomes very low so that moving solute atoms may diffuse towards the dislocations and pin them down.

7.2. Other manifestations of the dynamic strain ageing

The temperature dependence of the yield stress, σ_{02}, of Mg+0.7Nd alloy deformed in tension and compression (Fig. 51) shows that the course of the temperature dependence is non-monotonous. A local maximum in the temperature dependence of the yield stress obtained in compression and tension is observed in a temperature range of 150 – 250 °C.

Similar local minimum has been observed in the temperature dependence of the yield stress, σ_{02}, and the maximum compressive stress, σ_{max}, of ZE41 (Mg-4Zn-1RE) magnesium alloy as it can be seem in Fig. 54. While the local maximum in the temperature dependence is observed in alloys containing rare earths in the temperature interval 150-250 °C, alloys containing Al exhibit this local maximum between room temperature and 100 °C. This is demonstrated in Figs. 55 and 56 for AZ63 (Mg-6Al-3Zn) and AJ51 (Mg-5Al-0.6Sr), respectively. The strain rate dependence of the yield stress of Mg+0.7Nd alloy deformed in tension at 250 °C is presented

http://dx.doi.org/10.5772/58949

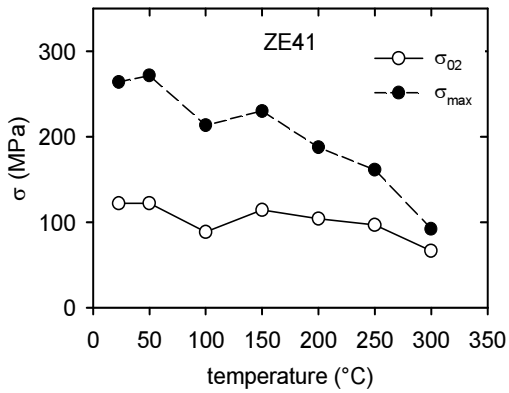

Figure 54. Temperature dependence of the yield and maximum stresses of ZE41 alloy

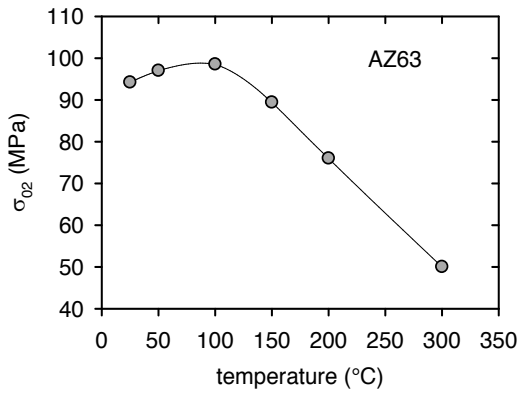

Figure 55. Temperature dependence of the yield stress of AZ63 alloy.

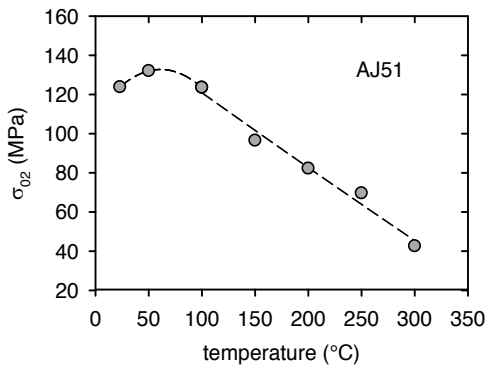

Figure 56. Temperature dependence of the yield stress of AJ51 alloy.

in Fig.57. Negative strain rate sensitivity was found for three strain rates from $5.5x10^{-5}$ to $5.5x10^{-4}$ s^{-1}. The strain rate dependence of the yield stress of ZE41 alloy deformed at three temperatures is given in Fig. 58. It can be seen that the strain rate dependences have an anomalous course. The yield stress usually increases with increasing strain rate. In this case, the yield stress increases only at lower strain rates. At strain rates higher than 10^{-4} s^{-1}, the yield stress decreases with increasing strain rate at 50 and 150 ºC. At 100 ºC the yield stress is practically independent of the strain rate. Again, the results indicate some dynamic strain ageing. It is also obvious that the values of the yield stress at 100 ºC are lower than those at 150 ºC at all imposed strain rates. Examples of short sequences of the stress strain curves of AZ91 alloy deformed at room temperature and two various strain rates are shown in Fig.59. It should be mentioned that the curves are not shifted; accordingly the negative strain rate sensitivity is obvious.

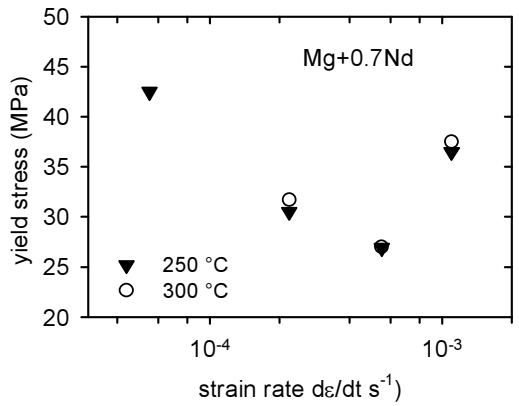

Figure 57. Strain rate dependence of the yield stress of Mg+0.7Nd alloy at two temperatures.

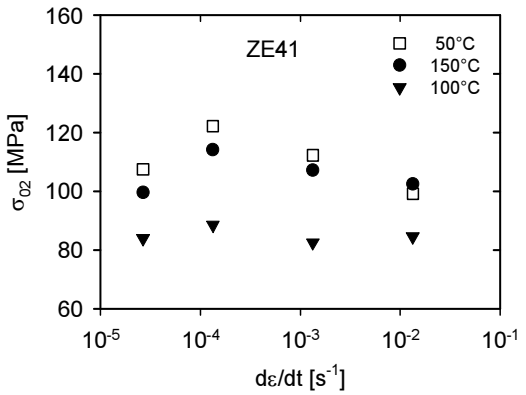

Figure 58. Strain rate dependence of the yield stress of ZE41 alloy deformed at three temperatures:

http://dx.doi.org/10.5772/58949

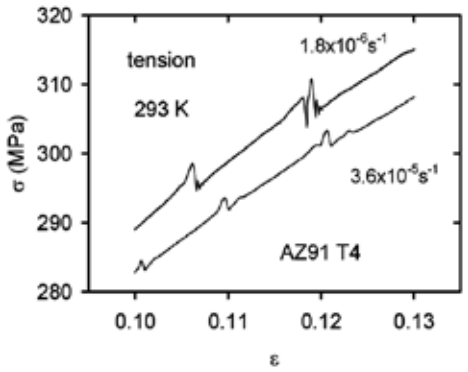

Figure 59. Sequences of the stress strain curves of AZ91 obtained for two strain rates. Negative strain rate sensitivity is obvious.

Very effective tool for studying of strain ageing phenomena are the stress relaxation tests. The SR curves are usually analysed assuming that the mobile dislocation density ϱ_m and internal stress σ_i are constant during the SR test. An unstable structure, changes in the mobile dislocation density and/or in the internal stress, may influence the course of the SR. In some SR tests, we observed a post relaxation effect. The flow stress at the beginning of deformation after stress relaxation σ_1 was higher (or lower) than the stress at the beginning of the stress relaxation $\sigma(0)$. The values of $\Delta\sigma=\sigma(0)-\sigma_1$ depend on strain, starting stress of the SR test and temperature. Examples of such dependences can be seen in Figs. 60-63 for magnesium alloys containing rare earth elements – Mg+0.7Nd alloy, ZE41 alloy, AE42 (Mg-4Al-2RE) and QE22 (Mg-2Ag-2RE). Similar dependences for alloys of the AZ series are presented in Figs. 64 and 65. It is obvious that the post relaxation effect is limited only on certain stress (strain) and temperature ranges. Local maxima are observed in these dependences. Such experimental results indicate that these phenomena are related to the dislocations and solute atoms mobility.

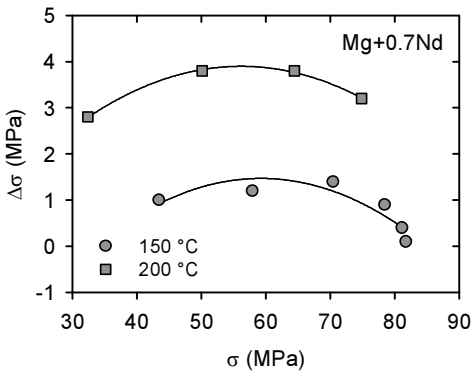

Figure 60. Dependence of the stress increment after the SR on the starting stress of SR estimated at two temperatures (Mg+0.7Nd).

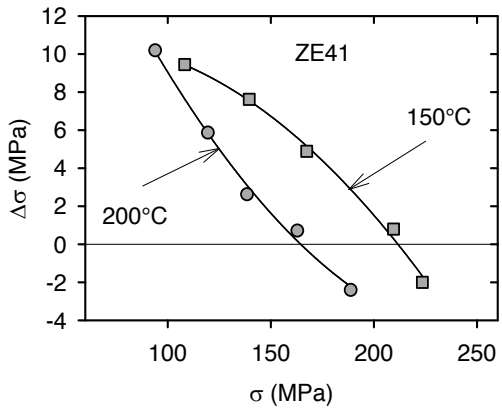

Figure 61. Dependence of the stress increment after SR on the starting stress of SR at two temperatures (ZE41 alloy).

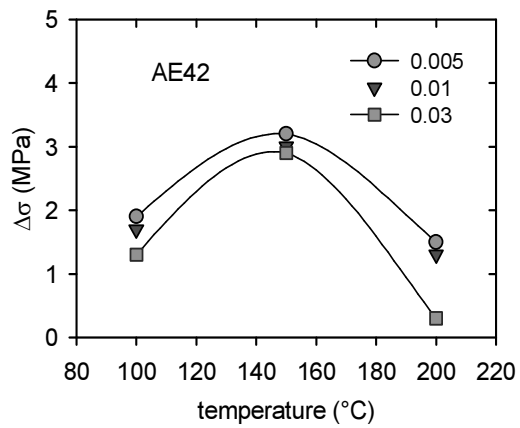

Figure 62. Temperature variation of the stress increment after SR at two starting strains of SR (AE42 alloy).

Solute atoms become mobile with increasing temperature. During a stress relaxation test, the dislocation velocity decreases, and at higher temperatures, the mobility of foreign atoms may be close to that of the dislocations. Thus, atmospheres of foreign atoms on dislocations may form. The dislocations are pinned by the solutes and hence, in order to restart their motion, they must be freed from the atmospheres after stress relaxation. Macroscopically, this results in a yield point due to dynamic strain ageing. The stress at the beginning deformation after the SR is higher than the stress at the beginning of the stress relaxation, which is observed experimentally.

http://dx.doi.org/10.5772/58949

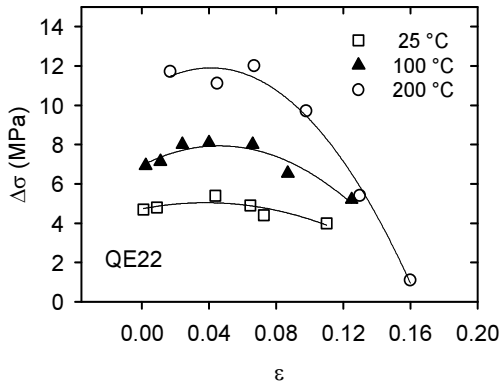

Figure 63. Strain dependence of the stress increment after SR at three temperatures (QE22 alloy).

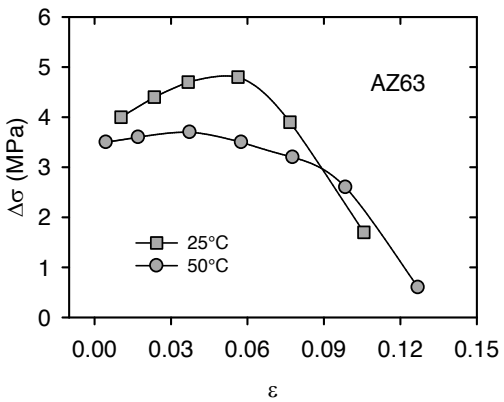

Figure 64. Strain dependence of the stress increment after SR at two temperatures (AZ63 alloy).

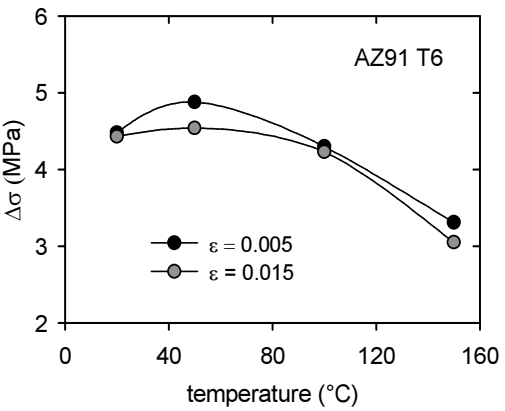

Figure 65. Temperature dependence of the stress increment after SR at two SR starting strains (AZ91 alloy).

The flow stress, necessary for the dislocation movement, may be expressed as a sum of two components

$$\sigma = \sigma_d + \sigma_f, \tag{15}$$

where σ_d is the dislocation component due to strong obstacles (e.g. forest dislocations, precipitates, grain boundaries) and σ_f is the friction stress due to the interaction between the solute atoms and moving dislocations. Mulford and Kocks [41] consider that the dislocation component of the flow stress rather than the friction stress is affected by dynamic strain ageing. Balík and Lukáč [42] take into account the influence of solute atoms on the both flow stress components in the dynamic strain ageing regime.

The local solute concentration increment, Δc, on the dislocations can be expressed as [43-45]

$$\Delta c = c - c_0 = \Delta c_M \left[1 - \exp\left(-t_a / t_0\right)^r \right]. \tag{16}$$

Here c is the local solute concentration in the dislocation core, c_0 is the nominal solute concentration in the matrix and Δc_M is the maximum concentration increment. The exponent r is equal 2/3 or 1/3 for bulk or pipe diffusion, respectively. The relaxation time t_0 depends on the binding energy between a dislocation and a solute atom, on solute concentration, and on the diffusion coefficient of solute atoms. t_0 is inversely proportional to the diffusion coefficient in the case of bulk diffusion, whereas for pipe diffusion $1/t_0 \sim D\rho_f^{3/2}$ [46], where ρ_f is the density of forest dislocations.

The mean ageing time t_a is identified with the mean waiting time t_w of mobile dislocations on the obstacles. t_w, is connected with the strain rate by the Orowan equation

$$\dot{\varepsilon} = b\rho_m \Lambda / t_w = b\Omega / t_w \tag{17}$$

where ρ_m is the mobile dislocation density, Λ is the mean free path of dislocations. If it is assumed that the forest dislocations are the rate controlling obstacles then $\Lambda = 1/\rho_f^{1/2}$. The elementary plastic strain per activation event $\Omega = b\rho_m\rho_f^{-1/2}$ is strain dependent; it may exhibit a local maximum at a certain strain [43, 44].

If we consider that both the dislocation stress component and the friction stress are influenced by solutes, then the flow stress may be decomposed into a non-aged part σ_{na} and a dynamic strain ageing part σ_a. The strain rate and temperature dependences of the stress increment due to dynamic strain ageing are simply related to the kinetic law $\Delta c(t_w)$ for the local concentration changes. Hence,

http://dx.doi.org/10.5772/58949

$$\sigma_a = \left(f_1 + f_2\right)\Delta c\left(t_w\right). \quad \text{(a)}$$
$$\text{or} \quad (18)$$
$$\sigma_a = \left(f_1 + f_2\right)\left[1 - \exp\left(-X\right)\right] \quad \text{(b)}$$

The first term f_1 corresponds to the dislocation-dislocation interaction influenced by dynamic strain ageing, while the second term f_2 results from the solute atoms-dislocation interaction influenced by dynamic strain ageing. $X=(b\Omega/\ \dot{\varepsilon}\ t_0)$. Combining the relations (16) – (18), the negative strain rate dependence of the dynamic strain-ageing component follows. This causes the negative strain rate dependence of the yield stress, which is observed at certain temperatures and in a certain strain rate range. The negative slope in the strain rate dependence of the yield stress was also observed in Mg+0.7Nd alloy deformed at room temperature (Fig. 57). The observed decrease in the flow stress (negative values of $\Delta\sigma$) due to changes from a lower strain rate to a higher one is also the result of dynamic strain ageing.

Solute atoms locking dislocations cause the observed stress increase after stress relaxation, which depends on strain and on temperature. An increase in the flow stress is needed to move the dislocations after the stress relaxation. It is reasonable to assume that $\Delta\sigma$ is proportional to the number of impurities on the dislocation line. The density of dislocations increases with strain, while the concentration of solute atoms is constant. Thus, the stress increase, $\Delta\sigma$, after relaxation due to dynamic strain ageing should decreases with strain, which is observed. The value of Ω decreases with strain [44, 45] and hence, t_w also decreases. This leads to the observed decrease in $\Delta\sigma$. It should be mentioned that the post relaxation behaviour and the values of $\Delta\sigma$ depend also on the time of relaxation [47].

8. Nomenclature

Quantities (selected)	Alloys
σ, ε true stress, true strain;	LA40 Mg-4wt%Li
σ_i, internal (athermal) stress;	LA43 Mg-4wt%Li-3wt%Al
σ^* effective (thermal) stress;	LA45 Mg-4wt%Li-5wt%Al
σ_f friction stress;	LA80 Mg-8wt%Li
σ_d dislocation stress;	LA83 Mg8wt%-Li-3wt%-Al
ΔG Gibbs free enthalpy;	LA85 Mg-8wt%Li-5wt%Al
V activation volume;	LA120 Mg-12wt%Li
$\dot{\varepsilon}$ plastic strain rate	LA123 Mg-12wt%Li-3wt%Al
b Burgers vector of dislocations	LA125 Mg-12wt%Li-5wt%Al
ϱ_m mobile dislocation density	AJ51 Mg-5wt%Al-0.6wt%Sr

Quantities (selected)	Alloys
ϱ_t total dislocation density	AJ91 Mg-9wt%Al-1wt%Sr
k Boltzmann constant	AJ62 Mg-6wt%Al-2wt%Sr
c atomic concentration of solute atoms	AX41 Mg-4wt%Al-1wt%Ca
CRSS critical resolved shear stress (τ_0)	AX62 Mg-6wt%Al-2wt%Ca
CYS compression yield stress (σ_{02})	AX91 Mg-9wt%Al-1wt%Ca
MCS maximum compression strength (σ_{max})	AZ63 Mg-6wt%Al-3wt%Zn
TYS tensile yield stress (σ_{02})	AZ91 Mg-9wt%Al-1wt.%Zn
MTS maximum tensile strength (σ_{max})	AE42 Mg-4wt%Al-2wt%RE
SR stress relaxation	ZE41 Mg-4wt%Zn-1wt%RE
SEM scanning electron micrograph	QE22 Mg-2wt%Ag-2wt%RE

Acknowledgements

Z.T. and P.L. are grateful for the financial support of the Czech Science Foundation (project P204/12/1360). P.P. is grateful for the financial support to the Slovak Grant Agency for Science (project VEGA No. 1/0797/12).

Author details

Zuzanka Trojanová[1], Peter Palček[2], Pavel Lukáč[1] and Zdeněk Drozd[1]

1 Charles University in Prague, Faculty of Mathematics and Physics, Czech Republic

2 University of Žilina, Faculty of Mechanical Engineering, Slovak Republic

References

[1] Haasen P. Mechanical Properties of Solid Solutions. In: Cahn RW, Haasen P, eds. Physical Metallurgy. 4th Edition, Amsterdam, Elsevier Science North Holland 1996, 2009-2073.

[2] Akhtar A, Teghtsoonian E. Solid Solution Hardening of Magnesium Single Crystals. Philosophical Magazine 1972; 25, 897-916.

[3] Stanford N, Barnett MR. Solute Strengthening of Prismatic Slip and {10-12} Twinning in Mg and Mg-Zn Binary Alloys. International Journal of Plasticity. 2013; 47, 165-181.

[4] Balík J, Lukáč P, Kužel R. Basal to Non-Basal Transition for In-Plane Deformation of AZ31 Magnesium Alloys. Acta Physica Polonica A 2012; 122(3), 435-438.

[5] Feltham P. Stress Relaxation in Magnesium at Low Temperatures. physica status solidi 1963; 3, 1340-1346.

[6] Levinson DW, McPherson DJ. Phase Relations in Mg-Li-Al Alloys. Transactions ASM 1956; 48, 689-705.

[7] Haferkamp H, Jaschik C, Juchmann P, Kaese V, Niemeyr M, Tai P. Entwicklung und Eigenschaften von Magnesium-Lithium-Legierungen. Materialwissenschaft und Werkstofftechnik 2001; 32, 25-30.

[8] Ando S, Tonda H. Non-Basal Slip in Magnesium-Lithium Alloy Single Crystals. Materials Transactions, Japan Institute of Metals 2000; 41, 1188-1191.

[9] Yoshinaga Y, Horiuchi R. On the Flow Stress of Solid Solution Mg-Li Alloy Single Crystals. Materials Transactions, Japan Institute of Metals 1963; 4, 134-141.

[10] Kamado S, Kojima Y. Deformability and Strengthening of Superlight Mg-Li Alloys. Metallurgical Science and Technolology 1998; 16, 45-54.

[11] Agnew SR, Yoo MH, Tomé N. Application of Texture Simulation to Understanding Mechanical Behavior of Mg and Solid Solution Alloys Containing Li or Y. Acta Materialia 2001; 49, 4277.

[12] Pawełek A, Piątkowski A, Kudela S, Jasieński Z. Acoustic Emission in Mg-Li-Al Alloys and Related Composites Based on Diphase α+β Matrix Subjected to Channel–Die Compression at Elevated Temperature 140 °C. Archives of Metallurgy and Materials 2006; 51, 245-252.

[13] Lukáč P, Balík J. Kinetics of Plastic Deformation. Key Engineering Material. 1994;97–98, 307–322.

[14] Pekguleryuz M. Creep Resistant Magnesium Alloys for Power-Train Applications. In: KU. Kainer (ed.), Magnesium Alloys and Their Applications. DGM, Willey-VCH 2003, 65-85.

[15] Trojanová Z, Lukáč P, Milička K, Száraz Z. Characterisation of Dynamic Strain Ageing in Two Magnesium Alloys. Materials Science and Engineering A 2004; 387–389, 80-83.

[16] Li JCM. Dislocation Dynamics in Deformation and Recovery. Canadian Journal of Physics 1967; 45, 493-509.

[17] Suzuki A, Saddock ND. Jones JW, Pollock TM. Structure and Transition of Eutectic $(Mg, Al)_2Ca$ Laves Phase in a Die-Cast Mg–Al–Ca Base Alloy. Scripta Materialia 2004; 51, 1005-1010.

[18] Ninomiya R, Ojiro T, Kubota K. Improved Heat Resistance of Mg-Al Alloys by the Ca Addition. Acta Metallurgica 1995; 43, 669-674.

[19] Gjestland H, Nussbaum G, Regazzoni G, Lohne O, BaugerØ. Stress-Relaxation and Creep Behaviour of Some Rapidly Solidified Magnesium Alloys. Materials Science and Engineering A 1991; 134, 1197-1200.

[20] Terada Y, Ishimatsu N, Sota R, Sato T, Ohori K. Creep Characteristics of Ca-Added Die-Cast AM50 Magnesium Alloys. Materials Science Forum 2003; 419-422, 459-464.

[21] Du W, Sun Y, Min X, Xue F, Zhu M, Wu D. Microstructure and Mechanical Properties of Mg–Al Based Alloy with Calcium and Rare Earth Additions. Materials Science and Engineering A 2003; 356, 1-7.

[22] Barnett MR. Twinning and the Ductility of Magnesium Alloys: Part II. "Contraction"Twins. Materials Science and Engineering A 2007; 464, 8-16.

[23] Koike J. Enhanced Deformation Mechanisms by Anisotropic Plasticity in Polycrystalline Magnesium Alloys at Room Temperature. Metallurgical and Materials Transaction A, 2005; 36A, 1689-1695.

[24] Jiang L. Jonas JJ, Mishra RK, Luo AA, Sachdev AK, Godet S. Twinning and Texture Development in Two Mg Alloys Subjected to Loading Along Three Different Strain Paths. Acta Materialia 2007; 55, 3899-3910.

[25] Kocks UF, Argon AS, Ashby MF. Thermodynamics and Kinetics of Slip. Progress in Materials Science 1975; 19, 1-288.

[26] Ono K, Temperature Dependence of Dispersed Barrier Hardening. Journal of Applied Physics 1968; 39, 1803-1806.

[27] Evans AG. Rawlings RD. The Thermally Activated Deformation of Crystalline Materials. physica status solidi 1969; 34, 9-31.

[28] Couret A, Caillard D. An in Situ Study of Prismatic Glide in Magnesium—I. The Rate Controlling Mechanism. Acta metallurgica 1985; 33, 1447-54.

[29] Couret A, Caillard D. An in Situ Study of Prismatic Glide in Magnesium—II. Microscopic Activation Parameters. Acta Metallurgica 1985; 33, 1455-62.

[30] Amadieh A, Mitchell J, Dorn JE. Lithium Alloying and Dislocation Mechanisms for Prismatic Slip in Magnesium Transactions AIME 1965; 233, 1130-37.

[31] Koike J, Ohyama R. Geometrical Criterion for the Activation of Prismatic Slip in AZ61 Mg Alloy Sheets Deformed at Room Temperature. Acta Materialia 2005; 53, 1963-72.

[32] Máthis K, Nyilas K, Axt A, Dragomir-Cernatescu I, Ungár T, Lukáč P. The Evolution of Non-Basal Dislocations as a Function of Deformation Temperature in Pure Magnesium Determined by X-ray Diffraction. Acta Materialia 2004; 52, 2889-2894.

[33] Milička K, Trojanová Z, Lukáč P. Internal Stresses During Creep of Magnesium Alloys at 523 K. Materials Science and Engineering A 2007; 462, 215-219.

[34] Trojanová Z, Lukáč P, Milička K, Száraz Z. Characterisation of Dynamic Strain Ageing in Two Magnesium Alloys. Materials Science and Engineering A 2004; 387-389, 80-83.

[35] Chatuverdi MC, Lloyd DJ. Onset of Serrated Yielding in Mg-10Ag Alloy. Philosophical Magazine 1974; 30, 1199-1207.

[36] Gärtnerová V, Trojanová Z, Jäger A, Palček P. Deformation Behaviour of Mg–0.7 wt. % Nd Alloy. Journal of Alloys Compounds 2004; 378, 180-183.

[37] Zhu SM, Nie JF. Serrated Flow and Tensile Properties of a Mg–Y–Nd Alloy. Scripta Materialia 2004; 50, 51-55.

[38] Corby C, Cáceres CH, Lukáč P. Serrated Flow in Magnesium Alloy AZ91. Materials Science and Engineering A. 2004; 387-389, 22-24.

[39] Trojanová Z, Cáceres CH, Lukáč P, Čížek L. Serrated flow in AZ91 Magnesium Alloy in Tension and Compression. Kovove Materialy-Metallic Materials 2008; 46, 249 – 256.

[40] Lavrentev FF. The Type of Dislocation Interaction as the Factor Determining Work Hardening. Materials Science and Engineering A 1980; 46, 191-208.

[41] Mulford RA, Kocks UF. New Observations on the Mechanisms of Dynamic Strain Aging and of Jerky Flow. Acta Metallurgica 1979; 27, 1125-1134.

[42] Balík J. Lukáč P. On the Kinetics of Dynamic Strain Ageing. Kovove Materialy-Metallic Materials 1998; 36, 3-9.

[43] Kubin LP, Estrin Y. Evolution of Dislocation Densities and the Critical Condition for the Portevin-Le Châtelier Effect. Acta Metallurgica et Materialia 1990; 38, 697-708.

[44] Balík J, Lukáč P. Portevin-Le Châtelier Instabilities in Al-3Mg Conditioned by Strain Rate and Strain. Acta Metallurgica et Materialia 1993; 41, 1447-1454.

[45] Louat N. On the Theory of the Portevin-Le Châtelier Effect. Scripta Metallurgica 1981; 15, 1167-1170.

[46] Friedel J. Dislocations. Pergamon, Oxford, 1964.

[47] Balík J. The Onset of Portevin– Le Châtelier Instabilities in Tensile Testing. Materials Science and Engineering A 2001; 316, 102-108.

Chapter 2

Texture, Microstructure, and Mechanical Properties of Calcium-Containing Flame-Resistant Magnesium Alloy Sheets Produced by Twin-Roll Casting and Sequential Warm Rolling

Masafumi Noda, Tomomi Ito, Yoshio Gonda,
Hisashi Mori and Kunio Funami

Additional information is available at the end of the chapter

http://dx.doi.org/10.5772/58940

1. Introduction

Magnesium (Mg) alloys are attracting attention as metallic materials of the next generation because of their good specific strength, specific rigidity, earthquake resistance, and machinability, as well as the abundance of resources available for their production [1]. Because of their lightness, Mg alloys are expected to be suitable materials for replacing aluminum alloys in automobiles and in rail and aerospace transportation devices [2,3]. Research has been performed on improving the mechanical properties, corrosion resistance, and workability of Mg alloys [4,5]. Hot working is required in plastic forming of Mg alloys because of their crystal structure [6]. Problems associated with Mg alloys include their high production costs, their high flammability, and the marked effects of additive elements on the various properties of the alloys. Most structural parts currently manufactured from Mg alloys are die cast, Thixomolded [7,8], semicontinuously cast, or gravity cast [8,9], or they are forged from such materials. The amount of wrought materials that are used is low, representing less than 10% of all Mg alloys that are used [10]. Recently, the problems associated with Mg alloys have been resolved by increasing their strength [11–13] and by improving their creep properties [14], heat resistance [15], and formability [16,17] by adding trace amounts of various elements [18,19], by age-hardening effects [20], by crystal-grain refinement [21,22], and by texture control [23,24]. However, there is still a need for incombustible or noncombustible Mg alloys [25-27] for use in structural or construction components. Flame-resistant and noncombustible Mg alloys have recently been developed by adding Ca to Mg alloys [25–28], and these materials

have received flame-resistance and noncombustion certifications in the rail, aerospace, and construction sectors.

There are many choices of starting material for manufacturing sheet products, and use of twin-roll cast (TRC) materials [29–32] should be examined if production costs are a consideration. However, TRC materials have a number of problems, such as solidifying segregation at the slab thickness center, intrusion of inclusions during casting, and restrictions on casting conditions, such as the casting length, liquid pressure, rolling speed, and quenching capacity [30–32]. Moreover, most generic TRC materials in use are Al alloys or AZ-type Mg alloys that do not preferentially form intermetallic compounds [30–33]. TRC materials described in the literature are subjected to a short TRC process, so that the melt is exposed to the air for only a short time and there is no blackening of the sheet surface through ignition during casting. There is a report that the manufacture of a sheet material from AZ-type Mg alloys can be problematic unless the twin-rolling speed is unusually slow at casting temperatures exceeding 620 °C [34], but there has been no discussion on the effects of the metal texture and the role of plastic deformation after casting. In addition, there has been insufficient discussion on the effect of melt purification before TRC casting and on the role of additive elements on twin-roll casting conditions and the internal texture. Furthermore, there is no report of any comparison with semicontinuous casting in the manufacture of sheet material. We have therefore describe our investigations on the effects of melt purification during melting before TRC on the production of sheet materials, as well as the microstructure and mechanical properties of twin-roll cast Ca-containing flame-resistant Mg alloys; we also provide an analysis of the effects on the cast sheets and their durability caused by precipitation of intermetallic compounds formed through addition of Ca.

2. Experimental procedures

To investigate the effects of the alloy composition on materials produced under TRC conditions, samples of AZ61 alloy and of AZX611 and AZX612 alloys containing 1 or 2 mass% of added Ca, respectively, were prepared from AM60B Mg and Mg–30%Ca master alloy, pure Al ingots (99.7%), and pure Zn ingots (99.9%). The metals were weighted to the required stoichiometry, placed in a steel crucible, and melted by heating to 700 °C in an electric furnace. Melting was carried out under an argon atmosphere, and argon gas was bubbled through the melt for 20 min. The slug was removed and immediately tapped when the melt temperature reached 660 °C. To prevent combustion of the weighed metals, the melt was isolated from the atmosphere by placing a steel lid on the crucible. The conditions for twin-roll casting were as follows. The speed of both the upper and lower rolls was 20–25 m min^{-1}, and the roll gap was 2 – 3 mm. The rolls used were metal rolls 300 mm wide with a diameter of 200 mm. The surface of the roll was heated to a temperature of more than 100 °C before twin-roll casting prior to decreasing the cooling rate. Grooves were cut into the rolls to facilitate peeling of sheets during twin-roll casting. Figure 1 is a schematic showing the twin-roll casting process. After twin-roll casting, the sheets were left to cool to room temperature and then subjected to strip processing. Sheets measuring 150 mm in width by 200 mm in length were cut from the TRC material for

http://dx.doi.org/10.5772/58940

strip processing, with the width direction of the cut sheets aligned in the casting direction. Strip processing was performed by using a two-high rolling mill with 300 mm diameter rolls. The thickness of the original sheet was reduced by 65% in one pass: the roll surface temperature was 245 °C, the workpiece was heated for 10 min at 200–400 °C, the roll speed during processing was 5–25 m min^{-1}, and the workpiece was cooled with water after the strip processing. Tensile-test specimens with a gauge length of 30 mm and a width of 4 mm were prepared from the strip-processed materials, and tensile tests were carried out in air at an initial strain rate of 1.3 × 10^{-3} s^{-1}. The microstructures of the TRC materials and the strip-processed materials were examined by optical microscopy (OM), and scanning electron microscopy (SEM), and the crystal orientation was analyzed by using electron backscattered diffraction (EBSD).

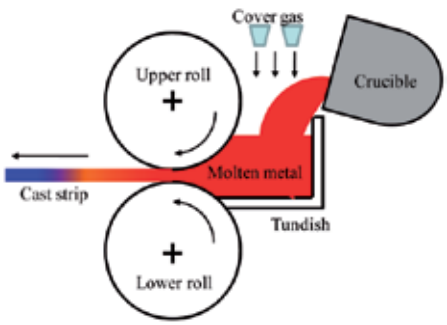

Figure 1. Schematic of a twin-roll caster for strips.

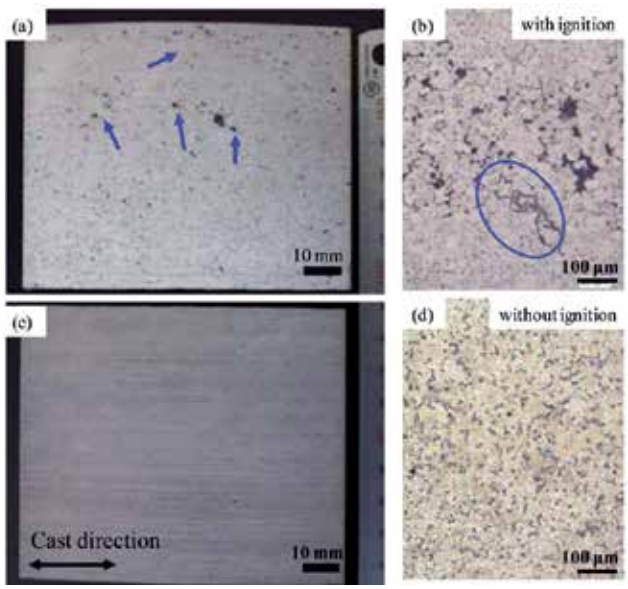

Figure 2. Surface of cast material plate with ignition (a) and without ignition (c), and optical micrographs of twin-roll cast material with ignition (b) and without ignition (d).

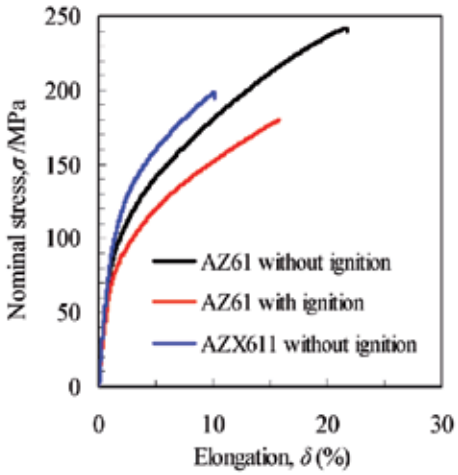

Figure 3. Nominal stress–strain curves for AZ61 and AZX611 twin-roll cast materials.

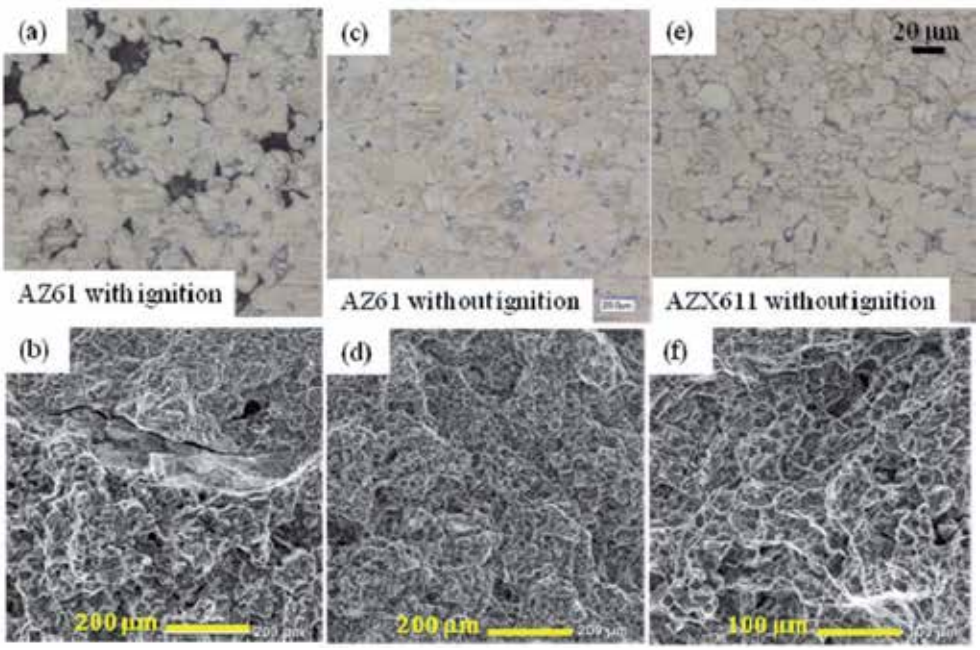

Figure 4. Cross-sectional optical micrographs [(a), (c), and (e)] and SEM micrographs of fracture surfaces [(b), (d), and (f)] of AZ61 [(a)–(d)] and AZX611 [(e) and (f)] twin-roll cast materials with ignition during heating [(a) and (b)] and without ignition during heating [(c)–(f)].

http://dx.doi.org/10.5772/58940

3. Results and discussions

3.1. The twin-roll casting process and microstructure

Figure 2(a)–(d) show external views and internal microstructures of sheets subjected to melting in an argon (Ar) atmosphere, bubbling with argon gas, and twin-roll casting. Slight combustion caused oxides to form in the melt and increased the frequency of intrusion of oxides and impurities. Figure 2(a) and 2(b) show the presence of black spots on the surface of the sheet and the inclusion of oxides and impurities in the microstructure. The nominal stress–strain curves of the TRC AZ61 and AZX611 alloys are shown in Figure 3, and the vertical cross-sections and fracture surface microstructure are shown in Figures 4(a)–(f). Two types of AZ61 alloys are shown in Figure 4(a)–(d), one in which combustion occurred during melting and one in which it did not occur. The AZX611 alloy melt did not undergo combustion during TRC. When no combustion occurred during melting, the yield stress (YS) was 116 MPa, the ultimate tensile strength (UTS) was 239 MPa, and the elongation was 19% [Figures 4(a) and 4(b)], whereas when combustion occurred, the YS was 82 MPa, the UTS was 180 MPa, and the elongation was 13% [Figures 4(c) and 4(d)]. Intrusion of inclusions and oxides caused early fracture without sufficient plastic deformation [35], and the tensile properties were stable when melts that had not undergone combustion were used. Figure 4 shows that intrusion of oxides caused by combustion results in propagation of cracks, formation of voids, and the appearance of partial brittle fracture. Most of the brittle fracture occurs near the surface of the TRC material, implying that the solidification rate is faster at the surface of the sheet than in its interior, that internal latent heat causes coarsening of the microstructure, and that crack propagation along grain boundaries is initiated from internal voids, resulting ultimately in fracture. In contrast, AZ61 alloy that had not undergone combustion showed a standard ductile fracture surface. In AZX611 alloy containing 1 mass% of Ca, no intrusions of oxides were found and the YS (139 MPa) was higher than that of AZ61 alloy; however, the elongation was only about 8%. Because Al–Ca compounds form at grain boundaries, as shown in Figures 4(e) and 4(f), the reason for early fracture compared with AZ61 alloy is likely to be inhibition of plastic deformation by Al–Ca compounds.

Figure 5 shows the SM and OM microstructures of TRC AZ61 and AZX611 alloys for the case where the roll was at room temperature, the melt temperature was 660 °C, and the roll speed was 25 m min^{-1}. Figures 5(a) and 5(b) show that no cracks were present at the surface of the TRC material in the AZ61 alloy, but that cracks appeared at grooves in the AZX611 alloy. Al–Ca compounds are known to form in AZX611 alloy [3,11]. Figures 5(c) and 5(d) show the OM microstructure after removal of 0.1 mm of material from the sheet surface by mechanical polishing, and they show that Al–Ca compounds formed near cracks in the AZX611 alloy. There was considerable segregation near the surface in the processed sheets shown in Figure 5(d), suggesting that the cooling rate in twin-roll casting is too rapid for alloy systems that form compounds.

Figure 6 shows an example in which Al–Ca compounds segregate at the surface of the TRC material. Because Al–Ca compounds form where the quenching capacity is largest, the rate of solidification of the melt in the twin-roll casting process was reduced by adjusting the

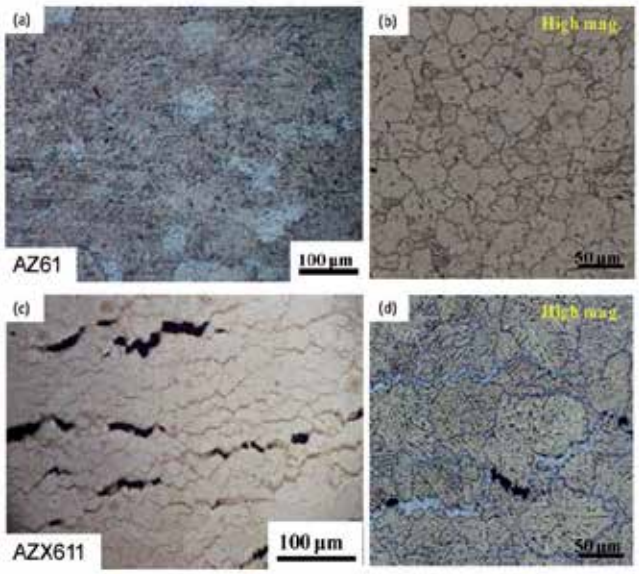

Figure 5. Optical micrographs of the surfaces of twin-roll cast strips of AZ61 [(a), (b)] and AZX611 [(c), (d)].

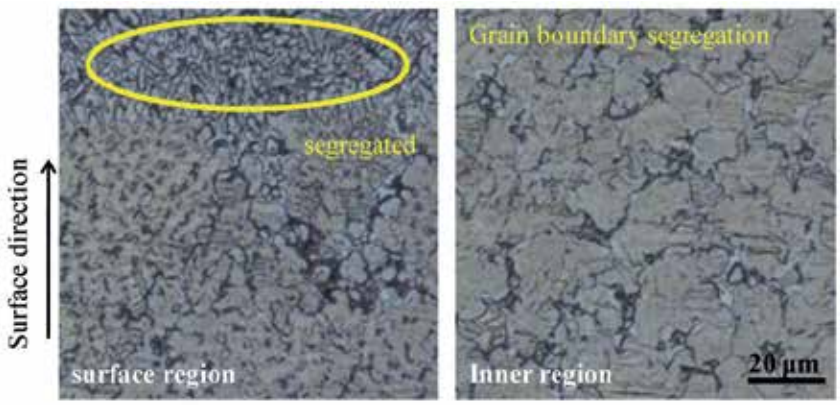

Figure 6. Example showing the segregation of Al–Ca compounds in a rapidly cooled region of twin-roll cast material.

temperature of the roll surface to 100 °C and decreasing the roll speed to 20 m min^{-1}. Optical micrographs showing the microstructure of the surface of the resulting sheet and of a cross section perpendicular to the surface are presented in Figure 7. No cracks were found and no segregation of Al–Ca compounds was observed in the prepared sheet. In this case, the sheet temperature immediately after twin-roll casting was 560 °C. By reducing the cooling rate from that of fast solidification at over 100 °C s^{-1}, characteristic of twin-roll casting [29,33], to around 50 °C s^{-1}, samples of TRC Mg alloy material 300 mm wide by 5 m long that form intermetallic compounds can be prepared, as shown in Figure 8.

http://dx.doi.org/10.5772/58940

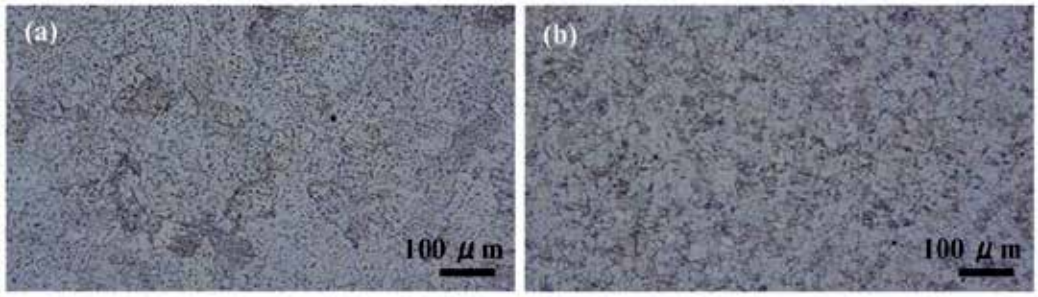

Figure 7. Optical micrographs of AZX611 twin-roll cast material solidified at a lower rate (rise to roll-surface temperature, lower roll-mill speed). Observations were made from the direction of the surface (a) and in the perpendicular direction (b).

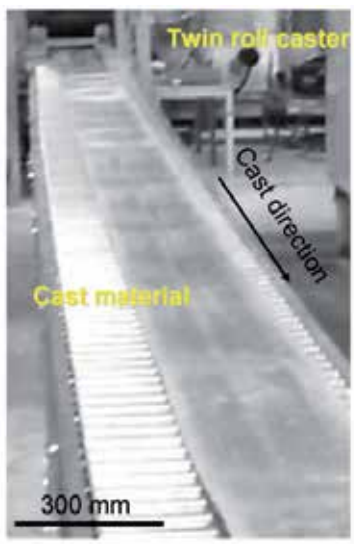

Figure 8. Twin-roll cast AZX611 Mg strip of thickness 2.5 mm and width 300 mm fabricated by using a pilot-plant twin-roll casting machine.

3.2. Comparisons of the texture, microstructure, and mechanical properties of twin-roll cast material with those of normally cast material

The thermal conductivities of AZ61, AZX611, and AZX612 alloy are 63.6, 70.2, and 77.2 W / mK, respectively; therefore, the thermal conductivity increases with addition of Ca. This means that the optimal twin-roll casting conditions will be different for each alloy and, for each sheet, the surface and the interior will have different microstructures. Figure 9 shows the surface and interior OM microstructures of AZ61 and AZX611 TRC alloys. The grain size at the surface of the TRC material is about 2.5 times larger than that in the interior. The surface microstructure consists of coarse grains 70–100 μm in size or dendrites, whereas the interior consists of refined

equiaxial grains 25–40 μm in size. The region with refined equiaxial grains account for two-thirds of the thickness of the sheet.

The inverse pole figure (IPF) map and the pole figure (PF) map obtained by EBSD analysis of the surface and interior of TRC AZX611 alloy are shown in Figure 10. TRC material does not show any specific crystal orientation in either the surface or the interior, regardless of grain size. As shown in Figure 9(a), the texture orientation is high (10.9) because of the large size of the crystal grains compared with the visual area for measurement. The microstructure orientation of the interior texture is 3.8, indicating a random orientation. One noteworthy point is that the OM microstructure and IPF map suggest that a grain boundary forms between the refined-grain region and coarse-grain region. However, measurement of the crystal orientation between adjacent grains showed that coarse grains adjacent to regions of refined grains are in fact agglomerates of refined subgrains. This means that differences between the surface and interior microstructure can be reduced by optimizing the twin-roll casting method or by a cooling and homogenization processes after twin-roll casting. No cracks at interfaces or grain boundaries were found in either the coarse-grain region or the refined-grain region.

Table 1 lists the average grain sizes at the surfaces and in the interiors of AZ61, AZX611, and AZX612 TRC alloys, as well as the proportion of compound formation and the hardness. These measurements were performed by using 3 mm thick TRC sheets. As the Ca content increases, the crystal grain size becomes smaller, the area ratio of intermetallic compounds increases, and the hardness increases. Figure 11 shows the OM structure and the IPF and FP maps for AZX611 alloy semicontinuously cast at a cooling rate of 25 °C s^{-1}. The average grain size of the standard gravity-cast material is around 600–800 μm [11]. This can be refined to about 100 μm by increasing the cooling rate, thereby making possible refined dispersion of Al–Ca compounds in the Mg phase [35]. Here, the texture orientation is 10.9 and a dendrite microstructure is present in the crystal texture, showing the same trends as the microstructure of the surface of TRC material. The YS and UTS of semicontinuously cast material have been reported to be 90 MPa and 155 MPa, respectively, and the elongation is 5%. The elongation is lower than that found in tensile tests on TRC AZX611 material, although the tensile behavior is similar. Therefore, large changes in single uniaxial tensile tests were not observed when the cooling rate exceeded a certain value and the average grain size after casting was less than 100 μm, Addition of Ca causes minute cracks to form more easily, as mentioned before, and similar results are found in semicontinuously cast material. On the other hand, as Al–Ca compounds are smaller and undergo refined dispersion in the Mg phase in TRC material, as shown in Figures 10 and 11, the rolling reduction per pass can be large in the strip-processing technique described later. The results agree with the maximum rolling reduction curve for extruded AZX311 determined by Noda *et al.* [11] The use of extruded materials or TRC materials instead of cast materials with a dendrite microstructure and/or coarse grains results in good strip-processing performance as a result of random crystal orientation, formation of a refined texture, and refined dispersion of Al–Ca compounds.

http://dx.doi.org/10.5772/58940

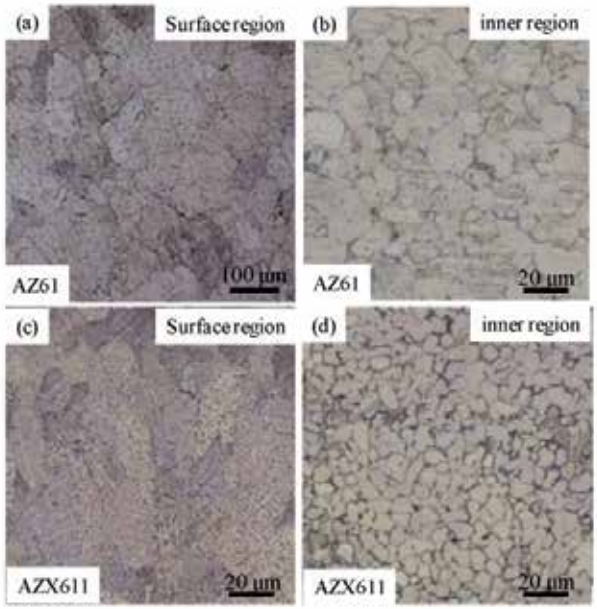

Figure 9. Optical micrographs of twin-roll cast strips of AZ61 [(a) and (b)] and AZX611 [(c) and (d)] showing the surfaces of the strips [(a) and (c)] and the interiors of the strips [(b) and (d)].

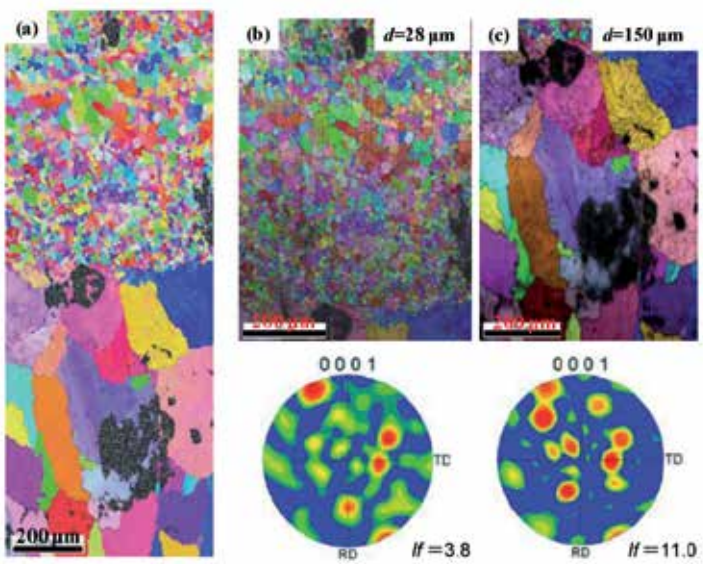

Figure 10. Inverse pole figure (IPF) maps and pole figure (PF) maps of AZX611 twin-roll cast material. The intensity of texture is indicated in the PF maps. Figures (b) and (c) were cropped from the IPF map; (b) shows the surface region and (c) shows the interior.

Material	Vickers hardness (HV)	Mean grain size Surface / Inner region	Thermal conductivity (W/mK)	Area frequency of compounds (%)
AZ61	64	93 μm / 37 μm	63.6	0.8
AZX611	66	70 μm / 24 μm	70.2	7.1
AZX612	68	73 μm / 17 μm	77.2	18.1

Table 1. Grain size, Vickers hardness, and area frequency of compounds for various twin-roll cast materials.

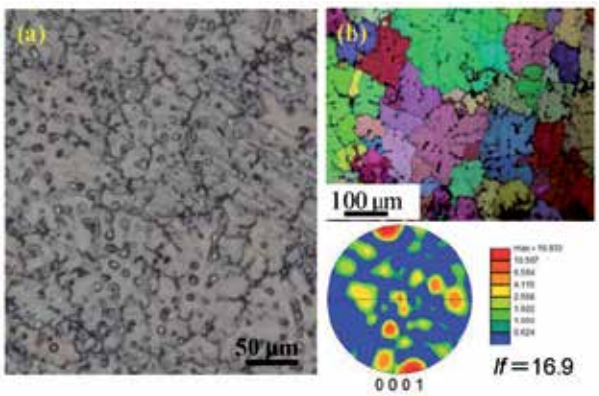

Figure 11. Optical micrograph and IPF and PF maps of AZX611 antigravity suction-cast material cooled at 25 °C s^{-1}. The intensity of texture is indicated in the PF map.

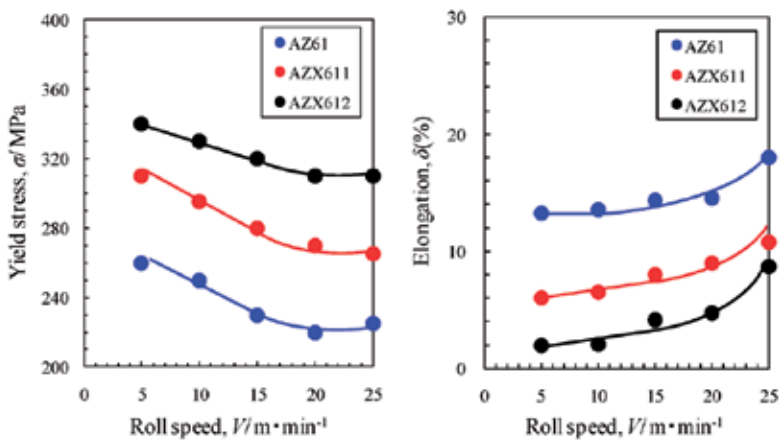

Figure 12. Relationship between tensile properties and roll-mill speed for AZ61, AZX611, and AZX612 twin-roll cast materials subjected to a single-pass rolling process.

http://dx.doi.org/10.5772/58940

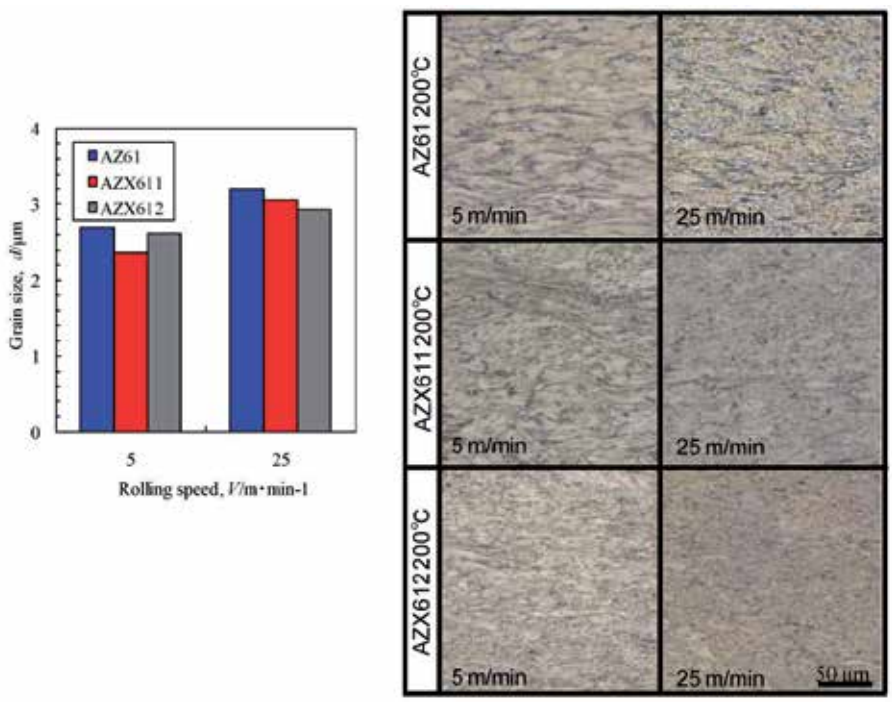

Figure 13. (a) Relationship between the grain size and the annealing temperature for single-pass rolled samples of AZ61, AZX611, AZX 612; and (b) optical micrographs of AZ61, AZX611, and AZX612 materials subjected to single-pass rolling at a sample temperature of 200 °C. The roll-mill speeds are indicated in the optical micrographs.

3.3. Mechanical properties and microstructures of rolled materials

Figure 12 shows the tensile properties of TRC AZ61, AZX611, and AZX612 alloys subjected to strip processing with large one-pass rolling reductions with a strip roll-surface temperature of 245 °C, a specimen temperature of 200 °C, and various roll speeds. The OM microstructures and recrystallized grain sizes are given in Figure 13. The rolling reduction was 65% of the original thickness. According to Figure 12, the YS of AZ61alloy decreased monotonously from 260 MPa to 230 MPa, and that of AZX611 decreased monotonously from 310 MPa to 270 MPa when the strip processing speed was increased to 15 m min^{-1}. Increasing the roll speed further to 25 m min^{-1} resulted in a decrease in the YS to 190 MPa for AZ61 and to 250 MPa for AZX611. The grain size of strip-processed AZ61 and AZX611 alloys was 3 μm regardless of the strip-processing speed. The grain size normally coarsens with increasing strip-processing speed; however, unlike the case of multipass strip processing, the rolling speed has no apparent effect on the crystal texture in the one-pass TRC process because of the effects of processing heating. The Al–Ca

compounds that form at the grain boundaries in TRC AZX611 alloy reorient parallel to the rolling direction after strip processing. On the other hand, the microstructure of processed AZX612 alloy is similar to that of AZ61 and AZX611 alloys, as described above, but the tensile properties are independent of the strip-processing speed. The area ratio of Al–Ca compounds in TRC AZX611 alloy is 7.1%. However, in AZX612 alloy, this value increases to 18.1%, and the decrease in strength for strips processed with a large reduction ratio is small. Furthermore, as shown in Figure 13, Al–Ca compounds dispersed in the Mg phase inhibit the growth of Mg phase grains. Solution treatment or homogenizing treatment is typically necessary when Al–Ca compounds develop. It is easier to strip process AZX612 alloy than gravity-cast material, and the dispersion of compounds is the dominant factor in plastic deformation. Figure 14 shows the relationship between the annealing temperature and the grain size when a material strip processed at a roll speed of 5 m min^{-1} is annealed for one hour; it also shows the OM microstructure of material annealed for one hour at 400 °C. Crystal grains of AZ61 alloy grew rapidly at an annealing temperature of 350 °C. However, as the amount of added Ca was increased, the ultimate grain size was 10 μm in AZX611 alloy and 7 μm in AZX612 alloy, even when the annealing temperature was increased. There are no compounds that inhibit grain growth in AZ61, whereas Al–Ca compounds inhibit grain growth in AZX611 and AZX612 alloys. The area ratio of Al–Ca compounds is higher in AZX612, and large amounts of dispersion into the Mg phase after strip processing effectively inhibit grain growth. These results suggest that adding more Ca results in an improvement in thermal resistivity, and agrees with a report on improvement of creep-resistance properties [14].

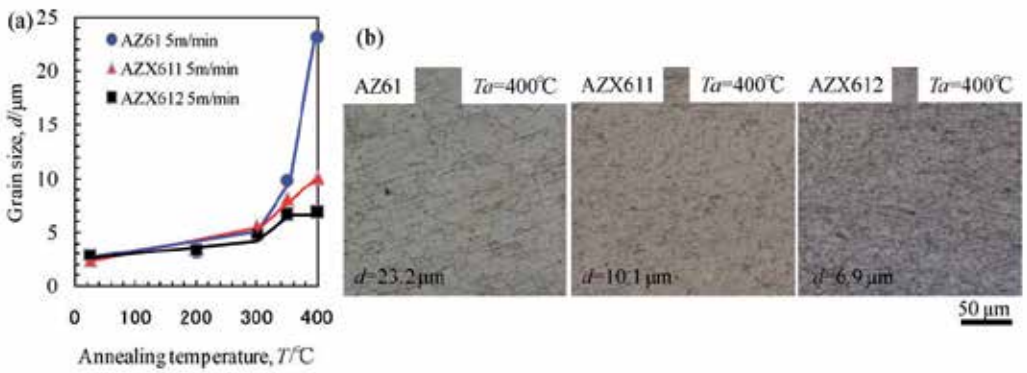

Figure 14. (a) Relationship between the annealing temperature and the grain size for AZ61, AZX611, and AZX612 single-pass-rolled materials. Annealing was performed at 200, 300, 350, or 400 °C for one hour. (b) Optical micrographs of materials annealed at 400 °C for one hour.

http://dx.doi.org/10.5772/58940

The TRC material prepared in this research had an equiaxial microstructure, permitting a large rolling reduction of about 65% per pass. For Mg alloys that form Al–Ca compounds on addition of Ca, resulting in deterioration of the plastic-deformation performance, twin-roll casting is an effective processing method, although it is limited to the manufacture of sheet materials. With regard to the microstructure after strip processing, although the internal microstructure of the TRC material varied with the twin-roll casting conditions, in no case was there mixing of grain size in the internal microstructure, that is, there was no mixing of the coarse microstructure at the surface of the sheets with the refined internal microstructure. No solution treatment or microstructure homogenization treatment is carried out after twin-roll casting of AZ61 alloy; as a result, the β-phase remains elongated along the rolling direction.

3.4. Corrosion behavior of rolled magnesium alloys

There are many reports on the corrosion resistance of generic AZ-type Mg alloys, but few reports on those of noncombustible Ca-containing Mg alloys. We therefore examined the corrosion properties of such alloys.

Samples of TRC Mg–3Al–1Zn–1Ca (AZX311), Mg–6Al–1Zn–1Ca (AZX611), and Mg–10Al–0.2Mn–1Ca (AMX1001) alloy sheets were warm-forged from a thickness of 3 mm to 1 mm. Although TRC materials have good strip-processing properties, to avoid mixing of grains in the internal microstructure as a result of strip processing, three-pass processing was employed with a roll speed of 10 m min^{-1}, a roll-surface temperature of 200 °C, and a specimen temperature of 250 °C. Reheating for 1 min was carried out between each pass, and the specimens were water cooled at the end of the process. Immersion tests were carried out in 5% aqueous NaCl at a constant temperature of 25 °C for up to 120 hours. Changes in weight and in surface microstructure were observed. After immersion, the material was prepared for examination by means of surface polishing, degreasing with acetone, and cutting into samples 20 mm long by 20 mm wide.

The average grain size of AZX311, AZX611, and AMX1001 strip-rolled alloys was 3.5 μm, and refined equiaxial grains and some elongated microstructure that had not recrystallized remained. The YS of all the alloys was around 330 MPa, the UTS was 350 MPa, and the elongation was 5% [3, 11, 35]. The relationship between the change in weight and the immersion time shown in Figure 15(a) indicates that, for noncombustible Mg alloy containing 1 mass % of Ca, an increase in the Al content reduces the change in weight with increasing immersion time in a manner similar to that shown by generic AZ-type Mg alloys. The weight monotonously decreased for immersion times of up to 100 hours, and then changed quadratically regardless of the Al content. In the region where the weight decreased monotonously, filiform corrosion and partial pitting was observed at the sheet surface, as shown in the OM microstructure of Figure 15(b); however, these processes did not lead to significant weight losses because the crystal microstructure was refined. On the other hand, filiform corrosion and pitting per unit area increased with time, and these propagated and combined, leading to pitting of the entire surface of the sheet and a significant reduction in weight. Refined disper-

sion of Ca or Al–Ca compounds in the more-refined Mg phase as a result of casting and strip processing does not result in significant reduction in the corrosion resistance caused by intermetallic compounds if the amount of added Ca is only 1 mass%.

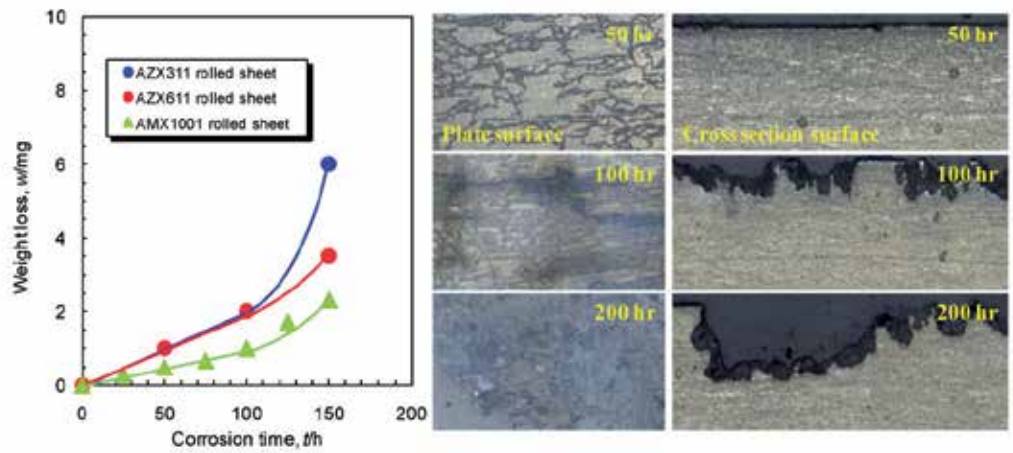

Figure 15. (a) Relationship between weight loss and immersion time for AZX311, AZX611, and AMX1001 rolled materials. (b) Optical micrographs of plate surfaces after immersion tests in an 5% aqueous NaCl solution.

4. Summary

In this present study, we investigated on the effects of melt purification during melting before twin-roll casting on the production of sheet metals. Using an Ar gas melting atmosphere prevented combustion at ingot alloy surface, and the amount of slug and oxide inclusions in the cast material decreased. By reducing the cooling rate from that of fast solidification at over 100 °C s^{-1}, characteristic of twin-roll casting, to around 50 °C s^{-1}, samples of TRC Mg alloy material 300 mm wide by 5 m long that form intermetallic compounds can be prepared without cracking. The grain size at the surface of the TRC material is about 2.5 times larger than that in the interior. As the Ca content increases, the crystal grain size becomes smaller and the area ratio of intermetallic compounds increases. The use of TRC materials instead of cast materials with a dendrite microstructure and/or coarse grains results in good strip-processing performance as a result of random crystal orientation, formation of a refined microstructure, and refined dispersion of Al–Ca compounds. Refined dispersion of Ca or Al–Ca compounds in the more-refined Mg phase as a result of casting and strip processing does not result in significant reduction in the corrosion resistance.

http://dx.doi.org/10.5772/58940

Author details

Masafumi Noda[1], Tomomi Ito[2], Yoshio Gonda[2], Hisashi Mori[3] and Kunio Funami[1]

*Address all correspondence to: mk-noda@s7.dion.ne.jp

1 Department of Mechanical Science and Engineering, Chiba Institute of Technology, Narashino, Chiba, Japan

2 Magnesium Division, Gonda Metal Industry Co., Ltd., Sagamihara, Kanagawa, Japan

3 Railway Technical Research Institute, Kokubunji, Tokyo, Japan

References

[1] Kamado S, Koike J, Kondoh K, Kawamura Y. Magnesium Research Trend in Japan. Materials Science Forum 2003; 419–422 21–34.

[2] Luo AA. Recent Magnesium Alloy Development for Automotive Powertrain Applications. Materials Science Forum 2003; 419–422 57–66.

[3] Mori H, Fujino K, Kurita K, Chino Y, Saito N, Noda M, Komai H, Obara H. Application of the Flame Retardant Magnesium Alloy to High Speed Rail Vehicles. Materia Japan 2013; 52(10) 484–490 (in Japanese). DOI 10.2320/material.52.484.

[4] Chen FK, Huang TB, Chang CK. Deep Drawing of Square Cups with Magnesium Alloy AZ31 Sheets. International Journal of Machine Tools and Manufacture 2003; 43(15) 1553–1559.

[5] Noda M, Matsumoto R, Kawamura Y. Forging Induces Changes in the Formability and Microstructure of Extruded $Mg_{96}Zn_2Y_2$ Alloy with a Long Period Stacking Order Phase. Materials Science and Engineering A 2013; 563 (15) 21–27.

[6] Yoo MH. Slip, Twinning, and Fracture in Hexagonal Close-Packed Metals. Metallurgical Transactions A 1981; 12(3) 409–418.

[7] Wang Y, Lui G, Fan Z. Microstructural Evolution of Rheo-Diecast AZ91D Magnesium Alloy During Heat Treatment. Acta Materialia 2006; 54(3) 689–699.

[8] Czerwinski, F., Magnesium Injection Molding,. New York, Springer Verlag, 2008; 19-21.

[9] Paliwal M, Jung IH. The Evolution of the Growth Morphology in Mg–Al Alloys Depending on the Cooling Rate During Solidification. Acta Materialia 2013; 61(13) 4848–4860.

[10] For examples, see: Kojima Y, Aizawa T, Kamado S., editors. Magnesium Alloys 2000: Volumes 350–351, Materials Science Forum, Trans Tech Publications, DOI: 10.4028/www.scientific.net/MSF.350-351.

[11] Noda M, Sakai N, Funami K, Mori H, Fujino K. High Strength and Grain Refinement of Mg-3Al-1Zn-1Ca Alloy by Rolling. Journal of the Japan Society for Technology of Plasticity 2013; 54(625) 143–147.

[12] Kawamura Y, Hayashi K, Inoue A, Masumoto T. Rapidly Solidified Powder Metallurgy $Mg_{97}Zn_1Y_2$ Alloys with Excellent Tensile Yield Strength above 600 MPa. Materials Transactions 2001; 42(7) 1172–1176.

[13] Jian WW, Cheng GM, Xu WZ, Yuan H, Tsai MH, Wang QD, Koch CC, Zhu YT, Mathaudhu SN. Ultrastrong Mg Alloy via Nano-Spaced Stacking Faults. Materials Research Letters 2013; 1(2) 61–66.

[14] Maruyama K, Suzuki M, Sato H. Creep Strength of Magnesium-Based Alloys. Metallurgical and Materials Transactions A 2002; 33(13) 875–882.

[15] Noda M, Kawamura Y, Mayama T, Funami K (2012), Thermal Stability and Mechanical Properties of Extruded Mg-Zn-Y Alloys with a Long-Period Stacking Order Phase and Plastic Deformation. In: Monteiro WA (ed.) New Features on Magnesium Alloys, Rijeka, InTech, 2012; DOI: 10.5772/48202.

[16] Matsumoto R, Osakada K. Effect of Heat Treatment on Forgeability of AZ31 Magnesium Alloy. Journal of Japan Institute of Light Metals 2007; 57(7) 274–279.

[17] Chino Y, Mabuchi M, Kishihara R, Hosokawa H, Yamada Y, Wen C, Shimojima K, Iwasaki H. Mechanical Properties and Press Formability at Room Temperature of AZ31 Mg Alloy Processed by Single Roller Drive Rolling. Materials Transactions 2002; 43(10) 2554–2560.

[18] Xu SW, Oh-ishi K, Sunohara H, Kamado S. Extruded Mg–Zn–Ca–Mn Alloys with Low Yield Anisotropy. Materials Science and Engineering A 2012; 558 356–365.

[19] Yim CD, You BS, Lee JS, Kim WC. Optimization of Hot Rolling Process of Gravity Cast AZ31-xCa (x=0–2.0 mass%) Alloys. Materials Transactions 2004; 45(10) 3018–3022.

[20] Furui M, Ebata Y, Yamada H, Ikeno S, Sakakibara K, Saikawa S. Grain Boundary and Intragranular Reactions During Aging in Mg-Al System Alloys Poured into Sand and Iron Molds. Materials Transactions 2011; 52(3) 285–291.

[21] Ion SE, Humphreys FJ, White SH. Dynamic Recrystallisation and the Development of Microstructure During the High Temperature Deformation of Magnesium. Acta Metallurgica 1982; 30(10) 1909–1919.

[22] Myshlyaev MM, McQueen HJ, Mwembela A, Konopleva E. Twining, Dynamic Recovery and Recrystallization in Hot Worked Mg–Al–Zn Alloy. Materials Science and Engineering A 2002; 337(1–2) 121–133.

[23] Watanabe H, Ishikawa K. Effect of Texture on High Temperature Deformation Behavior at High Strain Rates in a Mg–3Al–1Zn Alloy. Materials Science and Engineering A 2009; 523(1–2) 304–311.

[24] Agnew SR, Yoo MH, Tomé CN. Application of Texture Simulation to Understanding Mechanical Behavior of Mg and Solid Solution Alloys Containing Li or Y. Acta Materialia 2001; 49(20) 4277–4289.

[25] Akiyama S, Ueno H, Sakamoto M, Hirai H, Kitahara A. Development of Noncombustible Magnesium Alloys. Materia Japan 2000; 39(1) 72–74 (in Japanese).

[26] Kawamura Y, Yamasaki M. Ignition temperature and mechanical properties of nonflammable magnesium alloys with high strength. In: Collected abstracts of the 2013 Spring meeting of Japan Institute of Light Metals, 18–19 May 2013, University of Toyama, Japan. Japan Institute of Light Metals, Tokyo; 131–132.

[27] Czerwinski. F., Controlling the ignitions and flammability of magnesium for aerospace applications. Corrosion Science 2014; 86 1-16.

[28] Prasad A, Shi Z, Atrens A. Influence of Al and Y on the Ignition and Flammability of Mg Alloys. Corrosion Science 2012; 55 153–163.

[29] Haga T, Takahashi K. Casting of Composite Strip Using a Twin Roll Caster. Journal of Materials Processing Technology 2004; 157–158 701–705.

[30] Park SS, Bae GT, Kang DH, Jung IH, Shin KS, Kim NJ. Microstructure and Tensile Properties of Twin Roll Cast Mg–Zn–Mn–Al Alloys. Scripta Materialia 2007; 57(9) 793–796.

[31] Jiang B, Liu W, Qiu D, Zhang MX, Pan F. Grain Refinement of Ca Addition in a Twin Roll Cast Mg–3Al–1Zn Alloy. Materials Chemistry and Physics 2012; 133(2–3) 611–616.

[32] Zhao Hu, Li P, He L. Microstructure and Mechanical Properties of an Asymmetric Twin Roll Cast AZ31 Magnesium Alloy Strip. Journal of Materials Processing Technology 2012; 212(8) 1670–1675.

[33] Savage SJ, Froes FH. Production of Rapidly Solidified Metals and Alloys. JOM: The Journal of the Minerals, Metals & Materials Society 1984; 36(4) 20–33.

[34] Watari H, Davy K, Rasgado MT, Haga T, Izawa S. Semi-solid manufacturing process of magnesium alloys by twin-roll casting. Journal of Materials Processing Technology 2004; 155–156 1662–1667.

[35] Ito T, Noda M, Mori H, Gonda Y, Fukuda Y, Yanagihara S. Effect of Antigravity Suction Casting Parameters on Microstructure and Mechanical Properties of Mg–10Al–0.2Mn–1Ca Cast Alloy. Materials Transactions 2014; 55(8) 1184-1189

Chapter 3

Corrosion and Surface Treatment of Magnesium Alloys

Henry Hu, Xueyuan Nie and Yueyu Ma

Additional information is available at the end of the chapter

http://dx.doi.org/10.5772/58929

1. Introduction

The need for fuel efficiency and increased performance in transportation systems continually places new demands on the materials used. The design criteria which automobile and aerospace industries are primarily concerned with are density, strength, stiffness, and corrosion resistance. Low-density materials may reduce fuel costs, increase range, and allow larger payloads. High strength and stiffness are necessary for adequate performance and safety characteristics, while corrosion resistance helps to ensure that design lifetime is achieved.

Magnesium is the 8th most abundant element on the earth making up approximately 1.93% by mass of the earth's crust and 0.13% by mass of the oceans [1]. Other advantages of magnesium alloys have played an important role in a broad variety of structural applications in the automobile, aerospace, electronics, and consumer products industries. Magnesium has specific high strength to weight ratio, and it is 35% lighter than aluminium and 75% lighter than iron. Typical magnesium alloys weigh ~25% less than their aluminium counterparts at equal stiffness. Magnesium also has high thermal conductivity, good electromagnetic shielding characteristics, good ductility, excellent castability and better damping characteristics than aluminum, and Mg is easily recycled. The main use of magnesium by far is as an alloying addition to aluminum alloys. Other major uses of magnesium include desulphurization of steel and the production of ductile iron. As a structural material, it can be used in aerospace components, automobile and computer parts, mobile phones and sporting goods. Magnesium for structural applications is processed into castings (die, sand, permanent mold and investment), extrusions, forgings, impact extrusions and flat rolled products. Die castings account for 70% of the castings shipped. Magnesium can be joined by riveting, or any of the commonly used welding methods [2].

With the dramatically increased emphasis on weight reduction, magnesium is receiving a lot of attention as a material for use in the next generation automobiles. This is due to limited fossil

fuel supplies and arising environmental problems associated with fuel emission products. Magnesium alloys are a promising alternative to the aluminium alloys currently dominating the transportation industry. However, the limited use of magnesium in engineering applications results mainly from the shortcomings including high reactivity in the molten state, inferior fatigue and creep properties compared to aluminium, poor corrosion and wear resistance [22]. One of the main challenges in the use of magnesium, particularly for outdoor application, is to overcome its poor corrosion resistance. Magnesium and its alloys are extremely susceptible to galvanic corrosion, which can cause severe attack in the metal resulting in decreased mechanical stability and an unattractive appearance. Corrosion can be minimized by the use of high purity alloys in which the heavy metal impurities such as iron, nickel and copper are kept below a threshold value. The elimination of bad design, surface contamination, galvanic couples and inadequate or incorrectly applied surface protection schemes can also significantly decrease the corrosion rate of magnesium alloys in service [3].

In this chapter, the corrosion characteristic of Mg and Mg alloys are described. Fundamental aspects of magnesium corrosion such as general corrosion, galvanic corrosion, pitting, stress corrosion and corrosion fatigue are reviewed. The factors that control the corrosion behaviour of Mg and Mg alloys are discussed in some detail. Finally, the more recently developed corrosion science and engineering underpinning various surface treatment methods such as electrochemical plating, conversion coating, anodizing, gas-phase coating, organic coating, electrolytic plasma oxidation for magnesium alloys are described.

2. Corrosion characteristics of pure magnesium

Magnesium, like most metals and alloys, relies on a natural surface film to control its corrosion. However, the nature of this film is not thoroughly understood. Good passive films are those that restrict the outward flow of cations, resist the inward flow of damaging anions or oxidants, and rapidly repair themselves in the event of localized breakdown. The structure and composition of the surface films, which depends strongly on environmental and metallurgical factors, such as electrolyte species and impurities in the metal, determine the protective ability of a passive film.

2.1. Environmental effects

No material shows high corrosion resistance in all kinds of environments. The high corrosion resistance of materials always refers to some specific environments. Magnesium has its own preferred service environments. However, there are fewer media that are suitable for the magnesium and magnesium alloys compared with other materials, such as steels and aluminum alloys. For example, magnesium and magnesium alloys are usually stable in basic solutions, but in neutral and acidic media they dissolve at high rates [3]. This is quite different from aluminum alloys that are normally stable in neutral media but are unstable in both basic and acidic solutions.

http://dx.doi.org/10.5772/58929

2.1.1. General corrosion in aqueous solutions

With few exceptions, there is no appreciable corrosion of pure magnesium near room temperature unless water is present [4]. Magnesium dissolution in water or aqueous environments generally proceeds by an electrochemical reaction with water to produce magnesium hydroxide and hydrogen gas. Such a mechanism is relatively insensitive to the oxygen concentration, although the presence of oxygen is an important factor in atmospheric corrosion [5]. Reaction 1 describes the probable overall reaction:

$$Mg + 2H_2O = Mg(OH)_2 + H_2 \quad (1)$$

This net reaction can be expressed as the sum of the following partial reactions:

$$\text{Anodic reaction}: \quad Mg \rightarrow Mg^{2+} + 2e \quad (2)$$

$$\text{Cathodic reaction}: \quad 2H_2O + 2e \rightarrow H_2 + 2OH^- \quad (3)$$

$$\text{Products formation}: \quad Mg^{2+} + 2OH^- \rightarrow Mg(OH)_2 \quad (4)$$

The reduction process of hydrogen ions and the hydrogen overvoltage of the cathode play an important role in the corrosion of Mg. Low overvoltage cathodes facilitate hydrogen evolution, causing a substantial corrosion rate [6].

Fig. 1 shows the corrosion domains of Mg in the Mg-H_2O system. The region of water stability lies between the line a and line b. At a potential below line a, hydrogen is evolved; above line b, oxygen is evolved. The numbers identify the reactions that separate the different phases shown in reactions 5, 6, and 7. The horizontal and vertical parallel lines for reactions 5 and 6 give the concentration of Mg^{2+}in mol l^{-1} as a power of 10. As shown in Fig. 1, the ringed numbered lines separate the regions of corrosion (dissolved cations, e.g. Mg^{2+}), immunity (unreacted metal, Mg), and passivation (corrosion products, $Mg(OH)_2$) [5]. From Fig. 1, it can be seen that stable films would be expected to form depending on the values of the potential and pH. In neutral and alkaline environments, the magnesium hydroxide product can form a surface film that offers considerable corrosion protection to the pure magnesium or its common alloys, although this is not as effective as the oxide layer formed on aluminum. As corrosion proceeds, the metal surface experiences a local pH increase because of the formation of $Mg(OH)_2$, whose equilibrium pH is about 11. The protection supplied by this film is therefore highly dependent on the condition of exposure. High purity magnesium is reported to have a corrosion rate of 10^{-2}-10^{-3} mils per year (mpy) when exposed to 2 normal KOH solutions at 25 °C [3].

$$Linea: 2H^{+} + \ 2e \rightarrow H_2$$

$$Lineb: 4OH^{-} - \ 4e \rightarrow O_2 + H_2O$$

$$1.\ \ \mathrm{Mg} + 2\mathrm{H_2O} = \mathrm{Mg(OH)_2} + \mathrm{H_2} \tag{5}$$

$$2.\ \mathrm{Mg^{2+}} + \mathrm{H_2O} = \mathrm{MgO} + 2\mathrm{H^{+}} \tag{6}$$

$$3.\ \mathrm{Mg} = \mathrm{Mg^{2+}} + 2\mathrm{e} \tag{7}$$

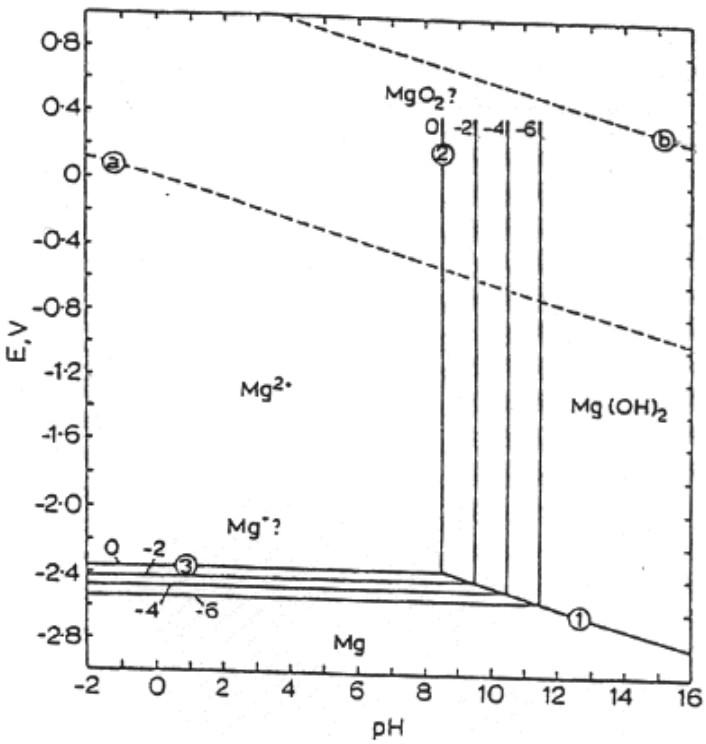

Figure 1. Electrochemical potential-pH equilibrium diagram for the magnesium-water system at 25°C [5].

Magnesium's corrosion performance in pure water is strongly dependent on temperature. At elevated temperatures, the resistance to corrosion in water decreases with increasing temperature, corrosion becoming particularly severe above 100°C [3].

Magnesium is subject to dissolution by most acids. Even in dilute solutions of strong and moderately weak acids, magnesium dissolves rapidly. There are a few exceptions, such as

http://dx.doi.org/10.5772/58929

chromic acid and hydrofluoric acid [6]. Very slow dissolution of magnesium in chromic acid is due to its becoming passive in this acid. An insoluble surface film of MgF_2 is formed which protects against further attack, is the reason why magnesium is resistant to hydrofluoric acid [66].

The strong alkalinity of the natural hydroxide film on magnesium means there is little tendency for the compound to give up a proton to strong alkalis; consequently, the film provides excellent protection even in strong hot alkali solutions that would readily attack aluminum or zinc alloys [6, 7]. Magnesium's resistance to alkali attack combined with the metal's lightweight has made it the preferred material for cement finishing tools for many years [7].

2.1.2. Corrosion in the solutions containing specific ions

Salt solutions vary in their corrosivity to magnesium [7-9]: alkali metal or alkaline-earth metal (chromates, fluorides, phosphates, silicates, vanadates, or nitrates) cause little or no corrosion. Chromates, fluorides, phosphates, and silicates in particular are frequently used in the chemical treatment and anodize for magnesium surfaces due to their ability to form somewhat protective films. Chlorides, bromides, iodides and sulfates normally accelerate the corrosion of magnesium in aqueous solutions. Practically all heavy metal salts are likely to cause corrosion since magnesium normally displaces heavy metals from solution due to its high chemical activity, except iron phosphate solution.

Song et. al [10] investigated the electrochemical corrosion of pure magnesium in 1N NaCl and Na_2SO_4 solutions. It was found that a partially protective surface film plays an important role in the electrochemical dissolution processes for magnesium in NaCl, and Na_2SO_4 solutions. The presence of Cl^-made the surface films more active or increased the broken area of the naturally-formed protective film, and also accelerated the electrochemical reaction rate from magnesium to univalent ions according to the reactions 8 and 9, thus increasing the corrosion rates. SO_4^-has less effect than Cl^-.

$$Mg \leftrightarrow Mg^+ + e \tag{8}$$

$$Mg^+ + H_2O \rightarrow Mg^{2+} + OH^- + \left(½\right)H_2 \tag{9}$$

In a review given by Makar and Kruger [17], it is revealed that films on magnesium immersed in 3% sodium chloride consist of $Mg(OH)_2$, $MgCl_2 \bullet 6H_2O$ and $Mg_3(OH)_5Cl \bullet 4H_2O$, which were identified by infrared spectroscopy and X-ray diffractions. In addition, the stabilized film on magnesium also includes MgH_2.

Oxidizing anions, especially chromates, dichromates, and phosphates, which form protective films, can strongly increase the corrosion resistance of magnesium in water or aqueous salt solutions [6].

2.1.3. Corrosion caused by organic compounds

In a review [7], it was revealed that organic compounds, with a few exceptions, have little effect on magnesium and its alloys. It has been indicated in references 7 and 9 that magnesium is usable in contact with aromatic and aliphatic hydrocarbons, ketones, esters, ethers, glycols, phenols, amines, aldehydes, oils, and higher alcohols. Ethanol causes slight attack, but anhydrous methanol causes severe attack unless significant water content is introduced. Most dry chlorinated hydrocarbons cause little attack on magnesium up to their boiling points. In the presence of water, particularly at high temperatures, chlorinated hydrocarbons may hydrolyze to form hydrochloric acid, causing corrosive attack of the magnesium. Dry fluorinated hydrocarbons, for example, refrigerants, do not attack magnesium at room temperature. When water is present, however, hydrolysis may cause corrosive attack. In acidic food stuffs, such as fruit juices and carbonated beverages, attack of magnesium is slow but measurable. Milk causes attack, particularly when souring [7, 9].

A magnesium engine block has been targeted for reducing the weight of an automobile and corrosion is a major issue in the cooling system of an engine block. It was reported by Song et al [11] that some inhibitors in the traditional coolants, whose main compositions is 30-70 vol % ethylene glycol and molybdate, phosphate, borate, nitrite, tolyltriazole, benzoate and silicate inhibitors, fail to provide adequate corrosion protection to magnesium and magnesium alloys. Hence, some companies are developing coolants with new inhibitors for magnesium and magnesium alloys. Song et al. [11] studied the corrosion behaviour of pure magnesium in ethylene glycol containing various ions. It was found that the corrosion rate of magnesium in aqueous ethylene glycol depends on the concentration of the solution. A dilute ethylene glycol solution is more corrosive than a concentrated solution at room temperature. An ethylene glycol solution contaminated by individual contaminants NaCl, $NaHCO_3$ and Na_2SO_4 is more corrosive to pure magnesium. NaCl is the most detrimental contaminate, while in a NaCl contaminated ethylene glycol solution, a small amount of $NaHCO_3$ or Na_2SO_4 has some inhibition effect [11]. Fluorides in ethylene glycol can effectively reduce the corrosion of magnesium due to the formation of a protective fluoride-containing film on the magnesium surface. It has been observed [11] that a small amount of contaminants (Na_2SO_4, $NaHCO_3$) addition decreases the corrosion of magnesium in the chloride containing ethylene glycol solution.

2.1.4. Corrosion in the air

Humidity plays a major role in the corrosion of magnesium [12]. Corrosion of magnesium increases with relative humidity. At 10% humidity, pure magnesium does not show evidence of surface corrosion after 18 months. However, at 30% humidity, a small amount of visible surface oxide haze and slight corrosion is evident, while at 80% humidity, an amorphous phase is clearly present over about 30% of the surface and the surface exhibits considerable corrosion. Crystalline magnesium hydroxide is formed only when relative humidity is at or above 93%. A theoretical explanation about less ordered films providing better protection was presented in reference 5 that a film without grain boundaries resists the movement of ions better than a crystalline film.

http://dx.doi.org/10.5772/58929

Furthermore, the presence of 300 ppm CO_2 and normally 1 ppm of SO_2 in the atmosphere also plays an important role in a formation of the surface films. In the atmosphere, an inhibitive effect of CO_2 in humid air has been reported [4]. Initially, the ambient levels of carbon dioxide enhance the corrosion attack, however, the rate of corrosion in the presence of CO_2 decreases with increased exposure time. It is suggested that the initial enhance of corrosion stems from the protolysis of carbonic acid, causing a pH decrease in the surface electrolyte as can be seen in reactions 10 and 11. The reduced pH in the surface electrolyte acts to increase the rate of dissolution of the air-formed film.

$$CO_2(aq) + H_2O \leftrightarrow HCO^-_3 + H^+ \tag{10}$$

$$HCO^-_3 \leftrightarrow CO_3^{2-} + H^+ \tag{11}$$

The hydroxide ions, generated in the cathodic reaction or dissolved from the film, can form carbonate with carbonic acid. In the presence of CO_2, a magnesium hydroxyl carbonate is formed (reaction 12).

$$2Mg^{2+} + CO_3^{2-} + 2OH^- + 3H_2O = Mg_2(OH)_2CO_3.3H_2O \tag{12}$$

Magnesium hydroxyl carbonate may also form by reaction of solid magnesium hydroxide with CO_2 and water. The presence of the carbonate film, which is thicker than the magnesium hydroxide film, interferes with both the anodic and the cathodic reaction and thus reduces the corrosion rate. Further, the protolysis of CO_2 counteracts the development of pH gradients on the surface, impeding the development of macroscopic corrosion cells, resulting in inhibition of pitting corrosion. Hence, high purity magnesium and magnesium alloys have the potential to be extremely corrosion resistant, and perform better in the atmosphere than iron.

In urban/industrial locations $MgSO_4$-$6H_2O$ and $MgSO_3$-$6H_2O$ can predominate in the surface films. $MgSO_4$-$6H_2O$ and $MgSO_3$-$6H_2O$ are highly soluble and are easily washed away, re-exposing the surface. Hence, pure magnesium has a poor corrosion resistance in industrial atmospheres [3, 9].

2.2. Metallurgical effects

Magnesium becomes susceptible to accelerated corrosion if there are significant impurity levels present or it is in contact with other metals. Due to the lack of a nature surface film on the impurities, the more positive potential allows impurities to be efficient cathodes for hydrogen discharge, thereby providing significant microgalvanic acceleration of the corrosion rate [13]. Therefore even small amount of impurities in pure magnesium with metals having low hydrogen overvoltages, such as Fe, Ni, Co, or Cu, drastically reduces its corrosion resistance. Metals with higher hydrogen overvoltages, such as lead, zinc, and cadmium, and

also strongly electronegative metals, such as manganese and aluminum, are less dangerous in this respect [6]. Fig. 2 shows effect of impurity and alloying elements on the corrosion of magnesium in a 3% NaCl solution at room temperature. Fe, Cu, Ni can increase the corrosion rate, while Cd, Pb, Sn, and Al can drastically reduce the corrosion resistance of pure magnesium. The effect of various elements on the corrosion of magnesium alloys will be discussed in detail in section 3.2.

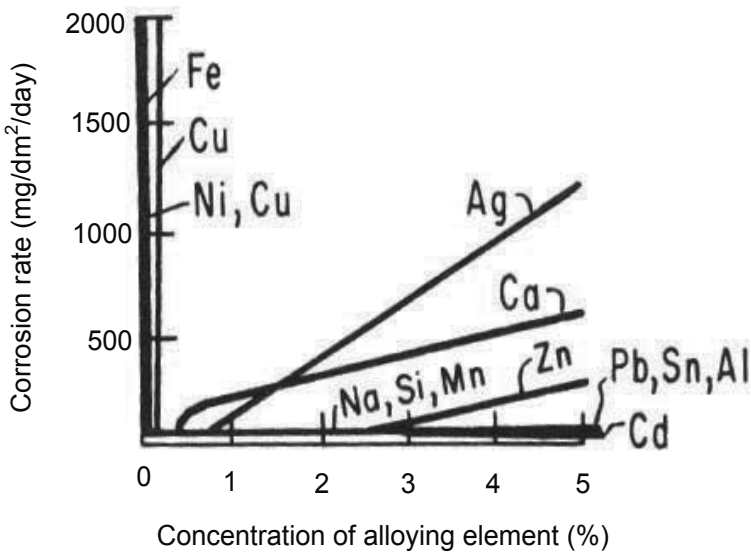

Figure 2. Effect of impurity and alloying elements on corrosion of magnesium (all alloys are formed by magnesium and the given element) in 3% NaCl solution at room temperature [6].

3. Corrosion characteristics of Mg alloys

Magnesium alloys in general can be divided into two main groups: (1) those containing aluminium as the primary alloying element; and (2) those free of aluminium and containing small additions of zirconium for the purpose of grain refinement. The most widely used magnesium alloys are those with aluminum (to 10%), zinc (to 3%), and manganese (to 2.5%). It is desirable that other metals, particularly Fe, Cu, Ni and Si be present in very small amounts not exceeding a total of 0.4% to 0.6% [13]. Mg alloys corrosion is governed by the characteristics of its surface film. The properties of film on Mg alloys depend on Mg alloys'metallurgy and environmental factors. Magnesium metallurgy includes alloying and impurity elements, phase components and microstructure. Metallurgical manipulation can provide an effective means to improve the corrosion resistance of magnesium alloys.

http://dx.doi.org/10.5772/58929

3.1. Influences of environment

3.1.1. Corrosion by atmosphere and solutions

In general, atmospheric attack in damp conditions is largely superficial. The corrosion reactions of magnesium alloys are similar to those for pure magnesium, as shown in reactions 1–4. Generally, the corrosion resistance of magnesium alloy is better than that of pure magnesium, because other corrosion resistant phases exist. An analysis of the films formed when magnesium alloys containing Al, Mn, or Zn are exposed to the atmosphere, shows an enrichment of the secondary constituents. It was suggested that the air-formed oxide on Mg-Al alloys has a layered structure composed of MgO/Mg-Al-oxide/substrate, with the Mg-rich oxide becoming thinner with increasing Al content. It is likely that this benefit of Al is related to the strong tendency for Al to form a stable passive film [13].

Lindstom et al [14] studied the influence of NaCl and CO_2 on the atmospheric corrosion of magnesium alloy AZ91. The combination of high humidity and NaCl is very corrosive towards AZ91. However, CO_2 inhibits atmospheric corrosion both in the presence of and in the absence of NaCl. In the absence of CO_2, the NaCl-induced corrosion is localized and the main corrosion product is $Mg(OH)_2$. Because of the cathodic reaction, high pH areas develop in the electrolyte adjacent to the AZ91surface, resulting in the dissolution of alumnia in the passive film. Due to the rapid hydrogen evolution, the metal disintegrates and pieces of un-reacted metal are embedded in the corrosion product. In the presence of CO_2, AZ91 suffers general corrosion and carbonate-containing corrosion products were formed. In the presence of NaCl, $Mg_5(CO_3)_4(OH)_2$ was detected by XRD. The inhibitive effect of CO_2 was suggested to be due to a combination of pH decrease in the surface electrolyte, stabilizing alumina in the passive film, and the formation of sparingly soluble carbonate-containing corrosion products that slow down the electrochemical reactions.

3.1.2. Corrosion in coolants

A magnesium alloy engine block has the potential to significantly reduce the weight of an automobile, and studies on the corrosion of magnesium alloys in automotive coolants has received increasing attention. Song and StJohn [15] studied the corrosion of a new magnesium alloys AM-SC1 and magnesium alloy AZ91 in commercial engine coolants. AM-SC1 is a new alloy with rare earth elements, zinc and zirconium as the main alloying elements, which was developed as an engine block material. It was found that AZ91 is more corrosion resistant than AM-SC1 in existing coolants, because the existing commercial coolants are non-corrosive to aluminium alloys and they also have a certain degree of inhibitive effect on an aluminium-containing alloy. Potassium fluoride, KF, was an effective inhibitor for the magnesium alloys and can reduce the general and galvanic corrosion rates, while it had no detrimental effect on the other engine block materials (such as cast iron, aluminium alloy) in terms of their corrosion performance. Furthermore, Toyota and Ford long life coolant (Toyota long life coolant: 934 ml/L ethylene and 10ml/kg denatonium benzoate, 1:1 diluted with demineralised water; Ford long life coolant: 950 ml/l ethylene glycol and 10 ppm denationium benzoate as a bittering agent, 1:1 diluted with demineralised water) [15] can be the most promising coolants for magnesium

alloys engine blocks, because the corrosion rates in them were acceptable. Slavcheva et.al [16] demonstrated that Lactobiono-tallowamide (a reaction product of lactobionic acid and tallowamine) had relatively high inhibition efficiency towards AZ91 alloy corrosion in ethylene glycol solution containing chloride ions at low as well as at high temperature. The inhibiting effect of lactobiono-tallowamide is a result of adsorption on the metal surface and formation of an adherent protective film. Hence, lactobiono-tallowamide can be considered as a promising inhibitor of magnesium alloy corrosion.

3.2. Metallurgical factors

Metallurgical factors include alloying and impurity elements, phase composition and micro-structure.

3.2.1. Impurity elements

Studies [12, 17-20] have confirmed that the most critical factor in the corrosion behaviour of Mg and Mg alloys is the metal purity. Iron, nickel, and copper are extremely deleterious because they have low solid-solubility limits and provide active cathodic sites which lead to galvanic corrosion and increase corrosion rates. At the same concentration, the detrimental effect of these elements decreases as follows: Ni>Fe>Cu. When the impurity concentration exceeds the tolerance limit, the corrosion rate is greatly accelerated, whereas the corrosion rate is low when the impurity concentration is lower than the tolerance limit. The tolerance limits in magnesium alloys are influenced by the presence of other elements. For example, the iron tolerance limit for magnesium-aluminum alloys depends on the Mn or Zn concentration [5]. Furthermore, impurity limits are different depending on the method of manufacture. For example, die cast AZ91 has higher nickel tolerance than gravity cast AZ91. And the slower solidification rates significantly affect the nickel tolerance, but not Fe and Cu [17]. Different alloys have different tolerance limits as summarized in Table 1. In Table 1, the impurity tolerance limit of 0.032 Mn actually means that if there is manganese in a magnesium alloy, then the alloy would be able to tolerate an amount of the iron impurity equal to 0.032 of the manganese concentration (by weight).

Iron, nickel, copper, and cobalt are the four main elements so far found to have significant detrimental influence on the corrosion resistance of magnesium alloys [13]. Besides these detrimental elements, there is one special element, manganese, which is usually closely related to the detrimental effects of other elements and their tolerance limits.

Iron

The deleterious effect of iron in pure magnesium is shown in Fig. 3, and it is suspected to be due to the galvanic coupling between the magnesium matrix and the iron particles scattered in the matrix because Fe has a very low solid solubility in magnesium (about 9.9 ppm) [13], while Hawke and Olsen [18] thought that in the absence of Mn, virtually all the Fe precipitates in magnesium alloys as $FeAl_3$ which has a high cathodic activity for corrosion, as shown in Fig. 4.

http://dx.doi.org/10.5772/58929

		Tolerance Limits*		
Specimen	**Condition**	**Fe**	**Ni**	**Cu**
Pure Mg		170 ppm	5 ppm	1000 ppm
Pure Mg		170 ppm	5 ppm	1300 ppm
AZ91		20 ppm	12 ppm	900 ppm
AZ91		0.032 Mn	50 ppm	400 ppm
AZ91	High pressure (F)	0.032 Mn	50 ppm	400 ppm
AZ91	Low pressure (F)	0.032 Mn	10 ppm	400 ppm
AZ91	Low pressure (T4)	0.035 Mn	10 ppm	100 ppm
AZ91	Low pressure (T6)	0.046 Mn	10 ppm	400 ppm
AZ91B			<100ppm	<2500 ppm
AS41	Die casting	0.032 Mn	50 ppm	400 ppm
AZ91	Die casting	50 ppm	50 ppm	700 ppm
AZ91	Die casting	0.032 Mn	50 ppm	700 ppm
AZ91	Gravity casting	0.032 Mn	10 ppm	400 ppm
AM60	Die casting	0.021 Mn	30 ppm	10 ppm
AE42		0.01 Mn	40 ppm	200 ppm

* Variation of tolerance limits results from different manufacturing processes used by various alloy producers

Table 1. Tolerance limits for magnesium and magnesium alloys [113]

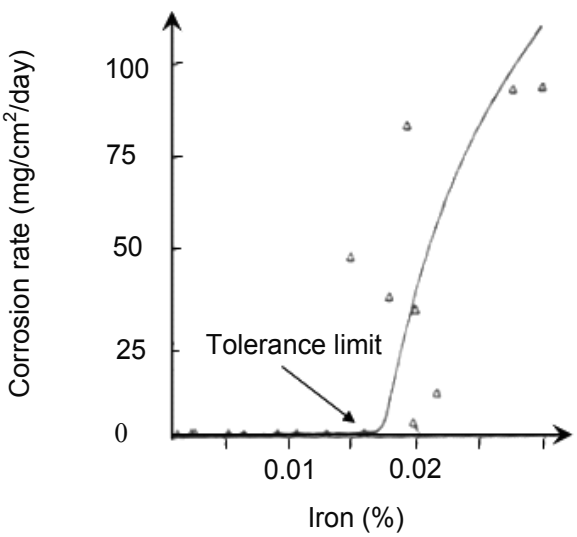

Figure 3. Effect of iron on the corrosion of pure magnesium immersed in 3% NaCl [13].

In Fig. 4, the effects of these phases are defined in terms of their electrode potential relative to the alloy matrix, and the overpotential values for the evolution of hydrogen gas. Within an appropriate medium, $FeAl_3$ acts as an effective cathode, catalyzing the reduction reaction, hydrogen evolution, which is responsible for the corrosion process. Due to the low solubility of $FeAl_3$ in Mg, increasing additions of Al result in increasingly smaller tolerance levels for Fe [17]. For example, when even as little as hundreds of ppm of aluminum is added to the magnesium, the tolerance limit for iron decreases from 170 wt.-ppm to a few wt.-ppm. With 7% Al, the tolerance is about 5 wt.-ppm Fe, while with 10% Al, the limit is too low to be determined [13].

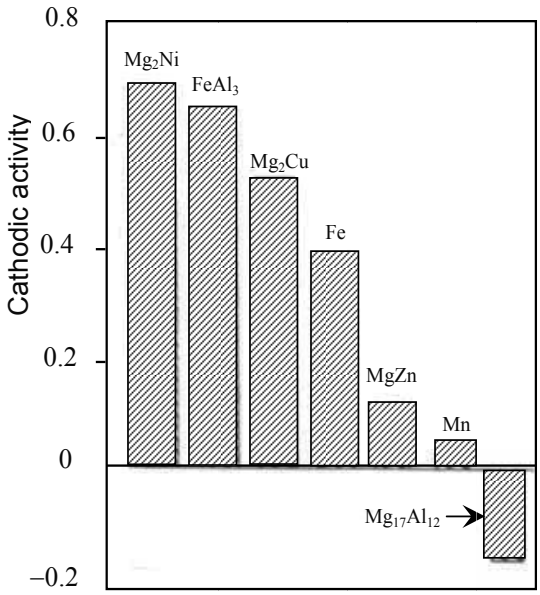

Figure 4. Cathodic activity of precipitated phases in Mg alloys in salt water relative to their alloy matrix [18].

Nickel

Nickel is more harmful than iron both in pure magnesium and in magnesium alloys, because nickel precipitates in magnesium alloys as Mg_2Ni which is more cathodically active than $FeAl_3$ and Fe, as shown in Fig. 4. Fig. 5 shows effect of nickel content on corrosion rates of pure Mg and Mg-Mn and Mg-Zn alloys using standard Dow immersion-emersion test in NaCl solution [5]. Furthermore, solidification rate changes the tolerance limit for Ni (higher tolerance limit for faster cooling, Fig. 6), but not for Fe, or Cu [17]. From Fig. 6, it was found that the nickel tolerance was significantly lower in the gravity cast (~ 10 ppm) than for the die cast (~55 ppm) [17].

http://dx.doi.org/10.5772/58929

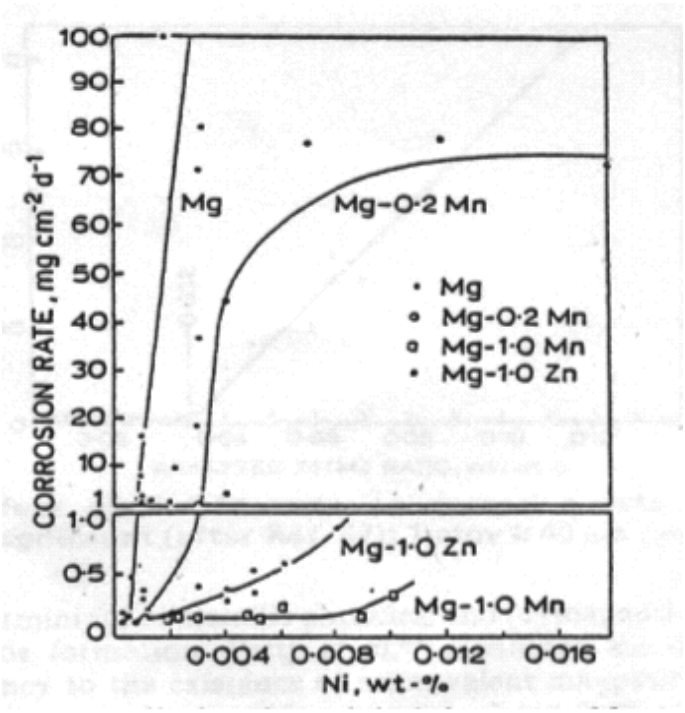

Figure 5. Effect of nickel content on corrosion rates of pure Mg and Mg-Mn and Mg-Zn alloys using standard Dow immersion-emersion test in NaCl solution [5].

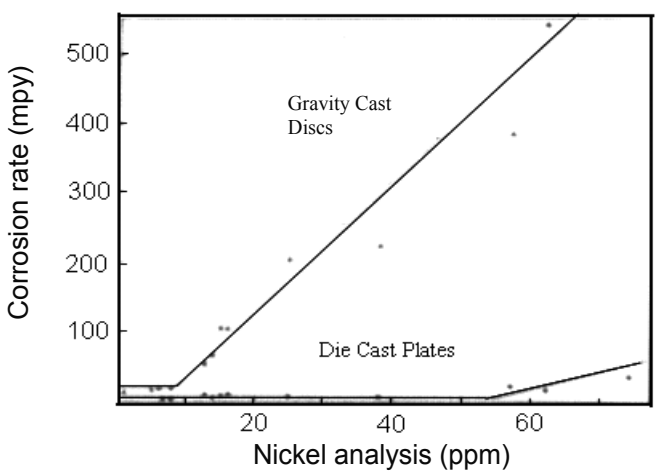

Figure 6. Salt spray corrosion performance vs nickel content for die cast and gravity cast samples [17].

Copper

A small amount of copper has a beneficial effect on the creep strength of magnesium die castings, but strongly accelerates salt water corrosion [113]. Cu is less harmful than iron in magnesium, because copper precipitates in magnesium as Mg_2Cu which has a lower potential than $FeAl_3$ [18]. Mg_2Cu acts as an effective cathode, catalyzing the hydrogen evolution. The addition of copper to Mg-Al-Zn alloys has also been shown to have a detrimental effect on the corrosion resistance. This may be attributed to the incorporation of the copper in the eutectic phase as Mg(Cu, Zn). The tolerance limit of copper has been set at 300 ppm, but it is known that higher levels can be tolerated if the zinc content is above the specification minimum of 0.4% [113].

Manganese

Manganese is added to many commercial alloys, particularly the Mg-Al-Zn alloys (AZ series) to improve corrosion resistance. Manganese itself does not improve the corrosion resistance, because it has a higher potential (see Fig. 4). However, it reduces the harmful effect of impurities. For example, manganese increased the Ni tolerance limit [17]. The Fe/Mn ratio seems to control the influence of iron upon the corrosion rate rather than the overall Fe content [17]. Fe tolerance limit was equal to 3.2% of the Mn content regardless of the melt temperature at the time of casting and the type of casting produced, as shown in Fig. 7.

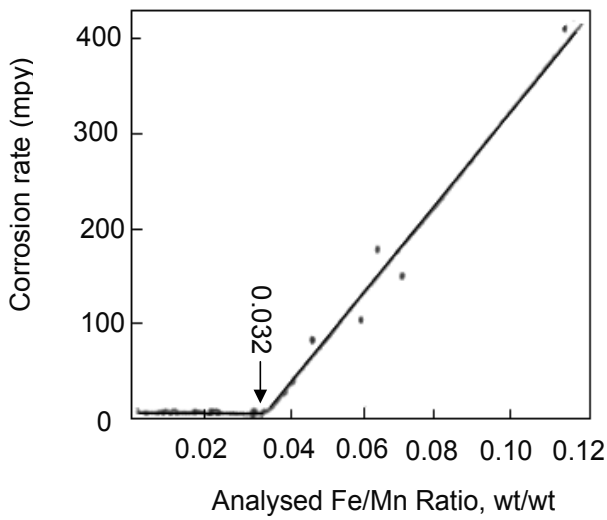

Figure 7. Effect of Fe/Mn ratio on corrosion rate of magnesium, 1 mpy≈ 40 μm/year [17].

Mn reduces the corrosion rate, probably by the following mechanisms [5]. Mn can reduce the corrosive effect of iron by wrapping the iron particles. A particle of iron embedded in a particle of manganese is less detrimental to magnesium because the galvanic activity between Mn and Mg is less than that between Mg and Fe [5]. Mn combines with the Fe and precipitates at the bottom of the crucible, where it reacts with the Fe left in suspension during solidification [19].

http://dx.doi.org/10.5772/58929

When Mn and Al are present together, the AlMnFe intermetallic compounds form preferentially relative to $FeAl_3$, which is known to be an active cathodic phase relative to the magnesium matrix [19]. Mn in excess of that needed to render to the Fe content ineffective could be detrimental to corrosion resistance. Low Mn binary AlMn particles: Al_4Mn, Al_6Mn, show a decreasing cathodic current density, while high Mn content Al_8Mn_5 particles show a continuously high cathodic current density. Thus, additions of Mn beyond that needed for the specified Fe/Mn ratio should be avoided [19].

3.2.2. Important alloying elements

Alloying elements not only enhance the mechanical properties of Mg but also have a significant impact on the corrosion behaviour of Mg-Al alloys. Alloying elements can form secondary particles which are noble to the Mg matrix thereby facilitating corrosion or enrich the corrosion product thereby possibly inhibiting corrosion [19].

Aluminium

Alloying magnesium with aluminium in general improves the corrosion resistance. Lunder et al reported [20] that there is a significant drop in the corrosion rate as the aluminium content is increased from 2 to 4%. Further aluminium additions up to 9% give only a modest further improvement, as shown in Fig. 8.

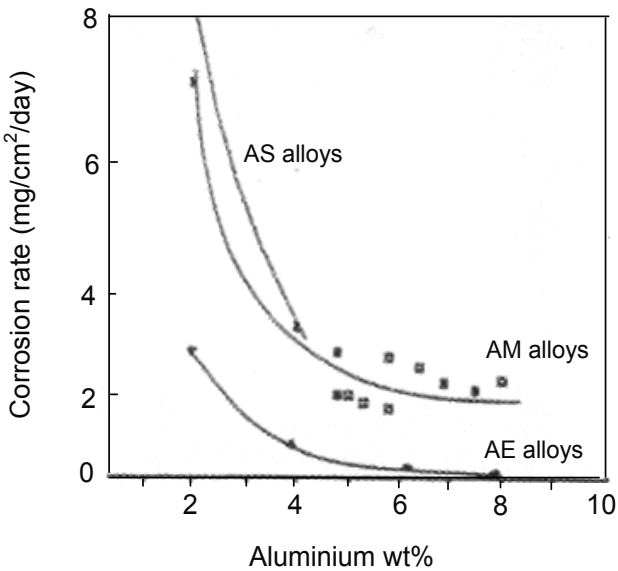

Figure 8. Corrosion rates of die ast Mg alloy immersed in 5% NaCl solution as a function of their Al content [19].

The aluminium is partly in solid solution, and partly precipitated in the form of $Mg_{17}Al_{12}$. Lefebvre and Nussbaum [21] discussed the role of Al in solid solution and role of $Mg_{17}Al_{12}$ in the corrosion process. Both Al in solid solution and $Mg_{17}Al_{12}$ can decrease corrosion rates. The

presence of Al in solid solution in the matrix decreases the corrosion rate of Mg alloys in 5% NaCl and $Mg(OH)_2$ solution, which is attributed to a change in the surface microstructures.

However, it has also been found that aluminum can have a negative influence on corrosion. Aluminium reduces the iron tolerance limit from 170 wt.-ppm to 20 wt.-ppm [17]. The tolerance limit of iron decreases almost linearly with increasing aluminium content. This trend in the iron tolerance limit appears to be consistent with the formation of a passive AlMnFe intermetallic phase on solidification [13].

Zinc

The presence of Zinc can increase the tolerance limits and reduce the effect of impurities once the tolerance limit has been exceeded. Zinc is believed to improve the tolerance of Mg-Al alloys for all three impurities (Fe, Cu, Ni), but its amount is limited to 1-3%. The addition of 3% Zn raises the tolerance limit to 30 wt.-ppm Fe and greatly reduces the corrosion rate for iron concentrations of up to 180 wt.-ppm for Mg-Al-Mn alloys. For the Mg-Al-Mn–Ni alloys, 3% Zn shifts the tolerance limit from 10 to 20 wt.-ppm Ni and reduces the corrosion rate at higher concentration of nickel [13].

Zirconium

Besides the improvement of mechanical properties, the zirconium containing magnesium alloys usually have a higher corrosion resistance than zirconium-free magnesium alloys. Zr reduces the corrosion rate, probably by the following mechanisms [22]: First, impurities combine with zirconium and form insoluble precipitates and purify the alloy. The second mechanism is that zirconium stablizes the magnesium solid solution making it less soluble in aqueous solutions. The third mechanism is that zirconium combines with some intermetallic precipitates which were originally active cathodic sites, making them less active. Apart from the above mechanisms, the grain refining effect provided by zirconium could be another reason for the higher corrosion resistance of magnesium containing zirconium.

Silicon

Si is intentionally added only to the Mg-Al-Si alloys (AS series) to combine with Mg and form Mg_2Si which precipitation strengthens the alloy and is relatively innocuous to the corrosion of Mg. Mg_2Si has a steady state corrosion potential of –1.65 V similar to –1.66 V for pure magnesium in 5% NaCl solution [19].

Rare earth additions

It is well known that the addition of rare earth elements (RE) is an effective way to improve the mechanical properties of magnesium alloys at elevated temperatures. The improvement has mainly been attributed to the formation of a metastable RE-containing phase along the grain boundaries which significantly increases the creep resistance [23]. The beneficial effect of the RE could be similar in nature to that of the Mn additions i.e. the formation of an AlFeMn intermetallic phase which mitigates the harmful effects of Fe. However, no ternary phase was found to form in Mg-Al-RE alloys as the chemical stability of the Al_4RE intermetallic is quite high. Rather, it appeared to be more likely that the rare earths influenced the corrosion products, thereby affecting the corrosion behaviour of the Mg-Al alloys [19].

http://dx.doi.org/10.5772/58929

3.2.3. Role of β phase

Phase contents have a pronounced influence on the corrosion of magnesium, because most elements only affect the corrosion resistance of magnesium alloys when they form second phases. For example, most impurities or alloying elements form second phases and either serve as effective cathodes during the corrosion processes, or eliminate the deleterious effect of impurities, as discussed in sections 3.2.2 and 3.2.1. In this section, the role of β phase ($Mg_{17}Al_{12}$) is discussed.

The detailed microstructure is determined by the casting method, particularly the rate of solidification, and any subsequent heat treatment. Fig. 9 shows a typical microstructure of die cast AZ91D [24]. AZ91 alloy contains three main phases: a substitutional solid solution of aluminium in magnesium (α phase) and two intermetallic phases: β ($Mg_{17}Al_{12}$) present in a eutectic phase (α+β) and an intermetallic phase containing Mn, Fe and Al present at a minor level [25].

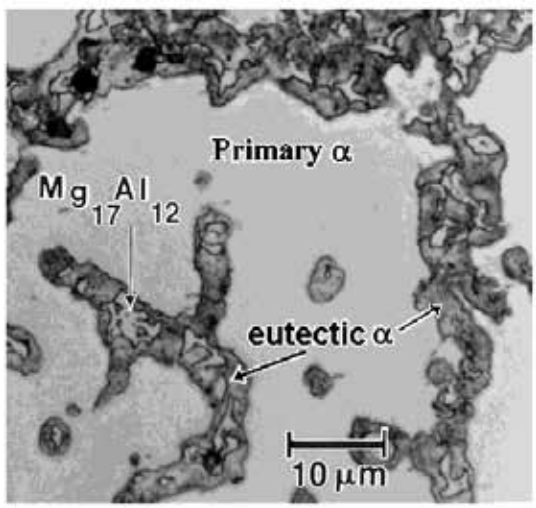

Figure 9. Microstructure of die cast AZ91D alloy [24].

In general, the β phase present in the alloy is considered more resistant to corrosion than the surrounding matrix alloy. Mathieu et al [25] studied the corrosion resistance of the different constituents of an AZ91 alloy in ASTM D1384 water, pH 8.3. It was found that Al contributed to the enhancement of the protection of the α phase through a superficial layer of a carbonate hydroxide of magnesium and aluminium. Song et al. [26] suggested that the role of the β phase in corrosion may be twofold: (1) The β-phase could have a barrier influence because it is very stable in a NaCl solution; (2) Theβ-phase is an efficient cathode for hydrogen evolution. First, when the β-phase is present in an alloy, it reduces the reactive surface area, so less area of the alloy is available to be corroded. Moreover, when corrosion is developing, a continuousβ-phase along the α-grain boundaries might be able to prevent corrosion from spreading from one α-grain to anotherα-grain directly across the β-phase. Then corrosion might be stopped

after the top layer α-grains have been dissolved and a continuous β-phase is exposed to solution. In this manner, the β-phase might improve the corrosion resistance of the alloy. Its barrier role is however limited to stopping the corrosion from either spreading laterally or from progressing deeper into the α-matrix. Unfortunately, in most cases the β-phase is discontinuous and then it does not stop corrosion completely. Second, the cathodic reaction of hydrogen evolution on the β-phase is much easier than on the α-phase. Consequently, if the β-phase is present in a alloy, it acts as an effective cathodic phase to the α-matrix. It causes significant acceleration of the α-phase corrosion by galvanic coupling. However, the role of β-phase strongly depends on the volume fraction. If the β-phase is present in the α-matrix as intergranular precipitates with a small volume fraction, then the β-phase mainly acts as a galvanic cathode, and accelerates the corrosion of the α matrix. If the β fraction is high, then the β-phase mainly acts as an anodic barrier to inhibit the overall corrosion performance.

3.2.4. Microstructure

Microstructural parameters such as composition, porosity, grain size, and amount and distribution of β-phase also play a role in determining the corrosion behaviour. For example, reduction of grain size increases the overall grain boundary area thereby optimizing the distribution and minimizing the size of any possible detrimental intermetallics such as $FeAl_3$. The microstructure can be controlled by the cooling rate, with more rapid cooling leading to a smaller grain size, more β-phase and a more finely distributed β-phase. For example, Mathieu et al [27] found that the casting method strongly influences the corrosion performance through control of the microstructure. The corrosion resistance of semi-solid cast AZ91D alloy is 35% higher than that of the same alloy processed by high pressure die-casting with the impurity level (Cu, Fe) being the same, and the difference in corrosion behaviour is attributed to the distribution, composition and volume fraction of the constituent phases (mainly α and β). Even for the same material, the corrosion resistance is different depending on the location of the material in the casting. For example, Song et al [24] found that the skin of die cast AZ91D shows a corrosion resistance significantly better (by nearly a factor of 10) than its interior in 1 N NaCl at pH 11. This is attributed to a higher β-fraction, and more continuous β-phase around finer α-grains and low porosity. The corrosion behaviour of the α-phases in AZ91 depends on both their aluminium contents and the local current density (which in turn depends on the details of the microstructure and the details of the environmental conditions). For high current densities, the eutectic-α at the grain boundaries tends to be corroded first. For low current densities, the primary-α, in the grain interior, would be preferentially corroded.

4. Forms of corrosion suffered by magnesium alloys

4.1. Galvanic corrosion

When two dissimilar metals are placed in contact in a corrosive or conductive solution, a potential difference produces electron flow between them. The more active metal then becomes anodic and is corroded, and the less active metal becomes cathodic and is protected. This kind

http://dx.doi.org/10.5772/58929

of corrosion is called galvanic corrosion, or two-metal corrosion. Magnesium and its alloys are highly susceptible to galvanic corrosion, because magnesium has the lowest standard potential of all the engineering metals as illustrated in Table 2 [288].

Galvanic corrosion can also occur between two different phases. Fig. 10 illustrated those kinds of galvanic corrosion, external and internal [13]. When magnesium and its alloys are placed contact with other metals, magnesium and magnesium alloys are corroded, while hydrogen gas is evolved on the other metals. When magnesium and magnesium alloys contain second phases because of impurities or alloying elements, the matrix α–phase is corroded, while the hydrogen gas is evolved on the second phases. Table 3 shows typical corrosion potential values for magnesium and common magnesium alloy second phases [29].

	Metal – metal ion equilibrium (unit activity)	Electrode potential vs normal hydrogen electrode 25 ºC, volts
↑	Au – Au+3	1.498
	Pt – Pt +2	1.2
	Pd – Pd+2	0.987
	Ag – Ag+	0.799
	Hg – $Hg_2$2+	0.788
Noble or cathodic	Cu – Cu +2	0.337
	H_2 – H +	0.000
	Pb – Pb^{+2}– 0.126	
	Sn – Sn^{+2}– 0.136	
	Ni – Ni^{+2}– 0.250	
	Co – Co^{+2}– 0.277	
	Cd – Cd^{+2}– 0.403	
Active or anodic	Fe – Fe^{+2}– 0.440	
	Cr – Cr^{+3}– 0.744	
	Zn – Zn^{+2}– 0.763	
	Al – Al^{+3}– 1.662	
	Mg – Mg^{+2}– 2.363	
↓	Na – Na^+ – 2.714	
	K – K^+	–2.925

Table 2. Standard EMF series of metals [28]

From Table 3, it was found that the most potent cathodes in Mg-Al alloy are iron-rich phases, in particular the iron-aluminum intermetallic phase $FeAl_3$. $FeAl_3$ is one of the most detrimental cathodic phases present in Mg-Al alloys on the basis of its potential and its low hydrogen overvoltage. Al-Mn phases are also detrimental, while Mg_2Si seems to have no influence.

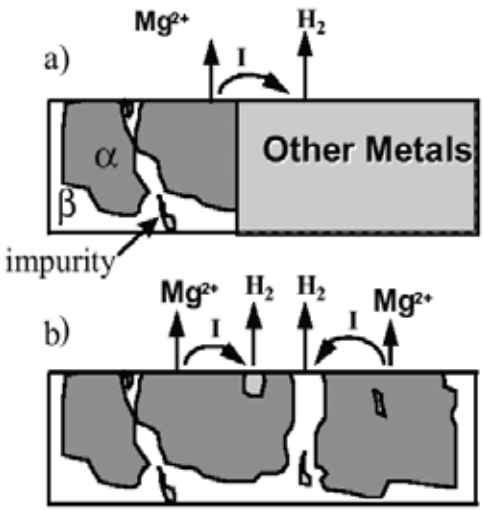

Figure 10. a) External galvanic corrosion. b) Internal galvanic corrosion [13].

Metal	E_{corr} V_{SCE}
Mg	–1.65
Mg_2Si	–1.65
Al_6Mn	–1.52
Al_4Mn	–1.45
Al_8Mn_5– 1.25	
$Mg_{17}Al_{12}$– 1.20	
Al_8Mn_5(Fe)	–1.20
Beta–Mn	–1.17
Al_4Mn	–1.15
Al_6Mn(Fe)	–1.10
Al_6(MnFe)	–1.00
Al_3Fe(Mn)	–0.95
Al_3Fe	–0.74

Table 3. Typical corrosion potential values for magnesium and for common magnesium second phases (after 2 h in deaerated 5% NaCl solution saturated with $Mg(OH)_2$ (pH 10.5)) [29]

The matrix α-phase in Mg alloys is normally anodic to the second phases and is usually preferentially corroded. Song and coworkers [24, 26] have suggested that the primary α and eutecticα phases, which have different aluminum contents, have different electrochemical behaviour. Both the primary and eutectic α can form galvanic corrosion cells with the β phase.

http://dx.doi.org/10.5772/58929

The galvanic corrosion rate is increased by the following factors: high conductivity of the medium, large potential difference between anode and cathode, large area ratio of cathode to anode, and small distance from anode to cathode [288]. Song et al [30] investigated the corrosion behaviour of AZ91D when it is in contact with 380 aluminium alloy, 4150 high strength steel and pure zinc. It was found that even though the galvanic effect offers some degree of cathodic protection for aluminium and zinc cathodes, the dissolution of these metals in the salt solution is still unavoidable, particularly in the region far away from the anode/cathode junction. The dissolved Zn^{2+}or Al^{3+}ions flushed to the surface of the AZ91D anode could react to form zinc or aluminium oxides or hydroxides and finally deposit on the AZ91D surface. These products can provide a certain degree of protection for the AZ91D surface.

4.2. Stress corrosion cracking (SCC)

Stress-corrosion cracking refers to cracking caused by the simultaneously presence of tensile stress and a specific corrosive medium [288]. Pure magnesium can be considered immune to stress corrosion cracking in both atmospheric and aqueous environments, with no reported failures occurring when loaded to its yield strength [7]. Aluminum containing alloys of magnesium are generally considered the most susceptible to SCC, with the tendency increasing with the aluminum content [7]. The alloys AZ61, AZ80, and AZ91 with 6, 8, and 9% aluminum, respectively, can show high susceptibility to SCC in laboratory and atmospheric exposures, while AZ31, a 3% aluminum alloy used in wrought product applications, is considered to show good corrosion resistance [7]. Magnesium-zinc alloys such as ZK60 and ZE41 that are alloyed with zirconium, or zirconium and rare earth elements, are typically considered only mildly susceptible, while magnesium alloys containing no aluminum or zinc are the most SCC-resistant. For example, M1 alloy, a 1% manganese alloy, like unalloyed Mg itself, shows no evidence of SCC when placed under tensile stresses as high as its yield strength [13].

SCC in magnesium is mainly transgranular. Sometimes intergranular SCC occurs as a result of $Mg_{17}Al_{12}$ precipitation along grain boundaries in Mg-Al-Zn alloys [13].

4.3. Corrosion fatigue

There is very little research on the corrosion fatigue of magnesium alloys. It has been indicated in reference 7 that corrosion fatigue has a close relationship with humidity. For example, AZ31 subjected to an axial load cycle at 10^5 cycles per hour in air and then subjected to increasing levels of humidity showed a slow decrease in the fatigue strength once the humidity exceeded 50%. At 93% relative humidity, the measured fatigue strength had declined to about 75% of that in dry air. It has also been found [13] that corrosion fatigue cracks propagate in a mixed transgranular-intergranular mode and that the corrosion fatigue crack growth rate was accelerated by the same environments that accelerate stress corrosion crack growth. And the corrosion fatigue resistance of AZ91-T6 was significantly reduced in 3.5% salt water relative to that in air.

4.4. Pitting corrosion

Few studies have addressed these forms of localised attack of Mg and Mg alloys because other forms of corrosion such as general, galvanic, or stress corrosion have been the cause of more serious failure of these materials. The studies of pitting of Mg and Mg alloys have been concerned with comparing the pitting behaviour of cast to that of rapidly solidified Mg alloys. Makar and Kruger [31] showed that rapidly solidified AZ61 exhibited better resistance to pitting than cast AZ61 in a buffered carbonate solution containing various levels of Cl^-. Pit initiation of rapidly solidified AZ61 is found to take place at a higher potential and the pit growth rate was apparently lower than cast AZ61. In a review given by Makar and Kruger [5], it is reviewed that the difference between rapidly solidified and cast Mg. A metallic glass $Mg_{70}Zn_{30}$ exhibited a better resistance to pitting. Also, the film on the metallic glass was more protective against pitting attack than the pure Mg. The glassy Mg alloy is found to exhibit a more stable passive film than pure Mg, Zn or several other crystalline Mg-based alloys. Heavy metal contamination promotes general pitting attack. In Mg-Al alloys, pits are often formed due to selective attack along $Mg_{17}Al_{12}$ network that is followed by the undercutting and falling out of grains [13].

Crevice corrosion does not occur with the Mg alloys because corrosion is relatively insensitive to oxygen concentration difference [3, 6].

4.5. Filiform corrosion

Filiform corrosion is caused by an active corrosion cell which moves across a metal surface. The head is the anode and the tail the cathode. Filiform corrosion occurs under protective coatings and anodized layers. Uncoated pure magnesium does not undergo filiform corrosion. However, filiform corrosion can occur on uncoated AZ91 and this indicates that a relatively resistant oxide film can naturally be formed on this alloy [13].

4.6. Oxidation at elevated temperatures

The research on oxidation at elevated temperatures is very limited. Magnesium corrosion resistance is typically considered to be good in dry air to about 400°C and to about 350°C in moist air [7]. At elevated temperatures, magnesium oxidizes easily in air according to a linear, kinetic oxidation curve (see Fig. 11) [6], which demonstrates the insufficient protective character of the magnesium oxides. Fig. 12 shows the effects of various elements on the oxidation rate of magnesium alloys in air at 475 °C. Additions of Pb, In, Ag, Cd, or Ti have little effect on the rate of oxidation. The additions of rare earths (Ce+La) somewhat retard the oxidation process of magnesium in air on heating. Additions of Cu, Ni, Ca, An, Sn, or even Al accelerate the oxidation rate of magnesium alloys in the air at elevated temperatures [6].

Czerwinski investigated the early stage oxidation and evaporation of AZ91D alloy [32]**.** Thermogravimetric technique was used to determine the oxidation and evaporation behaviour of AZ91D magnesium alloys with 5 and 10 ppm of beryllium at temperatures between 200 and 500 °C. The oxidation mechanism of AZ91D changes from protective to non-protective with linear or accelerated kinetics depending on the temperature and time of exposures. During

http://dx.doi.org/10.5772/58929

reaction in an oxidizing environment, the beryllium addition delays the onset of non-protective oxidation. It does not affect, however, the oxidation kinetics during the initial stages. During reaction in an inert atmosphere of argon, beryllium suppresses the magnesium evaporation [32]. Fig. 12 shows the effects of various alloying elements on the oxidation rate of Mg alloys in air at 475 °C.

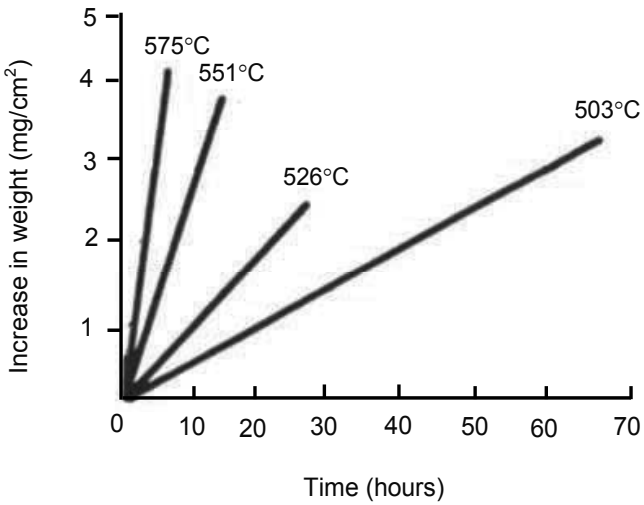

Figure 11. Pure Mg oxidation in an oxygen atmosphere under one atmospheric pressure at various temperatures [6].

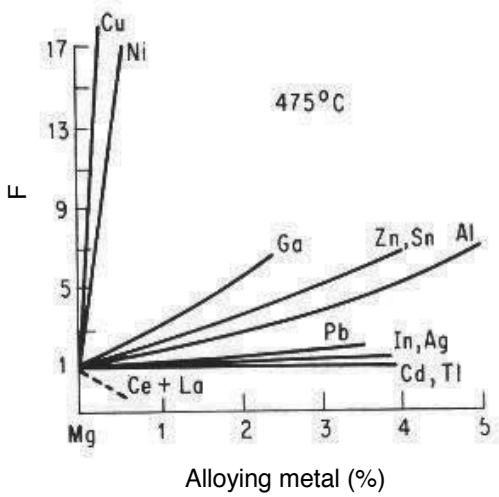

Figure 12. Effect of various alloying elements on the oxidation rate of magnesium alloys in air at 475 °C [6]. F – ratio of oxidation rate of the alloy to oxidation rate of pure magnesium.

5. Corrosion prevention

There are a number of approaches to overcoming the corrosion problems of Mg alloys [5]: (1) High purity or new alloys: Decrease impurities to below their tolerance limits and develop new alloys with new elements, phases, and microstructure distributions; (2) Surface modification: this includes ion implantation and laser annealing; (3) Refinement of the grain size and intermetallic particles: corrosion resistance can be affected through the microstructure; and (4) Protective films and coatings.

5.1. High purity or new alloys

Improving corrosion resistance by producing Mg alloys with low concentration of deleterious elements is an often-used strategy. This ensures the highest possible degree of uniform corrosion resistance of the starting material [5].

5.2. Surface modification

There are two main surface modification techniques which are discussed below.

Ion implantation is the technique whereby almost any elemental ions may be implanted into the surface of any solid using a beam of energetic ions accelerated into a target under vacuum conditions. This homogenization is the primary benefit of ion implantation in terms of corrosion resistance. Additional benefits include the ability to alter the surface while retaining the bulk properties, the creation of novel surface alloys, and the elimination of surface adhesion problems associated with coatings. The primary disadvantages are that it is a line–of–sight technique and it modifies only a thin film [33]. Akvipat and co-workers [34] examined the effects of iron implanted Mg and AZ91C in boric acid and borate buffer solution with 1000 ppm NaCl. It was known that iron degrades the corrosion resistance of magnesium alloys when introduced during conventional processing, and the goal of their work was to evaluate the effects of iron introduced by implantation. The implanted iron changed the nature of the attack on the AZ91. In the un-implanted case, $Mg_{17}Al_{12}$ islands acted as local cathodes, causing accelerated corrosion of the surrounding matrix to form a deep channel around these islands. The implanted iron shifted the attack to the $Mg_{17}Al_{12}$ particles themselves, which resulted in a more uniform attack without the rapid channelling suffered by the magnesium matrix in the un-implanted case. The results of these ion implantation studies are encouraging, but improvements in the economics and versatility of the implantation process are necessary for increasing the practical importance of this approach.

Laser annealing

Laser annealing technique involves the formation of metastable solid solutions as promoted at metal surfaces by laser annealing, where cooling rates as high as 1010 K/s are achievable using lasers pulsed in the nanosecond range [33]. It is, therefore, another form of rapid solidification processing, but involves the melting and solidification of surface layers only. Besides the advantages of ion implantation, the advantages include the ability of lasers to treat more complex geometries, the greater depth of treatment, inexpensive operation costs, and

http://dx.doi.org/10.5772/58929

greater control of the concentration of the modified layer [33]. The main disadvantage is the extra machining necessary because of dimensional changes during treatment. Akvipat and co-workers [34] examined the effects of thin layers of about 100nm of Al, Cr, Cu, Fe, and Ni on the pitting resistance of AZ91C in boric acid-borate solution with 1000 ppm NaCl. The role-played by these elements after laser treatment is certainly different from that when they are present in conventional processing, especially Cu, Fe, and Ni, which are detrimental, even in small concentrations under equilibrium conditions. This improvement is probably related to the structure and composition of the near-surface region [34].

5.3. Microstructure refinement

Corrosion resistance can be affected through modification of the microstructure. Recent studies [19, 35, 36] have centered on the refinement of the grain size and intermetallic particles and on developing a more homogeneous microstructure.

Grain Refinement

Reduction of grain size increases the overall grain boundary area thereby optimizing the distribution of detrimental intermetallics and minimizing the size of any possible detrimental intermetallics such as $FeAl_3$. The traditional grain refinement method in sand casting is to add an innoculent which facilitates heterogeneous nucleation during solidification. Indeed, additions of strontium to Mg-Al alloys have shown a marked reduction in grain size but also have pointed to a possible alteration of both the oxide layer structure and composition and the electrochemical properties of the phases present [19].

Effect of Rapid Solidification Processing

Rapidly solidified materials show improved corrosion resistance because of a refined microstructure which translates to a more homogeneous composition thereby minimizing the potential of any microgalvanic corrosion cell.

Govind et al [35] claimed that technology of making rapid solidification ribbon of highly reactive Mg-9%Al-1%Zn-0.2%Mn alloy was established successfully. Grain sizes of 1-3 μm could be achieved in as-spun ribbons in contrast to a 250-300 μm grain size normally attained in sand cast structure. Below a temperature of 200 °C no grain growth was observed in RS ribbons of Mg alloy as the precipitates of intermetallic compound $Mg_{17}Al_{12}$ pin the grain boundaries.

Effect of Heat-Treatment

Heat-treatment can drastically alter the size, amount and distribution of the precipitated β phase, $Mg_{17}Al_{12}$, which in turn, alters the corrosion behaviour of Mg-Al alloys. Aung and Zhou [36] studied an AZ91D ingot in the as-cast condition that was homogenized by solution treatment and then aged for various periods of time. The homogenization treatment of an AZ91D ingot at 420 °C for 24h was found to be effective in dissolving the β-precipitates. Artificial ageing at 200°C caused precipitation of the β-phase mainly along the grain boundaries. The volume fraction of the β-phase was observed to increase with ageing time. A homogenization treatment improved the corrosion resistance of the AZ91D ingot, but ageing

for 8 h, 16 h or 26 h lowered the corrosion resistance. These results support the suggestion that microgalvanic coupling exists between the cathodicβ-phase and the anodic α-matrix. The inhibiting effect of the β-phase in the artificially aged alloy predominated during the short interval of electrochemical testing but the accelerating effect of the decrease in aluminium content in the matrix predominated in the long period immersion testing. During immersion testing, the β phase may dissolve into the chemical solution and this also tends to accelerate the corrosion rate.

5.4. Protective coatings and films

There are a number of technologies available for coating magnesium and its alloys. These include electrochemical plating, conversion coatings, anodizing, hydride coatings, organic coatings and vapour-phase processes.

5.4.1. Electrochemical plating

One of the most cost effective and simple techniques for introducing a metallic coating to a substrate is by electrochemical plating. The electrochemical plating can be subdivided into two types: electroplating and electroless plating. In both cases a metal salt in solution is reduced to its metallic form on the surface of the substrates. In electroplating the electrons for reduction are supplied from an external source. In electroless or chemical plating the reducing electrons are supplied by a chemical reducing agent in solution or, in the case of immersion plating, the substrate itself.

Electroplating:

Besides some traditional disadvantages of electroplating such as non-uniform coatings and difficulties in coating complex shapes, there are some challenges to be met for electroplating on magnesium. The pre-treatment processes are complicated due to the fact that, in the presence of air, magnesium very quickly forms a passive oxide layer. Cu-Ni-Cr plating has been shown to have good corrosion resistance in interior and mild exterior environments [37]. Also, it is necessary to develop non-traditional plating baths since magnesium reacts violently with most acids and dissolves in acidic media. Furthermore, magnesium and its alloys are prone to galvanic corrosion, so the metal coating must be pore free otherwise the corrosion rate will increase. Usually, the coating is at least 40-50 μm thick to ensure pore-free coatings. Furthermore, the alloys are difficult to plate because intermetallic species such as Mg_xAl_y are formed at the grain boundaries, resulting in a non-uniform surface potential across the substrate, and therefore further complicating the plating process. Recently, Jiang et al [388] studied Zn-Ni alloy coatings pulsed-plated on magnesium alloy AZ91. Before deposition, the substrate surfaces were processed in a standard industrial way: polishing with alumina sand paper, alkaline degreasing, chemical pickling, activation, zinc immersion and Zn-Cu alloy plating. A Zn layer and a Zn-Cu layer under the Zn-Ni coating were applied to improve the adhesion and to protect the substrate using the small electrode potential difference between Zn-Cu and Zn-Ni layer. Zn-Ni coatings were deposited in an alkaline bath with a composition as ZnO 10g/l, NaOH 150 g/l, $NiSO_4 \bullet 6H_2O$ g/l, triethanolamine 50 g/l, and at 10-40°C, 500-4000

Hz, 0.04-0.1 A/cm^2. The bonding strength can be as high as 14.8 MPa. The corrosion life of the Zn-Ni coating can reach over 200 h in a salt spray test conducted according to ASTM B1117. However, no detailed data were given on the porosity of the coatings, which may increase the corrosion rate due to the galvanic corrosion effect.

Electroless plating:

Electroless plating has good throwing power and can produce a uniform coating thickness on complex objects. It also involves a simple pre-treatment and is suitable for magnesium alloys with high aluminium contents [1]. However, electroless deposited coatings cannot be too thick, the bath life is limited, and deposition rates are slow. In particular, electroless plating requires the use of hydrofluoric acid during the pre-treatment, which increases the danger of the operation and is not environmentally friendly [1]. Research on increasing the bath life and eliminating toxic chemicals is necessary in order to create a green-plating process for coating magnesium. Sharma et al. [39] studied the properties of an electroless nickel coating on magnesium alloy ZM21. The solution contains nickel carbonate, sodium hypophosphite (metal-reducing agent), citric acid and bifluoride (act as accelerators, complexing agent, and accelerators), thiourea (solution stabilizer and brightening agent) and ammonia solution. The paper put forward some reactions, and suggested that the autocatalytic reaction for nickel deposition is initiated by catalytic dehydrogenation of the reducing agent with release of hydride ion, which then supplies electrons for the reduction of nickel ions.

The coated samples were immersed in a 5% solution of sodium chloride at pH 7.0. No corrosion spots on the coatings were noticed after 96 hrs of immersion. The formation of corrosion spots initiated only after the fifth day of immersion. Recently, Huo et al.[40] developed an environmental-friendly combined technique of chemical conversion treatment followed by electroless nickel plating for AZ91D alloy to improve corrosion resistance. The presence of the conversion coating, which was mainly $MgSnO_3 \bullet H_2O$, between the nickel coating and the substrate reduced the potential difference and avoided any catastrophic galvanic corrosion between nickel and magnesium. The electroless nickel coating containing about 10 wt% phosphorus greatly enhanced the corrosion potential of AZ91D from −1.50 V to-0.60 V.

5.4.2. Conversion coatings

Conversion coatings are produced by chemical or electrochemical treatment of a metal surface to produce a superficial layer of substrate metal oxides, chromates, phosphates or other compounds that are chemically bonded to the surface. On magnesium, these coatings are typically used to enhance paint adhesion to the coatings and provide improved corrosion protection to the metal. There are a number of different types of conversion coatings including chromate, permanganate, phosphate, phosphate-permanganate and fluorozirconate treatments. The conventional conversion coatings are based on chromium compounds that have been shown to be highly toxic carcinogens. The development of an environmentally friendly process is a necessity due to the more stringent environmental protection laws currently in effect, or being proposed. The coatings on alloys also represent a significant challenge due to their non-uniform surface composition.

Phosphate–permanganate conversion coatings

Phosphate-permanganate treatments are being explored as an alternative to conventional chromate conversion coatings. These treatments are more environmentally friendly and have been shown to have corrosion resistance comparable to chromate treatments [1].

Chong and Shih [41] reported that a conversion coating on magnesium alloys AZ61A, AZ80A and AZ91D prepared from a solution containing permanganate ($KMnO_4$ 20g/l) and phosphate ($MnHPO_4$ 60g/l) showed an equivalent or slightly better passive capability than a conventional chromate-based conversion treatment, but an inferior passive capability for the pure Mg specimen. Hawke and Albright [42] studied a phosphate-permanganate treatment for the conversion coating of AM60B. The coating is based on magnesium phosphate, but contains significant amounts of aluminum compounds generated from the alloy's aluminum content, and manganese compounds formed by reduction of the permanganate ion. The manganese is considered to contribute manganese to the coating, and acts as an accelerator without depositing metallic manganese on the magnesium surface. The coatings were shown to have good corrosion resistance and paint adhesion.

It was found that the most important factor in producing the best quality conversion coatings was the control of the pH [1]. Since pH is the most important factor determining conversion coating quality, the research on stabilizing the pH of solutions has gained increasing attention. Umehara et al. [43] claimed that a pH-stabilizing solution was developed for the conversion coating on AZ91D. The surface film formed was composed of magnesium oxide, and manganese oxide, and contained boron oxide. The pH change was insignificant with increasing the surface area of the magnesium treated. After cleaning and surface activation, the samples were immersed in a solution containing potassium permanganate and either nitric or hydrofluoric acid. The coatings formed in the bath containing nitric acid were substantially thicker and crystalline manganese oxide was observed. The corrosion resistance of these coatings was equivalent to the protection afforded by a standard chromate treatment.

Stannate conversion coatings

A study on stannate treatment of ZC 71 and a metal matrix composite of ZC71+12% SiC particles has been undertaken by Gonzalez-Nunez et al [44]. After mechanical finishing and pickling, the samples were immersed in a stannate bath for selected periods of time. The treatment resulted in the formation of a 2-3 μm thick, continuous and adherent, crystalline coating of $MgSnO_3$ on both materials. The nucleation and growth of the coating was completed in about 20 min. The initial nucleation was found to occur at cathodic sites on the surface with crystal growth to a grain size of about 2-5 μm until they coalesced. There was an increase in the corrosion potential of the magnesium surfaces as the film formation proceeded indicating that the coating does have a passivating effect on the surface.

Rare earth process

The corrosion protection of cerium, lanthanum and praseodymium conversion coatings on magnesium and magnesium alloy WE 43 has been investigated by Rudd et al [45]. The samples were polished, cleaned in water and methanol and dried prior to immersion in a $Ce(NO_3)_3$,

http://dx.doi.org/10.5772/58929

$La(NO_3)_3$ or $Pr(NO_3)_3$ solution. A visible, adherent but easily removed coating was produced on the surface. It has been demonstrated that these coatings provide an increase in corrosion resistance for magnesium and its alloys. However, the coatings deteriorated on prolonged immersion in the test buffer solution so their protective effect is short term.

Conversion coatings have been known for some time, but it should be mentioned that a great deal of the work done on conversion coating of magnesium substrate is proprietary in nature. Thus, there is still a great deal of research to be done to better understand the surface reactions between magnesium based substrates and coatings [1].

5.4.3. Anodizing

Anodizing is an electrolytic process for producing a thick, stable oxide film on metals and alloys. These films may be used to improve paint adhesion to the metal, as a key for dying or as a passivation treatment. The stages for processing include [1]: (1) mechanical pre-treatment, (2) degreasing, cleaning, and pickling, (3) electrobrightening or polishing, (4) anodizing using AC or DC current, (5) dying or post-treatment and (6) sealing. Sealing of the anodized film is necessary in order to achieve an abrasion and corrosion resistant film. This can be accomplished by boiling in hot water, steam treatment, dischromate sealing and lacquer sealing [1]. One of the main challenges for producing adherent, corrosion resistant, anodic coatings on magnesium results from the eletrochemical inhomogeneity due to the phase separation in the alloy. Another disadvantage of this technique is that the fatigue strength of the base metal can be affected by localized heating at the surface during the treatment.

Dow 17 process: Chemical treatment no.17, developed by Dow Chemicals, can be applied to all forms and alloys of magnesium [46]. The anodizing bath employed in this treatment is a strongly alkaline bath consisting of an alkali metal hydroxide and a fluoride or iron salt or a mixture of the two. This process produces a two-phase, two-layer coating. The first layer is deposited at a lower voltage and results in a thin, approximately 5 μm, light green coating, The over layer is formed at a higher voltage. It is a thick dark green, 30.4 μm, layer that has good abrasion resistance, paint base properties and corrosion resistance [46].

HAE process: named after its discoverer, H.A. Evangelides [47]. This treatment can be applied to all magnesium alloys including the rare-earth magnesium alloys [47]. The HAE bath is a strongly alkaline and oxidizing solution, consisting of potassium-hydroxide-aluminate-fluoride-manganate and tribaisc sodium phosphate [48]. The treatment produces a two phase coating as in the DOW 17 process [46]. At a lower voltage a 5 μm thick, light tan subcoating is produced. At a higher voltage a dark brown, thicker (30 μm) film is produced. Upon sealing the HAE treatment provides excellent corrosion resistance. The corrosion resistance of AZ91D treated with this technique has been tested by a 3-year atmospheric exposure experiment. Superior corrosion reistance compared to conversion coating was observed [49].

Other processes: Mizutani et al. [50] studied the electrochemical behaviours of pure magnesium, AZ31 and AZ91 in 1 mol/dm^3 NaOH during the anodizing process. The anodizing films on Mg alloys at 3 V had the best effective corrosion resistance and these films consist of

magnesium hydroxide. However, the coatings were really thin and the film thickness of anodized AZ91 at 3, 10 and 80 V was approximately 4, 1, and 0.5 μm, respectively.

5.4.4. Gas-phase deposition processes

Protective coatings can also be produced from the gas phase. These are typically metallic coatings but can include organic coatings such as thermal spray polymer coatings and diamond like coatings. All of these processes have the advantage that they have little negative environmental impact. However, the capital costs associated with these techniques are usually high [1].

Chemical vapour deposition (CVD)

Chemical vapour deposition can be defined as the deposition of a solid on a heated surface via a chemical reaction from the gas phase. Advantages of this technique include deposition of refractory materials well below their melting points, achievement of near theoretical density, control over grain size, processing at atmospheric pressure and good adhesion [51]. However, CVD is limited to substrates that are thermally stable at ≥ 600 °C. Efforts are underway to reduce the high temperature requirements and plasma and organometallic CVD processes offset this problem somewhat. A further disadvantage of this process is high-energy cost due to the need for high deposition temperatures and sometimes low efficiency of the process.

A plasma-assisted CVD technique has been successfully used to deposit SiO_x thin films on magnesium alloy WE43 [52]. The coatings were deposited at low temperature (T< 60 °C) and 100 mTorr of pressure. Pre-treatments were performed immediately before the application of the SiO_x coating, in plasma fed with oxygen, hydrogen or CF_4–O_2 (20%). The SiOx coatings exhibited better corrosion resistance in 0.1 M NaCl with the pre-treatment in H_2 plasma than in CF_4-O_2 (20%) plasma. When the magnesium surface is treated in H_2 plasma, a preferential removal of OH groups occurs, resulting in a clean surface. The improvement of corrosion resistance of pre-treated magnesium alloy in CF_4-O_2 (20%) plasma has been attributed to the formation of MgF_2 [52].

Diamond-like carbon films (DLC)

Diamond like carbon films can be produced using a number of different processes such as physical vapour deposition (PVD), CVD and ion implantation. These coatings are desirable for many applications due to their high hardness, low friction coefficient, electrical insulation, thermal conductivity and inertness. Yamauchi et al. [53] reported that DLC films were deposited on the magnesium alloy substrate (Al 2.4 wt%, Zn 0.87 wt %, Si 0.001 wt%, Mn, Cu, Ni, Fe non-detected) by the plasma CVD method using radio frequency. The DLC coating was confirmed to be effective in decreasing the friction coefficient and improving the corrosion resistance in 3 wt% NaCl and 0.05 N NaOH solutions. However, DLC films showed poor corrosion wear resistance in 0.05 N HCl due to the existence of pits in the films.

Physical vapour deposition processes

PVD involves the deposition of atoms or molecules from the vapour phase onto a substrate. There are a few challenges to overcome in the PVD coating of magnesium substrates. The

http://dx.doi.org/10.5772/58929

deposition temperature must be below the temperature stability of magnesium alloys (180 °C) and good adhesion must be obtained despite this low temperature. Hollstein et al [54] compared the mechanical and chemical properties of various PVD coatings on a high purity AZ31 magnesium alloy, including single layer TiN, CrN, double layer TiAlN, NbN-(TiAl)N, CrN-TiCN, the multi-layer composite AlN/TiN, and superlattices CrN/NbN. The difference between the (TiAl)N layers and the TiN/AlN multilayers is that the (TiAl)N layers were produced using a Ti-50%−Al-50% target compound, whereas the TiN/AlN multilayers are produced by power switching between a titanium target and an aluminium target. NbN/CrN superlattices are characterised by a repeating layer structure of the two materials with a nanometric scale dimension. The best results in corrosion resistance, adhesion and hardness were obtained from the CrN and (TiAl)N coatings. The classical TiN monolayer coating with a thickness that is typical for decorative purposes (about 1 μm) is not suitable to protect Mg alloys against corrosion effectively. It seems that a minimum thickness of about 4 μm or more is necessary for industrial applications. Hoche et. al [55] developed a new method of plasma anodisation to ensure acceptable corrosion resistance, besides excellent wear protection on Mg alloy. The anodizing and PVD-coating can be done in one process. The 0.5 μm plasma anodisation layer and 1.5 μm PVD-Al_2O_3 coating was subjected to 120 hours salt spray.

5.4.5. Organic/ polymer coatings

Organic finishing is typically used in the final stages of a coating process. These coatings can be applied to enhance corrosion resistance, abrasion and wear properties, or for decorative purpose. An appropriate pre-treatment process is required in order to produce coatings with superior adhesion, corrosion resistance and appearance [1]. Many coating processes can be applied to magnesium and magnesium alloys, including painting, powder coating, e-coat, sol-gel process, and polymer plating. In the following section, we discuss the sol-gel process.

Sol-gel process

Synthesis of gels by the sol-gel process involves the hydrolysis and condensation polymerization of metal alkoxides. One of primary advantages of this technique is the excellent adhesion obtained with a minimum of sample pre-treatment [1]. The metal surfaces are simply degreased, rinsed and dried prior to dip-coating in the sol-gel mixture. A significant advantage is that irregular shapes and larger integral structures can also be coated. However, sol-gel coatings tend to fail if the film thickness exceeds 5 μm because of shrinkage strains during drying, and densification of the as-deposited xerogel film. Phani et al [56] reported that sol-gel coatings consisting of ZrO_2 as well as 15 wt% of CeO_2 could be deposited on magnesium alloys AZ91D and AZ31 by the dip coating technique. Adhesion measurements on the coatings showed good adhesion with critical loads of up to 25 N. Depth-sensing nanoindentation tests of the coatings showed a hardness of around 4.5 GPa and an elastic modulus of 98 GPa. Coatings deposited on AZ91D and AZ31 substrates exhibited good corrosion resistance in the salt spray test performed for 96 hr.

5.4.6. Electrolytic plasma oxidation

Electrolytic Plasma oxidation (EPO), also called plasma anodising or micro arcing, is a promising surface treatment for hexavalent chromium replacement in anti-corrosion protection or in the improvement of the tribological properties of lightweight metal structures. This electrolytic plasma oxidation can be distinguished from classical anodising by the use of voltages above the dielectric breakdown potential of the anodic oxide being formed. This leads to the local formation of plasmas, as indicated by the presence of sparks that are accompanied by a release of gas [57].

Some interesting historical comments are presented in a review by Yerokhin et al. [57]. Plasma anodizing dates back at least to 1932. At that time it was studied by two German scientists, Gunterschulze and Betz, while working on electrolytic capacitors using aluminium foil. During the 1970s oxide deposition on an aluminium anode under an arc discharge condition was also developed and studied. In the 1980s, the possibilities of utilising surface discharges in oxide deposition onto various metals were studied in more detail. Early applications were introduced in the textile and aerospace industries. Electrolytic plasma oxidation (EPO) is recently considered to be a promising technique to deposit ceramic coatings on magnesium alloys for corrosion protection.

The EPO process involves anode electrochemical dissolution, the combination of metal ions with anions to form ceramic compounds, and sintering on the substrate under the action of the sparks. Yerokhin et al [58] described three main steps leading to ceramic coating formation. First, a number of discrete discharge channels are formed in the oxide layer as a result of loss in its dielectric stability in a region of low conductivity. The material in the channel is heated-up to temperatures of 10^4 K by the generated electron avalanches. Due to the strong electric field, the anionic components are drawn into the channel. Owing to the high temperature, the elements are melted out of the substrate, enter the channel and are oxidized. Second, these oxidized metals are ejected from the channels into the coating surface in contact with the electrolyte, thereby increasing the coating thickness in that location. In the last step, the discharge channels are cooled and the reaction products are deposited on to its walls. The above process repeats itself at a number of discrete locations over the entire coating surface, leading to an overall increase in the coating thickness. However, there is no support experimentation to confirm the above interpretation.

Yerokhin et. al. [57] also described current –voltage characteristics during the EPO process. Fig. 13 is the current-voltage diagram for the process of plasma electrolytic oxidation. First, the previously formed passive film begins to dissolve at point $U_{1,}$ which, in practice, corresponds to the corrosion potential of the material. Then, in the region of re-passivation, U_1-U_2, a porous oxide film grows, and it is across this film that most of the voltage drops now occurs. At point $U_{2,}$ the electric filed strength in the oxide film reaches a critical value beyond which the film is broken through due to impact or tunnelling ionisation. In this case, small luminescent sparks are observed to move rapidly across the surface of the oxide film, facilitating its continued growth. At point U_3, the mechanism of impact ionisation is supported by the onset of thermal ionisation processes and slower, larger arc discharges arise. In the region U_3-U_4, thermal ionisation is partially blocked by negative charge build-up in the bulk of the thickening

http://dx.doi.org/10.5772/58929

oxide film, resulting in discharge-decay shorting of the substrate. This effect determines the relatively low power and duration of the resultant arc discharges, i.e. micro-discharges, which are termed "micro arcs". Owing to the 'micro-arcing', the film is gradually fused and alloyed with elements contained in the electrolyte. Above the U_4, the arc micro-discharges occurring throughout the film penetrate through to the substrate and transform into powerful arcs, which may cause destructive effects such as thermal cracking of the film.

Recently, Wang et al. [59] reported different characteristics of oxidized coatings at different voltages on AZ91D in an alkali-silicate solution. Three types of oxide coatings, passive film, micro-spark ceramic coating and spark ceramic coating, were prepared at 100 V, 195 V, and 235 V, respectively. The passive films are thin and cannot provide effective protection to the substrate. The micro-spark ceramic coatings are homogeneouswith compact internal layer and exhibit the highest resistance owing to to the highest effective thickness. The spark ceramic coatings are thickest, but due to the large pores in the oxide layer, they are loose and defective.

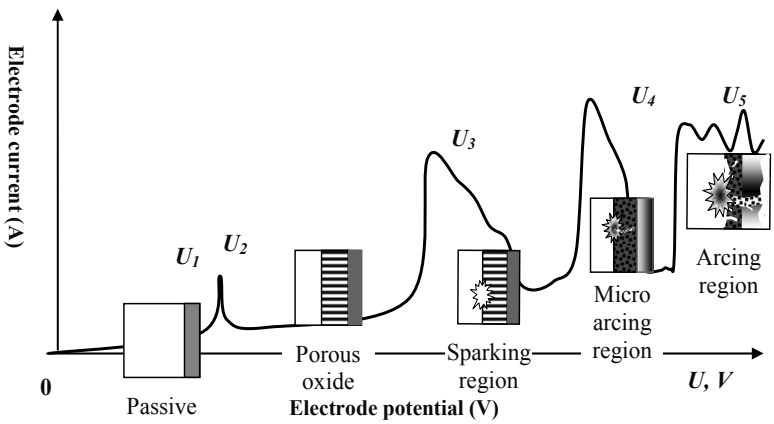

Figure 13. Current-voltage diagram for the process of plasma electrolysis: discharge phenomena are developed in the dielectric film on the electrode surface [57].

Electrolytic plasma oxidation (EPO) technology has been used for depositing ceramic coatings on magnesium alloys for corrosion protection [60-63]. The coatings can be as thick as a few hundreds of micrometers and their corrosion behaviour strongly depends on the process parameters employed, the chemical compositions of the materials studied, and the electrolytes used. The effect of electrolyte composition on properties of EPO oxide coatings on Mg and Mg alloys has also been an interesting subject of investigation to the automobile industry. The electrolytes consisted of potassium hydroxide and some other passive agents that can modify the characteristics of the oxide coatings. Hsiao and Tsai [62] studied the characteristics of anodic films formed on solutions containing 3M KOH, 0.21M $NaPO_4$, 0.6 MKF, with and without $Al(NO_3)_3$. It was found that the addition of $Al(NO_3)_3$ into 3 M KOH+0.21 M Na_3PO_4+0.6 M KF base electrolyte assisted uniform sparking on AZ91D magnesium alloy in anodizing. Either with or without a low concentration of $Al(NO_3)_3$, a porous and non-uniform anodic was formed. The presence of $Al(NO_3)_3$ in the base electrolyte resulted in the formation of Al_2O_3 and

$Al(OH)_3$ in the anodic film. The presence of Al_2O_3 in the films is beneficial to the corrosion resistance of films in 3.5 wt% NaCl solution.

The process parameters employed also play an important role in the characteristics of oxide coatings. Zhang et al. [61] found that the properties of oxide coatings were strongly influenced by the process parameters employed. With an increase of solution temperature, the film thickness decreased. On the other hand, the film thickness increased with an increase in treatment time and current density. The voltages rise during the EPO process is always accompanied by the increase of film thickness. Higher voltage indicates thicker film. Khaselev et al [60] investigated the characteristics of the oxide coatings on binary Mg-Al alloys in a solution containing 3 M KOH, 0.6 M KF, and 0.21 M Na_3PO_4 with 1.1 M aluminate. The breakdown voltages increased with an increase in Al content in the alloys. The growth of oxide films was non-uniform. The growth started on α-Mg and continued on the β-phase ($Mg_{17}Al_{12}$) when the voltage exceeded 80 V, and a uniform anodic film was formed on the alloy substrate when the voltages reached 120 V. Al was incorporated into oxide coatings from both the substrate and the electrolyte. The EPO coatings exhibited better corrosion resistance than the coatings treated by anodizing. Zhang et al [61] compared the oxide coatings produced by the EPO process with the anodic coatings prepared by the HAE and Dow 17 process. It was found that the EPO coatings were smooth, uniform, in contrast to rough, patchy film produced by HAE and relatively rough, even, partly powdery film produced by DOW17. Furthermore, the films produced by the EPO process are much more corrosion protective than those produced by HAE and DOW17.

Now studies on the effects of power supply modes on EPO coating properties have been paid more and more attention. Researchers [64] tried to modify the morphologies and structures of oxide coatings by altering the sparks during the EPO process. Originally, DC or amplitude-modulated AC was used in the EPO process, which allowed coating growth rates of only 1-2 $\mu m\ min^{-1}$. Yerokhin et al [64] utilized a pulsed bipolar current to make oxide ceramic layers dense and uniform with a fine-grained microstructure on a Mg alloy (2% Al, 1% Zn, 0.2% Mn, Mg-balance) and the coating growth rates was up to $10\mu\ m\ min^{-1}$. The pulsed bipolar current was also beneficial to elimination of the fatigue cracks by strain distortion of the metal subsurface layers induced during the oxidation process. The phase was mainly $MgAl_2O_4$ using pulsed bipolar power, while MgO and Al_2O_3 are mainly in the films using DC power.

Other methods have also been applied to the EPO process to improve the properties of coatings. Guo et al [65] demonstrated that ultrasonic power can play an important role in the coating formation and enhance the coating growth. The anodic coatings consisted of two layers when the ultrasound field was applied and the acoustic power value increased to 400W at a constant frequency of 25 kHz in 0.1 M potassium hydroxide, 0.15 M potassium fluoride, 0.30 M sodium aluminate, 0.004 M sodium pyrophosphate and 0.5-1.0 M additives. This was different from the situation without an ultrasonic field where the anodic coatings consisted of only one layer. For the two layer anodic coatings, the inner layer was compact and enriched in aluminum and fluorine, and had a uniform thickness. In contrast, the aluminum and fluorine contents in the external layer were very low and the thickness was non-uniform. Also, studies [66-73] demonstrate that Plasma Electrolytic Oxidation (PEO) is a relatively cost-effective and

http://dx.doi.org/10.5772/58929

environmentally friendly technique to improve the corrosion and wear resistance of magnesium and its alloys. The PEO method can be used to form a thin or thick, hard and adherent ceramic-like coating on the surface of Mg alloys for automotive applications.

It has been indicated [74-77] that magnesium is a good candidate as an implant material due to its bioabsorbability and high specific strength. To avoid the rapid degradation of the magnesium in the human body, techniques of surface treatment can be applied to improve magnesium corrosion resistance and consequently mitigate its degradation. Very recently, Hu and Nie [78] applied the plasma electrolytic oxidation (PEO) treatment to pure magnesium in an effort to develop an implant material with controllable degradation. This is because the PEO process is inexpensive and environmentally friendly and capable of producing a coating that is non-harmful to the human body. Magnesium is a strong candidate as due to its bioabsorbability and high specific strength. In their study, Potentiodynamic polarization corrosion tests, performed in a simulated body fluid (Hanks' Balanced Salt Solution) were carried out on coated and uncoated magnesium samples. The results of the testing showed that the coated magnesium exhibited higher corrosion resistance than the substrate. With the PEO coating thicknesses of 6.3 and 18.6 microns, the corrosion current density was decreased by 1.330×10^{-3} and 1.341×10^{-3} mA/cm^2 from the uncoated magnesium respectively, indicating a significant reduction in the degradation rate between pure magnesium and coated magnesium from 6.17×10^{-1} to 1.91×10^{-2} and 1.42×10^{-2} g/year respectively. A pin-on-disc tribometer was employed to measure the coefficient of friction (COF) for the coated and uncoated magnesium samples, lubricated with and without Hanks' solution. The measured COFs of the coated samples were very low. They were averaged to be 0.198 and 0.256 for the thick and thin coatings respectively, while the substrate exhibited an averaged COF of 0.203 under the lubricated condition. The COF measurements indicated the coatings had very comparable COFs to the substrate. By maintaining the low level of the COFs, the developed PEO coating on the Mg substrate could cause almost no irritation or harm to the surrounding tissue during the implant insertion operation.

6. Summary of the literature review

The examples described in the previous section demonstrate that it is possible to develop appropriate coating schemes for the protection of magnesium for use in automotive components. However, no single coating technology has been developed which functions to adequately protect magnesium from corrosion in harsh service conditions. For example, in winter, the mixture of deicing salt and sand often attacks Mg chassis components of automobiles, such as transfer cases. Also, coolants can cause corrosion on Mg alloy engine blocks.

One of the most effective ways to prevent corrosion is to coat the base material. In order for a coating to provide adequate corrosion protection for Mg and Mg alloys, the coating must be uniform, pore free, well adhered, and self-healing in case that physical damage to the coating may occur.

In the case of electrochemical plating, the capital investment is relatively small. Electroplating process is extremely difficult to achieve uniform coatings on complex shapes due to uneven throwing power. Electroless plating can obtain uniform coatings. However, there are some serious concerns over waste disposal.

Conversion coatings also represent a minimum capital investment, however the most widely used type of conversion coatings are chromate conversion coatings. These represent a serious environmental risk due to the presence of leachable hexavalent chromium in the coatings. A number of chromate free conversion coatings are under development but this technology is still in its infancy. Conversion coatings do not provide adequate corrosion and wear protection from harsh service conditions when used alone. However, they can act as a good base for producing adherent organic coatings and act to enhance corrosion resistance of a combined coating system by protecting the substrate at the defect sites in overlying layers.

Anodizing is the most widely commercially used coating technology for magnesium and its alloys. This process is technologically more complex than electroplating or conversion coating but is less sensitive to the type of alloy being coated. It does involve more capital investment due to the need for cooling systems and high power consumption but this may be balanced by the decreased cost of waste disposal. The coatings produced by anodizing are porous ceramic-like coatings. These properties impart good paint-adhesion characteristics and excellent wear and abrasion resistance to the coating. However, without further sealing, they are not adequate for use in applications where corrosion resistance is of primary importance.

The use of gas-phase coating processes and laser surface melting to modify the surface or create coatings is an excellent alternative for corrosion protection of Mg alloys with little environmental impact. However, the capital investment of equipment is really high.

Organic coatings such as sol-gel coatings on magnesium alloys require a minimum of pretreatment steps prior to deposition. But, their thicknesses might be limited.

It is evident that there is limited information comparing erosion and corrosion properties of the ceramic coatings prepared from different electrolytes. The relative significance of the EPO process parameters on effects of the corrosion resistance of magnesium alloys, in particular for bio-applications, needs to be fully investigated.

Author details

Henry Hu*, Xueyuan Nie and Yueyu Ma

*Address all correspondence to: huh@uwindsor.ca

Department of Mechanical, Automotive and Materials Engineering, University of Windsor, Windsor, Canada

http://dx.doi.org/10.5772/58929

References

[1] J. E. Gray and B. Luan, "Protective coatings on magnesium and its alloys − a critical review", Journal of Alloys and Compounds, 336 (2002) 88-113.

[2] D. Eliezer, E. Aghion and F. Froes, "Magnesium science, technology and applications", Advanced Performance Materials, 5 (1998) 201-212.

[3] W. A Ferrando, "Review of Corrosion and Corrosion Control of Magnesium Alloys and Composites", Journal of Materials Engineering, 11 (1989) 299-313.

[4] R. Lindstom, L. Johansson, G. Thompson, P. Skeldon and J. Svensson, "Corrosion of magnesium in humid air", Corrosion Science, 46 (2004) 1141-1158.

[5] G. L. Makar and J. Kruger, "Corrosion of magnesium", International Materials Reviews, 38 (1993) 138-153.

[6] N. D. Tomashov, "Theory of corrosion and protection of metals", The Macmillan Company, New York, 1966.

[7] R. Baboian, S. Dean, H. Hack, G. Haynes, J. Scully, D. Sprowls, "Corrosion Tests and Standards: Application and Interpretation", ASTM Manual Series: MNL 20, Philadelphia, USA, 1995.

[8] G. Song, A. Atrens, D. StJohn, J. Nairn and Y. Li, "The electrochemical corrosion of pure magnesium in 1N NaCl", Corrosion Science, 39 (2004) 855-875.

[9] Metals Handbook, Corrosion 9th ed., Vol. 13, "Corrosion of magnesium and magnesium alloys", ASM International, Metals Park, OHIO, USA, 1987.

[10] G. Song, A. Atrens, D. St John, X. Wu and J. Nairn, "The anodic dissolution of magnesium in chloride and sulphate solutions", Corrosion Science, 39 (1997) 1981-2004.

[11] G. Song and D. StJohn, "Corrosion behaviour of magnesium in ethylene glycol", Corrosion Science, 46 (2004) 1381-1399.

[12] N. S. McIntyre and C. Chen, "Role of impurities on Mg surfaces under ambient exposure conditions", Corrosion Science, 40 (1998) 1697-1709.

[13] G. Song and A. Atrens, "Corrosion Mechanisms of Magnesium Alloys", Advanced Engineering Materials, 1 (1999) 11-33.

[14] R. Lindstom, L. Johansson and J. Svensson, "The influence of NaCl and CO_2 on the atmospheric corrosion of magnesium alloy AZ91", Materials and Corrosion, 54 (2003) 587-594.

[15] G. Song and D. StJohn, "Corrosion of magnesium alloys in commercial engine coolants", Materials and Corrosion, 56 (2005)15-23.

[16] E. Slavcheva, G. Petkova and P. Andreev, "Inhibition of corrosion of AZ91 magnesium alloy in ethylene glycol solution in presence of chloride anions", Materials and Corrosion, 56 (2005) 83-87.

[17] K. N. Reichek, K. J. Clark and J. E. Hillis"Controlling the salt water corrosion performance of magnesium AZ91 alloy", SAE Technical Paper series #850417, 1985,1-12.

[18] D. Hawke and A. Olsen, "Corrosion properties of new magnesium alloys", Magnesium Properties and Applications for Automobiles, SAE, 1993, SP-962, 79-84.

[19] B. E. Carlson and J. W. Jones "The metallurgical aspects of the corrosion behaviour of cast Mg-Al alloys", CIM conference, Quebec, 1993, Light Metals Processing and Applications, 833-847.

[20] O. Lunder, K. Nisancioglu and R. Hansen, "Corrosion of die cast magnesium-aluminium alloys", SAE, 1993, SP-93/962, 117-126.

[21] F. Lefebvre and G. Nussbaum, "Influence of the microstructure on the corrosion resistance of Mg-Al based alloys", CIM Conference Proceedings, Extraction, Refining and Fabrication of Light Metals, 1991, 20-30.

[22] G. Song and D. StJohn, "The effect of zirconium grain refinement on the corrosion behaviour of magnesium-rare earth alloy MEZ", Journal of Light Metals, 2 (2002) 1-16.

[23] L. Y. Mei, G. L. Dunlop, and H. Westengen, "Age hardening and precipitation in a cast Mg-rare-earth alloy", Journal of Materials Science, 31 (1996) 387-397.

[24] G. Song, A. Atrens and M. Dargusch, "Influence of microstructure on the corrosion of die cast AZ91D", Corrosion Science, 41 (1999) 249-273.

[25] S. Mathieu, C. Rapin, J. Steinmetz and P. Steinmetz, "A corrosion study of the main constituent phase of AZ91magnesium alloys", Corrosion Science, 45 (2003) 2741-2755.

[26] G. Song, A. Atrens, X. Wu and B. Zhang, "Corrosion behaviour of AZ21, AZ501 and AZ91 in sodium chloride", Corrosion Science, 40 (1998) 1769-1791.

[27] S. Mathieu, C. Rapin, J. Hazan and P. Steinmetz, "Corrosion behaviour of high pressure die-cast and semi-solid cast AZ91D alloys", Corrosion Science, 44 (2002) 2737-2756.

[28] M. G. Fontana, "Corrosion Engineering", 3rd Ed., McGraw-Hill International Editions, USA, 1996.

[29] G. Song and A. Atrens, "Understanding magnesium corrosion", Advanced Engineering Materials, 5 (2003), 837-858.

[30] G. Song and B. Johannesson, S. Hapugoda and D. StJohn, "Galvanic corrosion of magnesium alloy AZ91D in contact with an aluminium alloy, steel and zinc", Corrosion Science, 46 (2004) 955-977.

[31] G. L. Makar and J. Kruger, "Corrosion studies of rapidly solidified magnesium alloys", Journal of the Electrochemical Society, 137 (1990) 414-421.

[32] F. Czerwinski, "The early stage oxidation and evaporation of Mg-9%Al-1%Zn alloy", Corrosion Science, 46 (2004) 377-386.

[33] P. L. Hagans, "Surface modification of magnesium for corrosion protection", in Proc. 41 st World Magnesium Conf., Dayton, OH, 1984. International Magnesium Association, 30-38.

[34] S. Akvipat, E. B. Habermann and P. L. Hagnas,"Effects of iron implantation on the aqueous corrosion of magnesium", Materials Science Engineering, 69 (1984), 311-316.

[35] Govind, K Nair, M. Mittal, K. Lal, R. Mahanti, and C. Sivaramakrishnan, "Development of rapidly solidified (RS) magnesium-aluminium-zinc alloy", Materials Science and Engineering, A304-306 (2001) 520-523.

[36] N. Aung and W. Zhou, "Effect of heat treatment on corrosion and electrochemical behaviour of AZ91D magnesium alloy", Journal of Applied Electrochemistry, 32 (2002) 1397-1401.

[37] W. P. Innes, In: Electroplating and Electroless Plating on Magnesium and Magnesium Alloys, Modern Electroplating, Wiley-Interscience, New York, 1974, p602.

[38] Y. F. Jiang, C.Q. Zhai, L.F. Liu, Y.P. Zhu, and W.J. Ding, "Zn-Ni alloy coatings pulse-plated on magnesium alloy", Surface and Coatings Technology, 191 (2005) 393-399.

[39] A. Sharma, M. Suresh, H. Narayanmurthy and R. P. Sahu"Electroless Nickel Plating on Magnesium Alloy", Metal Finishing, 96 (1998) 10-18.

[40] H. Huo, Y. Li and F. Wang, "Corrosion of AZ91D magnesium alloy with a chemical conversion coating and electroless nickel layer", Corrosion Science, 46 (2004) 1467-1477.

[41] K. Chong and T. Shih, "Conversion-coating treatment for magnesium alloys by a permanganate-phosphate solution", Materials Chemistry and Physics, 80 (2003) 191-200.

[42] D. Hawke and D. Albright,"A Phosphate –Permanganate Conversion Coating for Magnesium", Metal Finishing, 93 (1995) 34-38.

[43] H. Umehara, M. Takaya and S. Terauchi, "Chrome-free surface treatments for magnesium alloy", Surface and Coatings Technology, 169-170 (2003) 666-669

[44] M. Gonzalez-Nunez, C. A. Nunez-Lopez, P. Skeldon, G. E. Thompson, H. Karimzadeh, P. Lyon and T. E. Wilks"A non-chromate conversion coating for magnesium al-

loys and magnesium-based metal matrix composites", Corrosion Science, 37 (1995) 1763-1772.

[45] A. Rudd, C. Breslin and F. Mansfeld. "The corrosion protection afforded by rare earth conversion coatings applied to magnesium", Corrosion. Science, 42 (2000) 275-288.

[46] J. E. Hillis, "Surface engineering of magnesium alloys", in: ASM Handbook, Surface Engineering, Vol. 5, ASM International, 1994.

[47] H. A. Evangelides, "A new finish for magnesium alloys", Metal Finishing, 55 (1951) 56-60.

[48] Anon, "The HAE process to date", Light Metal Age, 15 (1957) 10-14.

[49] H. Umehara, S. Terauchi and M. Takaya, "Structure and corrosion behaviour of conversion coatings on magnesium alloys", Materials Science Forum, 350 (2000) 273-282.

[50] Y. Mizutani, S. J. Kim, R. Ichino and M. Okido, "Anodizing of Mg alloys in alkaline solutions", Surface and Coatings Technology, 169-170 (2003) 143–146.

[51] R. Bunshah, "Handbook of Hard Coatings", William Andrew Publisher, New York, USA, 2001.

[52] F. Fracassi, R. Agostino, F. Palumbo, E. Angelini, S. Grassini and F. Rosalbino"Application of plasma deposited organodilicon thin films for the corrosion protection of metals", Surface and Coatings Technology, 174–175 (2003) 107–111.

[53] N. Yamauchi, K. Demizu, N. Ueda, N.K. Cuong, T. Sone and Y. Hirose, "Friction and wear of DLC films on magnesium alloy", Surface and Coatings Technology, 193 (2005) 277–282.

[54] F. Hollstein, R. Eiedemann and J. Scholz, "Characteristics of PVD-coatings on AZ31hp magnesium alloys", Surface and Coatings Technology, 162 (2003) 261-268

[55] H. Hoche, H. Scheerer, D. Probst, E. Broszeit and C. Berger, "Development of a plasma surface treatment for magnesium alloys to ensure sufficient wear and corrosion resistance", Surface and Coatings Technology, 174–175 (2003) 1018–1023.

[56] A. Phani, F. Gammel, T. Hack, and H. Haefke, "Enhanced corrosion resistance by sol-gel-based ZrO_2-CeO_2 coatings on magnesium alloys", Materials and Corrosion, 56 (2005) 77-82.

[57] A. L. Yerokhin, X. Nie, A. Leyland, A. Matthews and S. J. Dowey"Plasma electrolysis for surface engineering", Surface and Coatings Technology, 122 (1999) 73-93.

[58] A. L. Yerokhin, V.V. Lyubimov and R.V. Ashitkov, "Phase formation in ceramic coatings during plasma electrolytic oxidation of aluminium alloys", Ceramics International, 24 (1998) 1–6.

[59] Y. Wang, J. Wang and J. Zhang, "Characteristics of anodic coatings oxidized to different voltage on AZ91D Mg alloy by micro-arc oxidization technique", Materials and Corrosion, 56 (2005) 88–92.

[60] O. Khaselev, D. Weiss and J. Yahalom, "Structure and composition of anodic films formed on binary Mg-Al alloys in KOH-aluminate solutions under continuous sparking", Corrosion Science, 43 (2001) 1295-1307.

[61] Y. Zhang, C. Yan, F. Wang, H. Lou and C. Cao, "Study on the environmentally friendly anodizing of AZ91D magnesium alloy", Surface and Coatings Technology, 161 (2002) 36-43

[62] H. Hsiao and W. Tsai, "Characterization of anodic films formed on AZ91D magnesium alloy", Surface and Coatings Technology, 190 (2005) 299-308

[63] W. B. Xue, Z. W. Deng, T. H. Zhang, R. Y. Chen and Y. L. Li, "Microarc oxidation mechanism of a cast magnesium alloy", Rare Metal Materials Engineering, 28 (1999) 353-356.

[64] A. L. Yerokhin, A. Ahatrov, V. Samsonov, P. Shashkov, A. Leyland and A. Matthews. "Fatigue properties of Keronite® coatings on a magnesium alloy", Surface and Coatings Technology, 182 (2004) 78–84.

[65] X. W. Guo, W.J. Ding, C. Lu and C.Q. Zhai, "Influence of ultrasonic power on the structure and composition of anodizing coatings formed on Mg alloys", Surface and Coatings Technology, 183 (2004) 359–368.

[66] H. Tamai, K. Igaki, E. Kyo, Initial and 6-Month Results of Biodegradable Poly-L-Lactic Acid Coronary Stents in Humans, Circulation, 102, 2000, 399–404.

[67] P. Zhang, X. Nie, H. Hu, Liu, Y., TEM analysis and Tribological Properties of Plasma Electrolytic Oxidation (PEO) Coatings on a Magnesium Engine AJ62 Alloy, Journal of Surface and Coatings Technology, Vol 205, 2010, 1508-1514.

[68] L. Han, X. Nie, Q. Zhang, H. Hu, Influence of Electrolytic Plasma Oxidation Coating on Tensile Behavior of Die Cast AM50 Alloy Subjected to Salt Corrosion, International Journal of Modern Physics B, Vol 23 (6&7), 2009, 960-965.

[69] Y. Ma, H. Hu, D. Northwood, X. Nie, Optimization of the Electrolytic Plasma Oxidation Processes for Corrosion Protection of Magnesium Alloy AM50 Using the Taguchi Method, Journal of Materials Processing Technology, Vol 182, 2007, 58–64.

[70] Y. Ma, X. Nie, D.O. Northwood, H. Hu, Systematic Study of the Electrolytic Plasma Oxidation Process on Mg Alloy for Corrosion Protection, Solid Thin Films, Vol 494, 2006, 296-301.

[71] Y. Ma, X. Nie, D. O. Northwood, H. Hu, Corrosion and Erosion Properties of Oxide Coatings on Magnesium, Thin Solid Films, Vol 469-470, 2004, 472-477.

[72] W. Zhang, B. Tian, K. Du, H. X. Zhang, F. H. Wang, Preparation and Corrosion Performance of PEO Coating With Low Porosity on Magnesium Alloy AZ91D In Acidic KF System, International Journal of Electrochemical Science, 6, 2011, 5228-5248.

[73] R.O. Hussein, P. Zhang, D.O. Northwood, and X. Nie, Improving the Corrosion Resistance of Magnesium Alloy AJ62 by a Plasma Electrolytic Oxidation (PEO) Coating Process, Corrosion & Materials, Vol. 36, No. 3, 2011, 38-49.

[74] B. Denkena, A. Lucas, Biocompatible Magnesium Alloys as Absorbable Implant Materials –Adjusted Surface and Subsurface Properties by Machining Processes, Annals of the CIRP, 56 (1), 2007, 113-116.

[75] B. Denkena, F. Witte, C. Podolsky, A. Lucas, Degradable Implants Made of Magnesium Alloys, Proc. of the 5th euspen International Conference – Montpellier – France, May 2005.

[76] G. Song, S. Song, A Possible Biodegradable Magnesium Implant Material, Advanced Engineering Matierals, 9, No. 4, 2007, 298-302.

[77] J. Li, P. Hanb, W. Ji, Y. Song, S. Zhang, Y. Chen, C. Zhao, F. Zhang, X. Zhang, Y. Jiang, The In Vitro Indirect Cytotoxicity Test and In Vivo Interface Bioactivity Evaluation of Biodegradable FHA Coated Mg-Zn Alloys, Materials Science and Engineering B, 176, 2011, 1785– 1788

[78] J. Hu and X. Nie, "Plasma Electrolytic Oxidation Treatment of Pure Magnesium for Potential Biological Application", Proceedings of Biomaterials, Smart Materials, and Structures, The 8th Pacific Rim International Congress on Advanced Materials, TMS, August 4-9, 2013, Waikoloa, Hawaii, USA, Page 1655-1662.

Chapter 4

Corrosion Protection of Magnesium Alloys in Industrial Solutions

Amany Mohamed Fekry

Additional information is available at the end of the chapter

http://dx.doi.org/10.5772/58942

1. Introduction

The main problem in our life is the corrosion of many types of alloys either industrialy or biologicaly. This work reviews the corrosion protection of magnesium based alloys in industrial solutions. Corrosion behavior had been studied using electrochemical impedance spectroscopy (EIS), Potentiondynamic polarization and scanning electron microscope (SEM) techniques. Magnesium is the lightest of all metals in practical use with density of 1.74 g cm^{-3}. Pure magnesium metal has useful properties such as shielding against electromagnetic waves, vibration damping, dent resistance and machinability, in addition to its recyclability as it has a lower specific heat and a lower melting point than other metals. On the other hand, magnesium has shortcomings such as insufficient strength, elongation and heat resistance as well as being subject to corrosion. It is necessary to deal with its shortcomings and improve its performance through alloying with various elements. Alloying magnesium improves its strength, heat resistance and creep resistance [1].

Magnesium alloys are the most versatile and attractive metallic materials. They are used for a broad range in commercial, industrial and aerospace applications due to their many advantages, such as light density, good mechanical properties and excellent castability [2-4]. The most common magnesium alloys are those containing aluminum, Zinc, manganese, zirconium, thorium and rare earth metals. The latter alloys are used when resistance to creep and high temperature strength are required. One of the major problems that limit magnesium alloys application is their high susceptibility to corrosion in different media [5] which depends widely on film formation and surface electrolyte interaction. A serious limitation for the wide-spread use of several magnesium alloys is their susceptibility to general and localized (pitting) corrosion. The AZ-based Mg system has been the basis of the most widely used magnesium alloys [6]. One of the most successful magnesium-aluminium alloy is AZ91D, which has a two-

phase microstructure typically consisting of α-Mg matrix with the β-phase (the intermetallic $Mg_{17}Al_{12}$) distributed along the α grain boundaries. The α-phase consists of α-Mg-Al-Zn solid solution with the same structure as pure magnesium [5]. Also AZ31E alloy have excellent mechanical properties. Extruded Mg alloys as AZ31E is getting more and more widely used because of their considerably high plasticity in comparison with the die-cast Mg alloys [7].

Corrosion is a major problem in the cooling system of an engine block. Currently, the main composition of a conventional coolant is 30–70 vol% ethylene glycol [7]. This can be used for studying the corrosion behavior of AZ91D alloy. Most existing commercial coolants fail to provide adequate corrosion protection to magnesium alloys [8]. Some companies have also realized the difficulty of using the conventional coolants for magnesium alloys, and are developing coolants with new inhibitors [9]. Song et al. [7] observed that the corrosion rate of magnesium in aqueous ethylene glycol depends on the concentration of the solution. A diluted ethylene glycol solution is more corrosive than a concentrated one at room temperature. Ethylene glycol solution contaminated by individual contaminants NaCl, $NaHCO_3$ or Na_2SO_4 is more corrosive to magnesium. NaCl is the most detrimental contaminant. In this work, a study for the corrosion behavior of AZ91D alloy in this coolant has been done, due to this issue is important industrially. The aim is to characterize the corrosion properties of AZ91D alloy in aqueous ethylene glycol-water solutions of different percentages. The influence of adding chloride or flouride ion in ethylene glycol solution on the corrosion behavior was studied. Also the effect of paractamol ((N-acetyl-para-aminophenol=APAP) as inhibitor in ethylene glycol for AZ91D alloy is investigated [6].

Electrochemical characterization and corrosion behavior of AZ31E alloy was done in aqueous Oxalic acid as industrial solution [10]. Oxalic acid is a relatively strong organic acid used as purifying agent in pharmaceutical industry. Oxalic acid's main applications include cleaning or bleaching, especially for the removal of rust [11]. The work aims to attain more information concerning the corrosion behavior of AZ31E alloy in oxalic acid solution containing Cl^-, F^-or PO_4^{3-} anions under various environmental conditions. The corrosion rate was found to increase with increasing oxalic acid concentration. The effect of adding Cl^-, F^-or PO_4^{3-} ions on the electrochemical behavior of AZ31E electrode was studied in 0.01 M oxalic acid solution at 298 K. It was found that the corrosion rate increases with increasing Cl^-or F^-ion concentration, however, it decreases with increasing PO_4^{3-} ion concentration [12].

2. The main problem

One of the major problems that limit magnesium alloys application is their high susceptibility to corrosion in different media. This makes studying the corrosion and corrosion control of Mg alloys an interesting point of research which can enable extending the potential use of these important materials in a broad range of many technical and innovative applications.

http://dx.doi.org/10.5772/58942

3. The aim

The aim is to study the corrosion resistance of Mg alloys which depends essentially on two main factors: (i) alloy microstructure and (ii) properties of the developed surface film.

Generally, it is aimed to find the best magnesium alloy with low cost and low corrosion rate and to find a possible way to improve corrosion resistance of either AZ91D or AZ31E alloy in different industrial solutions.

4. Experimental

Samples of die cast magnesium aluminum alloy (AZ91D or AZ31E) in the form of plates (200 x 100 x 5 mm) were donated from Department of mining, Metallurgy and Materials Engineering, Laval University, Canada. The chemical composition (wt%) of the two alloys are as follows: 9.0 Al, 0.67 Zn, 0.33 Mn, 0.03 Cu, 0.01 Si, 0.005 Fe, 0.002 Ni, 0.0008 Be and balance Mg for AZ91D alloy; and 2.8 Al, 0.96 Zn, 0.28 Mn, 0.0017 Cu, 0.0111 Fe, 0.0007 Ni, 0.0001 Be and balance Mg for AZ31E. They were used for preparing the working electrodes. The sample was divided into small coupons. Each coupon was welded to an electrical wire and fixed with Araldite epoxy resin in a glass tube leaving cross-sectional area of the specimen 0.2 cm^2 for AZ91D alloy and 0.196 cm^2 for both AZ31E alloy.

The solutions used were prepared using Analar grade reagents for each work are (ethylene glycol, sodium fluoride, sodium chloride and paracetamol [6]) and (oxalic acid, sodium fluoride, sodium chloride and sodium phosphate [12]). All solutions were prepared using triply distilled water.

The surface of the test electrode was mechanically polished by emery papers with 400 up to 1000 grit to ensure the same surface roughness, degreasing in acetone, rinsing with ethanol and drying in air.

The cell used was a typical three-electrode one fitted with a large platinum sheet of size 15×20×2mm as a counter electrode (CE), saturated calomel (SCE) as a reference electrode (RE) and the alloy as the working electrode (WE).

The impedance diagrams were recorded at the free immersion potential (OCP) by applying a 10 mV sinusoidal potential through a frequency domain from 100 kHz down to 100 mHz. The EIS was recorded after reading a steady state open-circuit potential. The polarization scans were carried out at a rate of 1 mV/s over the potential range from-2.5 to 0 mV vs. saturated calomel electrode (SCE). Prior to the potential sweep, the electrode was left under open-circuit in the respective solution until a steady free corrosion potential was recorded. Corrosion current, i_{corr}, which is equivalent to the corrosion rate is given by the intersection of the Tafel lines extrapolation. In the weight loss measurements, the treated samples were weighed before and after the immersion in Hank's solution in absence and in presence of different concentrations of glucosamine sulphate. The instrument used is the electrochemical workstation IM6e

Zahner-elektrik, GmbH, (Kronach, Germany).The electrochemical and weight loss experiments were always carried inside an air thermostat which was kept at 25°C, unless otherwise stated. The SEM micrographs were collected using a JEOL JXA-840A electron probe micro-analyzer.

5. Results and discussion

5.1. Electrochemical impedance measurements

5.1.1. AZ91D alloy in ethylene glycol solution [6]

The EIS scans of AZ91D alloy as a function of concentration for ethylene glycol were recorded (Figure 1) after leaving the working electrode for 2 h in the test solution until reaching a steady state potential value (E_{st}). As shown in Figure 1, an increase in ethylene glycol concentration leads to a decrease in the |Z| value, indicating that pure ethylene glycol is almost inert to magnesium alloy and the corrosion of magnesium alloy in ethylene glycol solution is closely related to the water content of the solution [7].

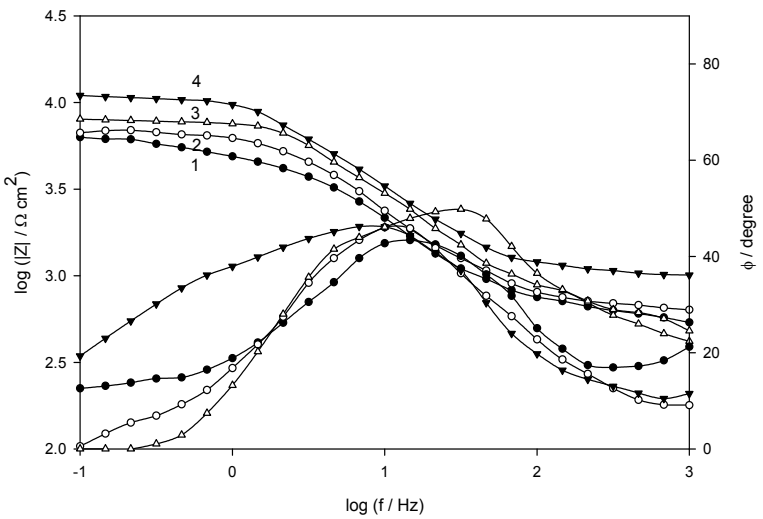

Figure 1. EIS data of AZ91D alloy exposed after 2 h immersion in various concentrations of ethylene glycol solution: (1) 30%, (2) 50%, (3) 70% and (4) 90%.

By studying the effect of adding either fluoride or chloride to the highest corrosive concentration(30% ethylene glycol-70% water), it was found that the impedance value decreases (Figure 2a) with increasing chloride ion concentration due to its aggressiveness [10]. However, for fluoride containing ethylene glycol solution impedance value increases with increasing F^- ion concentrations shown in Figure 2b.

http://dx.doi.org/10.5772/58942

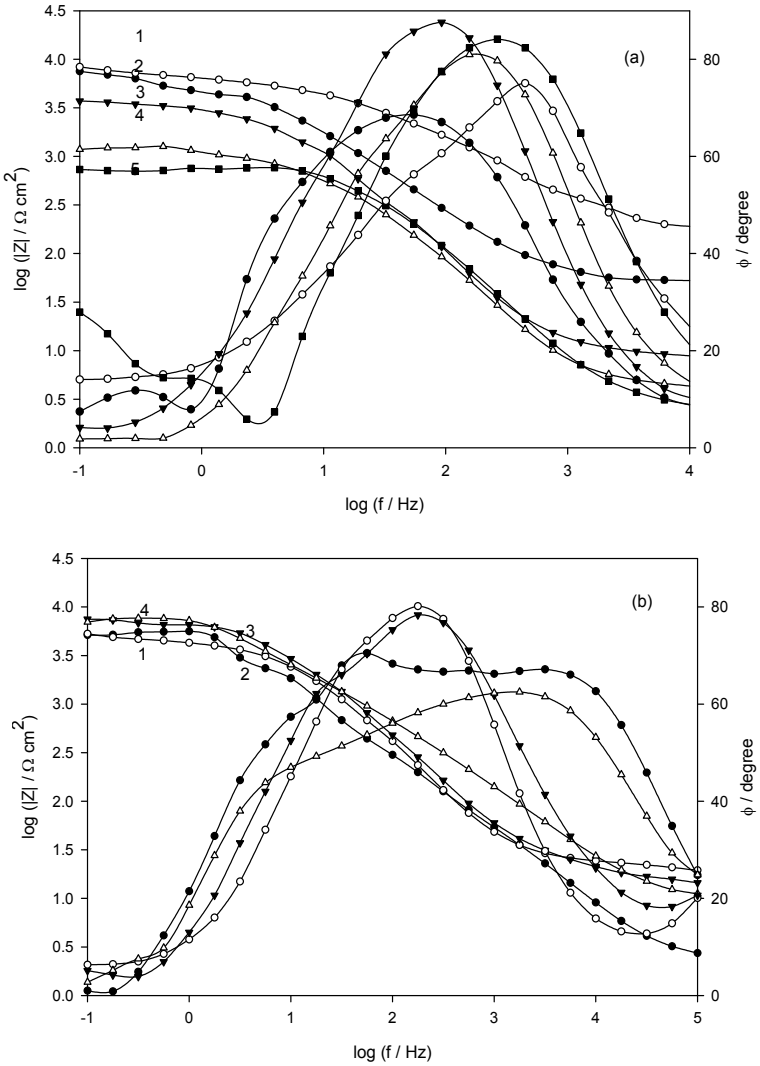

Figure 2. EIS data of AZ91D alloy exposed after 2 h immersion in 30% ethylene glycol solution with (a) chloride and (b) fluoride ions of various concentrations: (1) 0.01 M, (2) 0.05 M, (3) 0.1 M, (4) 0.3 M and (5) 0.6 M.

On adding paracetamol as inhibitor in the concentration range (0.01-1.0 mM) for corrosion of the blank (30% ethylene glycol-70% water), it was found that both |Z| value and phase angle maximum (φ) increase suddenly up to 0.05 mM then decrease regularly up to the highest concentration of inhibitor as shown in Figure 3(a,b) as Bode and Nyquist formats, respectively.

The results in general reveal two clear trends concerning the number of peaks observed in the patterns of the phase shift. The first one is for the behavior of AZ91D alloy in chloride, flouride and paracetamol containing ethylene glycol, where the Bode plots display only one maximum phase lag at all tested concentrations, however, for paracetamol, the phase angle maximum is

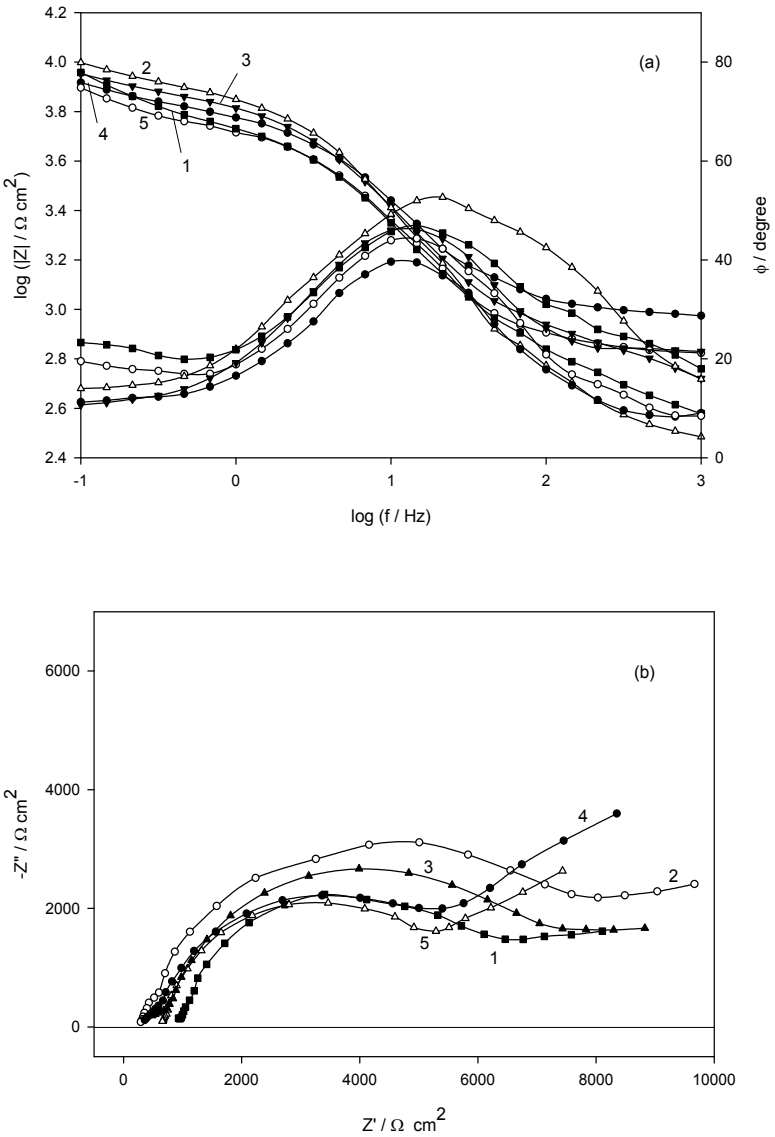

Figure 3. EIS data (a) Bode plots and (b) Nyquist plots of AZ91D alloy exposed after 2 h immersion in 30% ethylene glycol solution with paracetamol of various concentrations: (1) 0.01 mM, (2) 0.05 mM, (3) 0.1 mM, (4) 0.5 mM and (5) 1.0 mM.

nearly 45°, corresponding to a diffusion control in the passive layer. The second trend is for the alloy behavior in ethylene glycol medium with different concentrations where another peak of phase lag appears at the low frequency region and also the phase angle maximum is nearly 45° due to diffusion phenomenon. The impedance data were thus simulated to the appropriate equivalent circuit for the cases with one time constant (Figure 4a,b) and the others exhibiting two time constants (Figure 4c), respectively. This simulation gave a reasonable fit.

http://dx.doi.org/10.5772/58942

The estimated data for ethylene glycol is given in Table 1, for chloride and fluoride ions in Table 2 and for paracetamol ethylene glycol containing solution in Table 3.

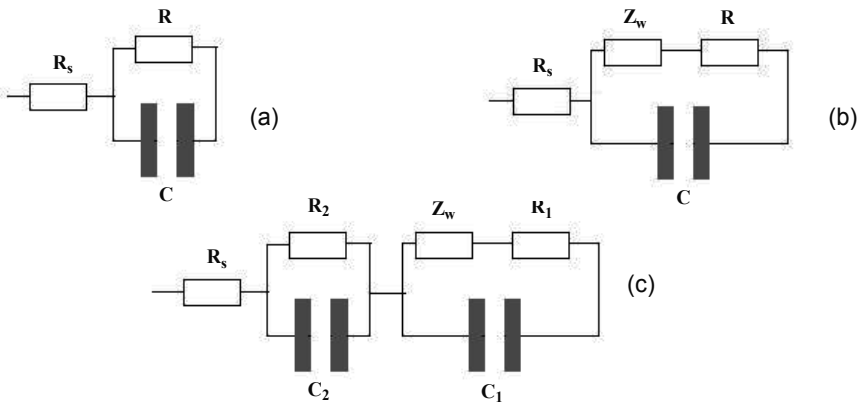

Figure 4. The equivalent circuit model representing (a,b) one and (c) two time constants.

$C_{ethylene\ glycol}$	R_s	R_1	C_1	R_2	C_2	W	R_T	$1/C_T$	i_{corr}	E_{corr}
(vol.%)	(Ω cm^2)	(kΩ cm^2)	(nF cm^{-2})	(kΩ cm^2)	(μF cm^{-2})	kΩ cm^2 s$^{-1/2}$	(kΩ cm^2)	(μF^{-1} cm^2)	(μA cm^{-2})	V
30	11.4	0.5	88.9	4.4	4.5	1.64	5.0	11.5	0.50	-1.45
50	21.9	0.7	77.9	6.2	4.3	1.52	6.9	13.1	0.41	-1.34
70	26.8	1.2	71.0	10.5	4.2	1.47	11.7	14.3	0.25	-1.26
90	30.0	1.4	66.4	15.4	4.0	1.33	16.8	15.3	0.1	-1.18

Table 1. Equivalent circuit and corrosion parameters for AZ91D alloy in various concentrations of ethylene glycol solution after 2 h immersion

Salt	C_{anion}	R	C	R_s	i_{corr}	E_{corr}
	(M)	(kΩ cm^2)	(μF cm^{-2})	(Ω cm^2)	(μA cm^{-2})	V
NaCl	0.01	7.7	2.67	154.8	0.47	-1.36
	0.05	5.8	4.36	50.2	0.49	-1.43
	0.10	3.1	7.44	9.0	0.64	-1.52
	0.30	1.1	8.50	4.2	3.40	-1.53
	0.60	0.6	9.58	2.5	30.4	-1.63
NaF	0.01	4.1	3.54	22.1	0.19	-1.41
	0.05	5.5	3.46	21.8	0.11	-1.43
	0.10	7.0	2.46	15.8	0.09	-1.45
	0.30	8.4	1.23	7.3	0.03	-1.51

Table 2. Equivalent circuit and corrosion parameters for AZ91D alloy after 2 h immersion in 30% ethylene glycol solution with different concentrations of Cl^- or F^- ions

$C_{paracetamol}$	R_s	R	C	W	i_{corr}	E_{corr}	IE
mM	(kΩ cm²)	(kΩ cm²)	(μF cm⁻²)	kΩ cm² s$^{-1/2}$	(μA cm⁻²)	V	%
0.01	0.33	6.1	2.7	2.90	0.100	-1.37	80.0
0.05	0.37	10.0	2.2	1.84	0.020	-1.26	96.0
0.1	0.47	8.5	2.4	1.39	0.040	-1.41	92.1
0.5	0.64	5.6	2.8	2.52	0.045	-1.44	91.0
1.0	0.92	5.1	3.6	1.46	0.051	-1.46	89.8

Table 3. Equivalent circuit and corrosion parameters for AZ91D alloy after 2 h immersion in 30% ethylene glycol solution with different concentrations of paracetamol

Generally, the impedance response is well simulated by the classic parallel resistor capacitor (RC) combination in series with the solution resistance (R_s). In this model [10] a charge transfer resistance (R) is in parallel with the double layer capacitance (C), as shown in Figure 4a. Figure 4b is one time constant model containing Warburg impedance (Z_w) in series to R [13], which is related to ion diffusion through passive film and indicates that the corrosion mechanism is controlled not only by a charge-transfer process but also by a diffusion process. The appropriate equivalent model for the impedance diagrams with two time constants, consists of two series circuits, $R_1Z_wC_1$ and R_2C_2 parallel combination and both are in series with R_s. C_1 is the capacitance of the outer layer, C_2 pertains to the inner layer, while R_1 and R_2 are the respective resistances of the outer and inner layers constituting the surface film, respectively [14]. A linear region at the lower frequencies in the Nyquist plot in Figure 3b would be related to diffusion phenomena [15, 16] thereby an equivalent circuit with Warburg component Z_w is more appropriate. Analysis of the experimental spectra were made by best fitting to the corresponding equivalent circuit using Thales software provided with the workstation where the dispersion formula suitable to each model was used [14]. In this complex formula an empirical exponent (α), varying between 0 and 1, is introduced to account for the deviation from the ideal capacitive behavior due to surface inhomogeneties, roughness factors and adsorption effects [10]. An ideal capacitor corresponds to α=1 while α=0.5 becomes the CPE in a Warburg component [17]. In all cases, good conformity between theoretical and experimental results was obtained for the whole frequency range with an average error of 5%.

The effect of concentration for ethylene glycol or additive ions or inhibitor on the relative thickness($1/C_T$) [18] of AZ91D. Figure 5 reveals features generally concurrent to the behavior of the film resistance. It shows that the resistance (R_T) and the relative thickness ($1/C_T$) of the surface film on AZ91D sample increase with increasing the concentration of ethylene glycol. Thus, 30% ethylene glycol (blank) is an aggressive solution as shown in SEM image in Fig. 6a, where corrosion products appear on the surface. Pure ethylene glycol has very poor electrical conductivity and is almost an insulator [7]. However, dilution by water facilitates the hydrolysis of the hydroxyl groups in ethylene glycol increasing its electrical conductivity. Ethylene glycol molecule is larger than water, so the adsorption of the former at the surface of AZ91D alloy can result in a lower capacitance value [7]. When the concentration of ethylene

http://dx.doi.org/10.5772/58942

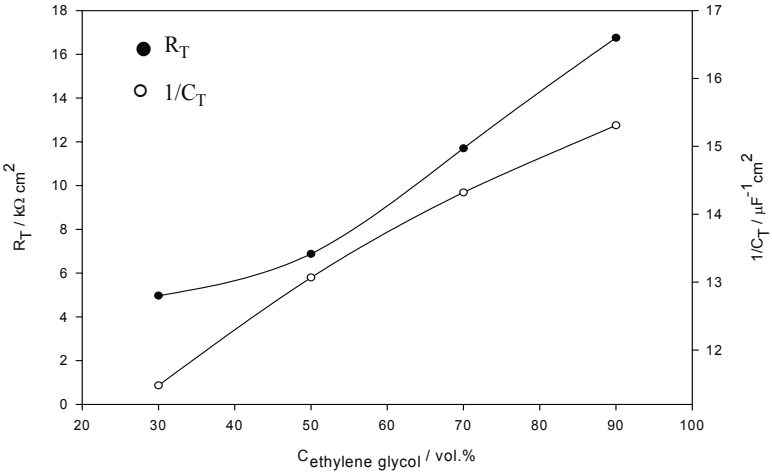

Figure 5. The total resistance (R_T) and relative thickness ($1/C_T$) for AZ91D alloy at various concentrations of ethylene glycol solution, measured after 2 h immersion.

glycol increases, more ethylene glycol will be adsorbed on the surface, leading to a lower C_T. This explains the decreasing corrosion rate of AZ91D alloy with increasing concentration of ethylene glycol and also the decrease in the Warburg impedance diffusion.

As given in Table 2, in ethylene glycol solution contaminated with chloride ions, the resistance decreases sharply at first then reaches a quasi state value with increasing concentration of contaminant [6]. The addition of chloride does not significantly increase the capacitance value until the amount of the added Cl^-ions is above a certain level (> 0.05 M). At concentrations > 0.05 M, they are more corrosive than the blank, indicating film dissolution, which can be attributed to the more aggressive nature of the chloride anion. The increase in capacitance should be due to the replacement of ethylene glycol on the alloy surface by the chloride ions as contaminant.

Fluoride is also an important substance that could exist in normal water and can easily be introduced into vehicle coolant systems [19]. As given in Table 2, in fluoride medium at concentrations > 0.05 M, R and 1/C of the surface film increase steeply than the blank due to the formation of less soluble and more stable magnesium fluoride (MgF_2) film [17]. This is confirmed by SEM micrograph of 0.3 M fluoride in ethylene glycol concentration (Figure 6b), the grain particles of the salt film grow laterally during the prolonged exposure (2 h) covering nearly the whole surface of the alloy indicating more stability as compared to the blank shown in Figure 6a. In fact, F^-has recently been used as an inhibitor in coolants for magnesium alloys [7]. However, the inhibition mechanism has not been systematically studied. Gulbrandsen et. al. [20] reported that crystalline $KMgF_3$ was identified on magnesium at higher F^-concentration in the more alkaline solutions. At 0.01 M fluoride concentration ethylene glycol may help in the formation of this compound, so that the resistance decreases than the blank. Table 2 shows that the addition of F^-into ethylene glycol strikingly enhanced

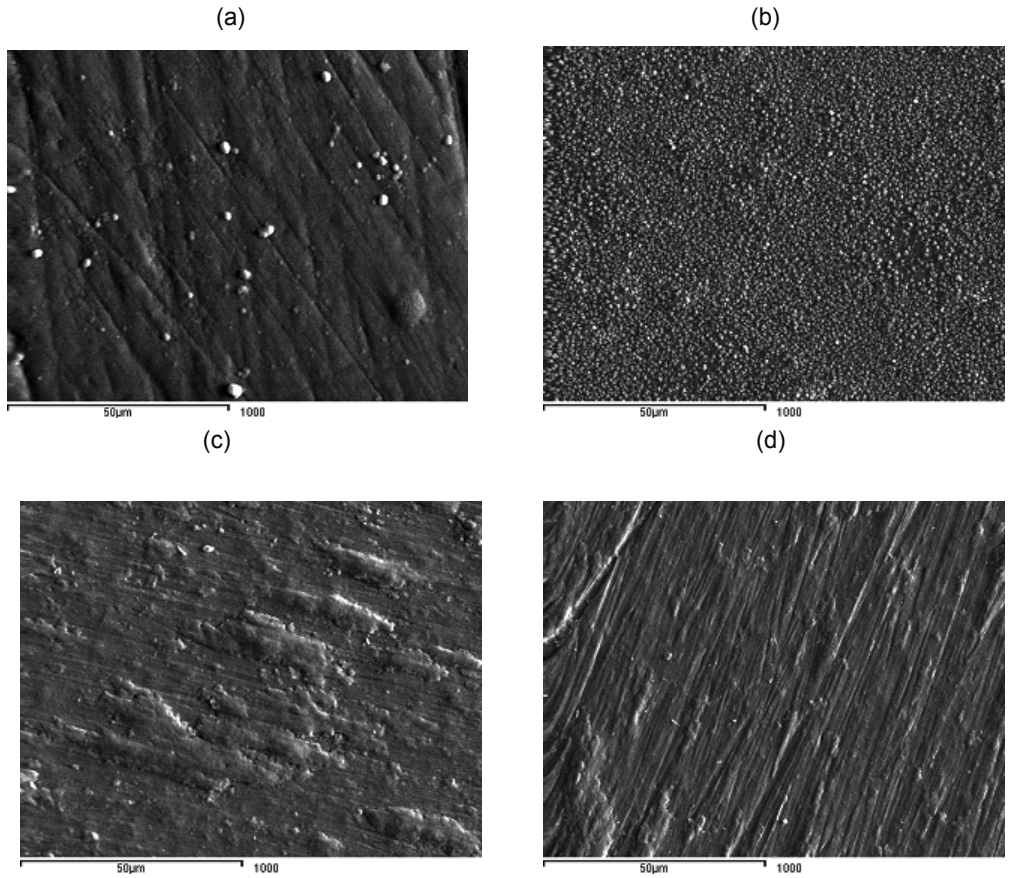

Figure 6. (a-d). SEM micrograph of the (a) blank (30% ethylene glycol solution), (b) 0.3 M F^-(c) 0.05 mM paracetamol and (d) 1.0 mM paracetamol, ethylene glycol containing solution.

R but decreased R_s and C. The significantly reduced C and dramatically improved R suggest that [7] a three-dimensional film was formed on the magnesium surface which is much thicker than the adsorbed film and thus can effectively separate the magnesium alloy from the solution, making the corrosion reaction at the interface very slow. As to the solution resistance R_s, its decrease after the addition of F^-can be simply attributed to the increased total concentration of ions by adding F^-into the solution.

Finally, the effect of adding paracetamol as inhibitor was studied; it was found that all concentrations give good inhibition as compared to the blank which may be due to the adsorption of the inhibitor through the adsorption. The rate of adsorption is usually rapid and hence, the reactive metal surface is shielded from the aggressive environment [21]. However, it was found that there is a critical concentration for the inhibitor at 0.05 mM which has the highest resistance as shown in Table 3, and the resistance decreases with increasing the inhibitor concentration > 0.05 mM. This behavior is confirmed by SEM micrographs shown in

http://dx.doi.org/10.5772/58942

Figure 6(c,d), where Figure 6c is for 0.05 mM and Figure 6b for 1.0 mM paracetamol containing ethylene glycol solution. Figure 6c shows a denser and smoother film adsorbed on the alloy surface than that formed on 1.0 mM concentration Figure 6d, Also the two are much better than the blank shown in Figure 6a.

5.2. Potentiodynamic polarization measurements

5.2.1. AZ91D alloy in ethylene glycol solution [6]

The anodic and cathodic (E-log i) plots of AZ91D alloy in the ethylene glycol solution of different concentrations were also studied using potentiodynamic polarization measurements at a scan rate of 1.0 mV s^{-1}. The curves were swept from-2.5 V to-1.0 V vs. SCE. Prior to the potential scan the electrode was left for 2 h until a steady free corrosion potential (E_{st}) value was recorded. The electrochemical parameters shown in Tables 1 and 2 were obtained by analyzing the I/E data as described elsewhere [10]. The corrosion potential (E_{corr}) and current density (i_{corr}) were calculated by Tafel extrapolation method for the cathodic branches of the polarization curves. Furthermore, to illustrate the relative stability of the surface film on AZ91D alloy in the investigated solutions, i_{corr} values are found to decrease and E_{corr} values shifts positively with increasing ethylene glycol percentage. Since increasing water percentage in ethylene glycol is responsible for the corrosivity of the solution to the alloy. However, in chloride containing solution i_{corr} values increases and E_{corr} values shifts to more negative values with increasing Cl^-concentration. This behavior reflects the harmful influence of Cl^-ions on the corrosion performance of AZ91D in aqueous liquids [7]. In Flouride containing solutions, a strange behavior occurs, where i_{corr} decreases and E_{corr} values tend to more negative values with increasing F^-concentration. Particularly, the role of the β-phase in corrosion is extensively addressed for AZ91D, and it is generally accepted that the β-phase is a corrosion barrier and its presence in an AZ91D alloy is beneficial to the corrosion resistance of the alloy. The reason is fluoride refined AZ91D magnesium alloy by blocking the growth of primary fir-tree crystals in the crystal boundary [22]. Thus, the dimension of β phase is decreased. In the cathodic reaction process, the overpotential of the hydrogen generation increased due to the dispersion of β phase, which resulted in the corrosion potential of the AZ91D.

Fig. 7 shows polarization scans for paracetamol, from which i_{corr} values is calculated and drawn against inhibitor concentration (Fig. 8). As can be seen, i_{corr} value is the lowest at 0.05 mM paracetamol concentration, which is a critical concentration and shows the highest inhibition efficiency (IE) of 96% which calculated from the following equation:

$$IE\% = 1 - \frac{i_{inh}}{i_{corr}} \times 100 \quad (1)$$

Generally, impedance and polarization measurements confirm each other and all are confirmed by SEM images.

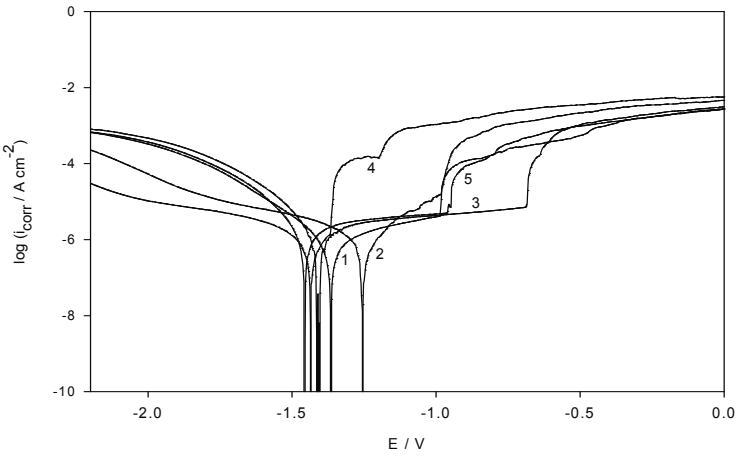

Figure 7. Cathodic and anodic scans of AZ91D alloy exposed after 2 h immersion in 30% ethylene glycol solution with paracetamol of various concentrations: (1) 0.01 mM, (2) 0.05 mM, (3) 0.1 mM, (4) 0.5 mM and (5) 1.0 mM.

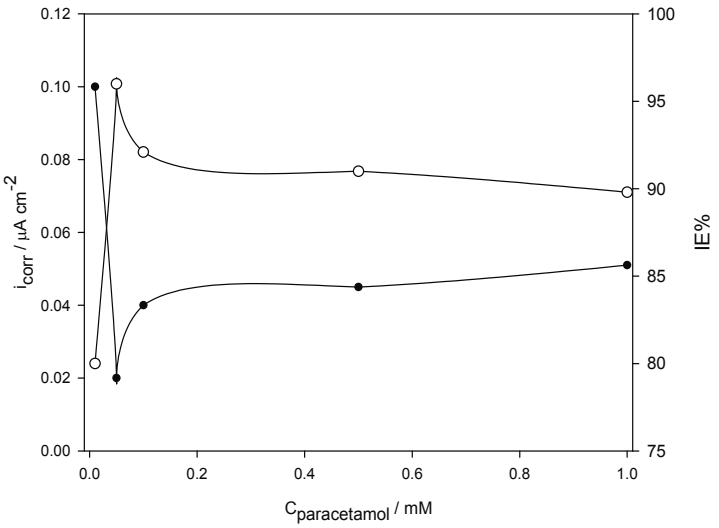

Figure 8. Variation of i_{corr} and IE% for AZ91D alloy exposed after 2 h immersion in 30% ethylene glycol solution with various concentrations of paracetamol.

5.2.2. AZ31E alloy in oxalic acid solution [12]

The impedance measurements recorded after 2 hours of immersion for AZ31E electrode in oxalic acid solution with different concentrations are presented in Figure 9. Bode plots show an intermediate frequency phase peak shifts to lower frequency and higher phase angle

http://dx.doi.org/10.5772/58942

maximum with decreasing oxalic acid concentration. Also, impedance values increase with decreasing the concentration of oxalic acid. The appropriate equivalent model used (Figure 4c) consists of two circuits in series from $R_1C_1Z_W$ and R_2C_2 parallel combination and both are in series with R_s as discussed above. In all cases, good conformity between theoretical and experimental results was obtained with an average error of 4%. The evaluated experimental values are given in Table 4.

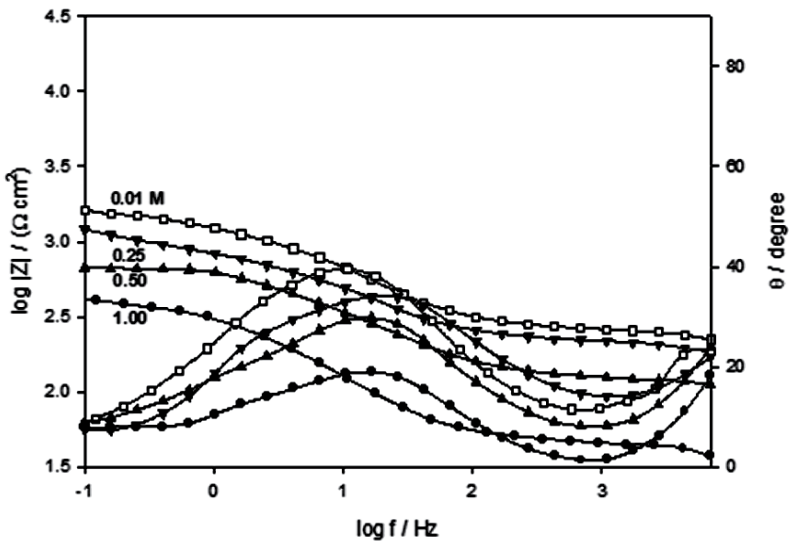

Figure 9. Bode plots of AZ31E electrode in naturally aerated oxalic acid solution of different concentrations, at 298 K.

$Na_2C_2O_4$	R_1	C_1	α_1	R_2	W	C_2	α_2	R_s
M	kΩ cm²	μF cm⁻²		Ω cm²	kDW	μF cm⁻²		Ω cm²
0.01	2.1	4.7	0.94	58.3	10.2	19.2	0.58	243
0.25	1.3	5.4	0.93	35.6	9.7	20.1	0.56	200
0.50	0.8	6.6	0.91	22.3	7.5	21.3	0.55	100
1.00	0.7	8.3	0.90	14.4	5.2	22.0	0.52	44

Table 4. Impedance parameters of AZ31E electrode in naturally aerated oxalic acid of different concentrations, at 298 K.

It was found that, when AZ31E electrode was immersed in oxalic acid solution, two competitive processes occur. The first one is oxide formation which yields a compact magnesium oxide film with good corrosion resistance. The second one is the formation of magnesium oxalate complexes, which yields a thick porous film as in case of Aluminum alloys [23] with expected

low corrosion resistance, where oxalate ions are bidentate ligands capable of forming strong surface complexes. With increasing of oxalic acid concentration the alternation of the compact oxide film by porous one will increase leading to an increase in the corrosion rate. This also is due to increasing of the acidity of the medium.

In Table 4, R_1 represents the resistance of the passive film which decreases with increasing of oxalic acid concentration due to alternation of compact film by porous one. Consequently, the decrease in the relative thickness of the passive film ($1/C_1$) supports this concept. As the most stable formula for magnesium oxalate is dehydrated one [24], so R_2 can represent the resistance of the hydrated layer and the decreasing of relative thickness ($1/C_2$) of this layer with increasing of oxalic acid concentration reflects the strong adsorption of the oxalate anion with increasing of its concentration and increasing of hydrogen evolution. Moreover, the presence of diffusion process at the interfacial layer of the electrode indicates again the formation of porous film and the decreasing of diffusion impedance indicating the increase of electrolyte diffusion through the pores, as a sequence of increasing of the porosity with the increase of oxalate concentration.

At the lowest concentration of oxalic acid (0.01 M) with highest corrosion resistance, the tested electrode was immersed in this solution containing either Cl^-, F^-or PO_4^{3-} ions with various anion concentrations (0.01 to 1.0 M). Figures 10 and 11 show Bode plots as examples for $Cl^-$and PO_4^{3-} ions, respectively. The EIS results of the tested electrode were analyzed, following the suitable proposed model in Figure 4c.

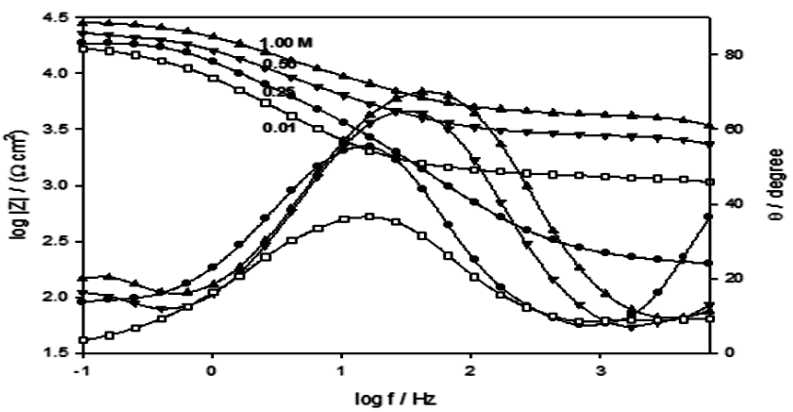

Figure 10. Bode plots of AZ31E electrode as a function of concentration for Cl^-anion in naturally aerated 0.01 M oxalic acid solution, at 298 K.

The theoretical simulated parameters for the tested alloy at each concentration from the added anions (Cl^-, F^-or PO_4^{3-}) to the forming 0.01 M oxalic acid solution were computed and summarized in Table 5.

http://dx.doi.org/10.5772/58942

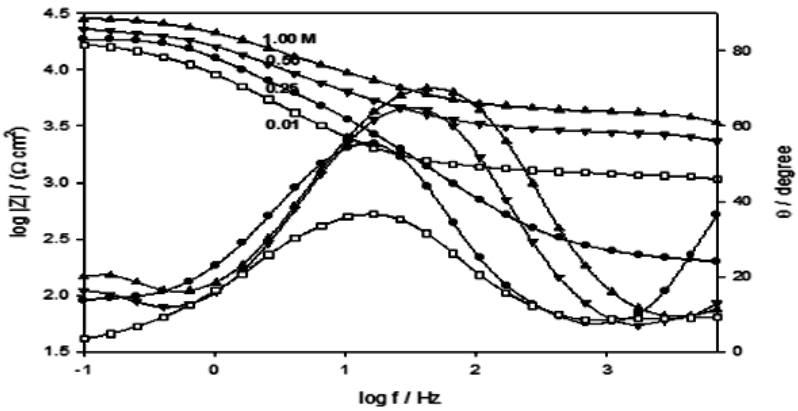

Figure 11. Bode plots of AZ31E electrode as a function of concentration for PO_4^{3-} anion in naturally aerated 0.01 M oxalic acid solution, at 298 K.

Anion	C	R_1	C_1	α_1	R_2	W	C_2	α_2	R_s	i_{corr}
	M	KΩ cm²	μF cm⁻²		Ω cm²	kDW	nF cm⁻²		Ω cm²	μA cm⁻²
Cl^-	blank	2.10	4.7	0.84	58.3	10.2	19.2	0.58	243	31.7
	0.01	20.0	2.5	0.83	94.1	5.30	7.60	0.57	501	13.4
	0.25	14.3	2.9	0.83	87.4	4.30	11.9	0.56	80	16.7
	0.50	10.5	3.9	0.81	82.1	3.10	14.9	0.54	100	20.6
	1.00	6.70	4.1	0.84	63.7	1.50	18.6	0.53	589	25.1
F^-	blank	2.10	4.7	0.84	58.3	10.2	19.2	0.58	243	31.7
	0.01	23.8	2.1	0.81	110	9.30	5.30	0.59	208	10.8
	0.25	21.3	2.5	0.87	106	8.60	6.40	0.67	80	11.2
	0.50	18.6	2.6	0.87	91.6	7.50	9.60	0.62	100	12.1
	1.00	15.8	2.8	0.81	69.2	6.70	10.1	0.59	589	14.0
PO_4^{3-}	Blank	2.10	4.7	0.84	58.3	10.2	19.2	0.58	243	31.7
	0.01	17.0	2.4	0.87	121	4.20	7.40	0.57	1075	30.0
	0.25	20.1	2.1	0.88	143	5.40	6.10	0.52	199	15.8
	0.50	24.2	1.2	0.85	165	6.20	5.60	0.56	2290	3.50
	1.00	28.9	0.6	0.82	198	8.10	4.70	0.65	3388	2.41

Table 5. Impedance and corrosion parameters of AZ31E electrode as a function of concentration for Cl^-, F^- and PO_4^{3-} anions in naturally aerated 0.01 M oxalic acid, at 298 K.

In chloride or fluoride additive solutions, the total resistance (Figure 12), Warburg resistance and 1/C decreases with increasing its concentrations. As stated previously, this is due to the

deleterious effect of chloride ions [10]. For F^- ions, an oxidation reaction occurred in the formation of MgF_2 as follows:

$$Mg + 2H_2O \rightarrow Mg(OH)_2 + H_2 \uparrow \quad (2)$$

Since $Mg(OH)_2$ was not stable in acidic solution [25], reactions should occur as follows:

$$Mg(OH)_2 + 2HF \rightarrow MgF_2 + 2H_2O \quad (3)$$

$$Mg(OH)_2 \rightarrow MgO + H_2O \quad (4)$$

The overall reaction occurred as follows:

$$Mg + H_2O + 2F^- \rightarrow MgO + MgF_2 + H_2 \uparrow \quad (5)$$

The pores in the film should be generated by the hydrogen evolution. These pores might be decreased or filled by the precipitation of MgF_2 particles [25], thus the presence of fluoride ions decreases the corrosion of the tested alloy than the blank (0.01 M oxalic acid). However, depassivation process occurs by increasing fluoride concentration due to breakdown of the formed grained layer of MgF_2 that leads to drastic increase in the surface roughness. Furthermore, in presence of F^- ions, aluminum which becomes enriched in the surface can form the soluble complex $(AlF_6)^{3-}$, thereby, participates at higher F^- ions concentrations in decreasing the stability of the passive surface film on AZ31E alloy [14]. However, Cl^- ion is more strongly adsorbed on the alloy surface than F^- ions, so, its resistivity is lower than fluoride ion.

For phosphate anion as additive, increasing the total resistance (R_T) (Figure 12), W and $1/C_1$ with increasing of phosphate concentration indicates that interaction between oxalic acid and phosphate forms phosphate complexes that increase with increasing phosphate concentration and leads to passivation of AZ31E surface. Also, by measuring the pH of the medium, it increases slightly from acidic ~ 6.8 to basic medium reaching to 11.1 at 1.0 M phosphate concentration, leading to passivation. At pH 11.1, HPO_4^{2-} species has almost equal tendency for existing in solution as PO_4^{3-} anions and thus the solution at this pH will contain the two phosphate species with nearly equal relative fraction [2, 26-27]. Therein the electrolyte pH plays a determinant influence on film properties, where films formed in phosphate solutions at higher pH values are thicker of better protection for the alloy than those formed in acidic ones.

http://dx.doi.org/10.5772/58942

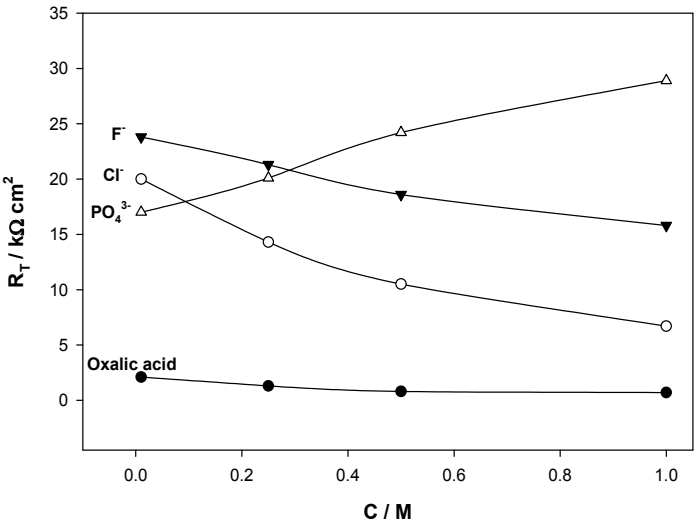

Figure 12. Variation of R_T of AZ31E electrode as a function of concentration for oxalic acid and Cl^-, F^-or PO_4^{3-} anions in naturally aerated 0.01 M oxalic acid solution, at 298 K.

Impedance results are in good agreement with polarization data.

5.2.3. AZ31E alloy in oxalic acid solution [12]

The Potentiodynamic polarization behavior of the AZ31E electrode was studied in relation to concentration of oxalic acid electrolyte. Figure 13 shows the scans for the tested electrode in 0.01 M oxalic acid solution with different concentrations (0.01-1.0 M) of PO_4^{3-} ion, at a scan rate of 1 mV/s over the potential range from-2.0 to 1.0 V vs. SCE. Prior to the potential sweep, the electrode was left for 2 hours until a steady state potential was reached.

On increasing the concentration of oxalic acid, an increase in the corrosion current density was observed (Figure 14). This may reflects the changing of the nature of the film formed on the surface (may represents the replacement of MgO by $Mg_2C_2O_4$).

The effect of added Cl^-or F^-or PO_4^{3-} ions on the electrochemical behavior of the tested AZ31E electrode in 0.01 M $H_2C_2O_4$ solution at 298 K is shown in Figure 15. It was found that i_{corr} value increases with increasing either Cl^-or F^-ion concentration reflecting the harmful effect of both ions leading to an increase in hydrogen evolution [28-29] and corrosion rate. For phosphate ion, i_{corr} value decreases with increasing its concentration that is the corrosion rate decreases. So, phosphate is useful in reducing the corrosion or hydrogen evolution rate [30-31]. These results coincide with that drawn from EIS data.

Generally, for comparing corrosion rate obtained from Tafel and EIS measurements, it is well known that the polarization resistance R_p is related to the corrosion rate through Tafel slopes β_a and β_c by Stern–Geary equation [32]:

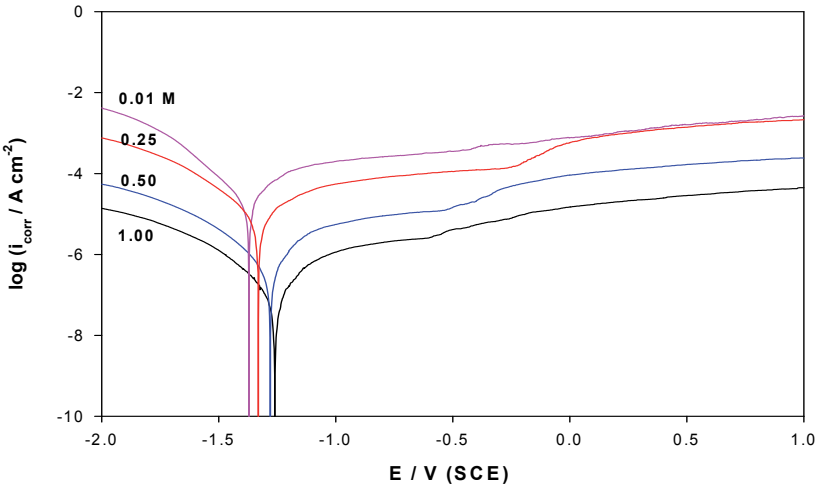

Figure 13. Potentiodynamic polarization scans of AZ31E electrode as a function of concentration for PO_4^{3-} anion in naturally aerated 0.01 M oxalic acid solution, at 298 K.

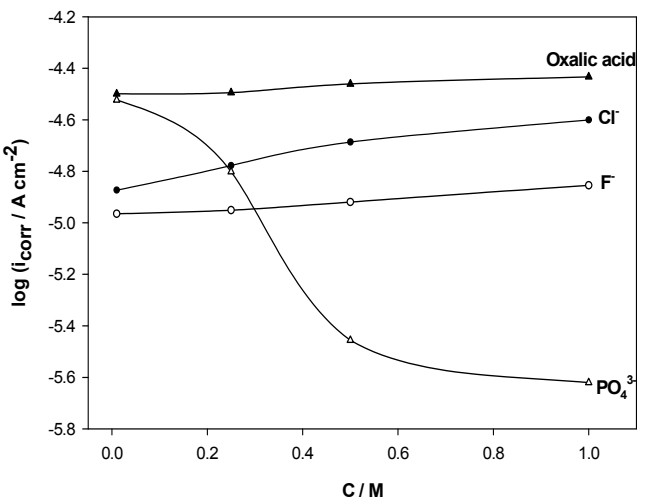

Figure 14. Variation of logarithm of corrosion current density (i_{corr}) for AZ31E electrode as a function of concentration for oxalic acid and Cl^-, F^-or PO_4^{3-} anions in naturally aerated 0.01 M oxalic acid solution, at 298 K.

$$i_{corr} = \frac{1}{2.303R_P\left(\frac{1}{\beta_a} + \frac{1}{|\beta_c|}\right)} \tag{6}$$

http://dx.doi.org/10.5772/58942

Anion	C	R_T	$i_{corr\ (EIS)}$	$P_{i\ (EIS)}$	$i_{corr\ (Tafel)}$	R_p	$P_{i\ (Tafel)}$
	M	KΩ cm²	μA cm⁻²	mm/y	μA cm⁻²	kΩ cm²	mm/y
Cl^-	blank	2.10	109.4	2.50	31.7	7.24	0.72
	0.01	20.0	14.28	0.33	13.4	21.3	0.31
	0.25	14.3	19.41	0.45	16.7	16.7	0.38
	0.50	10.5	26.16	0.59	20.6	13.4	0.47
	1.00	6.70	41.1	0.93	25.1	10.9	0.57
F^-	blank	2.10	109.43	2.50	31.7	7.24	0.72
	0.01	23.8	18.93	0.43	10.8	41.5	0.25
	0.25	21.3	21.44	0.49	11.2	40.8	0.26
	0.50	18.6	25.57	0.58	12.1	39.5	0.28
	1.00	15.8	27.07	0.62	14.0	30.6	0.32
PO_4^{3-}	blank	2.10	109.43	2.50	31.7	7.24	0.72
	0.01	17.0	41.98	0.96	30.0	23.8	0.69
	0.25	20.1	32.36	0.74	15.8	41.2	0.36
	0.50	24.2	8.391	0.19	3.50	58.1	0.08
	1.00	28.9	5.883	0.13	2.41	70.8	0.06

Table 6. Corrosion rate (P_i) calculated from EIS and Tafel methods of AZ31E electrode as a function of concentration for Cl^-, $F^-$and PO_4^{3-} anions in naturally aerated 0.01 M oxalic acid, at 298 K.

As given in Table 6, it can be seen that evaluated R_p values obtained from Tafel measurements have the same trend as R_T obtained from EIS measurements. By calculating i_{corr} from EIS measurements using cathodic, anodic slopes and R_T, it was found that they also have the same trend as that obtained from Tafel measurements. By calculation of corrosion rate, where i_{corr} (mA cm^{-2}) is related to the average corrosion rate in mm/y (P_i) using [4]:

$$P_i = 22.85 i_{corr} \tag{7}$$

It was found that corrosion rate obtained from EIS method is comparable with that obtained from Tafel extrapolation method. Thus there is a good agreement between corrosion rates determined by both techniques.

6. Conclusions

The corrosion rate of magnesium alloy in aqueous ethylene glycol depends on the concentration of the solution. A diluted ethylene glycol solution is more corrosive than a concentrated

one at room temperature. Ethylene glycol solution containing Cl^- > 0.05 M or F^- < 0.05 M are more corrosive than the blank (30% ethylene glycol-70% water). However, at concentrations < 0.05 for chloride or > 0.05 M flouride ions, some inhibition effect has been observed. The corrosion of AZ91D alloy in the blank can be effectively inhibited by addition of 0.05 mM paracetamol that reacts with AZ91D alloy and forms a protective film on the surface at this concentration.

The corrosion rate of AZ31E magnesium alloy in oxalic acid solution depends on the concentration of the solution and the additive. A concentrated oxalic acid solution with lowest pH and highest hydrogen evolution is the more corrosive one. Oxalic acid solution of 0.01 M concentration containing Cl^- or F^- are more corrosive with increasing the concentration from 0.01 to 1.0 M for the anions as observed from impedance or polarization techniques. For PO_4^{3-} anion in 0.01 M oxalic acid solution, it acts passivator. The corrosion rate decreases with increasing its concentration.

Author details

Amany Mohamed Fekry

Cairo University (Faculty of Science, Chemistry Department), Egypt

References

[1] Fekry A., Electrochemical Corrosion Behavior of Magnesium Alloys in Biological Solutions, In Czerwinski F. (Ed.), Magnesium Alloys-Corrosion and Surface Treatments. Rijeka: InTech; 2011. p 65-92.

[2] Heakal F, Fekry A, Fatayerji M. Electrochemical behavior of AZ91D magnesium alloy in phosphate medium-Part I. Effect of pH. J. Applied Electrochemistry 2009;39(5) 583-591.

[3] Zhang T, Liu X, Shao Y, Meng G, Wang F. Electrochemical noise analysis on the pit corrosion susceptibility of Mg–10Gd–2Y–0.5Zr, AZ91D alloy and pure magnesium using stochastic model. Corrosion Science 2008; 50(12) 3500-3507.

[4] Song G, Bowles A, StJohn D. Corrosion resistance of aged die cast magnesium alloy AZ91D. Materials Science and Engineering 2004;A366(1) 74-86.

[5] Song G, Atrens A, Dargusch M. Influence of microstructure on the corrosion of diecast AZ91D. Corrosion Science 1998;41(2) 249-273.

[6] Fekry A, Fatayerji M. Electrochemical Corrosion Behavior of AZ91D Alloy in Ethylene Glycol. Electrochimica Acta 2009;54(26) 6522-6528.

[7] Song G, StJohn D, Corrosion behaviour of magnesium in ethylene glycol Original Research ArticleCorrosion Science 2004 46(6) 1381-1399.

[8] Song G. Corrosion and its inhibition of engine block magnesium alloys in coolants, CAST Report 2001081, 2001 (confidential).

[9] PCT/IB99/01659, 1999.

[10] Fekry A. The influence of chloride and sulphate ions on the corrosion behavior of Ti and Ti-6Al-4V alloy in oxalic acid. Electrochimica Acta 2009;54(12) 3480-3489.

[11] Maruthamuthu P, Ashokkumar M. Hydrogen generation using Cu(II)/WO_3 and oxalic acid by visible light. International Journal of Hydrogen Energy 1988;13(11) 677-680.

[12] Fekry A. Impedance and hydrogen evolution studies on magnesium alloy in oxalic acid solution containing different anions. International journal of Hydrogen Energy 2010; 35(23) 12945-12951.

[13] Beccaria A, Bertolotto C. Inhibitory action of 3-trimethoxysilylpropanethiol-1 on copper corrosion in NaCl solutions. Electrochimica Acta 1997; 42(9) 1361-1371.

[14] Heakal F, Fekry A, Fatayerji M. Influence of halides on the dissolution and passivation behavior of AZ91D magnesium alloy in aqueous solutions. Electrochimica Acta 2009;54(5) 1545-1557.

[15] Macdonald J, In Macdonald J. (Ed.), Emphasizing Solid Materials and Systems. John Wiley & Sons, 1987.

[16] Macdonald D. Reflections on the history of electrochemical impedance spectroscopy. Electrochimica Acta 2006 51(8-9) 1376-1388.

[17] Retter U, Widmann A, Siegler K, Kahlert H. On the impedance of potassium nickel(II) hexacyanoferrate(II) composite electrodes—the generalization of the Randles model referring to inhomogeneous electrode materials. Journal of Electroanalytical Chemistry 2003;546, 87-96.

[18] Heakal F, Fekry A. Experimental and Theoretical Study of Uracil and Adenine Inhibitors in Sn-Ag Alloy/Nitric Acid Corroding System. Journal of Electrochemical Society 2008;155(11) C534-542.

[19] Song G, Atrens A, Wu X, Zhang B. Corrosion behaviour of AZ21, AZ501 and AZ91 in sodium chloride. Corrosion Science 1998;40(10) 1769-1791.

[20] Gulbrandsen E, Tafto J, Olsen A. The passive behaviour of Mg in alkaline fluoride solutions. Electrochemical and electron microscopical investigations. Corrosion Science 1993;34(9) 1423-1440.

[21] Chao C, Lin L, Macdonald D. Point defect model for anodic passive films, Journal of Electrochemical Society 1981;128(6) 1181-1187.

[22] Liu Y, Wang Q, Song Y, Zhang D, Yu S, Zhu X. A study on the corrosion behavior of Ce-modified cast AZ91 magnesium alloy in the presence of sulfate-reducing bacteria. Journal of Alloys and Compounds 2009;473(1-2) 550-556.

[23] Jain AK, Acharya NK, Kulshreshtha V, Awasthi K, Singh M, Vijay YK. Study of hydrogen transport through porous aluminum and composite membranes. International Journal of Hydrogen Energy 2008;33(1) 346-349.

[24] Fekry A, El-Sherief R. Electrochemical corrosion behavior of Magnesium and Titanium alloys in simulated body fluid. Electrochimica Acta 2009;54(28) 7280-7285.

[25] Ma L, Wang P, Cheng H. Hydrogen sorption kinetics of MgH_2 catalyzed with titanium compounds. International Journal of Hydrogen Energy 2010;35(7) 3046-3050.

[26] Heakal F, Fekry A, Fatayerji M. Electrochemical behavior of AZ91D magnesium alloy in phosphate medium–Part II. Induced passivation. Journal of Applied Electrochemistry 2009;39(9)1633-1642..

[27] Muñoz L, Bergel A, Féron D, Basséguy R. Hydrogen production by electrolysis of a phosphate solution on a stainless steel cathode. International Journal of Hydrogen Energy 2010;35(16) 8561-8568.

[28] Uan JY, Cho CY, Liu KT. Generation of hydrogen from magnesium alloy scraps catalyzed by platinum-coated titanium net in NaCl aqueous solution. International Journal of Hydrogen Energy 2007;32(13) 2337-2343.

[29] Ameer M, Fekry A. Inhibition effect of newly synthesized heterocyclic organic molecules on corrosion of steel in alkaline medium containing chloride. International Journal of Hydrogen Energy 2010;35(20) 11387-11396.

[30] Fekry A, Ameer M. Corrosion inhibition of mild steel in acidic media using newly synthesized heterocyclic organic molecules. International Journal of Hydrogen Energy 2010;35(14) 7641-7651.

[31] Azizi O, Jafarian M, Gobal F, Heli H, Mahjani MG. The investigation of the kinetics and mechanism of hydrogen evolution reaction on tin. International Journal of Hydrogen Energy 2007;32(12)1755-1761.

[32] Boudjemaa A, Boumaza S, Trari M, Bouarab R, Bouguelia A. Physical and photoelectrochemical characterizations of α-Fe_2O_3. Application for hydrogen production. International Journal of Hydrogen Energy 2009;34(10) 4268-4274.

Chapter 5

Corrosion of Materials in Liquid Magnesium Alloys and Its Prevention

Frank Czerwinski

Additional information is available at the end of the chapter

http://dx.doi.org/10.5772/59181

1. Introduction

Magnesium alloys with their unique physical and chemical properties are important candidates for many modern engineering applications. Their density, being the lowest of all structural metals, makes them the primary choice in global attempts aimed at reducing the weight of transportation vehicles. However, magnesium also creates challenges at certain stages of raw alloy melting, fabrication of net-shape components and their service. The first one is caused byvery high affinity of magnesium to oxygen, which requires protective atmospheres increasing manufacturing cost and heavily contributing to greenhouse gas emissions [1] [2] [3]. While magnesium exhibits high affinity to oxygen, at temperatures corresponding to semisolid or liquid states it is also highly corrosive towards materials it contacts [4] [5] [6]. This imposes challenges to the selection of materials used to contain, transfer or process molten magnesium during manufacturing operations.

Understanding the reactivity of liquid magnesium with engineering materials to eliminate or at least reduce the progress of corrosion is paramount not only during fabrication processes but also in other unique applications. They include joining of dissimilar materials where magnesium is one part of the joint couple and involves similar liquid/solid interface phenomena [7] [8]. Another example is the liquid battery cell, having two liquid metal electrodes, e.g. magnesium and antimony, separated by a molten salt electrolyte, that self-segregate into three layers based upon density and immiscibility. Such an assembly faces also corrosion issues [9]. During joining by exploring so-called compound casting [10], where two Mg alloys, one in the solid state and another one in the liquid state, are brought together, an interface formation by solid-liquid reaction is the essence of the phenomena leading to a metallurgical bond. Thus, at present, there are still challenges to be addressed to understand the mechanism of corrosion

attack, compatibility of materials in respect to liquid magnesium and designing protection methods.

The aim of this chapter is to review fundamental aspects of corrosion in liquid magnesium alloys, assess degradation of selected metallic and ceramic materials in this environment and define methods of corrosion prevention.

2. Liquid metal corrosion

Liquid metal corrosion is understood as a physical or physico-chemical process that follows the formation pattern of metallic alloys. In contrast to corrosion of metals in aqueous solutions, no transfer of electrons is involved. The essential part of the process is dissolution accompanied by formation of a liquid alloy with mixed composition and chemical reactions resulting in creation of intermetallic compounds. Liquid metals are a group of coolants with increasing importance for high-temperature processes and power engineering. Due to great heat-transfer properties, liquid metals are used in the nuclear industry as heat transfer media [11]. Therefore, the majority of operating experience with liquid metal systems has been accumulated within the nuclear industry. The favorable thermo-physical properties of liquid metals allow for high rates of heat removal in comparison to other coolants, e.g., water/steam. Although nuclear reactor engineering with light liquid metal/alloy sodium and sodium-potassium and heavy liquid metal/alloy liquid lead and lead bismuth differ substantially from a liquid magnesium environment, general aspects of corrosion are similar. Common issues show also other applications such as liquid metal spallation targets in elementary particle sources, galvanizing of steel by hot dipping in a molten metal bath of Zn [12], as well as glass production or electronics cooling. Using liquid metals may enable alternative technologies like direct thermal-electric conversion or use of solarhigh temperature heat in chemical processes [13].

2.1. Factors affecting progress of corrosion

Three major steps that control the corrosion progress include (i) transport in solid state; (ii) reactions at the solid/liquid interface dominated by dissolution of the solid alloy and its transport into liquid magnesium and (iii) transport of species within the liquid state (Fig. 1). In a hypothetical static system, corrosion would continue until reaching the solubility limit. In the case of an engineering environment, alloying elements and impurities react with atmosphere forming oxides and nitrides that make the process more complex. In particular, the temperature gradient and the concentration gradient make the system dynamic, leading to mass transfer.

According to early research [14], the corrosive attacks are classified as: (i) simple dissolution, (ii) alloying between liquid metal and solid metal, (iii) intergranular penetration, (iv) impurity reactions, (v) temperature gradient mass transfer, (vi) concentration-gradient mass transfer or dissimilar-metal mass transfer. As variables controlling liquid metal corrosion, such factors as temperature, its gradient or cyclic fluctuation, surface area to volume ratio, metal purity, flow velocity and some characteristics of material being in contact with liquid metal, are named.

http://dx.doi.org/10.5772/59181

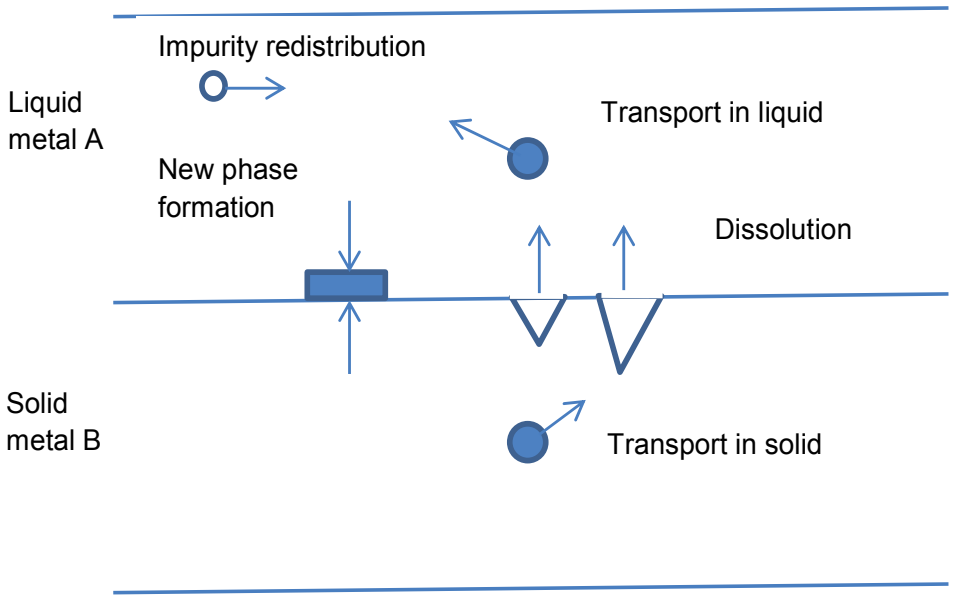

Figure 1. Schematics emphasizing phenomena involved during corrosion in liquid metals.

For certain liquid metals, the progress of corrosion may be reduced by adding to the liquid alloy either metallic or non-metallic corrosion inhibitors. It is believed that inhibitors decrease the corrosion rate by forming a protective film, separating the metallic surface from corrosive media. For example, metallic inhibitors added to liquid Pb and Pb-Bi caused the formation on a steel surface of a protective layer of nitrides or carbides by the chemical reaction between inhibitors and carbon and nitrogen in steel [11]. In particular, for carbon steels and low-alloy steels, additions of Zr and Ti were confirmed to be effective. At the same time, the effectiveness of Zr and Ti for stainless steel, being in contact with liquid Pb and Pb-Bi alloys, was very low.

An essential factor in corrosion progress is the corrosion front morphology. The ideally uniform corrosion front is possible in theory when the diffusion rate in the solid is fast enough to balance the mass transfer rate in the liquid. In practice, due to the fact that diffusion in solid is the slowest step, there is a development of the front morphology. In single-phase materials, the grain orientation, grain boundaries and impurities will contribute to different rates of corrosion progress over the surface. In multi-phase materials, phase chemistry and their crystallography impose additional complexity. A particular case is the preferred penetration of liquid metal along grain boundaries of the adjacent solid material, causing its embrittlement.

2.2. Models of liquid metal corrosion

At early stages of corrosion, the dissolution reaction is considered to be the fastest step, with mass transport in the liquid seen as the controlling step of the entire process. In contrast, at the steady state, either dissolution at the solid/liquid interface or mass transport in the bulk liquid is in control of the corrosion progress. It was revealed during experiments between austenitic

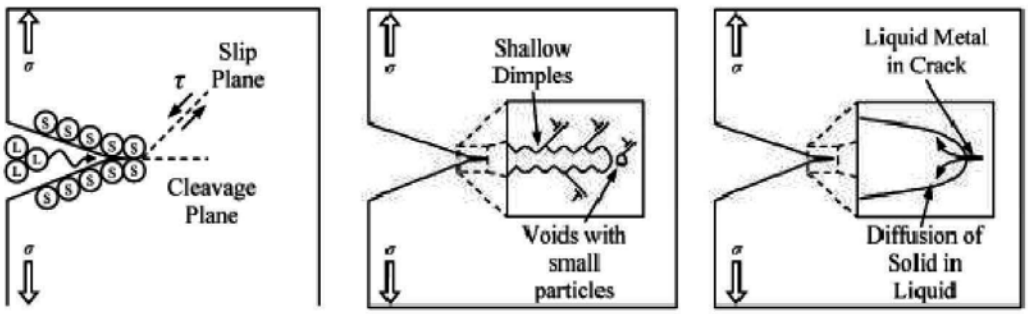

Figure 2. Existing failure mechanisms of corrosion in liquid metals: (a) decohesion model; (b) adsorption induced dislocation emission model; (c) dissolution condensation mechanism model [19].

stainless steel AISI 316L and liquid Ga, along with its alloys (Ga-14Sn-6Zn, Ga-8Sn-6Zn), the corrosion progress gravimetrically measured by metal losses, was significantly lower in Ga alloys than in pure Ga [15]. As an explanation, the lower diffusivity of species in pure liquid Ga than in Ga alloys was proposed.

For a nuclear reactor coolant system, a number of models were developed allowing the calculation of the corrosion rate and corrosion layer thickness [16]. They explore a mathematical analysis of the transport of various species in the solid phase, in flowing liquid phase and mass exchange at the interface between solid and liquid. The negative side of modelling so far is an exclusion of the pitting corrosion, stress corrosion cracking and liquid metal embrittlement due to a lack of theoretical and experimental data.

2.3. Liquid metal embrittlement

While being in contact with liquid metal under stress, certain metals experience a drastic reduction in ductility [17] [18]. It should be pointed out that the loss of ductility takes place in normally ductile metals. Often the phenomenon is seen as the crack propagation associated with a change of the fracture surface from ductile into brittle of an intergranular type. According to the conventional mechanism, the lower melting point liquid metal fills a crack in the solid metal, thereby weakening material at the crack tip and allowing it to propagate at much lower stress. Moreover, the traditional models considered the grain boundary segregation associated with formation of the interfacial phase. Existing failure mechanisms, including the decohesion model, adsorption induced dislocation emission model and dissolution condensation mechanism model are shown schematically in Fig. 2 [19]. There are many combinations of the matrix and embrittling solute [20], including steel embrittlement by liquid Cu, aluminum by Hg, or stainless steel by liquid Zn. The literature does not report that liquid magnesium is the embrittling solute but some alloying elements of magnesium alloys, e.g. Zn, are known as causing embrittlement.

There are also practical observations, which point out that: (i) liquid metal must be present and (ii) the area affected must be under stress [21]. According to Ref. [22] , the embrittlement will occur even when the liquid metal is removed from the solid metal surface before stressing.

http://dx.doi.org/10.5772/59181

As factors controlling the material susceptibility to liquid metal embrittlement, the low mutual solubility between the liquid and solid metals and an absence of intermetallic compound formation between the solid-liquid couple are frequently quoted. As revealed by a number of advanced analytical techniques of surface investigation, the micro-mechanism of liquid metal corrosion is more complex. For example, in the case of nickel infused with bismuth atoms a bilayer interfacial phase was detected by aberration-corrected scanning transmission electron microscopy [23]. This observation showed that adsorption can induce a coupled grain boundary structural and chemical phase transition leading to embrittlement. Experiments with several reactive couples including liquid Ga into Al, Hg into Ag and Ag into Cu showed that the size of the brittle fracture surface area is proportional to logarithm of the exposure time. There is also evidence [22] of the existence of an incubation period, being inversely proportional to the penetration speed of the liquid metal into solid metal. During a study of the 9%Cr martensitic steel in stagnant liquid environments of Pb, Pb-Bi or Sn the steel embrittlement can be explained by a reduction of the surface energy of the bare metal induced by some adsorption of the liquid metal [24]. This fact allowed understanding some experimental observations including (i) instantaneous effect of embrittlement with no requirements of solid-state diffusion; (ii) reduction of embrittlement with increasing temperature; increased propagation of surface crack into bulk alloy caused by cyclic loading.

2.4. Ceramic materials in contact with liquid metals

In contrast to metallic materials, ceramics show generally higher resistance to corrosive attack at high temperatures [25]. Due to degradation of mechanical properties of metallic materials, at a certain temperature range, ceramics represent the only choice for many advanced engineering designs. This applies also to an environment of liquid metals.

In the case of ceramics being in contact with molten metals, the destructive process involves a reduction-based removal of non-metallic elements from the solid, undermining their structural integrity [26] [27]. It is also claimed that ceramics when in contact with liquid low-melting metals experience the strength reduction. According to experiments with A-995 alumina exposed to liquid Sb, Pb, Ca, Bi and 50Bi-30Pb-20Sn*alloy (* all alloy compositions are in weight % unless indicated otherwise), a considerable reduction in strength by alumina was experienced [28]. In all cases, alumina ceramic was wetted by liquid metal, which adhered to their surface after solidification.

3. Corrosive nature of liquid magnesium and its alloys

In engineering practice, to generate the sufficient strength and other mechanical properties, magnesium is alloyed with other metals such as Al, Zn, Mn, Si, Cd, Ag, Zr, Ca, Sr, Be or rare earths. Moreover, magnesium alloys contain difficult to remove impurities, mainly Fe, Ni or Cu. Both the alloying elements and impurities change the corrosivity of liquid Mg in regards to materials they contact.

3.1. Corrosivity of pure magnesium

A selection of materials to sustain liquid magnesium, in terms of resistance to its corrosive attack and mechanical properties degradation due to high temperatures is a key task for engineering applications. It is generally known that iron is inert to molten magnesium. According to the Mg-Fe equilibrium phase diagram, below 1000 °C, Mg does not dissolve in Fe. In a Mg-Fe system, some solubility of Mg is possible only at high pressures and high temperatures. As reported in Ref. [29], the maximum solid solubility of Mg in Ni is 0.00043 at. % and the eutectic composition is at 0.008 at. % Fe.

In contrast to Fe, liquid magnesium reacts with nickel. According to Ref. [30], the solid solubility of Mg in Ni is less than 0.2. at. % Mg at 500 °C. In a Mg-Ni system there is one peritectic and two eutectic reactions [31]. There are two intermetallic compounds with Mg_2Ni melting at 760 °C and $MgNi_2$ melting at 1147 °C [32]. As pointed out in [33], the $MgNi_2$ phase extends from 66.2 to 67.3 at. % Ni.

During analysis of the liquid Mg-solid Ni reaction couple it was noticed that the compounds which are at the Mg/Ni interface, rich in the lower melting point elements, are the first phases formed in metal/metal binary reactions, i. e., Mg_2Ni [34]. It is quite surprising to find that the minority elements, such as Cu or Ni impurities, are the dominant diffusing species. This fact differs from results obtained in many metal/metal systems where the major diffusion species are usually the majority elements in the initially formed compounds. During an experiment with a diffusion couple of 99.999% purity liquid Mg at a temperature of 660 – 680 °C and solid Ni plate the intermetallic phase of Mg_2Ni grew at the interface and the Ni layer dissolved by diffusion throughout the intermetallic phase into liquid Mg [35]. Although according to the equilibrium phase diagram both phases Mg_2Ni and $MgNi_2$ could form, only the former one was detected.

3.2. Effect of major alloying elements

The number of elements that can be added during alloying is rather low due to their limited solubility in magnesium and a competition from phases formed between additions themselves. Of all alloying elements, aluminum is the most often used and its content, reaching up to 11%, is the largest of all metals explored for that purpose. Under equilibrium conditions the solubility of Al in α-Mg is 12.7% at 437 °C but in as-cast alloys a solid solution below 437 °C is enriched only with 2 – 3% of Al [36]. In general, Al is not distributed uniformly and in addition to macro-segregation, also micro-segregation occurs and is related to formation of precipitates and grain boundary enrichment.

The role of aluminum in liquid metal corrosion is substantial due to its large concentration in many Mg alloys and extremely high corrosivity [37]. An example showing Al reactivity when Mg-10%Al alloys contacts carbon steel is shown in Fig. 3. Molten aluminum dissolves practically all conventional alloys including, Fe, Ni, Cr and Co based grades. Although some alloys, such as Ni-Cr-Fe are used with molten Al, their lifespan is rather short. There is some potential ofTi alloys where protection against molten Al is believed to be provided by Ti oxides forming on Ti surface, thus separating both metals. The literature emphasizes also a strong influence

http://dx.doi.org/10.5772/59181

of small amounts of Al present in Mg alloys. For example, less than 0.002 wt. % of Al or Si in liquid Mg at 723 °C reacts with Fe from steel creating α-Fe (Al, Si) solid solution [38]. By combining carbon from steel, impurities present in Mg form a compound of Fe_2 (Al,Mg)C. It has been concluded that the above phases were formed not only by solid-state diffusion in steel but also by dissolution-precipitation processes and migration of Fe in liquid magnesium. During a contact of molten magnesium alloys with H13 steel Al content was found to be the controlling factor in the type of phases formed [39]. For Al contents below 6%, FeAl/ (Fe, Mn)Al was the major phase formed with traces of $FeAl_2$ and Fe_2Al_5. For higher Al contents, the Fe_2Al_5 phase dominated and for Al exceeding 12%, the $Fe_{14}Al_{86}$ was the dominant one.

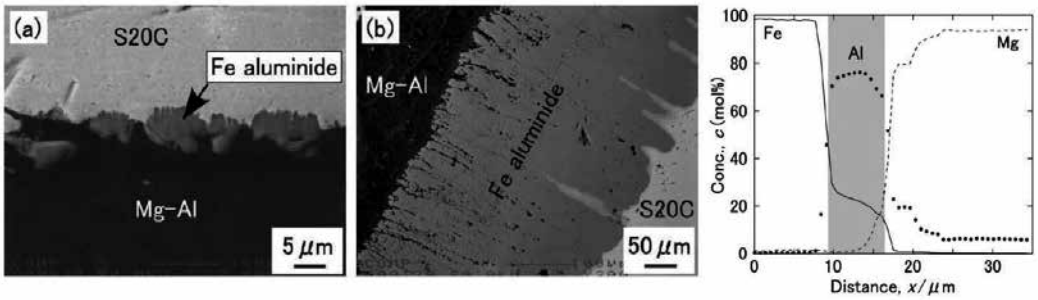

Figure 3. Microstructure of the interface between Mg-10% Al alloy and S20C carbon steel after short term (a) and long term (b) exposures. The concentration profile across interface (a) is shown in (c) [82]

A common ingredient of magnesium alloys is also zinc with a maximum solubility of 8.4%. Additions of zinc are used often in a combination with aluminum to improve the alloy strength at room temperatures or with zirconium and rare earths to generate precipitates that are stable at increased temperatures. From the shape of the αMg-β boundary at the equilibrium phase diagram of Mg-Al-Zn [40], it is seen that the addition of Zn allows more β precipitates to form at a fixed Al content of 8%. The β compound has a part of Al atoms substituted by Zn. Since for Mg-9Al-1Zn alloy at temperatures below 437°C it has the form of Mg_{17} $(Al,Zn)_{12}$, likely $Mg_{17}Al_{11.5}Zn_{0.5}$, the Zn content is expected to be higher [41].

Zinc, which melts at 419°C is a commonly used low melting metal with vast data and broad application experience. Both molten zinc and its alloys are used for hot-dip galvanizing of steel. There is solid evidence that they may cause liquid metal embrittlement of steel at temperatures as low as 400 °C. For example, liquid metal embrittlement can be induced into austenitic stainless steels by molten Zn during its welding with galvanized carbon steel [42]. It is known that refractory metals like Mo, W and their alloys withstand the corrosive attack by molten Zn up to 500 °C. During an experiment with testing Mo, Mo-30%W, W, DIN 1.4841 steel and graphite in a molten Zn environment at 500, 600, 650 and 700 °C for 168 h, differences in corrosion behavior were recorded [43]. While steel was dissolved, Mo was only partly attacked at 500 and 650 °C. At the same time, Mo-30%W, pure W and graphite showed satisfactory corrosion resistance.

3.3. Effect of minor elements and impurities

As emphasized already in section 3.2, the chemical compatibility of molten magnesium towards other materials may be altered by the presence of small amounts of other elements. They are not only limited to difficult-to-remove impurities but also to elements deliberately added in small quantities. Many magnesium alloys contain manganese; its major role is designed to bind harmful impurities of iron and heavy metals into harmless intermetallic compounds. In general, Mn has very limited solid solubility, reaching 2.2%, which in the presence of aluminum is further reduced to about 0.3% due to formation of MnAl, $MnAl_6$ and $MnAl_4$ compounds. Its maximum content in commercial magnesium alloys does not exceed 1.5 – 2 %. Based on free energy of oxide formations, Mn looks to be much less reactive than Mg or Al. According to observations in Ref. [44], in liquid Al alloys, a presence of Mn increased oxide layer thickness. Although oxide layer thickness increased with Mn content in Al alloy, oxide contained very small amounts of Mn. It was noticed during industrial practice that e.g. soldering is more likely to occur when die casting magnesium alloys such as AM60 with higher manganese content are used [39]. The die casting trials were also carried out to confirm the soldering development in high pressure die casting conditions [45]. The results showed that the formation of intermetallics started with the nucleation of the η-Fe_2Al_5phase. During the next stage, manganese substituted some of iron and this phase became $(Fe,Mn)_2Al_5$. Finally, a metastable phase $Mn_{23}Al_{77}$was formed at the outer layer of the surface exposed to liquid magnesium alloy.

During reaction of solid mild steel and liquid Mg-Mn alloys at 727 °C the chemical interaction was found to depend on the Mn content [46]. In all cases, the interface reactions led to formation of phases from the Fe-Mn phase diagram with the mechanism being dominated by solid state volume diffusion of Fe and Mn. The intergranular melt infiltration was added as the secondary phenomena. As shown in Fig. 4, for 0.6 – 0.7 at. %Mn, two sublayers were formed with chemistry of αFe (Mn) and γFe (Mn) [46]. For higher content of 1.3 at. %Mn, corresponding to the Mn saturated solution, the layer contained βMn (Fe).

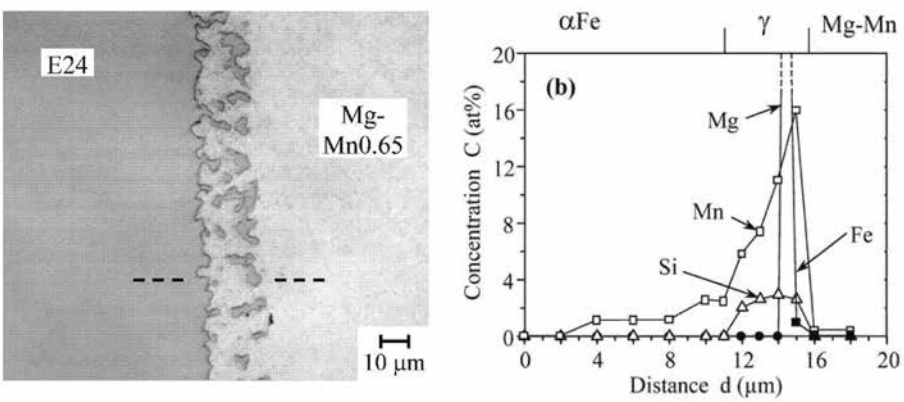

Figure 4. Interface between E24 mild steel and Mg-0.65 at% Mn liquid alloy after 65 h exposure at 727 °C (a) along with concentration profile across the interface (b) [46].

http://dx.doi.org/10.5772/59181

The reactivity of liquid Mg-Si alloys containing up to 3.1 at. % Si with mild steel at temperature between 677 and 727 °C led to formation of a continuous layer at the solid/liquid interface [47]. For very low Si content of 0.025 at. % the layer consisted of αFe solid solution with less than 2 at. % Si. For higher Si contents from 0.045 at. % to 3.1 at. % the reaction layer consisted of α_1Fe_3Si ordered phase with Si content from 24.5 to 27 at. %. The reaction phase was formed by the solid-phase volume diffusion. Morphology of the solid/liquid interface and accompanying concentration profiles are shown in Fig. 5.

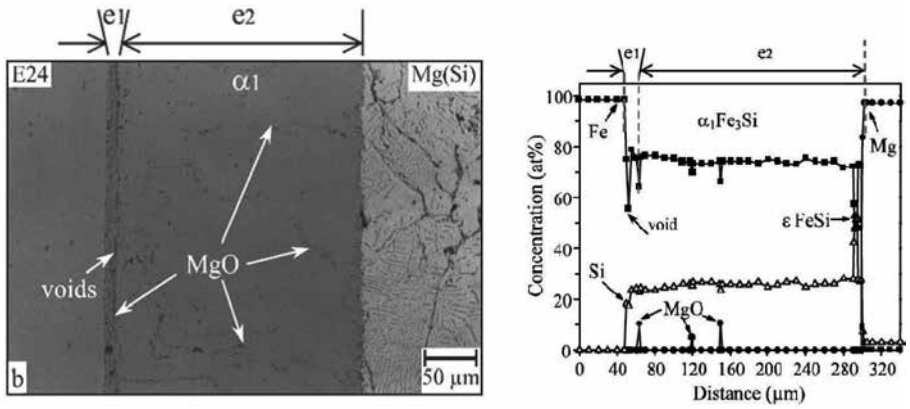

Figure 5. Interface between E24 mild steel and liquid Mg-3 at% Si after 250 min at 727 °C (a) and concentration profile showing location of Si in the reaction zone (b) [47].

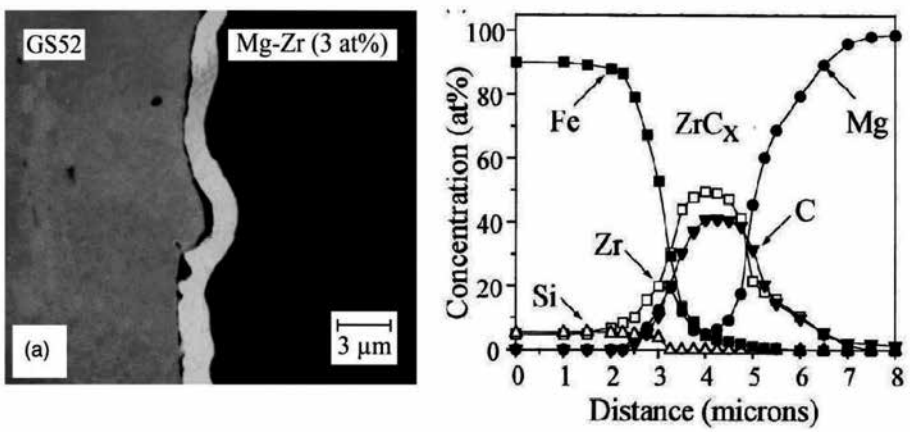

Figure 6. Interface between cast iron and Mg-3 at% Zr alloy after exposure of 65 h at 727 °C (a) and concentration profile showing Zr location in the reaction zone (b) [48].

The role of transition alloying elements in Mg alloys on their corrosivity in liquid state was also studied. It includes, for example the reaction between liquid Mg-Zr alloy at 727 °C and pure Fe, steel and cast iron [48]. Although iron is chemically compatible with liquid magnesium, it reacted with Mg-Zr alloys (Fig. 6). The primary reaction took place between Zr in liquid Mg-Zr alloys and iron, forming in the liquid the Fe-Zr compounds, mainly Fe_2Zr. The reaction mechanism is based on dissolution of the solid steel and crystallization within the Mg-Zr liquid alloy, enriched by the solute. The secondary reaction is between Zr and C from the steel substrate to form ZrC_x as a surface layer inhibiting corrosion progress.

4. Complex nature of material degradation by liquid magnesium in engineering applications

The materials in contact with liquid magnesium during manufacturing operations are subjected to multiple deteriorating effects which accompany the corrosive attack by molten metal. In addition to the corrosive attack of a purely chemical nature, there is an influence of accompanying heat and stress. Depending on processing details, the relative proportion of individual deteriorating factors and their contribution to overall damage experienced by materials are different.

4.1. Simultaneous effect of stress and corrosion

The components of magnesium processing equipment in direct contact with liquid metal are a subject of very demanding requirements in terms of materials used. In some cases, tight tolerances may not allow for substantial size change due to wear or corrosion during service. Similarly, high strength requirements may not allow for a reduction in mechanical properties over service time. The most common mechanisms of material degradation in liquid magnesium include [1]: (i) high temperature fatigue; (ii) thermal fatigue; (iii) corrosion fatigue, (iv) creep and stress rupture and/or (v) oxidation. The relative contribution of each mechanism depends on the specific application. An example of a combination of liquid metal, corrosion and fatigue (corrosion fatigue) is shown in Fig. 7. Under a cyclic load caused by melt pressure, corrosion sites act as stress risers, causing progressive crack propagation and premature failure.

4.2. Stress due to difference in thermal expansion

At relatively high service temperature, materials experience large dimensional changes due to thermal expansion. As may be deduced from Table 1, for components with a length of 2 m and service temperatures over 620 °C, an elongation may reach several millimeters. Such a difference should be considered during material selection. The key challenge occurs when two or more different materials are in direct contact at high temperatures. For example, when tool steel components are connected with each other by using Ni based alloy Inconel. As seen in Table 1, the coefficient of thermal expansion of the bolts is larger than that for the steel. To maintain a bolt preload, it is necessary to re-torque the bolts once the component reaches the

http://dx.doi.org/10.5772/59181

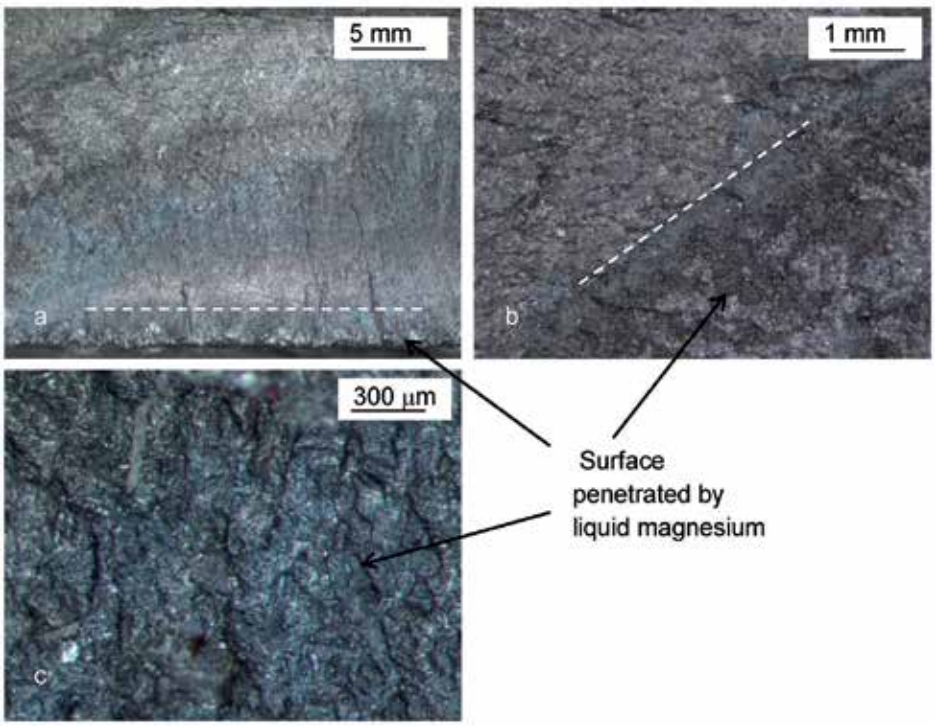

Figure 7. Fracture surface of tool steel after service in an environment of liquid magnesium alloy.

service temperature. Conversely, when the assembly is subsequently cooled to ambient temperature, bolts will shrink more than the steel component. Hence, without loosening of fasteners, this will cause large tensile stress to develop and fastener stretching that may eventually lead to premature failure. Similarly, materials of a die of a high pressure die casting machine or molten alloy distribution systems should exhibit similar thermal expansion or differences should be incorporated into design.

Alloy	100	200	300	400	500	600	700	900	1000 [°C]
AISI H13	11. 9	12. 4	12. 3	12. 7	13. 0	13. 3	13. 5		
DIN 1. 2888	9. 9	10. 4	10. 9	11. 3	11. 6	11. 8	11. 9		
Inconel 718	12. 8	13. 6	13. 9	14. 4	14. 8	15. 1			
Stellite 6	11. 3	12. 9	13. 6	13. 9	14. 2	14. 5	14. 7	15. 5	17. 5
Stellite 12	11. 5	12. 1	12. 6	12. 9	13. 3	13. 8	14. 3	15. 2	15. 6
Stellite 21	11. 0	11. 2	12. 0	12. 6	13. 1	13. 6	14. 3	15. 21	

Table 1. Example showing differences in coefficients of thermal expansion for selected alloys applicable in processing liquid magnesium (10^{-6} m/ (m K). Temperature range from 20 °C to the value indicated [86] [87]

4.3. Stress due to low thermal conductivity

Heat that is required for high temperature processing is not applied directly to magnesium. Instead, it is provided entirely from an external source and transferred through walls of a furnace crucible or the sleeve of a transfer pump. To achieve the fast rate of heat transfer, thermal conductivity of material used is of key importance. If a material has low thermal conductivity it not only requires a longer time to melt magnesium but creates a steep temperature gradient across the component wall thereby generating thermal stress. For thick walls the stress build-up may lead to thermal shock failure. It is seen in Table 2, that Ni-base and Co-base alloys with high strength at temperatures of liquid magnesium processing have rather low thermal conductivities. A particular case has a place when a material is in intermittent contact with liquid magnesium as with a nozzle, die/mold or elements of the melt transfer system. If a surface is subjected to frequent heating/cooling cycles, e.g. every 1-2 min, surface fatigue leads to crack formation. A top view of a steel surface damaged by intermittent contact with liquid magnesium is shown in Fig. 8. Surface microcracks, formed as a result of thermal fatigue, are cyclically filled with liquid alloy.

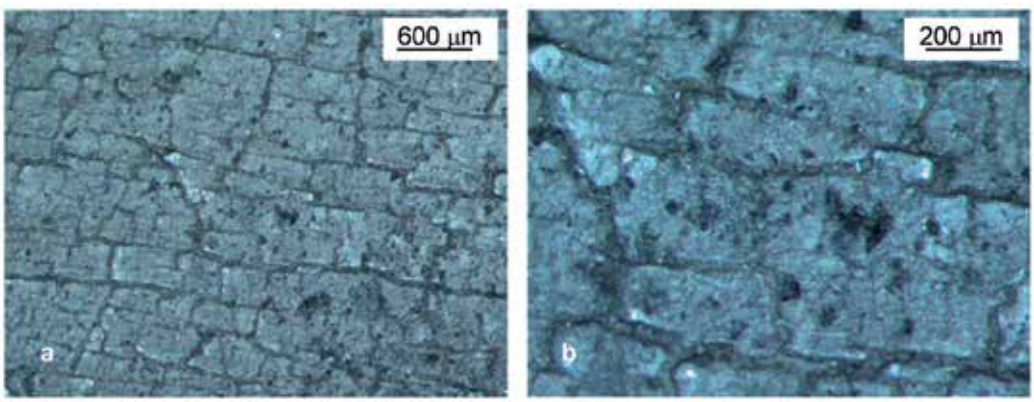

Figure 8. Top view showing surface of tool steel after intermittent exposures to liquid magnesium alloys.

Alloy	20	200	300	400	500	600	700	800	1000 [°C]
AISI H13	25. 5	27. 1		27. 7					
DIN 1. 2888	20. 5	24. 2		27. 5					
Inconel 718	11. 1	14. 1	16. 0	17. 7	18. 8	19. 9	22. 1	23. 7	
Stellite 6	14. 82								
Stellite 12	14. 6								
Stellite 21	14. 5								

Table 2. Example showing differences in coefficients of thermal conductivity for selected alloys applicable in processing liquid magnesium (W/m °C) [86] [87] [88]

5. Material solutions in melting and casting equipment

The industrial equipment for magnesium processing, with components entirely or partly exposed to liquid metal, include crucibles of melting furnaces, elements of die casting and other machinery, parts of pumps and transfer systems. Although the primary requirement imposed on materials used includes the chemical resistance to molten magnesium, there are also other essential properties needed, depending on specific service conditions such as a sustainable level of strength and toughness, creep resistance as well as the resistance to oxidation in air at high temperatures. There are a number of commercial alloys applicable for this purpose that differ in chemical composition, as well as physical and mechanical properties. Examples of most common industrial solutions are listed in Table 3.

Resistance against liquid magnesium only		**Resistance against liquid magnesium accompanied by high temperature strength and wear resistance**	
Group of alloys	**Grade examples**	**Group of alloys**	**Grade examples**
Majority of tool steels	excluding (AISI A8, A9, A10)	Highly alloyed special steels	DIN 1. 2888, DIN 1. 2886
Low alloy steels	AISI 1330-4161 5115-6150	Chromium hot work steels	AISI H10-H19
Ferritic stainless steels	AISI 405, 430, 444	Tungsten hot work steels	AISI H21-H26
Martensitic stainless steels	AISI 403, 410, 440		
Special alloys	Nb-30Ti-30W		

Table 3. Metallic alloys applicable for components of magnesium processing equipment exposed to liquid magnesium alloys.

5.1. Crucibles and melting furnaces

The magnesium melting furnaces utilize as a heat source the electric resistance or gas heaters. Thus, an external surface of the crucible is additionally degraded by an exposure to the heat source. Because carbon steel scales on the outside of the melting crucible, being in contact with flame, other material combinations have been tried. The present furnace crucibles are manufactured of (i) ferritic stainless steel; (ii) bimetallic materials with an interior made of low carbon steel and an exterior of stainless steel; (iii) bimetallic design where an interior of low carbon steel is protected from the outside by nickel alloys, forming the oxidation resistant surface adjacent to the furnace heat source. An example of crucibles for handling liquid magnesium is shown in Fig. 9.

Magnesium crucibles for operation up to 850 ^{o}C could be manufactured of wrought or cast mild carbon steels with negligible nickel content. Welding is the dominant joining technique. In the case of using just carbon steel, a crucible lifetime is generally short, sometimes of the order of several days. An improved design of the single material crucible utilizes a ferritic stainless steel, such as AISI 444 [49] [50]. The steel is welded using a nickel-free and high

Figure 9. Commercial processes requiring equipment resistant to liquid magnesium: (a, b, c) crucibles for magnesium melting [83];

chromium stainless rod. As a result, the crucible lifetime is increased from six to ten times. Since ferritic stainless steels exhibit a tendency to brittle cracking, as a further improvement, bimetallic crucibles were introduced. During melting at 650°C, magnesium tends to leach the Ni out of Ni-containing alloys, a thick austenitic steel base such as AISI 316 is overlaid with a mild carbon steel liner such as AISI 1005 to protect it from a corrosive attack [51]. Another design suggests mild steel crucibles or a lining of 430 stainless grade. The nickel-chromium-iron alloy outside provides high temperature strength and oxidation resistance while the carbon steel inside is more compatible with the molten magnesium [52]. An example of reactivity of Mg with a crucible and a melt transfer pump is shown in Fig. 10.

http://dx.doi.org/10.5772/59181

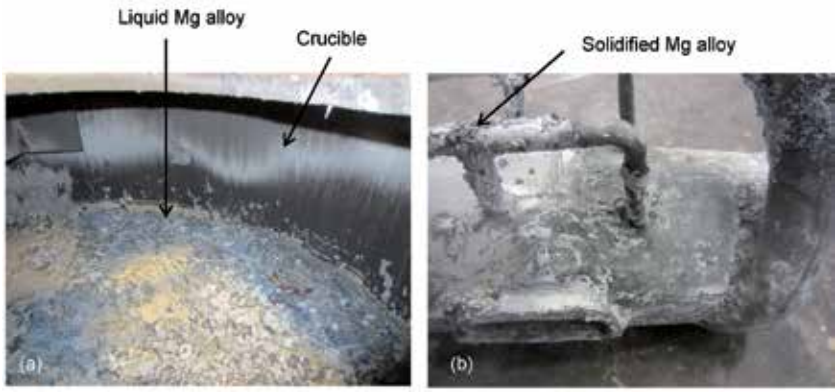

Figure 10. Magnesium reactivity with (a) crucible holding liquid magnesium alloy; (b) element of transfer system for liquid magnesium alloy with surface covered by solidified alloy.

5.2. Die casting machines

There are two techniques of die casting and corresponding machines for both processes with essentially different exposure conditions of their components to liquid magnesium. As a result, both applications require quite different material solutions.

During cold-chamber die casting, shown schematically in Fig. 11, the alloy melting is performed in a separate furnace. Then, a portion of molten material is transferred from the furnace crucible into the machine shot sleeve, where a hydraulically operated plunger pushes the metal into the die. The amount of liquid alloy transferred to the sleeve is larger than the part volume so the extra material is used to apply pressure during solidification in the die cavity, thus reducing the generated shrinkage. The typical injection pressure of a cold chamber system exceeds 70,000 kPa. Due to a need to transfer the molten metal from the furnace to the cold-chamber machine, the cycle time is reduced depending on the melt transfer solution.

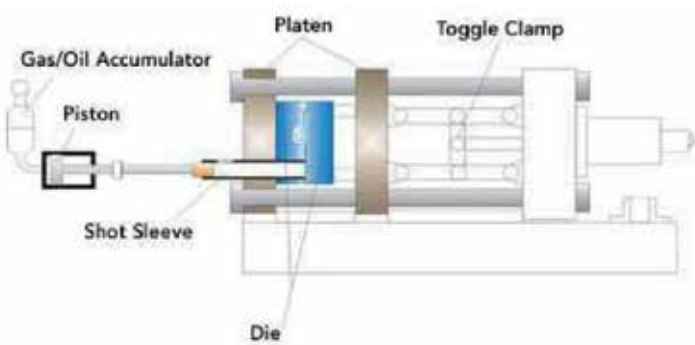

Figure 11. Schematics of cold chamber die casting machine with major components exposed to liquid magnesium alloys [84]

There are a number of components within the machine that are exposed to liquid magnesium, including shot sleeve, plunger, seal rings of the plunger, nozzle, sprue etc. An example of the shot sleeve is shown in Fig. 12a. The shot sleeve walls are in an intimate contact with liquid magnesium for only 1-2 seconds or 5% of the entire cycle duration so its average temperature is well below the melting point of magnesium alloy. However, the non-uniformity in temperature distribution as suggested in Fig 12b causes non-uniform deformation with a tendency to bending. As a result, a piston cannot slide smoothly inside the shot sleeve, causing friction and wear on both components. During flow into shot sleeve, the liquid alloy heats the inner wall surface reaching the highest temperature within the entire component. In extreme cases the sleeve deformation may lead to plunger seizing. A combination of high temperature, chemical attack, along with abrasion imposed by flowing alloy, contributes to the degradation observed. A similar wear location is also reported for shot sleeves used in die casting of Al alloys. A frequent location of the sleeve deterioration area is shown in Fig. 12c

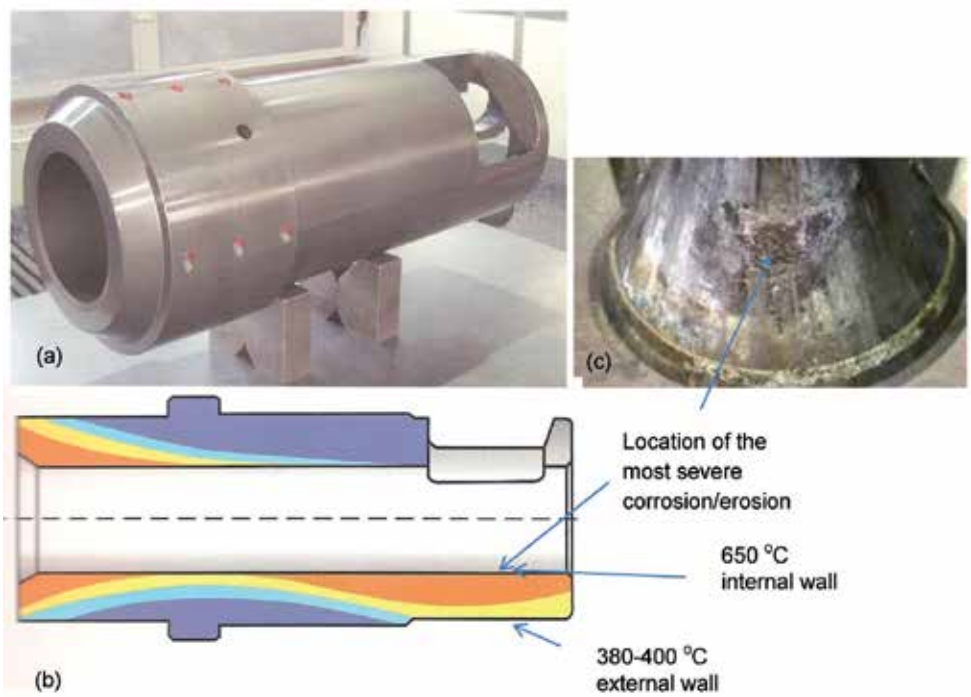

Figure 12. Design of a shot sleeve of a cold chamber die casting machine (a), schematics of temperature distribution (b) and surface deterioration due to a contact with liquid metal (c) [85].

To improve the temperature uniformity within the shot sleeve, thermoregulation is used, employing sleeve channels with circulating cooling/heating media (Fig. 13). The cooling channels help to take away the heat brought by molten alloy. As shown in Fig. 14, this solution substantially lowers the temperature difference between sleeve locations, reducing the extent of thermal fatigue. During selection of material for the shot sleeve there is a trade between

http://dx.doi.org/10.5772/59181

durability and cost. As a result, the hot work tool steel of AISI H13 grade performs satisfactorily there.

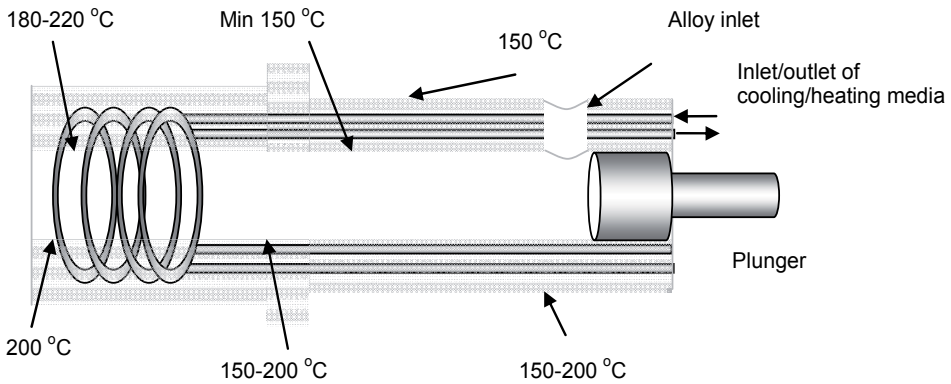

Figure 13. Schematics of thermoregulation within shot sleeve of cold chamber die casting machine [85].

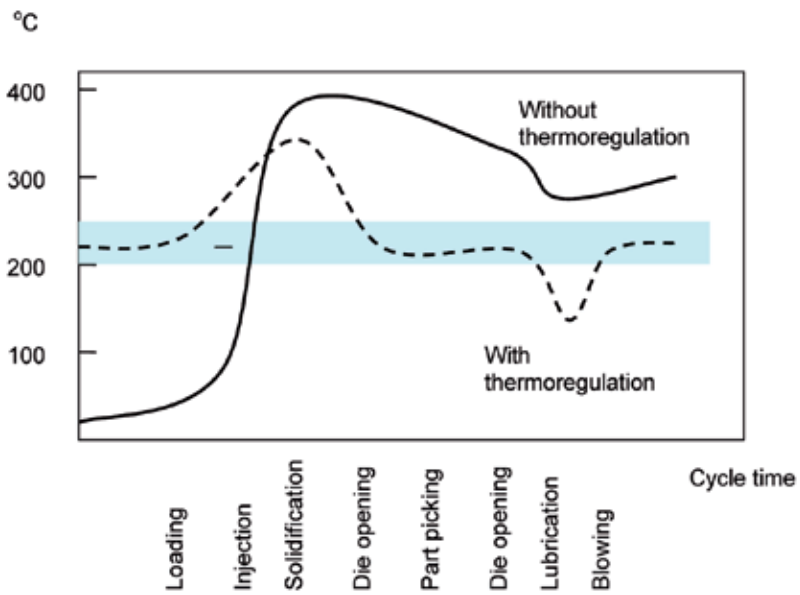

Figure 14. Temperature distribution profile within shot sleeve of cold chamber die casting machine with and without thermoregulation [85].

The hot chamber magnesium die-casting process uses a gooseneck and piston to inject molten magnesium into a die. As shown schematically in Fig. 15, the gooseneck is submerged into molten magnesium so through the side fill holes its cavity is filled with molten magnesium. The piston then forces the molten metal down from the top, delivering it through the gooseneck vertical delivery hole, nozzle and into the die without exposure to the environment. After the metal turns solid inside the die cavity, the die opens, the part is ejected and at the same time the piston retracts to its initial position above the fill holes. Then again, the die is closed, and the gooseneck is filled with molten metal and ready for the next injection cycle.

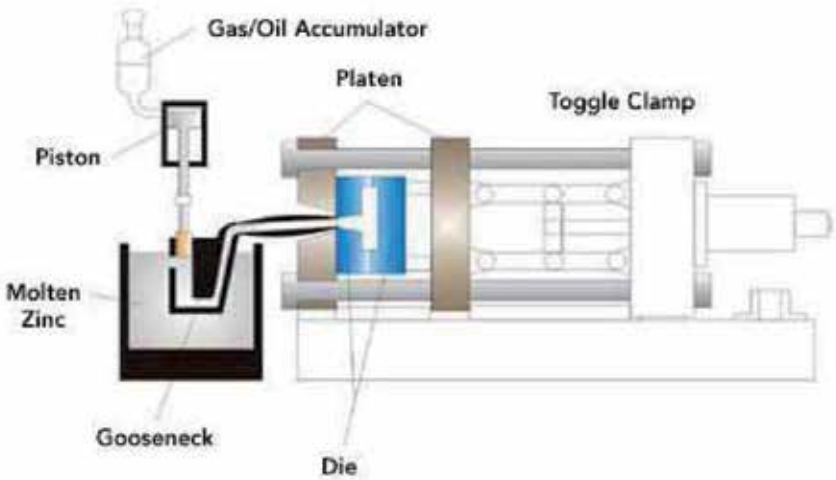

Figure 15. Schematics of hot chamber die casting machine with major components exposed to liquid magnesium alloys [84]

It is clear that more harsh conditions exist in the hot chamber machine. This is mainly because during all processing cycles, the hot chamber has a gooseneck completely submerged in molten magnesium. As a result, reduction in material strength caused by high temperature occurs, which has to be compensated by an increased size (Fig. 16). As such, the goosenecks are relatively robust. The massive component can be made of a casting using steel with high heat resistance, e.g. 1.2888 type. Due to issues with casting defects, it is frequently being replaced with wrought martensitic stainless steels, e.g. of AISI 420 type. Forging is an attractive alternative for the cast goosenecks. In the forging process, a solid billet can be shaped on open die presses, which consolidate the ingot center and eliminate porosity. It delivers a finished product that is more reliable and lasts longer [53]. Although the chemistry of AISI 420 steel provides lower resistance to tempering than DIN 1.2888, its high integrity in a wrought state may contribute to overall better performance. Another component exposed to liquid magnesium is the machine nozzle (Fig. 17a). Liquid magnesium along with melt pressure and non-uniform temperature distribution (Fig. 17b) often contribute to premature nozzle failure as seen in Fig. 17c.

http://dx.doi.org/10.5772/59181

Figure 16. Goosenecks of hot chamber die casting machine: (a) part before exposure to liquid magnesium; (b, c) gooseneck after service with extensive corrosive attack [85].

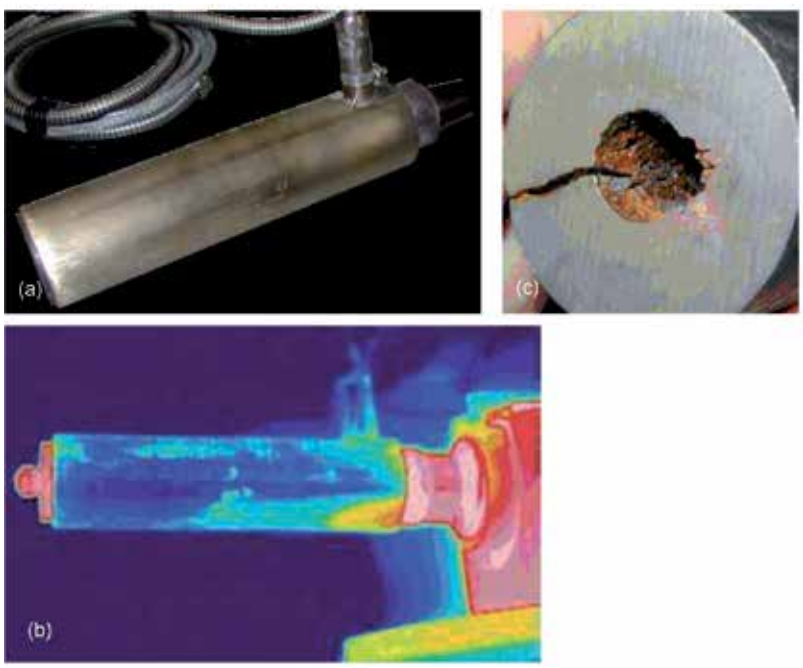

Figure 17. Nozzle of hot chamber die casting machine: (a) general view; (b) thermal profile showing temperature distribution; (c) section showing extensive corrosive attack and radial cracking [85].

5.3. Equipment of novel techniques of magnesium processing

In addition to high pressure die casting, there are a number of novel technologies at different advancement stages of commercialization, aimed at manufacturing net shape components from liquid or semisolid precursors [54] [55] [56] [57] [58] [59]. Of particular interest is equipment for semisolid processing of magnesium alloys and their composites. The key feature of machines for semisolid processing operating in thixo-mode, i. e., exploring only partial melting before injection, is reduced service temperature. Depending on the solid fraction targeted, the temperature reduction may be substantial. Instead of the overheated liquid used in die casting with a temperature of 670 °C, the process may require only 580 – 600 °C. This reduction may be of critical importance, affecting performance or even the applicability limit of some materials. At the same time, there is an essential difference in operating mode between die-casting and injection molding [1]. As opposed to short time intermittent contact, encountered between the shot sleeve of a cold chamber die casting machine and a molten metal, during injection molding the exposure of some machine components to molten alloy is permanent, reaching continuously in one interval up to thousands of hours. Moreover, while the shot sleeve of a die-casting machine has cooling channels, an injection molding barrel is extensively heated from outside. As a result, a substantial difference in service conditions renders the majority of solutions from melting and casting equipment not applicable to novel techniques of magnesium processing. Some materials with a sufficient combination of strength and corrosion resistance are still being researched [60].

6. Manufacturing techniques utilizing material combinations

The majority of materials maintaining strength at high temperatures are not chemically resistant to liquid magnesium. In fact, alloys with the best ability to maintain strength at high temperatures, easily react with molten magnesium. Therefore, separating thermal and corrosive factors increases the choices of material selection during the design of the magnesium processing equipment. The most typical techniques applicable to explore material combinations are characterized below.

6.1. Mechanical shielding

An interference-fit type connection may be used with components of specific shapes to cover the surface of an alloy which is prone to chemical attack by liquid magnesium while another alloy may be resistant against such attack. The technique applicable is called shrink-fitting and explores thermal expansion and contraction of metals to create a strong joint of a mechanical nature between two pieces, where one of each is inserted into the other. While in the past blow torches, hot plates and oil baths dominated as a heat source, the electric resistance and electromagnetic induction techniques are the commercially viable ones at present. Modern equipment allows uniform distribution of temperature with no danger of overheating by continuous monitoring the component temperature and adjusting its own heating power.

http://dx.doi.org/10.5772/59181

The typical example involves shrink-fitting of two tubes where the larger one is preheated to expand its diameter. At the same time, the inner tube remains at room temperature or is additionally cooled using, e.g., dry ice (CO_2 at a temperature of –180 °C) to further reduce its diameter (Fig. 18). After an insertion of one tube into another and cooling to room temperature, both tubes are joined together. The interference value within the connection should be calculated to avoid exceeding the yield stress in both materials [61]. After excessive heating during service, simultaneous expansion of both tubes may eliminate interference and release preload. Thus, the high temperature applicability of such a connection depends on differences in coefficients of thermal expansion. The outer material cannot expand substantially more than the inner one. The connection is penetrable to air; so high temperature oxidation should be taken into account.

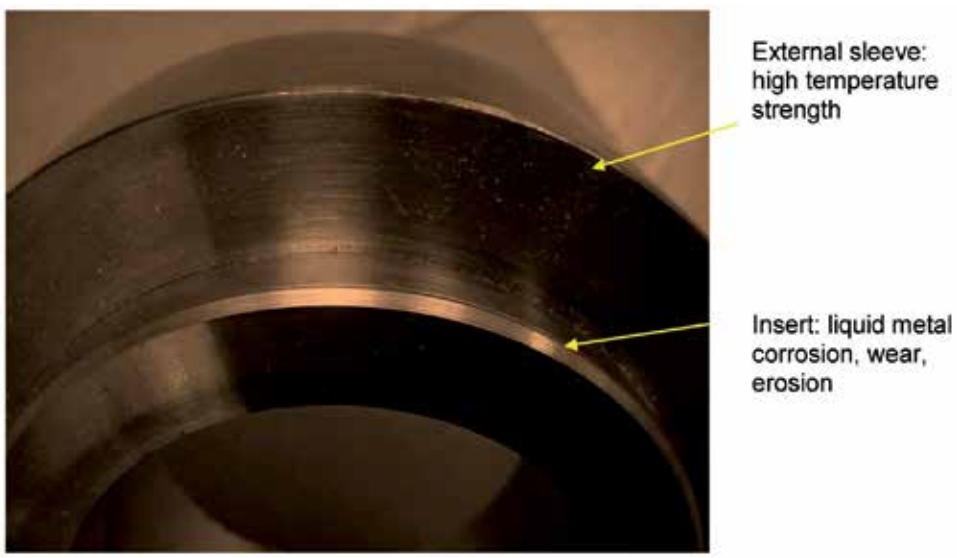

Figure 18. Concept showing tubes joined by a shrink fit method.

An application of shrink fitting is suggested for the manufacture of barrels for injection molding of magnesium [60]. In this design, an external shell with high temperature strength made of Inconel 718 superalloy is connected through shrink fitting with an internal liner made of Stellite 12 alloy. The latter one is corrosion resistant to liquid magnesium but it does not have sufficient ductility and tensile strength to withstand internal melt pressure.

6.2. Plasma transferred Arc (PTA) cladding

Cladding is a deposition of an alloy on the metallic substrate in order to modify the structure and physical characteristics of its surface required for certain applications. The most commonly used cladding techniques utilize the plasma transferred arc (PTA) and laser. PTA cladding is performed by melting of metallic, ceramic or cermets powder in a plasma arc before deposition.

Typical characteristics include high deposition rate and minimum penetration into the base (<5%). Layers up to 5 mm in a single pass can be formed with very low losses of the deposited powder. PTA gradually replaces older methods of conventional weld overlays with tungsten inert gas (TIG) or metal inert gas (MIG). The generally simple concept may become complex when applied to specific material combinations. Of particular importance for processing liquid magnesium is cladding alloys having high temperature strength with alloys resistant to wear and corrosive attack by molten magnesium.

6.3. Weld cladding of Ni-based with Co-based superalloys

Inconel 718 has good weldability and preferred techniques include gas tungsten arc, plasma arc and electron beam welding [62]. The process is performed on annealed material but the age-hardened alloys are also weldable. The post-welding treatment includes most often annealing and aging but in many instances aging is sufficient if material was welded in annealed condition. Preheating is not usually required, excluding warming up to prevent moisture condensation.

The typical defects during welding involving Inconel 718 alloy include:

i. solidification cracking, which occurs within a newly formed weld when the semisolid region experiences tensile stress and the high fraction of solid restricts the flow of liquid to fill interdenfritic regions;

ii. grain boundary liquation cracking or heat affected zone fissuring, which occurs within the heat affected zone as a result of local dissolution of grain boundary phases. Under rapid heating, the grain boundary phases area that is unable to dissolve fully into the surrounding matrix leads to formation of a low melting point eutectics and a melting of the grain boundary region;

iii. strain age cracking, which occurs during a post-weld heat treatment or high temperature service as a result of residual or applied stress. The microstructural image usually shows intergranular microcracks in either weld or heat affected zones due to precipitation and hardening of the alloy and transfer of stress on grain boundaries where hard precipitates may act as a crack nucleolus.

The Co-based alloys with high carbon content are difficult to weld. To prevent cracking, the alloy should be preheated and maintained at 540 ^{o}C minimum. The cooling rate should also be slower. While cladding Ni-base with Co-based alloys the requirements in regards of heat control are contradictory: fast cooling rate for Ni-based alloy to avoid hot cracking versus slow cooling rate for Co-based alloy to avoid cold cracks. As a possible solution it is suggested to use an underlayer. For this purpose a pure Ni or Inconel 82 layer with a thickness of 1-2 mm is recommended [63].

An application of PTA cladding for equipment used with liquid magnesium is specified in Ref. [64]. It was proposed that barrel head be manufactured of a Ni-based superalloy, such as Inconel 718, the melt channel clad with low C content, Co based compact (crack free) Stellite 21. The seal surfaces of the barrel head were clad with high C content Co based superalloy

such as Stellite 12. The microstructure of Inconel 718 cladded with Stellite 21 is shown in Fig. 19. With Stellites in general, the primary face cubic centered cobalt dendrites are surrounded by a network of eutectic lamellae composed of cobalt and eutectic M_7C_3 carbides. The composition of M_7C_3 depends on alloy type and cooling conditions with a typical example of $Cr_{0.85}$ $Co_{0.14}$ $W_{0.01})_7C_3$ [65]. In addition to pure alloys it is also formed in a mixed zone, where chemistry of molten alloys combines.

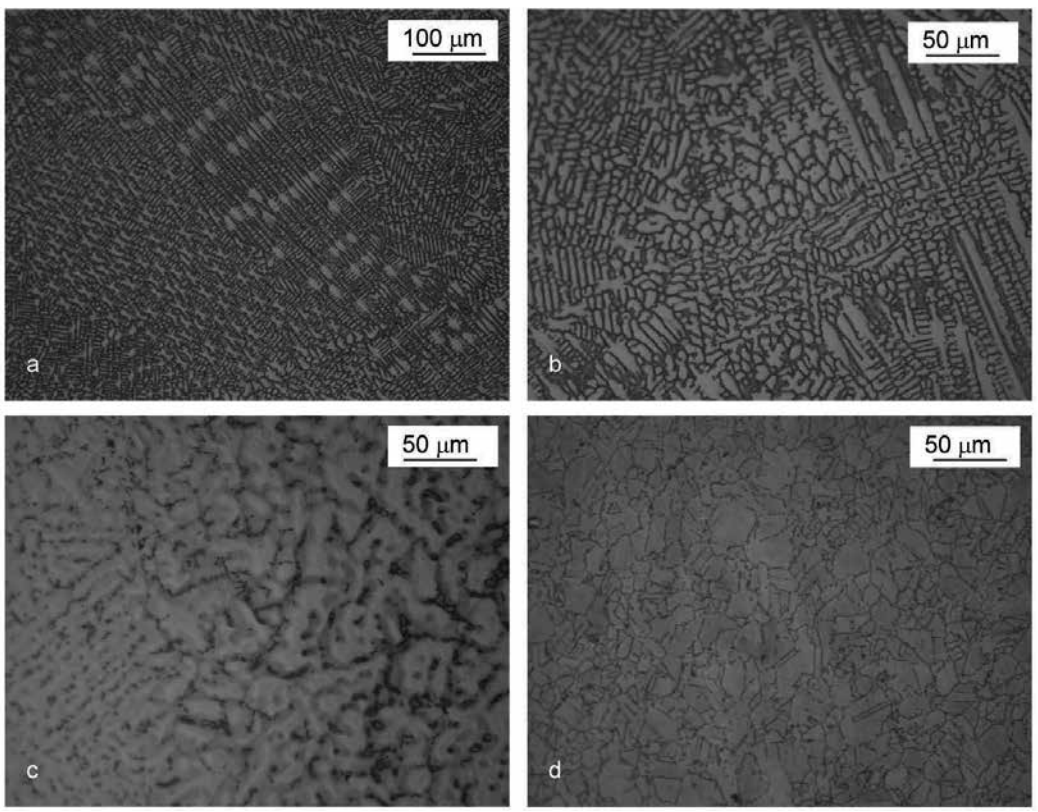

Figure 19. PTA cladding of Inconel 718 with Stellite 12 alloy: (a, b) microstructure of surface clad of Stellite 12; (c) transient zone between base and clad; (d) Inconel 718 in the substrate.

6.4. Laser cladding

Laser cladding represents the fusion of a different material to a substrate surface while ensuring the metallurgical bond with minimal melting of the substrate and chemistry dilution, as well as the small heat affected zone. It can be conducted in a single or two-stage process. In a single stage, called the blown powder cladding, the alloy powder, transported into the interaction zone between the laser beam and substrate, is subjected to heating. Melting starts at the substrate surface and powder particles form a pool. Selection of the laser energy allows to control the substrate melting. In the generally simpler, two stage cladding; the powder is

first pre-deposited on the substrate. To keep the powder on the surface, various binders are applied. Then, the powder is scanned by the laser beam while covered by an inert gas. Three distinct stages during melting of the powder are distinguished [66]:

i. first, the powder is rapidly melted by the laser before the melt gets in contact with the substrate;

ii. when the melt reaches the substrate surface, it solidifies due to a rapid flow of the heat into the substrate by conduction. There is no movement of the melt-liquid interface into the substrate;

iii. further applying the laser energy will move the former melt-solid interface deeper into the substrate.

Benefits of laser cladding include [67]: (i) very small heat-affected zone, which results in tiny deformation and stress; (ii) can be applied to virtually all metal materials; (iii) operation time is significantly shortened compared to arc welding; (iv) final product has high dimensional accuracy and integrity.

Laser cladding has application potentials in magnesium casting, e.g. in extending life time of dies/molds by increasing their wear resistance with hard surface layers to reduce erosion. By combining high wear with high tensile strength and high ductility, thermal or stress induced cracking during the casting process can be reduced. Since commonly used hot working tool steels have limited wear resistance, laser cladding is a very useful technique to improve their surface properties by multi-graded layers [68]. An application of laser cladding to deposit-Stellite 1 on AISI 4340 steel is described in Ref. [69]. Cobalt-based/carbide type alloys are well-known for their "hot hardness" and are extensively used for hardfacing of components made of conventional steels. The main challenge in deposition of Stellite 1 using laser cladding is crack sensitivity of this alloy during hardfacing process. To reduce the possibility of cracking, preheating of the substrate prior to the deposition process was tested to be effective. Investigation of die soldering during high pressure die casting led to a promising treatment with the laser clad Fe-W alloys [39]. An increased W content in the powder mix led to reduction in formation of intermetallic phases on die surface due to negligible possibility of a reaction between W and Al from Mg alloy during casting.

6.5. Centrifugal cast cladding

During centrifugal casting a liquid metal is poured into a rotating tube-like crucible and after solidification removed from it [70]. By replacing the crucible with the sleeve material, the process can be used for cladding of its inner surfaces. In addition, the liner material may be pre-applied as powder and subsequently melted while inside the sleeve [71]. The basic requirement is a safe difference between melting ranges of both alloys. The downside of this technique is that the cladded part has to be preheated to high temperatures causing coarsening of the microstructure and property reduction. An example of cladding the Inconel 718 with Stellite 12 is shown in Fig. 20. The metallurgical bonding formed assures strong connection. Due to severe overheat the grain growth occurred from an initial number 7 to number 00 according to the ASTM scale. Subsequent aging does not produce optimum phase morphol-

http://dx.doi.org/10.5772/59181

ogy. On the other hand, a requirement to keep the temperature as low as possible causes incomplete melting of Stellite and individual powder particulates still remain within the liner.

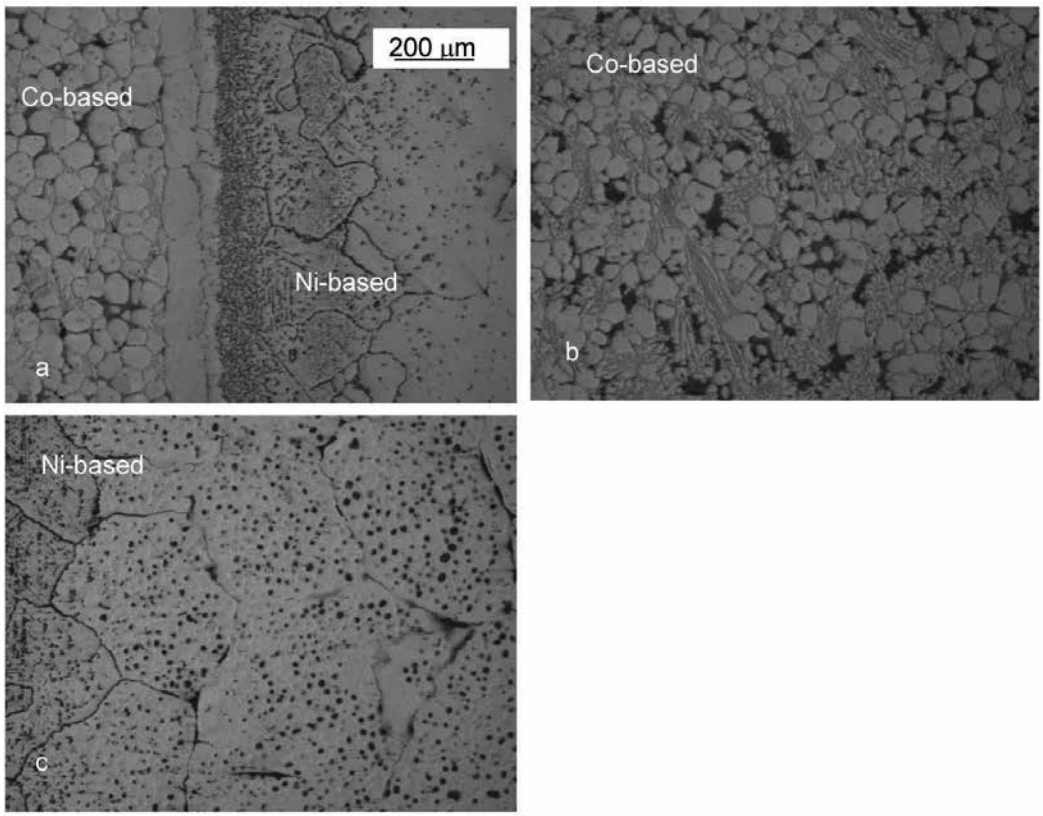

Figure 20. Microstructure of centrifugal inlay casting of Co-based alloy inside Ni-based shell: (a) interface region; (b) Co-based inner layer; (c) outer layer of Ni-based alloy.

6.6. HIP-cladding

Hot isostatic pressing (HIP) is a densification process for both encapsulated powders and pre-formed parts, e.g. castings. It was developed in 1955 at Battelle Laboratories, Columbus, Ohio to bond components of small Zircaloy-clad pin-type nuclear fuel elements while maintaining strict dimensional control. The technique involves the simultaneous application of a high pressure and elevated temperature. The isostatic nature of pressure is achieved due to its application through a gas, most frequently inert, and it should be distinguished from a conventional unidirectional pressing. The isostatic pressure in HIP-ing arises from molecules or atoms of gas colliding with the surface of the object [72]. Under conditions of heat and pressure the encapsulated powder or sintered components are densified to improve properties.

HIP-ing creates homogeneous material with a uniformly fine grain size and near 100% density. Internal voids are healed and a strong metallurgical bond is created within the entire volume. There also exists the Liquid HIP-ing, typically used for densification of castings, where to lower cost, molten salts and mechanically generated pressures are explored. HIP should also be distinguished from cold isostatic pressing (CIP) which is a compaction of powders enclosed in an elastometer mold. During manufacturing of near net shape components from a single alloy, a powder mixture of several elements is placed in a steel can container. Then air and moisture is removed from the powder by applying high temperature and vacuum. Finally, the container is sealed and HIPed. During application of HIP-ing for manufacturing of bimetallic structures, two different chemistry powders are placed into two separated chambers of the steel container. After HIP-ing is completed and external shape machined, the both alloys are separated by the interface layer, being the container wall. There is a metallurgical bond between the steel layer and alloys on its both sides. HIP ing is used to manufacture alloys such as Ni-based and Co-based superalloys [73], Nb-30Ti-20Wand also near-net shape components used for processing of molten magnesium. Besides, HIP-ing can be used for cladding selected surfaces of wrought substrates with another alloy [74]. In this process, a portion of the container is the wrought alloy. After HIP-ing, the thin steel container is machined out, leaving a bimetallic structure of wrought sleeve and powder cladding. In this technique, the HIP-ing behavior in the formation of an interfacial diffusion bonding among dissimilar materials is explored. A drawback of this type of cladding is a deteriorating effect of high temperatures required for HIP-ing on the structure of wrought alloy. In principle, the process may employ the same alloys as described above for weld cladding.

7. Surface modifications

The purpose of surface engineering is to enhance properties of superficial layers of materials by changing their chemistry and/or structure. There are two essentially different cases of surface protection, which depend on the substrate (base) material and its compatibility with molten magnesium. For materials resistant to chemical attack by molten magnesium, surface engineering aims at improving this resistance. In this case the coating failure does not lead to the catastrophic failure of the part. For materials not resistant to molten magnesium, surface engineering offers basic protection to the substrate. In this case, however, failure of the coating leads to catastrophic failure of the entire part.

7.1. Thermochemical diffusion treatments

Thermochemical diffusion is a surface treatment where the chemistry of superficial layers of materials is altered by introduction of some chemical elements from outside [75]. The atoms introduced combine with alloy elements, thus modifying existing phases and forming new ones. The major processes applicable to protection against liquid magnesium include nitriding, nitrocarburizing and boriding.

http://dx.doi.org/10.5772/59181

7.1.1. Nitriding

Nitriding is a process of enriching the surface layer with nitrogen. In case of steel substrate a compound layer is developed on the surface constituted primarily of iron nitrides, Fe_4N called γ′ (gamma prime) or $Fe_{2-3}N$, called ε (epsilon). The structure of this compound zone is mainly determined by the underlying diffusion zone, which serves as a transition zone with declining hardness from the high hardness at the surface to that of the core of the material. There are several distinct approaches to nitriding [75]:

i. conventional gas nitriding, carried out in partially dissociated ammonia gas at 500-600 °C. The disadvantage is a lack of adequate control of the nitrogen concentration;

ii. gas nitriding where nitriding potential is continuously controlled taking into account varying compositions of the nitriding atmosphere during each stage of the cycle (Nitreg);

iii. ion nitriding where a plasma glow process ionizes nitrogen gas with heat causing the positive ions of nitrogen created to be drawn onto the surface of the component forming a uniform layer.

7.1.2. Ferritic nitrocarburizing

Nitrocarburizing is considered as a complementary process to nitriding and can be carried out in liquid, gaseous and plasma environments. During nitrocarburizing, the steel surface is enriched simultaneously with nitrogen and carbon. The process is carried out at 550 – 580 °C and depending on the composition of the base material and exposure time the penetration depth reaches from 200 μm to 1000 μm with a surface hardness from 700 to 850 HV. Assuming sufficiently high activities of carbon and nitrogen, the compound layer, formed at the surface, consists predominantly of ε and/or γ′ phases. Beneath it, there is a diffusion zone with N and C atoms dissolved interstitially in the ferrite lattice. While the compound layer brings a combination of resistance to wear and atmospheric corrosion, the diffusion zone improves the endurance limit [76].

It should be stated that steel nitriding is widely used for cold chamber die casting shot sleeves, die/mold surface, die pins, piston rings etc. Its effectiveness is limited, at least for some applications, first because chemistry of steels used for machinery of magnesium processing are not optimized for nitriding or nitrocarburizing. Moreover, high service temperature may diffuse away nitrogen from the surface layer, deteriorating its properties over time. An example of an H13 commercial piston ring from a cold chamber die casting machine is shown in Fig. 21. Although due to temperature experienced in service the initial case hardness, along with hardness of the base substrate are reduced, the overall ring performance after nitriding is substantially improved.

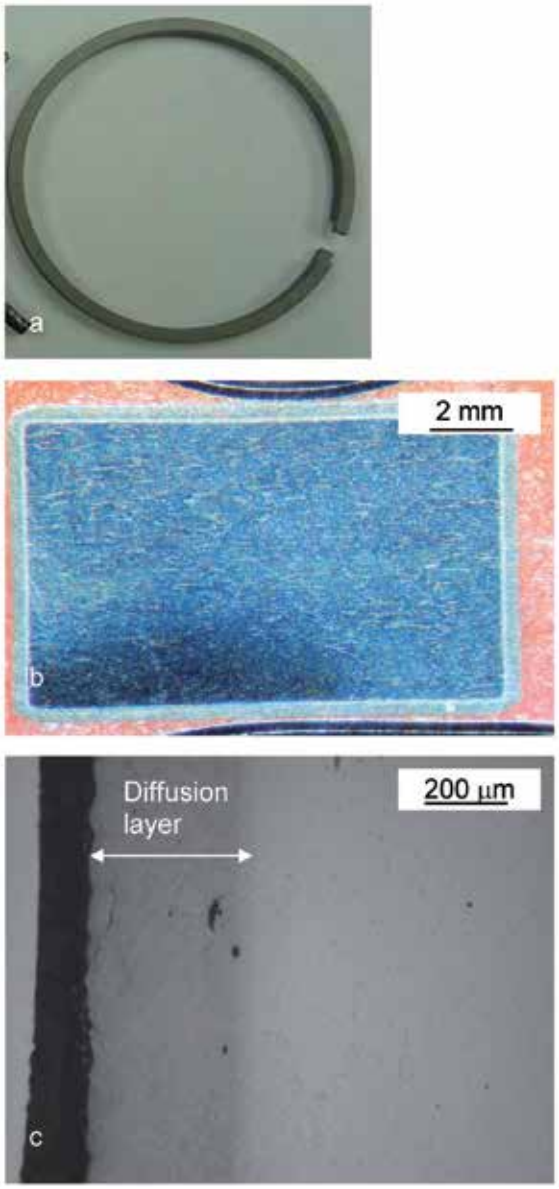

Figure 21. Nitrided layer on the H13 steel used for die cast piston ring: (a) piston ring; (b) macro cross section showing thick nitrided layer; (c) micro image showing the nitrogen penetration range.

7.1.3. Boriding (boronizing)

Boriding means an enrichment of the surface layer of the material with the elemental boron. Unlike nitriding, boriding is carried out at significantly higher temperatures, typically between 800 and 1000 °C [77]. Various implementation technologies include packing with solid

http://dx.doi.org/10.5772/59181

mixtures of boron carbide and borax as the boron source, molten salt performed using anhydroux borax mixed with reducing agents, electrolytic carried out in an argon atmosphere using borax-based melts, plasma and vacuum boriding [78]. The surface hardness is in the range of 1500-2000 HV, which exceeds nitriding and nitrocarburizing. The technique may be applied to ferrous and nonferrous metals and alloys, e.g. Ti, Ni or Co. Depending on the substrate chemistry, the surface layer forms different compounds. For steel, Fe_2B is the major compound formed. For Ni the major compound is Ni_3B while boriding Co produced both Co_4B and Co_3B. The boriding treatment was explored to prevent soldering during Mg die casting.

7.1.4. Thermo-reactive diffusion (TRD)

The vanadium carbide thermo reactive diffusion creates a 5 – 10 μm thick surface layer with a hardness of 3200 – 3800 HV. The process is conducted in a packed or molten salt environment, where active vanadium enters the surface and combines with carbon atoms from steel to form vanadium carbides [79]. Vanadizing is performed at temperatures of 800 – 1000 °C. Thickness is well controllable by adjusting diffusion time and temperature for a given environment and steel chemistry. The layer has a very strong metallurgical-diffusion bond to the substrate, providing high peeling resistance. Thermo-reactive diffusion was originally developed to improve wear resistance. It has a thermal expansion mismatch with chromium hot work tool steel AISI H13. According to some data a minimum carbon content should be 0.3%. The process is effective in die casting operations and explored especially in Europe and Japan. The major parts treated include die casting cores and pins. According to [80], for Al casting, TRD coatings led to higher increase in tool life than nitriding. As a partial explanation is given that VC resists aluminum diffusion through the surface layer.

7.2. Coatings

According to general selection rules the coating should have high hardness and strength and moderate ductility. Its thermal conductivity, melting point and density should also be high while the coefficient of thermal expansion and coefficient of friction should be low [81]. Due to harsh environment of molten Mg, of a large number of coating techniques and coating chemistries, only several were found to provide improvement. Below is provided their brief characterization.

7.2.1. Physical vapor deposition (PVD)

PVD includes coating techniques where the transport of atoms or molecules to the coated surface is accomplished by a physical process. The technique of line-of-sight coating of complex geometries is difficult. The low deposition temperature of 100 – 500 °C minimally affects the substrate structure. Due to low temperature, however, it is difficult to achieve great adhesion. The coating chemistries applicable to Mg processing are given in Table 4 with indications of their thermal stability.

Name	Formula	Colour	Thermal Stability, °C	Hardness, HV	Typical thickness, μm	Characteristic features
Titanium nitride	TiN	Gold	600	2300	2-5	Used for moderate abrasions, ductile hard coat
Titanium carbonitride	TiCN	Grey-pink	410	3000	2-5	Shock resistance
Titanium aluminum nitride	TiAlN	Brown	800	3500	2-5	Extreme heat resistance
Zirconium nitride	ZrN	Yellow-gold	650	2600	2-5	Excellent lubricity
Chromium nitride	CrN	Silver	1750	695	2-10	Good wear resistance
Titanium diboride	TiB2	Silver	900	4000	1-2	High corrosion resistance, chemical stability at elevated temperatures
Titanium boron nitride	TiBN	Silver	800	3500	1-5	Heat-checking resistance, abrasive wear resistance

Table 4. Selection of PVD coatings applicable for components of magnesium processing equipment exposed to liquid magnesium alloys [89] [90] [91]

The general finding in regards to selected components of Mg processing equipment is that coatings provide substantial improvement against sticking of Mg to the surface and reduction of an overall degradation of a corrosive nature. This often allows the elimination of an acidizing step during cleaning and caused by this hydrogen ingress into the base. At the same time, however, 2-5 micron thick TiAlN coatings with mechanical bond to the substrate show severe limitations since they:

i. do not provide long lasting improvement in the extent of wear between metallic couples;

ii. do not provide a lasting chemical barrier with high integrity to separate the base material from liquid magnesium.

The barrier integrity is lost not only by the above named surface degradation mechanisms, but also by localized wear caused by hard particles which may enter the melt stream. During die casting of magnesium, tests of several PVD coatings [39], TiN on ground H13 steel were showing good performance. In contrast, PVD coating of CrN was dissolving with an intermetallics formed on its top, especially in Mg alloys with higher Al content.

http://dx.doi.org/10.5772/59181

7.2.2. Chemical vapor deposition (CVD)

The CVD process uses chemical reactions to deposit coatings on the substrate. In general, the process is carried out at higher temperatures than PVD, up to 2200 °C which provides excellent adhesion. The temperature requirement reduces markedly a number of applicable substrates. Since the nature of CVD is non line-of-sight, it can be used to evenly coat complex geometries and internal surfaces. The typical chemistries deposited with CVD include CrC, TiN and VC. An applicability to liquid Mg of CVD coating itself is the same as discussed above for PVD method.

7.2.3. Thermal spray

During thermal spraying, the wire or powder materials are melted into droplets, and then propelled onto the selected substrate. Upon impact, they form platelets that bond to the surface, creating a dense coating with no alteration to the substrate structure. The technique allows the deposition of pure metals, alloys, intermetallics, carbides and ceramics. There are several techniques applicable for deposition spray coatings:

i. combustion flame spray, achieved by burning a mixture of oxygen and fuel gas in a torch having a flame-accelerating nozzle. Powder is injected into the nozzle by the carrier gas, where it melts and is projected to the surface;

ii. electric arc spray, achieved by energizing two wires of the coating material at different electrical potentials. Molten particles are generated by arcing the wire tips which are then atomized and accelerated towards the substrate by a compressed gas;

iii. hypervelocity oxygen fuel spray (HVOF) is achieved by burning a pressurized mixture of the fuel gas and oxygen. Powder is fed into the stream of hot gases and discharged through a flow expansion zone;

iv. plasma spray, achieved by exploring the heat transfer for electric arc to a plasma-forming gas. In the spray device the gas flow contains an axial stick cathode while the nozzle forms the anode. Heated to high temperatures gas ionizes to plasma. Powder, injected into the exit melts and is accelerated by hot gases towards the surface. Special cooling techniques keep the surface temperature low.

An example of thermal spray coating is shown in Fig. 22a. The top end represents a 0.13 mm thick ceramic coating of YSZ (yttria stabilized zirconia) which exhibits very low thermal conductivity and provides thermal insulation. The lower cylindrical portion is covered with a 0.2 mm thick metallic coating of NiCr6Al providing oxidation resistance up to 980 °C. In some cases the ceramic coatings are too brittle to withstand mechanical stress. To minimize their brittle nature the ceramic coatings may be used in a combination with metallic support. An example of the solution is given in Fig. 22b. The metallic grid provides support and reduces surface contact while the ceramic coating, filling gaps between them, reduces the heat transfer.

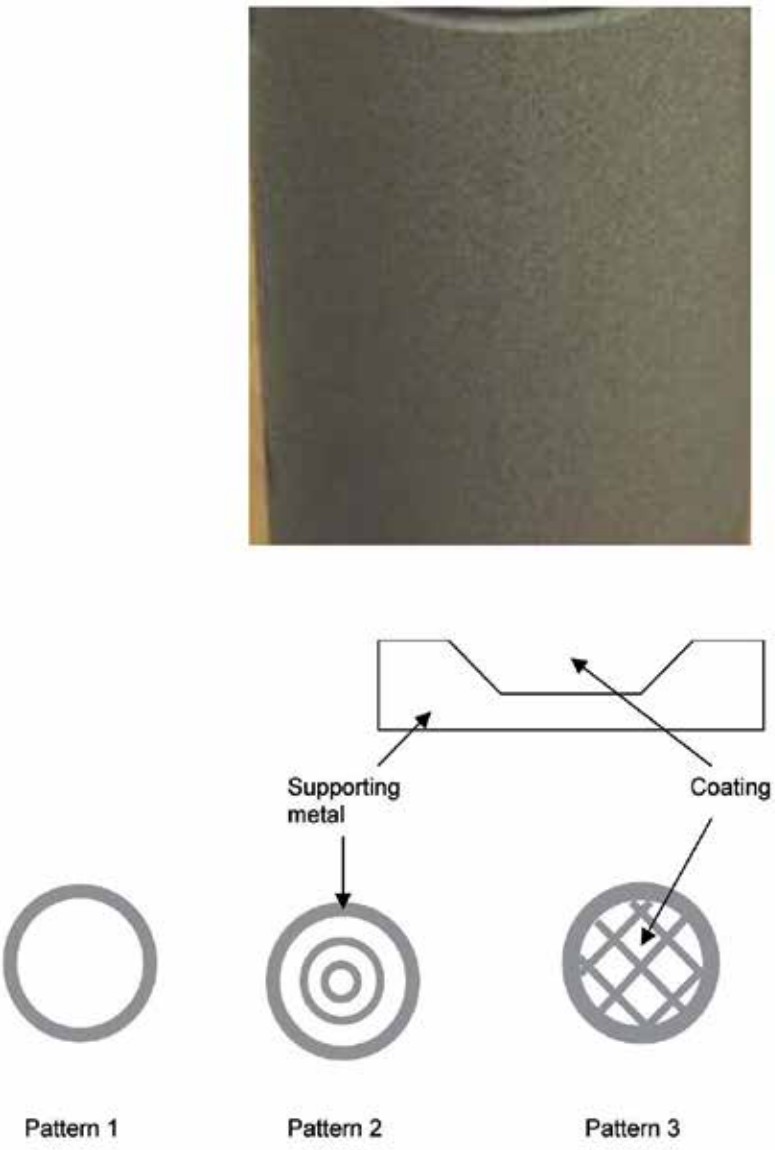

Figure 22. Ceramic coating of YSZ (yttria stabilized zirconia) deposited by thermal spray (a) macro view of the coating; (b) concept of the surface grooving pattern to support the brittle ceramic coating during impact.

7.3. Hybrids of surface treatments

Due to harsh service conditions of Mg processing, in some cases a single surface treatment may not be sufficient. It is claimed that single coating cannot eliminate completely the deteriorating effect of liquid magnesium alloys. Thus, in order to maximize the substrate protection, two or more surface modification techniques are combined. The multilayer hybrids

http://dx.doi.org/10.5772/59181

combine advantages of individual layers. A concept, explaining the mechanism of substrate protection by multilayer coatings is shown in Fig. 23.

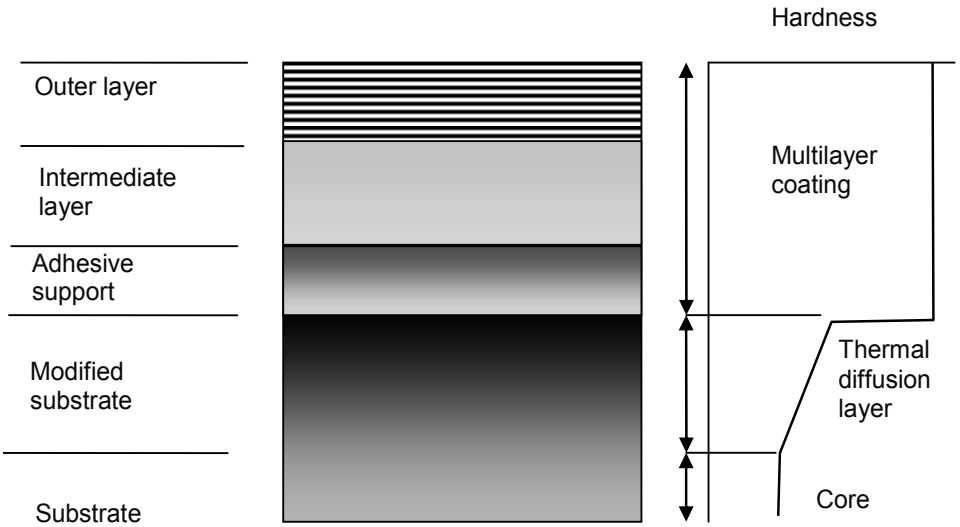

Figure 23. Concept of multilayer coatings deposited by PVD onto a steel surface enhanced by thermochemical diffusion

7.3.1. A combination of thermal diffusion layers with coating

The performance of coatings, especially those thin ones, depends on the properties of the substrate. It is clear that a hard coating will not last on soft substrate since it will crack and spall. In order to improve coating performance, substrates are subjected to special treatments. The most common is thermochemical diffusion treatment e.g. nitriding. Then, a coating is deposited on the top of the diffusion layer. An additional benefit is that in case of local failure of the coating, a diffusion layer may still protect the substrate. While this combination generally provides improvement, for some cases the substrate effect is negative. According to [39], TiN and CrN PVD coatings deposited on nitrided H13 steel showed poor adhesion and during Mg die casting process peeled off from the substrate. The poor performance was attributed to the decomposition of Fe-N nitride layer at increased temperatures due to diffusion of nitrogen.

7.3.2. Multilayer coatings

The progress in deposition technology allows the automatic control of the process so multilayer coatings may be formed. In practice, individual sub-layers will differ in terms of chemistry and structure. The properties of such a conglomerate exceed the properties of individual sub-layers. This method represents new type of surface treatment. In addition to coating conglomerates, multi-layer coating can be combined with diffusion treatment of the substrate. During trials with die casting of magnesium [39], the best performance was reached with multilayer

PVD TiN/CrN coatings which completely suppressed formation of intermetallics. In contrast, duplex TiN/CrN coatings did not show an improvement over single layer of TiN. When deposited on nitrided steel surface, decomposition of the Fe-N white layer due to internal diffusion reduced the coating performance.

8. Summary

The high temperature and corrosive attack of molten magnesium alloys impose a challenge on the selection of materials applicable for the hardware used for their processing. This challenge is magnified in the case of novel processing techniques where performance of materials used in conventional equipment of magnesium casting and handling is not satisfactory. Although modern metallurgy provides solutions to present requirements, the research continues to develop alloys capable of increasing the processing temperatures and extending the service life time of processing equipment.

Author details

Frank Czerwinski*

Canmet MATERIALS, Natural Resources Canada, Hamilton, Ontario, Canada

References

[1] F. Czerwinski, Magnesium Injection Molding, New York: Springer Verlag, 2008.

[2] F. Czerwinski, "Surface oxidation of magnesium alloys during liquid state processing," *Die Casting Engineer,* vol. 57, no. 5, pp. 16-19, 2013.

[3] F. Czerwinski (Ed.), Magnesium Alloys, Corrosion and Surface Treatment, Rijeka: INTECH, 2011.

[4] F. Czerwinski, "Oxidation characteristics of magnesium alloys," *The Journal of The Minerals, Metals and Materials Society,* vol. 54, no. 12, pp. 1477-1483, 2012.

[5] F. Czerwinski, "Controlling the ignition and flammability of magnesium for aerospace applications," *Corrosion Science,* vol. 86, pp. 1-16, 2014.

[6] F. Czerwinski, "Overcomming barriers of magnesium ignition and flammability," *Advanced Materials and Processes,* vol. 172, no. 5, pp. 28-31, 2014.

[7] L. Liu (Ed), Welding and Joining of Magnesium Alloys, Woodhead Publishing, 2010

[8] F. Czerwinski (Ed.), Magnesium Alloys-Design, Processing and Properties, Rijeka: INTECH, 2011.

[9] D. Bradwell, H. Kim, A. Sirk and D. Sadoway, "Magnesium-antimony liquid metal battery for stationary energy storage," *Journal of the American Chemical Society,* vol. 134, no. 4, pp. 1895-1897, 2012.

[10] K. Papis, J. Loeffler and P. Uggowitzer, "Interface formation between liquid and solid Mg alloy-An approach to continuously metallurgic joining of magnesium parts," *Materials Science and Engineering A,* vol. 527, pp. 2274-2279, 2010.

[11] J. Zhang, "A review of steel corrosion by liquid lead and lead-bismuth," *Corrosion Science,* vol. 51, pp. 1207-1227, 2009.

[12] X. Liu, E. Barbero, J. Xu, M. Burris, K. Chang and V. Sikka, "Liquid metal corrosion of 316L, Fe3Al and FeCrSi in molten Zn-Al baths," *Metallurgical and Materials Transactions A,* vol. 36, pp. 2049-2058, 2003.

[13] T. Wetzel et al, "Liquid metal technology for concentrated solar power systems: contribution by the German research program," *AIMS Energy,* vol. 2, no. 1, pp. 89-98, 2014.

[14] W. Manly, Fundamentals of liquid metal corrosion, Oak Ridge: Oak Ridge National Laboratory, 1956.

[15] S. Shin et al, "A study on corrosion behavior of austenitic stainless steel in liquid metals at high temperature," *Journal of Nuclear Materials,* vol. 422, pp. 92-102, 2012.

[16] J. Zhang, P. Hosemann and S. Maloy, "Models of liquid metal corrosion," *Journal of Nuclear Materials,* vol. 404, pp. 82-96, 2010.

[17] T. Auger, Z. Hamouche, L. Medina-Almazan and D. Gorse, "Liquid metal embrittlement of T91 and 316L steels by heavy liquid metals: A fracture mechanics assessment," *Journal of Nuclear Materials,* vol. 377, pp. 253-260, 2008.

[18] K. Meshinchi Asl and J. Luo, "Impurity effect on the intergranular liquid bismuth penetration in polycrystalline nickel," *Acta Materialia,* vol. 60, pp. 149-165, 2012.

[19] S. Keller and A. Gordon, "Experimental study of liquid metal embrittlement for the aluminum 7075-mercury couple," *Engineering Fracture Mechanics,* vol. 84, pp. 146-160, 2012.

[20] P. Lejcek, Grain Boundary Segregation in Metals, Berlin, Heidelberg: Springer Verlag, p. 183, 2010.

[21] R. Clegg and R. Jones, "Liquid metal embrittlement in failure analysis," *Soviet Materials Science,* vol. 27, no. 5, pp. 453-459, 1991.

[22] K. Ina and H. Koizumi, "Penetration of liquid metals into solid metals and liquid metal embrittlement," *Materials Science and Engineering A,* Vols. 387-389, pp. 390-394, 2004.

[23] J. Luo, H. Cheng, K. Meshinchi ASL, C. Kiely and M. Harmer, "The role of a bilayer interfacial phase on liquid metal embrittlement," *Science,* vol. 333, no. 6050, pp. 1730-1733, 2011.

[24] A. Legris, J. Vogt, A. Verleene and I. Serre, "Wetting and mechanical properties, a case study: liquid metal embrittlement of a martensitic steel by liquid lead and other liquid metals," *Journal of Materials Science,* vol. 40, pp. 2459-2463, 2005.

[25] H. Migge, "Thermodynamic stability of ceramic materials in liquid metals illustrated by beryllium compound in liquid lithium," *Journal of Nuclear Materials,* vol. 103, no. 1-3, pp. 687-692, 1982.

[26] W. Cook, Corrosion resistance of various ceramics and cerments to liquid metals, Oak Ridge: Oak Ridge National Laboratory, 1960.

[27] R. Sangiorgi, "Corrosion of ceramics by liquid metals," *Corrosion of Advanced Ceramics, NATO Science Series E,* vol. 267, pp. 261-284, 1994.

[28] E. Shchukin and V. Bravinskii, "Reduction in strength of ceramic materials under the influence of molten metals," *Soviet Materials Science,* vol. 4, no. 3, pp. 216-219, 1968.

[29] A. Nayeb-Hashemi, J. Clark and L. Swartzendruber, "The Fe-Mg (Iron-Magnesium) system," *Bulletin of Alloy Phase Diagram,* vol. 6, no. 3, p. 235, 1985.

[30] P. Merica and R. Waltenberg, *Technical Papers of, National Bureau of Standards (USA),* vol. 19, pp. 155-182, 1925.

[31] A. Nayeb-Hashemi and J. Clark, "The Mg-Ni (Magnesium-Nickel) system," *Bulletin of Alloy Phase Diagram,* vol. 6, no. 3, pp. 238-239, 1985.

[32] K. Micke and H. Ipser, *Monatsh. Chemistry,* vol. 127, pp. 7-13, 1996.

[33] P. Bagnoud and P. Peschotte, *Z. Metallkunde,* vol. 127, pp. 114-120, 1978.

[34] Q. Hong and F. d'Heurle, "The dominant difusing species and initial phase formation in Al-Cu, Mg-Cu and Mg-Ni systems," *Journal of Applied Physics,* vol. 72, p. 4036, 1992.

[35] C. Tsao and S. Chen, "Interfacial reactions in the liquid diffusion couples of Mg/Ni, Al/Ni and Al/ (Ni)-Al2O3 systems," *Journal of Materials Science,* vol. 30, pp. 5215-5222, 1995.

[36] C. Roberts, Magnesium and Its Alloys, New York: John Wiley and Sons, 1960.

[37] M. Yan and Z. Fan, "Durability of materials in molten aluminum alloys," *Journal of Materials Science,* vol. 36, pp. 285-295, 2001.

[38] J. Viala, D. Pierre, F. Bosselet, M. Peronnet and J. Bouix, "Chemical interaction processes at the interface between mild steel and liquid magnesium of technical grade," *Scripta Materialia,* vol. 40, no. 10, pp. 1185-1190, 1999.

[39] C. Tang, Soldering in magnesium high pressure die casting and its prevention by surface engineering, Hawthorn, VIC, Australia: Swinburne University of Technology, 2007.

[40] C. Brooks, Heat Treatment, Structure and Properties of Non-ferrous Alloys, Metals Park, OH: ASM International, 1982.

[41] E. Agnion and B. Bronfin, in *Proceedings of the 3-rd International Magnessium Conference, p. 313*, The Institute of Materials, London, 1997.

[42] R. Bruscato, "Liquid metal embrittlement of austenitic stainless steel when welded to galvanized steel," *Welding Research Supplement,* vol. December, pp. 455-s-460-s, 1992.

[43] H. Martinz, B. Nigg and A. Hoffmann, "The corrosion behavior of refractory metals against molten and evaporated zinc," in *The 17th Plansee Seminar*, Reutte, Austria, 2009, RM 56A1-7.

[44] S. Wilson, A. Kvithyld, T. Engh and G. Tranell, "Oxidation of manganese-containing aluminum alloys studied by SEM," *Materials Science Forum,* Vols. 794-796, pp. 1095-1100, 2014.

[45] C. Tang, M. Jahedi and Brandt, "Investigation of the soldering reaction in magnesium high pressure die casting dies," in *2002 International Tooling Conference*, Karlstad, Sweden, 2002.

[46] D. Pierre, J. Viala, M. Peronnet, F. Bosselet and J. Bouix, "Interface reactions between mild steel and liquid Mg-Mn alloys," *Materials Science and Engineering A,* vol. 349, pp. 256-264, 2003.

[47] D. Pierre, M. Peronnet, F. Bosselet, J. Viala and J. Bouix, "Chemical interaction between mild steel and liquid Mg-Si alloys," *Materials Science and Engineering B,* vol. 94, pp. 186-195, 2002.

[48] D. Pierre, F. Bosselet, M. Peronnet, J. Viala and J. Bouix, "Chemical reactivity of iron base substrates with liquid Mg-Zr alloys," *Acta Materialia,* vol. 49, pp. 653-662, 2001.

[49] K. Humberstone, "Method of forming crucibles for molten magnesium". USA Patent 4,424,436, 3 January 1984.

[50] K. Humberstone, "Crucibles for molten magnesium and method of forming". USA Patent 4,353,535, 12 October 1982.

[51] J. Leland, "Method for protecting austenitic stainless steels from solvent attack by molten magnesium by forming crucible". US patent 5,227,120, 13 July 1993.

[52] A. Ditze and C. Sharf, Recycling of Magnesium, Clausthal-Zellerfeld: Papierfllleger Verlag, 2008.

[53] "Forging improves magnesium die casting," Industry Sourcing, [Online]. Available: http://www. industrysourcing. com/articles/255033. aspx. [Accessed 15 06 2014].

[54] S. Moore, "Magnesium molding-technique expands options," *Modern Plastics,* vol. July, p. 33, 2002.

[55] K. Kono, "Method and apparatus for manufacturing parts by fine die casting". US patent 5,983,976, 16 November 1999.

[56] S. Moore, "Thixotropic molding broadens process capabilities," *Modern Plastics,* vol. March, pp. 24-30, 2002.

[57] F. Czerwinski, "Near-liquidus injection molding process". US Patent 7,255,151, 2007 August 2007.

[58] L. Rogal, F. Czerwinski, L. Litynska-Dobrzynska, P. Bobrowski, A. Wierzbica-Miernik and J. Dutkiewicz, "Effect of hot rolling and equal-channel angular pressing on generation of globular microstructure in semi-solid Mg-3%Zn alloy," *Solid State Phenomena,* Vols. 217-218, pp. 381-388, 2015.

[59] F. Czerwinski, "Semisolid processing of magnesium alloys: microstructure-properties relationship," *Soli State Phenomena,* Vols. 217-218, pp. 3-7, 2015.

[60] F. Czerwinski, "Metal molding conduit assembly of metal molding system". US Patent 20090107646, 30 April 2009.

[61] T. Ozben, A. Yardimended and O. Cakir, "Stress analysis of shrink-fitted pin-pin hole connections via Finite Element Method," *Journal of AMME,* vol. 25, pp. 45-48, 2007.

[62] J. Gordine, "Some problems of welding of Inconel 718 alloy," *Welding and Research Supplement of AWS,* vol. November, pp. 480s-484s, 1971.

[63] J. Kelly, "Speciality alloys welding," Rolled Alloys, 2002. [Online]. Available: http:// www. rolledalloys. ca. [Accessed 29 07 2014].

[64] "Prior Art Database: IPCOM000012407D Bimetallic barrel head for processing corrosive metals and a method of manufacturing thereof," 03 05 2003 UTC USA. [Online]. Available: https://priorart. ip. com. [Accessed 24 07 2014].

[65] J. Cassina and I. Machado, "Low-stress sliding abrasion resistance of cobalt-based surfacing deposits welded with different processes," *Welding Research Supplement AWS,* vol. April, pp. 133s-138s, 1992.

[66] H. Gedda, Laser cladding: an experimental and theoretical investigation, Ph. D. Thesis: Lulea University of Technology, 2004.

[67] J. Wang, S. Prakash, Y. Joshi and F. Liou, "Laser aided part repair-a review," University of Missouri-Rolla, [Online]. Available: http://utwired. engr. utexas. edu/lff/

symposium/proceedingsArchive/pubs/Manuscripts/2002/2002-07-Wang. pdf. [Accessed 03 06 2014].

[68] S. Ocylok, A. Weisheit and I. Kelbassa, "Functionally graded multi-layers by laser cladding for increased wear and corrosion resistance," *Physics Procedia,* vol. 5, pp. 359-367, 2010.

[69] "Laser cladding of Stellite 1 on AISI 4340 steel," University of Waterloo, [Online]. Available: http://alfa. uwaterloo. ca/Research. html. [Accessed 03 06 2014].

[70] M. Gooover, Fundamentals of Modern Manufacturing: Materials, Processes, and Systems, Hoboken, NJ: John Wiley & Sons Ltd, 2010.

[71] "Highly wear resistant barrels for extrusion and injection molding," Reiloy Reifenhausergroup, [Online]. Available: http://www. reiloy. com/fileadmin/reiloy/download/zylinder_A4_engl. pdf. [Accessed 25 07 2014].

[72] H. Atkinson and S. Davis, "Fundamental aspects of hot isostatic pressing: an overview," *Metallurgical and Materials Transactions A,* vol. 31, p. 2981, 2000.

[73] K. Pinnow et al., "Injection system of high density powder of cobalt, chromium, tungsten carbide". US patent 5996679 A, 7 November 1999.

[74] "HIP-Cladding," Avure Technologies, [Online]. Available: http://industry. avure. com. [Accessed 29 07 2014].

[75] F. Czerwinski, "Thermochemical treatment of metals," in *Heat Treatment-Conventional and Novel Applications Edited by F. Czerwinski*, Rijeka, INTECH, 2012, pp. 73-112.

[76] H. Du, M. Sommers and J. Agren, *Metallurgical and Materials Transactions A,* vol. 31, p. 2981, 2000.

[77] K. Antymidis, G. Stergioudis, D. Roussos, P. Zinoviandis and D. Tsipas, "Boriding of ferrous and non-ferrous metals and alloys in fluidized bed reactor," *Surface Engineering,* vol. 28, pp. 255-259, 2002.

[78] S. Timur et al, "Ultra-fast boriding of metal surfaces for improved properties". US Patent 2010/0018611 A1, 28 January 2010.

[79] U. Sen, "Friction and wear properties of thermo-reactive diffusion coatings against titanium nitride coated steels," *Materials and Design,* vol. 26, no. 2, pp. 167-174, 2005.

[80] T. Arai, "Tool treatment extends core and pin life in die casting operations," *Die Casting Engineer*, vol. March/April, 1999.

[81] K. Strattford, C. Subramanian and T. Wilks, Surface Engineering vol. II: Engineering Applications, Cambridge, UK: Royal Society of Chemistry, 1993.

[82] T. Ohmi and M. Iguchi, "Bonding strength of interafce between cast Mg-Al alloy and cast-in inserted transition metal cores," *Journal of JSEM,* vol. 13, pp. s189-s193, 2013.

[83] "Magnesium Melting Crucibles," W. Pilling, Kesselfabrik GmbH & Co, KG, Altena, D-58762 Germany

[84] "Magnesium die casting," [Online]. Available: http://www. dynacast. com. [Accessed 17 07 2014].

[85] "Products for cold and hot chamber die casting of magnesium," [Online]. Available: www. omb-brondolin. com. [Accessed 5 07 2014].

[86] "Materials datasheets," Exocor, 2014. [Online]. Available: www. exocor. com. [Accessed 2 09 2014].

[87] Metals Handbook Vol 2, Materials Park, OH: ASM International, 1990.

[88] "High performance steels for die casting," Kind & Co Edelstahlwerk, [Online]. Available: www. kind-co. de. [Accessed 02 09 2014].

[89] "PVD Coatings Application Guide," Chessen Group Inc., Mississauga, Ontario, 2000.

[90] F. Lofaj et al., "Nanohardness and tribological properties of nc-TiB2 coatings," *Journal of the European Ceramic Society*, vol. 33, pp. 2347-2353, 2013.

[91] "Certess SD Titanium Boron Nitride Coating," HEF USA, [Online]. Available: www. hefusa. net. [Accessed 2 09 2014].

Edited by Frank Czerwinski

Magnesium alloys with their unique physical and chemical properties are important candidates for many modern engineering applications. Their density, being the lowest of all structural metals, makes them the primary choice in global attempts aimed at reducing the weight of transportation vehicles. However, magnesium also creates challenges at certain stages of raw alloy melting, fabrication of net-shape components and their service. The first one is caused by very high affinity of magnesium to oxygen, which requires protective atmospheres increasing manufacturing cost and heavily contributing to greenhouse gas emissions. The second challenge relates to very high corrosivity of liquid magnesium towards materials it contacts. This imposes restrictions on the selection of materials used to contain, transfer or process molten magnesium during manufacturing operations. A mixture of unique benefits and serious challenges of magnesium alloys in solid and liquid states described here makes the book very useful for a broad audience of scientists and engineers from academia and industry.

ISBN 978-953-51-6366-4

Photo by CGinspiration / DollarPhoto

IntechOpen